

The Pennsylvania State University
The Graduate School
College of Earth and Mineral Sciences

DESIGNING ION-CONTAINING POLYMERS FOR FACILE ION TRANSPORT

A Dissertation in
Materials Science and Engineering
by

Wenjuan Liu

© 2014 Wenjuan Liu

Submitted in Partial Fulfillment
of the Requirements
for the Degree of

Doctor of Philosophy

August 2014

The dissertation of Wenjuan Liu was reviewed and approved* by the following:

Ralph H. Colby

Professor of Materials Science and Engineering and Chemical Engineering
Dissertation Advisor
Chair of Committee

Michael J. Janik

Associate Professor of Chemical Engineering
Dissertation Co-Advisor

James P. Runt

Professor of Polymer Science

Michael A. Hickner

Associate Professor of Materials Science and Engineering

Gary L. Messing

Distinguished Professor of Ceramic Science and Engineering
Head of the Department of Materials Science and Engineering

*Signatures are on file in the Graduate School

ABSTRACT

The development of polymer electrolytes with sufficient ionic conductivity will enable the design of flexible, efficient Li ion batteries and is also of primary interest for actuators, alternative battery membranes, and within the membrane-electrode assembly of fuel cells. Optimization of ionic polymer (ionomer) compositions will provide single-ion conductors with the required conductivity for energy conversion applications, and further, that the identification of optimal compositions can be facilitated.

Ab initio methods use the first principles of quantum mechanics to determine the electronic state of a system, and can therefore quantify interaction energies between species without parameterization from experimental studies. A bottom-up design strategy based on *ab initio* calculations can be rapidly applied to a wide variety of anions and cations in different polar media, enabling a detailed understanding of ion interactions and solvation by polar groups, in the aim of suggesting anion, polar side group, backbone combinations worthy of synthesis. Collaboration with on-going experimental efforts on ionomer synthesis and dielectric spectroscopy that measures populations of conducting ions and ion pairs, will allow for realization of ionomer compositions suggested by theory, as well as serve to validate models.

TABLE OF CONTENTS

List of Figures	vi
List of Schemes	xvi
List of Tables	xvii
Acknowledgements.....	xx

Chapter 1 Introduction and Motivation	1
1.1. U.S. Energy Facts	1
1.2. Electric vehicles.....	3
1.3. Rechargeable Batteries	6
1.4. Rechargeable Lithium Ion Batteries	8
1.4.1. Liquid electrolyte lithium-ion batteries	8
1.4.2. Solid State Lithium-Polymer Batteries.....	11
1.4.3. Can we achieve 158 hp with single-ion conductor lithium batteries?.....	13
1.5. Ionomeric Single-Ion Polymer Conductors	16
1.5.1. Application in Li Ion Battery	16
1.5.2. Application in Ionic Actuators	18
1.6. Dielectric Spectroscopy and Electrode Polarization Analysis.....	30
1.6.1. What is Electrode Polarization?	30
1.6.2. How to Separate Conducting Ion Concentration and Ion Mobility from Conductivity with EP Analysis	33
1.6.3. A Macroscopic Model for Actuation.....	35
1.7. Ion Size and Diffusion Coefficient	36
1.7.1. How to Estimate Ion Size	36
1.7.2. How to Estimate Ion Diffusion Coefficient.....	40
1.8. Physical Fundamentals of Dielectrics – Static Dipoles	43
1.9. Some basics about ab initio Calculations	49
1.10. Ion/Molecule Equilibria & Van 't Hoff Equation	53
References.....	56

Chapter 2 First Principles Design of Ionomers for Facile Ion Transport..	60
2.1. Introduction.....	61
2.2. Computational Methods.....	64

2.3. Interactions and Dipoles of Isolated Ion Pairs	71
2.4. Polarizable Continuum Model for Solvation and Dielectric Constant	75
2.5. Specific Solvation with Dimethyl Ether	81
2.6. A Simple Four-State Model based on 0 K Interactions in Vacuum	85
2.7. Conclusion	89
References	91
Chapter 3 A Four-State Model to Screen for Weak Association of Ion Pairs	95
3.1. Introduction.....	95
3.2. Association energies of various ion states using a simple hard sphere model	103
3.3. Four-State Model and Quadrupole-Pair-Triple Ion (QPT) State Diagram	117
3.3.1. Background on Four-State Model Analysis in ionomer systems	117
3.3.2. The Quadrupole-Pair-Triple Ion (QPT) State Diagram.....	123
3.3.3. Explanations for trends in the QPT diagram	128
3.3.4. Validation of QPT-State Diagram Predictions	138
3.4. Inspirations from the QPT State Diagram	147
3.4.1. F ⁻ Anion Battery	147
3.4.2. Li ⁺ Cation Battery.....	151
3.5. Summary.....	154
References	156
Chapter 4 The Applications of Four State Model in Rational Ionomer Design and Understanding the Dynamics and Ion Conduction Mechanism in Ionomers	160
4.1. Background of Four State Model	160
4.2. Lithium Ion Conduction of Polysiloxane Single-Ion Conductors Containing Novel Weak-Binding Borates.....	167
4.3. Ionic Conduction and Dielectric Response of Poly(imidazolium acrylate) Ionomers	182
4.4. Influence of various cationic counterions on Tg of PEO-based polyurethane carboxylate ionomers.....	197
4.5. Summary.....	208
References	211

LIST OF FIGURES

Figure 1.1: U.S. Primary Energy Consumption by Source and Sector, 2012 (Quadrillion Btu)..	2
Figure 1.2: Comparison of the power density and energy density for batteries, capacitors, and fuel cells.....	5
Figure 1.3: Discharging and charging mechanism of a lithium-ion rechargeable battery.	9
Figure 1.4: Rechargeable Li-metal battery. Dendrite formation on a lithium electrode causes capacity loss by redistributing lithium from the bulk to isolated islands in the electrolyte....	10
Figure 1.5: Conductivity as a function of temperature for six conducting polymer electrolyte systems in solid state lithium-polymer batteries. 1. First generation: PEO-LiCF ₃ SO ₃ ; 2. Newer solute with higher dissociation: PEO-LiTFSI; 3. Low- <i>T_g</i> combination polymer; 4. Plasticized polymer electrolyte: PEO-LiTFSI+25% w/w PEG-dimethylether; 5. Gel-type polymer: PEO-dimethacrylate-LiTFSI-PC70%; 6. Gel electrolyte: P(VDF-HFP)/EC/DMC-LiPF ₆ . Data collected by U Hyeok Choi.....	12
Figure 1.6: Li ⁺ cation in PEO-based ionomer a) solvated by -C≡N polar group attached to polymer backbone, b) solvated by a cation acceptor, 12-Crown ether... ..	17
Figure 1.7: Ionic polymer metal composites are a form of artificial muscle that depends on the movement of ions for motion. Flexible metal foils sandwich a wet polymer filling. With the foils oppositely charged, free ions flow toward one side, expanding it and bending the actuator.....	18
Figure 1.8: Steric hindrance effect on ion pair interaction energy, which exponentially leverages the conducting ion concentration.....	20
Figure 1.9: Exploring steric hindrance effect by comparison of relative dissociation energy to LiF of bulky cation tetraethyl ammonium with F ⁻ , bulky anion tetraphenyl borate with Li ⁺ and an ionic liquid formed by these bulky cations and anions.....	21

Figure 1.10: Ion pairing energy as a function of reciprocal distance from the cation to the charge center of the anion. Anions are indicated by different symbols in the legend with cations and indicated in the plot: Li = lithium, Na = sodium, K = potassium, TMA = tetramethyl ammonium, TBA = tetrabutyl ammonium, EBI = ethylbutyl imidazolium.....	22
Figure 1.11: Comparison of the dissociation energy of F^- with 19 bulky cations, using the pairing energy of LiF as the reference..	23
Figure 1.12: Comparison of the dissociation energy of Li^+ with 19 bulky anions.	24
Figure 1.13: Comparison of the dissociation energy of small ion (Li^+ or F^-) with its bulky counterion and ionic liquids.....	25
Figure 1.14: Comparison of pairing energy of F^- with hydrocarbon ammonium cation, TBA^+ , and O containing ammonium cations. Replacing CH_2 by O on alkyl cations weakens the ion pair interaction.....	26
Figure 1.15: Comparison of pairing energy of Li^+ with hydrocarbon borate cation ($TPhB^-$, $TBuB^-$) and O containing borate cations. Apparently, replacing C by O on anions enhances the ion pair interaction, which works oppositely as replacing H by F.	27
Figure 1.16: Structure of a series of IL monomers used in Dr. Hiroyuki Ohno's group to synthesize PILs to study the effect of cation structure on their electrochemical and thermal properties.	28
Figure 1.17: Schematic of a single ion conductor with cations fixed along the polymer chains and the anions as mobile counterions between two electrodes in the dielectric spectrometer.....	31
Figure 1.18: Schematic of electrode polarization occurs at low frequencies.	31
Figure 1.19: The electrode polarization relaxation	32
Figure 1.20: Molecular structures and molecular dimensions of 1-ethyl-3-methyl-imidazolium ($[EMI^+]$), 1-butyl-3-methylimidazolium ($[BMI^+]$), Tetrafluoroborate ($[BF_4^-]$) and Trifluoromethanesulfonate ($[Tf^-]$)...	39

- Figure 1.21: Experimental values of limiting ionic conductivity (Λ_0) and the Walden product ($\Lambda_0\eta_0$) of rigid, monpositive ions in water (*open triangle*), acetonitrile and fomamide (*open squares*) at 298 K are plotted as a function of the inverse of the crystallography ionic radius (r_{ion}^{-1}).. 42
- Figure 2.1: Schematic anion-cation interaction potential energy surface (black curve) including perturbations introduced by changes in the ionomer composition that sterically hinder ions (red dashed), raise dielectric constant ϵ (blue) or solvate ions (green).. 63
- Figure 2.2: Dipole moment of neutral polar small molecules calculated by B3LYP/6-31+G* (filled circles) and MP2/6-311+G* (open circles) plotted versus experimentally measured values in the vapor phase... 67
- Figure 2.3: Comparison of calculated and experimental interaction enthalpies and free energies between neutral polar small molecules with a Li^+ cation. Filled symbols are calculated with B3LYP/6-31+G* and open symbols with MP2/6-311+G*. Blue circles represent interaction enthalpies and pink triangles represent interaction free energies, both with zero-point vibrational energy.. 70
- Figure 2.4: Equilibrium pair structures of a) Li-methyl sulfonate, b) Li-methyl phosphonate, c) Li-methyl carboxylate, and d) Li-tetraphenylborate.. 73
- Figure 2.5: The PCM molecular cavities of three ion pairs a) $\text{Li}[\text{TfO}]$, b) LiF , and c) $[\text{TMA}][\text{TfO}]$ in the presence of diethylether... 77
- Figure 2.6: Ion pairing energies with no ZPVE correction for six salts as a function of reciprocal dielectric constant of the PCM medium..... 78
- Figure 2.7: PCM calculated ion interaction energies with no ZPVE correction for six salts as a function of reciprocal of the product of dielectric constant ϵ and cation-anion distance d , defined carefully in the first paragraph of Section 2.4. The line is the Coulomb energy (Equation 2.2)..... 80
- Figure 2.8: The cumulative specific solvation energy from interaction with 1 to 6 dimethyl ether molecules for cations (blue) Li^+ and Na^+ ; anions (green) $\text{C}_6\text{H}_5\text{SO}_3^-$ (benzene sulfonate) and CF_3SO_3^- (triflate) and their four ion pairs (red and black)... 82

Figure 2.9: The specifically solvated pair interaction energy of $\text{Li}^+ \text{C}_6\text{H}_5\text{SO}_3^-$ (red circles), $\text{Li}^+ \text{CF}_3\text{SO}_3^-$ (red crosses), $\text{Na}^+ \text{C}_6\text{H}_5\text{SO}_3^-$ (black down triangles) and $\text{Na}^+ \text{CF}_3\text{SO}_3^-$ (black up triangles), in the gas phase (no PCM) as functions of the number of dimethyl ether molecules interacting with the ions and the ion pairs.....	83
Figure 2.10: Equilibrium structures of $\text{Li}-(\text{C}_6\text{H}_5)\text{SO}_3$ species, a) pair, b) negative triple ion, c) positive triple ion, and d) quadrupole.	87
Figure 3.1: In ionomers, nearly all counterions are strongly condensed onto the ion that is covalently bonded to the chain, and additionally these neutral ion pairs may form neutral aggregates, such as the quadrupoles shown here. These physical crosslinks increase the T_g of the ionomer and lower ionic conductivity.	96
Figure 3.2: Combined SAXS and WAXD intensities (arbitrary units and offset for clarity) as a function of scattering wavevector for the sodium salt of sulfonated polyester ionomers made from $M = 400, 600$ and 900 g/mol PEG, and a neutral polymer (PE400-0) made from $M = 400$ g/mol PEG and a neutral isophthalate. The peak at $q = 1.8 \text{ \AA}^{-1}$ is the amorphous halo of PEO. There is no large-scale aggregation / microphase separation in these single-ion conductors.....	98
Figure 3.3: a) Wide-angle X-ray scattering intensity from PEG600-100%M ($M = \text{Li, Na, Cs}$) and PEG600-0% normalized by sample thickness, collection time, and percent of transmission. b) Difference intensity of PEG600-100%M after subtracting scattering intensity of PEG600-0% from PEG600-100%M.....	99
Figure 3.4: Equilibrated configurations for a Li – benzene sulfonate ion pair, quadrupole, and 8-ion-pair ion chain, each equilibrated at 0 K in vacuum using <i>ab initio</i> calculations..	100
Figure 3.5: Structures of two types of triple ions.....	105
Figure 3.6: Structures and force analysis of two types of quadrupoles, A, D and C, B are of opposite charge	106
Figure 3.7: Structure and force analysis of a four-ion single chain.....	106
Figure 3.8: Structures of a five-ion chain and n -ion single chain.....	107

Figure 3.9: The ratio of energies of n -ion single chains and an isolated ion pair as the function of numbers of ions in the chain.	108
Figure 3.10: Structures of 2D 4, 9, 16 and 25- ion square sheets... ..	109
Figure 3.11: Comparison of energy levels of $n/4$ quadrupoles, n -ion single chain, n -ion double ion chain and n -ion square sheet as functions of the number of ions in the ion structures.	110
Figure 3.12: The ratios of quadrupole, double ion chain and square ion sheet energies to single ion chain energy as functions of the number of ions.	112
Figure 3.13: The configurations for a Li / Na / Cs– benzene sulfonate 5 / 6 / 7 / 8 ion pair – double ion chains built in Chem3D and MM optimized... ..	114
Figure 3.14: The relative energies of possible coordination states of Li^+ ions in an ionomer with benzene sulfonate anionic groups. (a) a quadrupole state with two Li^+ cations shared between two anionic groups, (b) an ion pair state, (c) a triple ion state, and (d) the free ion state. All of these ion states expose cations for solvation from the surrounding media; such solvation is only shown here for the free ions.....	118
Figure 3.15: Populations of ion states as a function of binding energy of a contact pair: circles are free ions, squares are ion pairs, diamonds are quadrupoles, triangles are higher order aggregates.....	120
Figure 3.16: Two equilibria in ionomers depicted by the simple hard sphere model: On the left one quadrupole is in equilibrium with two pairs; and on the right two asymmetric triple ions are in equilibrium with three pairs.....	123
Figure 3.17: The Quadrupole-Pair-Triple Ion (QPT) State Diagram, plotting the triple ion factor against the quadrupole factor	125
Figure 3.18: QPT diagram for fluoride anions with a variety of cations. Extrema are noted: TMP^+ is tetramethyl phosphate, TEP^+ is tetraethyl phosphate, TBP^+ is tetrabutyl phosphate and $\text{TrB}(\text{CCOC})\text{P}^+$ is the only other phosphate cation studied. The three cations closest to the hard sphere expectation point (1.293, 1.0) are Li^+ , Na^+ and K^+	127
Figure 3.19: QPT diagram for eight anions with a variety of cations.....	128

Figure 3.20: Comparison of tetrabutyl ammonium (left) and tetrabutyl phosphonium (right) Mulliken charge distributions	132
Figure 3.21: General structure of the size mismatched hard-sphere quadrupole and the angular dependence of the quadrupole potential energy well (see Equation 3.5).	133
Figure 3.22: Two possible contact ground states of size mismatched quadrupoles. ...	134
Figure 3.23: The contact quadrupole is the ground state of highly asymmetric ions ..	135
Figure 3.24: The stable quadrupole with weakly asymmetric hard sphere ions (with $0.414 < s < 1$) always has $\theta = \pi/4$, with quadrupole factor identical to the symmetric case.....	135
Figure 3.25: Quadrupole factors of asymmetric ions with anion larger than cation at 0 K in vacuum.....	136
Figure 3.26: Quadrupole factors of asymmetric ions at 0 K in vacuum. For $0.414 < s < 2.415$, $E_Q/2E_p$ is identical to the symmetric hard sphere model, for $0.121 < s < 0.414$ or for $2.415 < s < 8.264$, contact quadrupoles are the ground state, and for extremely asymmetric quadrupoles with $s < 0.121$ or $s > 8.264$, linear ion chains are the ground state of four ions.....	137
Figure 3.27: QPT-State Diagram of $[\text{MEBIm}]^+ [\text{TfSI}]^-$, $[\text{MEBIm}]^+ [\text{BF}_4]^-$, $[\text{MEBIm}]^+ [\text{PF}_6]^-$, representing poly(MEBIm-TfSI), poly(MEBIm-BF ₄) and poly(MEBIm-PF ₆)	141
Figure 3.28: Measured dielectric response showing the electrode polarization relaxation via the in-phase dielectric constant ϵ' (blue), the out-of-phase dielectric loss ϵ'' (red), $\tan\delta = \epsilon''/\epsilon'$ (green), and the in-phase part of the conductivity σ' (purple) for poly(MEBIm-TfSI) at 50°C ($T_g + 62\text{K}$), with peak frequencies, dielectric constant after polarization ϵ_{EP} , and static dielectric constant (a material property without electrode polarization) ϵ_s , and d.c. conductivity σ_{DC} denoted. Data of U Hyeok Choi.....	142
Figure 3.29: The frequency dependence of dielectric constant for poly(MEBIm) at 50 °C with three different anionic counterions (TfSI ⁻ green > BF ₄ ⁻ red ≥ PF ₆ ⁻ blue). Data of U Hyeok Choi.....	143

- Figure 3.30: Temperature dependence of static dielectric constant ϵ_s of poly(MEBIm) ionomers with three different counterions TfSI (green) $>$ BF_4^- (red) \geq PF_6^- (blue). Data of U Hyeok Choi. 144
- Figure 3.31: Fractions of conducting ions (lower, filled symbols) and ion pairs (upper, open symbols) as a function of inverse temperature for poly(MEBIm) ionomers with three different counterions TfSI (green) $>$ BF_4^- (red) \geq PF_6^- (blue). Data of U Hyeok Choi 146
- Figure 3.32: The comparison of interaction energies of F^- (green), Li^+ (red) and Na^+ (blue) with various neutral molecules representing polar groups of interest 149
- Figure 3.33: Comparison of QPT Diagrams for F^- with Li^+ , each paired with varieties of counterions. Li^+ only has very low quadrupole factor for tetra-substituted borates (tetrabutyl borate and tetraphenyl borate) while F^- has many choices of cation to pair with that have even lower quadrupole factors (mostly phosphonium cations)..... 150
- Figure 3.34: Comparison of QPT Diagrams for F^- with OH^- for a wide range of cations.. 151
- Figure 3.35: R_4B^- ($\text{R} = \text{Et}, \text{Bu}, \text{Ph}, \text{PrFPh}, \text{etc.}$). TFSI has high conducting ion concentration..... 152
- Figure 3.36: The equilibrated ion pair for lithium tetraphenyl borate shows that the Li^+ cation goes between two of the negatively charged benzene rings making it challenging for such ion pairs to form quadrupoles.. 153
- Figure 4.1: Schematics of the relative energies of possible coordination states of Li^+ ions in an ionomer with benzene sulfonate anionic groups (inset). (a) a quadrupole coordination with two Li^+ cations shared between two anionic groups, (b) an ion pair coordination, (c) a triple ion coordination, and (d) the separated ions are coordinated with neutral, polar ionomer side-chain or backbone groups. These four states are all solvated by the ionomer with the dielectric constant ϵ 162
- Figure 4.2: Temperature dependence of (a) static dielectric constant ϵ_s with lines shown as predictions of the Onsager equation and (b) Kirkwood g factor for

ethylene carbonate, propylene carbonate, CECA monomer and CECA siloxane homopolymer.	172	
Figure 4.3: Electronic charge distribution in (a) tetraphenyl borate anion and (b) perfluorinated tetraphenyl borate anion, calculated by Gaussian 03 using the B3LYP/6-31+G* basis set. Light green denotes a positive charge; red denotes a negative charge, with brighter red indicating stronger negative charge. The boron in the center of these borate anions is positively charged. The tetraphenyl borate anion has the negative charge distributed on the 24 carbons in the phenyl rings, particularly the ortho carbons (each with roughly $-0.5e$). The perfluorinated tetraphenyl borate anion has the negative charge distributed on the 20 fluorines (roughly $-0.3e$ each), with strong positive charge on boron (roughly $+0.5e$), the alpha carbons (roughly $+0.7e$) and the para carbons (roughly $+0.8e$). The charge distributions impart strong dipoles to these anions (shown by arrows) of 16 D for tetraphenyl borate and 13 D for perfluorinated tetraphenyl borate..		173
Figure 4.4: Chemical structures of a) lithium triphenylstyrylborate (B1); b) lithium triphenyl(4-((2-(2-vinyloxy)ethoxy)ethoxy)methyl) phenyl) borate (B2) and c) lithium tris (perfluorophenyl) (2,3,5,6-tetrafluoro-4-(2-(2-vinyloxy) ethoxy)ethoxy)phenyl) borate (B3)..		174
Figure 4.5: Synthesis of comb polysiloxanes with CECA and B1, (B2, or B3 anions) as side chains.....		175
Figure 4.6: Temperature dependence of ionic conductivity for siloxane borate ionomers vs. T/T_g (and vs. $1000/T$ in the inset). The short EO spacer between the borate ion and the siloxane backbone raises the conductivity by lowering T_g		179
Figure 4.7: Temperature dependence of simultaneously conducting ion concentrations for three siloxane borate ionomers with borate fraction 5%.		179
Figure 4.8: Chemical structures of poly(N-alkylimidazolium acrylate)s <i>a–d</i> and nonionic polymer <i>e</i>		186
Figure 4.9: Temperature dependence of ionic conductivity for PF_6^- and Tf_2N^- ionomers. Tf_2N^- (C₄-Tf₂N (b) and C₁₂-Tf₂N (d)) ionomers have consistently higher conductivities than PF_6^- (C₄-PF₆ (a) and C₁₂-PF₆ (c)) ionomers. The inset shows ionic conductivity at room temperature as a function of glass transition temperature for these four ionomers (a (■), b (●), c (▲), and d (▼))..		187

Figure 4.10: Temperature dependence of simultaneously conducting ion concentration p . Solid (PF_6^- ionomers) and dashed (Tf_2N^- ionomers) lines are Arrhenius fits to Equation 4.14 with two fitting parameters (E_a and p_∞ , listed in Table 4.5). The inset displays the fraction of anions simultaneously participating in conduction (p divided by the total anion concentration p_0)..... 189

Figure 4.11: Temperature dependence of simultaneously conducting ion mobilities for PF_6^- and Tf_2N^- ionomers, determined from (1) the EP model (filled symbols) and (2) dividing the DC conductivity data by the product of the elementary charge e and the Arrhenius fit to Equation 4.14 of simultaneously conducting ion number density p (open symbols, referred to as extended mobility). Tf_2N^- ionomers ($\text{C}_4\text{-Tf}_2\text{N}$ (b) and $\text{C}_{12}\text{-Tf}_2\text{N}$ (d)) have consistently higher mobilities than PF_6^- ionomers ($\text{C}_4\text{-PF}_6$ (a) and $\text{C}_{12}\text{-PF}_6$ (c))..... 191

Figure 4.12: Temperature dependence of static dielectric constant ϵ_s for imidazolium-based ionomers and a non-ionic polymer. The lines are predictions of the Onsager equation with fixed concentration and strength of dipoles: the purple dotted line is Equation 4.15 for non-ionic polymer e with $\sum_i v_i m_i^2 / (9\epsilon_0 k) = 249 \text{ K}$ as the sole fitting parameter and the colored solid and dashed lines are Equation 4.16 for the four imidazolium-based ionomers, assuming all ions exist as isolated contact pairs ($v_{\text{pair}} = p_0$) with dipoles given by the *ab initio* estimates in Table 4.3 and assuming the Kirkwood correlation factor $g=1$ 192

Figure 4.13: Chemical structures of polyurethane anionomer. (The cations' structures are shown in Figure 4.14.) 200

Figure 4.14: Chemical structures of cations studied: Na^+ , Me_4N^+ , Bu_4N^+ , $(\text{EO}_c)_2\text{Me}(\text{MOE})\text{N}^+$, $(\text{MOEOE})_3\text{MeN}^+$, BuMeIm^+ , $(\text{MOE})\text{MeIm}^+$, Bu_4P^+ , $\text{Bu}_3(\text{MOE})\text{P}^+$ (from left to right, top to bottom) 201

Figure 4.15: T_g from DSC as a function of reciprocal size of corresponding acetate salts (assuming the same density ρ of 1.0 g/cm^3). Open symbols are cations containing ether oxygen. Solid symbols are cations without ether oxygen. Purple X is Na^+ ; orange plus is Me_4N^+ ; cyan solid star is BuMeIm^+ ; pink open star is $(\text{MOE})\text{MeIm}^+$; green open square is $(\text{EO}_c)_2\text{Me}(\text{MOE})\text{N}^+$; dark red solid diamond is Bu_4N^+ ; blue solid triangle is Bu_4P^+ ; olive green open

triangle is $\text{Bu}_3(\text{MOE})\text{P}^+$; red open circle is $(\text{MOEOE})_3\text{MeN}^+$; solid line is fitting result of equation $T_g = 200 + 65.4 [M/(\rho N_{av})]^{1/3}$ 203

Figure 4.16: T_g from DSC as a function of quadrupole energy at 0K in vacuum. Open symbols are cations containing ether oxygen. Solid symbols are cations without ether oxygen. Purple X is Na^+ ; orange plus is Me_4N^+ ; cyan solid star is BuMeIm^+ ; pink open star is $(\text{MOE})\text{MeIm}^+$; green open square is $(\text{EO})_2\text{Me}(\text{MOE})\text{N}^+$; dark red solid diamond is Bu_4N^+ ; blue solid triangle is Bu_4P^+ ; olive green open triangle is $\text{Bu}_3(\text{MOE})\text{P}^+$; red open circle is $(\text{MOEOE})_3\text{MeN}^+$; dash line is acid form for the reference.. 205

LIST OF SCHEMES

Scheme 3.1: PEG-based sulfonated polyester ionomers with well-defined PEG spacer (PEG M_n = 400, 600, 900 g/mol, and m = 9, 13, 20). M represents the cationic counterion (M = Li, Na, or Cs) associated with the sulfonate group.....	97
Scheme 3.2: Synthesis of Polymerizable Ionic Liquid MEBIm-BF ₄	138
Scheme 3.3: Structures of Polymerized Ionic Liquid Poly(MEBIm).	140

LIST OF TABLES

Table 1.1: Comparison of battery types in terms of the gravimetric energy density, the volumetric energy density, the gravimetric power density, and the reciprocal cost in watt-hours per dollar.	7
Table 1.2: Molecular weights and densities of four neutral molecules (in analogy to the four ions) and four ionic liquid (formed by the four ions), and their volumes calculated through Equation (1.13).....	37
Table 1.3: Comparison of the sum of molecular volumes of two neutral molecules and that of the ionic liquid, which has the same molecular formula estimated by Equation (1.13)..	38
Table 1.4: Molecular volumes estimated by <i>ab initio</i> method and by molecular weight and density... ..	38
Table 2.1: Comparison of calculated dipole moments with vapor phase measurements for small polar molecules.....	67
Table 2.2: Interaction energies of a Li^+ cation with a series of polar species. Values calculated with B3LYP/6-31+G* and MP2/ 6-311+G* with zero-point vibrational energy correction and thermal corrections are compared with experimentally measured dissociation enthalpies and free energies in kJ/mol.	69
Table 2.3: The mean squared error of the calculated enthalpies and free energies of interaction versus experimental values for the DFT (B3LYP/6-31+G*) and MP2/6-311+G* basis sets.	71
Table 2.4: Ion pair interaction energies (ΔE_{int}) without ZPVE correction, dipole moment (μ), distance calculated from dipole moment ($d \equiv \mu/e$, where e is the elementary charge) and the distance of the Li^+ or Na^+ cation from the sulfur or phosphorus or carbon or boron ($d_{\text{cation-S/P/C/B}}$) of 21 anions.	72
Table 2.5: The names and dielectric constants of the 22 solvents used for PCM solvation calculations.....	76

Table 2.6: Interaction energies of ion pairs, positive triple ions, negative triple ions and quadrupoles for Li^+ and Na^+ cations with various aromatic anions and their perfluorinated counterparts and also tetrabutyl borate for comparison.....	86
Table 3.1: <i>Ab initio</i> calculations of interatomic spacings at 0 K in vacuum for benzene sulfonate with alkali cations ($\text{M} = \text{Li}^+, \text{Na}^+, \text{K}^+$ or Cs^+).....	101
Table 3.2: Comparison of energy levels for all nine possible single-state aggregation states of 12 ions.....	111
Table 3.3: Energies of ion pairs, quadrupoles and ion chains with the same number of ions calculated by <i>ab initio</i> methods for Li / Na / Cs– benzene sulfonate.....	115
Table 3.4: Pair energies, quadrupole factors, triple ion factors and cation – F^- spacings for selected alkali fluorides, ammonium fluorides and phosphonium fluorides..	130
Table 3.5: Ion pair, positive triple ion, negative triple ion, and quadrupole energies and quadrupole factors and triple ion factors of three ionic liquids, representing three ionomers. Dipole moment of the isolated ion pairs are also listed, to be used later	139
Table 3.6: The total ion concentration of the three ionomers calculated from the molecular weight of one repeat unit and the density of the ionomers.	145
Table 3.7: Comparison of estimated ion pairing energies and the energy gain in forming a quadrupole from two ion pairs, for lithium salts with benzene carboxylate, benzene sulfonate, tetraphenyl borate and perfluorinated tetraphenyl borate anions, in PEO-based ionomers at 300K.	154
Table 4.1: Lithium Ion Pair and Positive Triple Ion Energies at 0 K in vacuum (left two columns) and in polar polymers at 300 K (PEO middle two columns; CECA right two columns).....	171
Table 4.2: Physical Properties of Polysiloxane Single-ion Conductors	177
Table 4.3: <i>Ab Initio</i> Interaction Energies and Pair Dipole Moment at 0 K in a Vacuum for 1-Butyl-3-methylimidazolium Cation with Tf_2N^- and PF_6^- Counterions.....	184

Table 4.4: DSC thermal analysis of ionomers..	187
Table 4.5: Fitting Parameters (Equation 4.14) for the Temperature Dependence of the Number Density of Simultaneously Conducting Ions	190
Table 4.6: Refractive Index n and Total Ion Concentration p_0 of ionomers.....	194
Table 4.7: The size of cationacetate salt, ^a glass transition temperature of the ionomers and quadrupole formation energy $\Delta E_{quadrupole}$ ^b of the ion pair in the gas phase calculated by <i>ab initio</i> at 0K in vacuum.....	202
Table 4.8: Charge distribution of Bu_4P^+ , Bu_4N^+ and BuMeIm^+ from <i>ab initio</i> calculations	202

ACKNOWLEDGEMENTS

First and foremost, I would like to express my gratitude and appreciation to my advisor Professor Ralph H. Colby. This research program has been a very enriching learning experience in all aspects, mainly thanks to his continuous support and advice during the past three years.

We are very thankful for the financial support for this research program provided by the National Science Foundation Division of Materials Research, the Department of Energy, and the U.S. Army Research Office.

I am also thankful to Professor Michael J. Janik, who has helped me greatly improve my understanding of the theoretical aspects of my work. I would also like to thank my other committee members, Prof. Runt and Prof. Hickner, for their excellent comments regarding this research. Next, I would like to thank Shih-Wa Wang, U Hyeok Choi, Gregory J. Tudryn, Sheng Liu, Reuben Bushnell, Henry Huai-Suen Shiau and Helen Jing-Han Wang for their support and comments, as well as Dr. Robert Klein for his help in the dielectric spectroscopy measurements.

Finally, I wish to dedicate this work to my parents and my brother, for their love, encouragement and support.

Sept. 29 2009

At State College, PA

Introduction and Motivation

The development of polymer electrolytes with sufficient ionic conductivity will enable the design of flexible, efficient Li ion batteries and such materials are also of primary interest for ionic actuators. Optimization of ionic polymer (ionomer) compositions will provide single-ion conductors with higher ionic conductivity for energy conversion applications, and further, that the identification of optimal compositions can be facilitated. *Ab initio* methods can quantify interaction energies between species without parameterization from experimental studies. Collaboration with on-going experimental efforts on ionomer synthesis and dielectric spectroscopy that measures populations of conducting ions and ion pairs, will allow for realization of ionomer compositions suggested by theory, as well as serve to validate models.

1.1. U.S. Energy Facts

In 2012, the total energy consumed by the United States is 95 Quadrillion Btu. 1 Quadrillion Btu is 293 billion kWh, therefore, the total energy consumed in US in 2012 is 27835 billion kWh. At the price of \$0.12/kWh, it is 3.34 trillion US dollars, 21% of the

GDP of the US in 2012. And every year, the US spends about \$200 billion on energy research, a large amount, but still only 6% of the total energy consumption.

Most of the energy consumed in the US comes from fossil fuels, petroleum 36%, natural gas 27% and coal 18%. Experts claim the world oil consumption will plateau soon, particularly in developed nations that are pushing for greater reliance on renewable energy sources, which supply a relatively small (9%) but steady portion of the U.S. total energy consumption in 2012. Renewable energy breakdown: hydropower 30%, biomass 49%, solar 2%, geothermal 3%, wind 15% (**Figure 1.1.**).

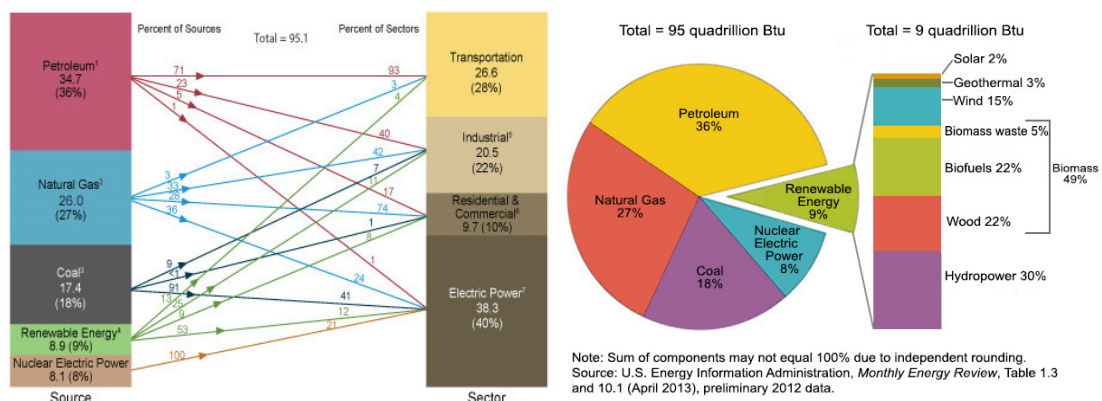


Figure 1.1. U.S. Primary Energy Consumption by Source and Sector, 2012 (Quadrillion Btu) [1,2].

Generation of electricity from renewable resources and the use of electricity in transportation offer great potential to reduce our dependence on foreign oil and reduce global warming caused by CO₂. However, widespread implementation of these and other sources of electrical energy will be possible only if there are effective systems of electrical energy storage. Current electrical energy storage technologies are based on chemical energy storage (batteries) and electrical or electrochemical capacitive energy

storage (capacitors). Batteries store energy in chemical reactants capable of generating charge whereas capacitors store energy directly as charge. Batteries can store more energy than capacitors (per unit volume or mass), whereas capacitors have higher power density. Batteries release energy at a fairly constant voltage, but capacitors' voltage varies strongly with the rate of discharge. Fuel cells, operating on liquid fuels such as methanol, can also have high energy storage, but their power output is limited.

1.2. Electric vehicles

The automobile manufacturers realize that the time to develop an electric automobile is now. Ecological pressure is on to move away from hydrocarbon-fueled vehicles including bio-diesel and methanol derived from the fermentation of grain or bio mass. Although the latter fuels may be considered renewable resources, they still produce carbon dioxide when burned, contributing to global warming. Electric vehicles may be charged using energy produced by solar, hydro-electric and wind power or other sources of non-polluting electricity such as thermal power and wave and tidal power from the oceans.

Are electric cars more economical comparing with gasoline cars based on the cost of electricity and gas? Taking the BMW MINI E as an example, its gas mileage is about 25 miles/gallon; to run 25 miles, it takes about 5kWh of electricity, at the price of \$0.1/kWh, it costs \$0.5. This compares favorably with about \$2.7 spent at the gas pump for an equivalent trip.

Can the current electrical storage devices store enough energy to run an electrical car for 5 hours? To answer this question, we need to know how much energy is needed to run a standard internal combustion gasoline-powered automobile for five hours. 2009 Toyota Camry, LE 5-Speed MT 5-Speed 2.4L I4 Manual FWD generates the power of 158 horsepower; 2009 Honda Acura, 4WD 4-Dr, RDX has the power of 225 horsepower @ 5600RPM; the new G35s power figure has finally come to light to the tune of an impressive, 306 horsepower. Let us take the 2009 Toyota Camry as an example. 158 horsepower (1 hp \equiv 746 W) is about 118 kW. To run this Camry for 5 hours requires the energy of 590kW. Using the plot from Dr. Whittingham's 2008 review [3], shown as **Figure 1.2**, the ratio of y-axis, energy density with the x-axis, the power density, gives the duration, in units of hour. The devices can supply energy for 5 hours satisfy Energy Density = 5 x Power Density, considering the logarithmic scale in **Figure 1.2**, we need to draw a line of

$$\log (\text{Energy Density}) = \log (\text{Power Density}) + \log 5$$

We firstly draw a solid blue line though (1, 1) with the slope of 1, and then shift it upward by log 5. The dashed blue line only crosses with fuel cells and batteries, suggesting, they are the only two among all available energy storage and conversion devices that can be considered as the alternative energy recourse based on duration. And the dashed blue line crosses the boundary of batteries at power density about 10 W/kg and 30 W/kg, hence to achieve 590kW using current technology, it needs 4000 – 12000 kg of batteries. That is to say we need at least 4 tons of the best battery we have now to run an electric car with equivalent power as 2009 Toyota Camry for five hours!

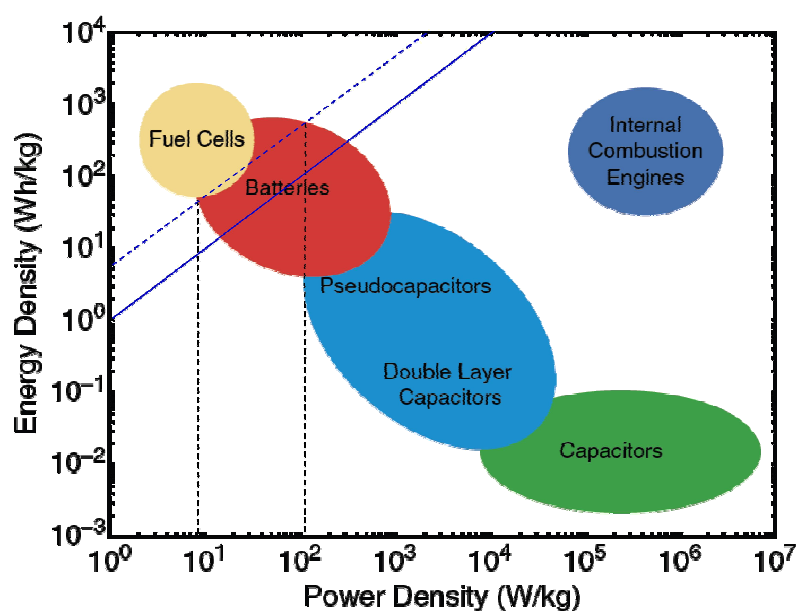


Figure 1.2. Comparison of the power density and energy density for batteries, capacitors, and fuel cells. (Energy is the capacity to do work; power is the rate at which work is done.)

This example strongly suggests that the current battery technology falls far short of meeting these future needs. Limited energy storage capacity is not the only problem. The current rechargeable batteries also have slow recharge cycles and limited lifetimes because of degradation of their electrode materials during charge/recharge cycles. Restrictions in operating temperatures, especially below 0°C , also impact their widespread use. These limitations can be overcome only by major advances in new materials whose constituent elements must be available in large quantities in nature. New cathode materials with higher storage capacity are needed, as well as safer and lower cost anodes and stable electrolyte systems [3].

To achieve the goals of using electrical energy in transportation, a major advance in battery technology is needed - a step that can be taken only by obtaining a fundamental

understanding of the physical and chemical processes that occur in these complex systems to enable breakthroughs in batteries, including electrode materials and electrolyte chemistries. These studies will require close coupling of new analytical and computational tools to understand these processes at the atomic and molecular level. The knowledge gained from these studies will catalyze the design of new multifunctional materials that are tailored to provide the optimal performance required for future electrical energy storage applications. Ultimately, we expect our research in developing single ion conducting electrolytes for advanced lithium battery to be used in electric vehicles.

1.3. Rechargeable Batteries

Battery performance involves complex, interrelated physical and chemical processes between electrode materials and electrolytes. Although some recent improvements have made rechargeable batteries ubiquitous in today's portable electronic devices [3], the design of batteries has not changed substantially since their invention 200 years ago. All batteries are electrochemical cells, composed of two electrodes separated by an electrolyte. During discharge, ions from the anode are released into the solution and deposit oxides on the cathode. Reversing the electrical charge through the system recharges the battery. When the cell is being recharged, the chemical reactions are reversed, restoring the battery to its original condition.

A number of battery technologies exist for use as utility-scale energy storage facilities [5-9]. Primarily, these installations have been lead-acid, but other battery

technologies like sodium sulfur (NaS) and Lithium ion are quickly proving to be commercially viable. The share of worldwide sales for Ni-Cd, Ni-MeH and Li-ion portable batteries is 23, 14 and 63%, respectively. The use of Pb-acid batteries is restricted mainly to SLI (starting, lighting, ignition) in automobiles or standby applications, whereas Ni-Cd batteries remain the most suitable technologies for high-power applications (for example, power tools). The Li battery has by far the highest volumetric and gravimetric energy density in current battery technologies, including Lead-acid, Ni-Cd, and Ni-MeH. [5]

Table 1.1. introduces four criteria help choose which battery type is best for a given application: the gravimetric energy density, the volumetric energy density, the gravimetric power density, and the cost in watt-hours per dollar, to help choose which battery type is best for a given application.

Table 1.1 Comparison of battery types in terms of the gravimetric energy density, the volumetric energy density, the gravimetric power density, and the reciprocal cost in watt-hours per dollar.

Battery Type	Energy/weight Watt-hours/kg	Energy/volume watt-hours/L	Power/weight watt/kg	Energy/US\$ watt-hr/\$
Lead-acid	30-40	60-75	180	4-10
Nickel-Zinc	60-70	170	900	2-3
Lithium-Ion	160	270	1800	3-5
Lithium-Polymer	130-200	300	Up to 2800	3-5

In comparison, the lead-acid battery is probably the least desirable to run an electric vehicle, whereas lithium ion and lithium polymer batteries are strong candidates,

in fact, they have been chosen by most auto makers for their vehicles (except in the case of hybrid vehicles, which uses Ni-MeH batteries.).

1.4. Rechargeable Lithium Ion Batteries

Rechargeable lithium ion batteries are key components of portable electronic devices. They are also becoming crucial storage media for electric automobiles, wind & solar energy, and other energy sources. They employ a wide range of electrode and electrolyte materials, providing a diverse number of electrochemical couples compared with other battery systems. Several systems are used in today's commercial batteries, but many materials are still in the R&D phase. This area is so attractive that many researchers are now working on preparation, characterization, electrochemical performance and safety of materials possibly used in rechargeable lithium batteries. However, electrolytes with low cost, high safety and efficiency have not been available yet. PEO-based electrolytes show potential to be useful polymeric electrolytes for lithium ion batteries.

1.4.1 Liquid electrolyte lithium-ion batteries

In a lithium cell, the anode's purpose is to generate electrons to do work in the external electrical circuit. At the same time, Li^+ cations migrate in the electrolyte (the electrolyte must be stable in the presence of both electrodes) inside the cell to the cathode. The most common anode and cathode materials in current lithium ion cells are graphite (Li_xC_6) and lithium cobalt oxide $\text{Li}_{1-x}\text{CoO}_2$ ($1 \geq x \geq 0$), respectively. Some anodes contain lithium metal held within graphite have also been commercialized, but

these systems currently comprise only a small sector of the lithium battery market. The current collectors allow the transport of electrons to and from the electrodes. Lightweight aluminum is a preferred current collector material, but it reacts with lithium, and therefore cannot be used for lithium-based anodes; copper is used instead. In practice, the anode and cathode are complex composites with structures that are challenging to characterize. Besides the active material, they often contain polymeric binders to hold their powder structure together and conductive diluents such as carbon black to give the whole structure electronic conductivity so that electrons can be transported to the active material. In addition these components are combined so as to leave sufficient porosity to allow the liquid electrolyte to penetrate the powder structure and the ions to reach the reacting sites. **Figure 1.3.** depicts the discharging and charging mechanism of a lithium-ion rechargeable battery.[4]

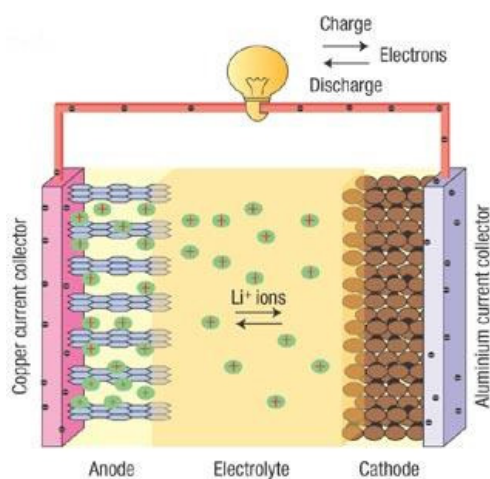


Figure 1.3. Discharging and charging mechanism of a lithium-ion rechargeable battery.[4]

The choices for anode and cathode determine the voltage of each lithium cell.

Cathode: $\text{MO}_x + \text{Li}^+ + \text{e}^- \rightarrow \text{LiMO}_x$ (where M is Co, Ni, Mn, V, etc.)

Anode 1: $\text{LiC}_6 \rightarrow \text{Li}^+ + \text{e}^-$ 2.5 to 4.5 volt, ~600 Whr/kg

Anode 2: $\text{Li} \rightarrow \text{Li}^+ + \text{e}^-$ 3 to 5 volt, ~900 Whr/kg

Lithium batteries with metallic lithium anodes require high conductivity electrolyte with, $10^{-3} \text{ S/cm} < \sigma < 10 \text{ S/cm}$, however, when liquid electrolytes are used, the rechargeability of each lithium cell is severely compromised by reactions that can occur between the nonaqueous, flammable electrolytes and the cycled lithium electrode, which becomes moss-like with extremely high surface area. Dendrite growth at the lithium electrode (**Figure 1.4**) causes capacity loss by redistributing lithium from the bulk to isolated islands in the electrolyte and eventually causes internal shorts, presenting a fire hazard a severely shortened the lifetime of the battery. Overcoming this hurdle presents an enormous immediate challenge to the lithium battery industry.

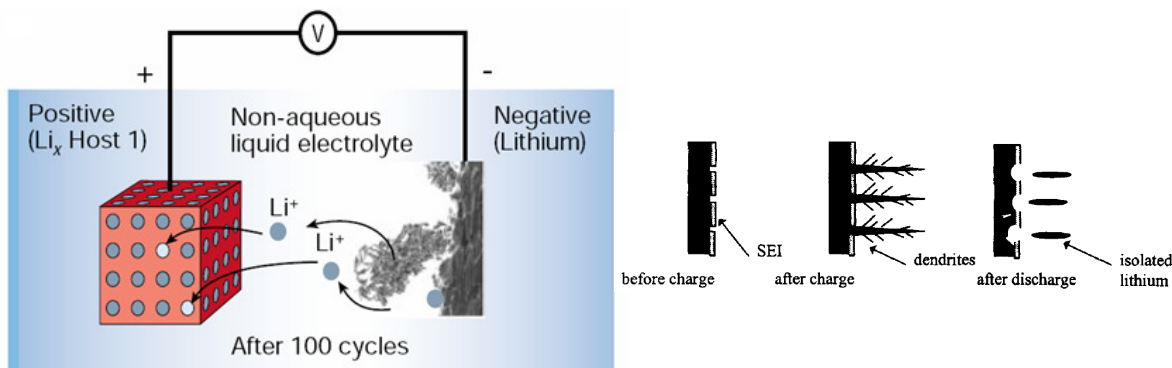


Figure 1.4. Rechargeable Li-metal battery (the picture of the dendrite growth at the Li surface was obtained directly from in situ scanning electron microscopy measurements) [5]. Dendrite formation on a lithium electrode causes capacity loss by redistributing lithium from the bulk to isolated islands in the electrolyte [6].

1.4.2 Solid State Lithium-Polymer Batteries

One possible solution to overcome the safety barriers of metallic lithium/liquid electrolyte battery systems is to change the liquid electrolyte to a polymer electrolyte. This immobile conducting material can effectively suppress the dendritic growth, and requires less package materials, making the batteries much smaller and lighter. The thickness of current lithium-polymer batteries range from 3 to 7 mm. The power of any battery is reciprocally related to the distance between two electrodes, so thinner batteries have a higher power. Polymer electrolytes offer another significant advantage over liquid electrolytes. Once they form a stable passivating layer (electron-insulating but ion-conducting) at an operating electrode interface, their lack of continued access to the electrode surface renders them kinetically inert. Designing polymers with tailored architectures could allow higher ion mobilities. The pore surfaces could be modified to permit ions (rather than an ion pair or ion clusters) to diffuse through a weakly interacting medium. Novel systems with tailored structures, such as ion-conducting glasses and metal oxides, in which ion mobility is facilitated by vacancies, defects, or well defined channels, may provide alternative approaches, but these suffer from being very challenging to manufacture in thin film form.

In these respects, an all solid state Li / lithium salt - polyethylene oxide electrolyte / LiV_3O_8 battery has been manufactured for the telecommunications industry for uninterrupted power supply applications. The first-generation was LiCF_3SO_3 - PEO, and to increase the inadequate conductivity, a higher dissociating salt was used LiTFSI, but still the lithium-ion conductivity of the polymer electrolyte is too low to allow high-rate

cycling at room temperature, so it functions typically at about 60°C or higher. Other attempts have been made, such as low- T_g combination polymer; plasticized polymer electrolyte, gel-type polymer and gel electrolyte, whose conductivities are compared in

Figure 1.5.

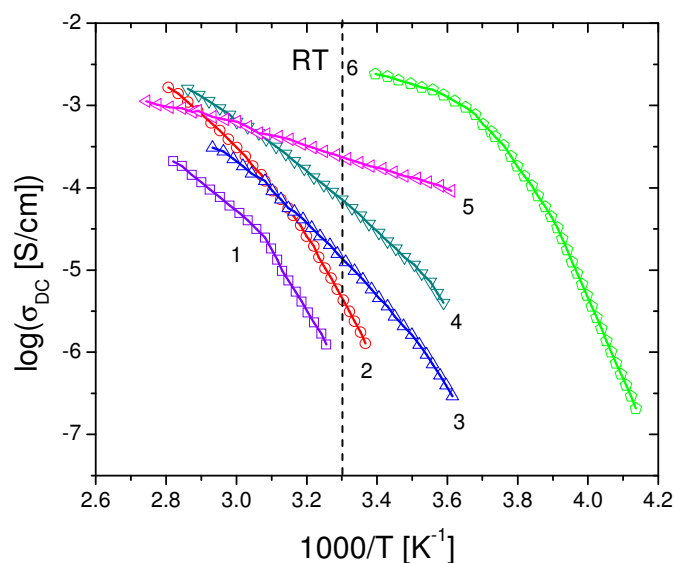


Figure 1.5. Conductivity as a function of temperature for six conducting polymer electrolyte systems in solid state lithium-polymer batteries. 1. First generation: PEO-LiCF₃SO₃; 2. Newer solute with higher dissociation: PEO-LiTFSI; 3. Low- T_g combination polymer; 4. Plasticized polymer electrolyte: PEO-LiTFSI+25% w/w PEG-dimethylether; 5. Gel-type polymer: PEO-dimethacrylate-LiTFSI-PC70%; 6. Gel electrolyte: P(VDF-HFP)/EC/DMC-LiPF₆. Data collected by U Hyeok Choi [49].

However, the polymer-salt complex generally has low conductivity; plasticized electrolyte has higher conductivity but also safety concerns. Therefore we see a great opportunity for **Low- T_g single-ion conducting polymer electrolytes**, which has the

highest transference number ($=1$); thermally and electrochemically more stable; ease of processing. But it still requires insightful design to achieve adequate ionic conductivity by increasing the conducting ion concentration (high dissociation ion pairs; high dielectric constant of the ionomer) and mobility (amorphous at RT with low T_g). The design scheme is Molecular Design Synthesis \rightarrow Single-Ion Conductor with Well-defined Molecular Structures and Compositions \rightarrow Structure / property relationship \rightarrow Advanced Ion Battery with High Conductivity.

A successful solution, thin-film lithium-metal-polymer battery, was developed by Avestor, Boucherville, Québec, Canada, which has merged into the Bolloré Group in France. One of their reprints is still available: Designing Lithium-Metal-Polymer Batteries for Safety. Because there is no liquid or paste electrolyte, they are maintenance free, with service life as long as 10 years, functioning in a wide temperature range from -40°C to $+65^{\circ}\text{C}$.

1.4.3. Can we achieve 158 hp with single-ion conductor lithium batteries?

In [Section 1.2](#), we used 2009 Toyota Camry as an example to evaluate whether the current batteries can supply enough energy for an electric car for five hours. The answer was NO. In this Section, we are going to find out whether we can design lithium batteries, with single-ion conductor (ionomer) separator membranes, to generate the power of a 2009 Toyota Camry, 158 horsepower, i.e., 118 kW.

Assuming the capacities of electrodes are sufficiently high to store enough energy and the charge/discharge efficiency of the one cell is η .

$$\text{Power produced per unit volume: } P_0 = \frac{E}{t} = \frac{e \cdot p_0 \cdot V}{L/v}$$

Where E is the energy stored per unit volume, t is the duration of use, p_0 is conducting ion concentration, V is chemical potential between two electrodes, L is the distance between two electrodes (i.e., the thickness of thin conducting polymer film); v is the average velocity of the mobile ions, which is rarely used in dielectric studies and needs to be written in terms of ionic mobility, μ .

The ionic mobility is defined as the velocity attained by an ion moving through a gas under unit electric field, which has the unit of $\text{m}\cdot\text{s}^{-1}(\text{volt}\cdot\text{m}^{-1})^{-1} = \text{m}^2/(\text{volt}\cdot\text{s})$.

Dimensionless analysis tells us $\mu = \frac{v \cdot L}{V}$, hence we have $v = \frac{\mu \cdot V}{L}$.

So that power per unit volume is

$$P_0 = \frac{e \cdot p_0 \cdot \mu \cdot V^2}{L^2} \quad (1.1)$$

As known, the conductivity in a single ion conductor is the multiply of charge, with the conducting ion concentration and its mobility

$$\sigma = e \cdot p_0 \cdot \mu \quad (1.2)$$

Substitute **Equation (1.2)** into **Equation (1.1)**, we have

$$P_0 = \frac{\sigma \cdot V^2}{L^2} \quad (1.3)$$

Unit Checking:

Unit of conductivity σ : S/m = amp / volt / m; unit of the right hand side of

Equation (1.3) $\sigma V^2 / L^2 = (\text{amp} / \text{volt} / \text{m}) \cdot \text{volt}^2 / \text{m}^2 = \text{amp} \cdot \text{volt} / \text{m}^3 = \text{watt} / \text{m}^3$. The unit of power per unit volume is watt / m³. Unit Checking Completed.

Based on this result, the power per cell can be estimated by **Equation (1.4)**

$$P = P_0 \cdot A \cdot L \cdot \eta = \frac{\sigma \cdot V^2 \cdot A}{L} \cdot \eta = \frac{V^2}{R} \cdot \eta = I \cdot V \cdot \eta \quad (1.4)$$

where A is the cross-sectional area of the polymer film and the surface area of each electrode. This equation tells us the power of the battery depends on dimensions and conductivity of the membrane, and its efficiency.

Figure 1.5. suggests at RT, a current low- T_g single ion conductor has a conductivity of $10^{-5} \sim 10^{-4}$ S/cm. Hopefully by clear design, we can achieve a similar conductivity as a gel electrolyte, which is close to 10^{-2} S/cm. As mentioned in **Section 1.4.1.**, the choices of anode and cathode determine the voltage of each lithium cell, with MO_x ($M = \text{Co}, \text{Ni}, \text{Mn}, \text{V}, \text{etc.}$) as cathode, the choice of LiC_6 using as anode gives the cell a voltage of 2.5 to 4.5 volt; if using Li metal as the anode the voltage is even higher, 3 to 5 volt. To optimize the battery power, we will use the higher voltage 5 volt for estimation. One advantage of single-ion conductor is its flexibility; it can be made very thin, as long as it can still hold the distance between two electrodes. The thickness of current lithium-polymer batteries ranges from 3 to 7 mm. It is practicable to make the membrane 1mm thick, with the dimension of the cross-sectional area 1dm x 1dm. The traditional lithium-ion chemistry involves a lithium cobalt oxide cathode and a graphite anode. This yields cells with 80 to 90% charge/discharge efficiency. We therefore assume that our single-ion conductor lithium battery has 85% charge/discharge efficiency.

To sum up, we have $\sigma = 10 \text{ S/m}$, $V = 5 \text{ volt}$, $A = 0.01 \text{ m}^2$ and $L = 0.001 \text{ m}$ and 85% efficiency for our ideal single-ion conductor membrane lithium battery. Put in these numbers in [Equation \(1.4\)](#), assuming no energy loss in ion transportation in the membrane, at the interface of electrode and polyelectrolyte, and through the porous media in anode, the power of this battery is as high as 212 watt!

To obtain 118 kW, considering the stacking with extra 10% energy loss, we need a stack of 620 such batteries.

Assuming with electrodes the thickness of each battery is 2mm, this stack is about 1.2 m long. The density of ionomer is generally $1.1 \sim 1.5 \text{ g / cm}^3$, considering the density of electrode, assuming the density of this battery is 3 g/cm^3 , this stack of lithium batteries weighs 37 kg.

If we can achieve all the goals we set for conductivity, voltage, dimension, and high efficiency, we have a stack of cells 1.2m long, 0.01 m^2 in cross section, weighs 37 kg and gives us the same power as a 2009 Camry!

1.5. Ionomeric Single-Ion Polymer Conductors

1.5.1. Application in Li Ion Battery

The previous crude estimation encourages us to fully explore the potential of Ionomeric Single-Ion Polymer Conductors in the application of Lithium Ion Battery!

Single-ion conductors can be prepared from polymers simply by covalently attaching ions to the chain [\[13-15,50,52,53\]](#). Those materials are termed ionomers, with conduction solely due to the motion of unbound Li counterions. Conventional

hydrocarbon ionomers are poor ion conductors because without strong solvation, the ions microphase separate from the polymer.[16,17] Sulfonated ionomers based on poly(ethylene oxide) (PEO) have been synthesized in our lab, whose ether oxygen atoms provide sufficient cation solvation so that microphase separation of ions from the polymer is minimized, with reasonable ion conductivity, but far below that required for electric vehicles.

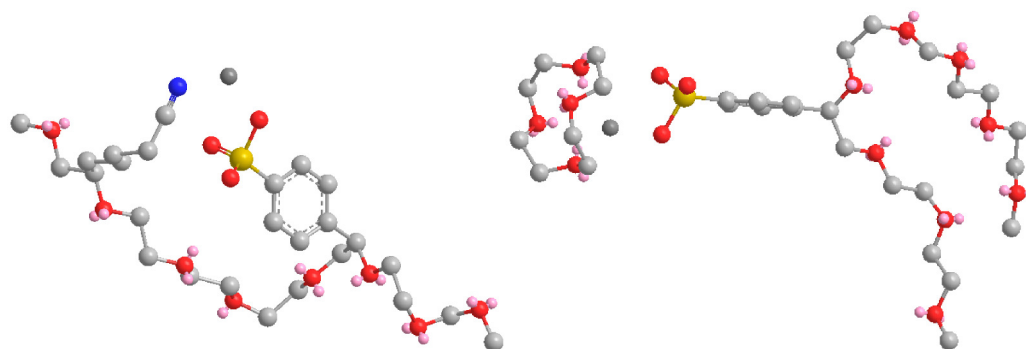


Figure 1.6. Li^+ cation in PEO-based ionomer a) solvated by $-\text{C}\equiv\text{N}$ polar group attached to polymer backbone, b) solvated by a cation acceptor, 12-Crown ether.

Our current research has identified two useful strategies for boosting conductivity, both aimed at increasing the fraction of counterions participating in conduction: (1) Replace sulfonate with weak-binding bulky diffuse anions that do not bind Li^+ so strongly and (2) replace PEO with more polar functional groups that effectively raise the dielectric constant of the polymer (**Figure 1.6. a**). At this stage we know that we want those functional groups to not prefer to ‘pair-up’ to form symmetric quadrupoles (**Chapter 3**) that do not raise dielectric constant but instead act as temporary cross-links that raise T_g and retard ion mobility. However, it is not entirely clear yet whether those groups should solvate the counterion (**Figure 1.6. b**) (as PEO does) and/or solvate the anion attached to the polymer [51]. The design space for ionomer optimization is extensive, involving at

least 30 possible functional groups and 20 possible anions, and we propose to use *ab initio* methods towards a “bottom up” design strategy to determine anion-side chain-backbone functional group combinations that will maximize Li^+ conductivity.

Collaboration with on-going experimental efforts on ionomer synthesis and dielectric spectroscopy that measures populations of conducting ions and ion pairs, will allow for realization of ionomer compositions suggested by theory, as well as serve to validate models.

1.5.2. Application in Ionic Actuators

Another application of single-ion conducting polymer (ionomer) is the ionic actuator.

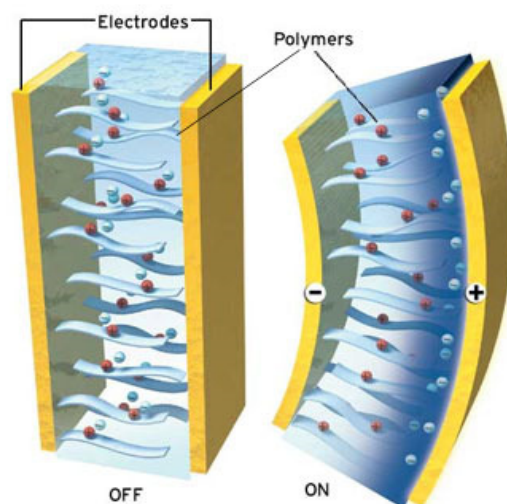


Figure 1.7. Ionic polymer metal composites are a form of artificial muscle that depends on the movement of ions for motion. Flexible metal foils sandwich a wet polymer filling. With the foils oppositely charged, free ions flow toward one side, expanding it and bending the actuator. [18]

Instead of Li^+ in Li batteries, actuators require bulky fast ions. [Figure 1.7.](#) is the schematic of the bending actuator made of poly-cations with mobile anions: initial state with electronic fillers uncharged and ions uniformly distributed; charged state with electronic fillers carrying negative and positive charge in the anode and cathode, respectively; bulky anions moving into the cathode cause depletion and accumulation of anions at the cathode and anode, respectively, resulting in bending actuation.

I. Ionic Actuators based on Nafion Swollen with Ionic Liquid

Ionic electroactive polymer (EAP) actuators are attractive because they can be operated under a few volts. [\[19-25\]](#). Actuators using polymers (such as Nafion) swollen with enough ionic liquids to make continuous channels for conduction, have been intensively studied [\[26-29\]](#). They have several advantages for actuators. The near zero vapor pressure and high thermal stability over a broad temperature range improve actuator lifetime and also make operation at high temperatures ($>100\text{ }^{\circ}\text{C}$) possible. The high mobility and wide electrochemical window of ILs can lead to fast actuation. The disadvantages are also obvious. Because the actuation is proportional to the volume difference of vicinity of two electrodes, while both ions are mobile, the volume change is remarkably decreased. Typically one ion is faster than the other, leading to bending followed by back bending [\[29\]](#). Even though it seems like there are large numbers of cations and anions available with various ionic sizes, our choices are actually limited. Apparently, the ions cannot be too large, otherwise their mobility greatly reduces, nor can they be too small, because the pair interaction energy strongly depends on the distance of cation and anion ([Figure 1.8.](#)). Small ions strongly bind to their counterion, lowering the

conducting ion concentration and increasing the T_g (and T_m) of the ionic liquid, thereby also reducing their motility. Moreover, ionic liquid dramatically reduces the modulus of the actuator, jeopardizing the work able to be done by the actuator.

Just like the hydrated Fuel Cell, a critical amount of IL needs to be added and conductivity rises rapidly as more IL is added [30].

II. Steric Hindrance Effect

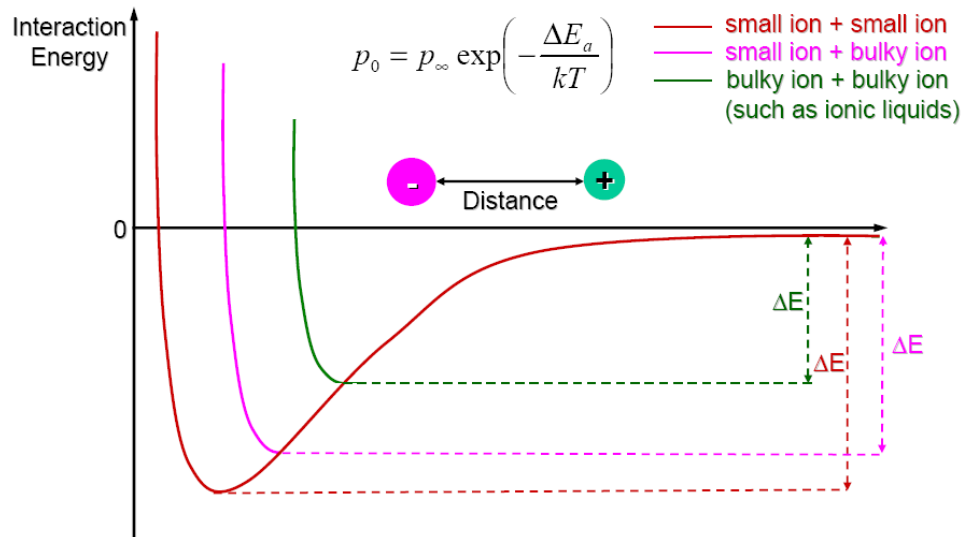


Figure 1.8. Steric hindrance effect on ion pair interaction energy, which exponentially leverages the conducting ion concentration [50].

To future explore the steric hindrance effect, we choose Li^+ and 19 more bulky cations, including 8 imidazolium (EMI^+ , BMI^+ , EPI^+ , BPI^+ , DMBI^+ , etc), 4 pyridinium, 4 isoquinolinium, and 3 ammonium (TMA^+ , TBA^+ , DiMDiBA^+), each interacting with F^- and other 19 bulky anions, BF_4^- , AlCl_4^- , NO_3^- , CH_3COO^- , CF_3COO^- , CH_3SO_3^- , CF_3SO_3^- , $\text{C}_2\text{F}_5\text{COO}^-$, $\text{C}_2\text{F}_5\text{SO}_3^-$, $\text{C}_6\text{H}_5\text{COO}^-$, $\text{C}_6\text{F}_5\text{COO}^-$, $\text{C}_6\text{H}_5\text{SO}_3^-$, $\text{C}_6\text{F}_5\text{SO}_3^-$, TfSI^- , TPhB^- . Using the pairing energy of Li^+ with F^- , ΔE_{LiF} as reference, the average interaction energy of F^-

with 19 bulky cations is 72.5% of ΔE_{LiF} ; the average interaction energy of Li^+ with 19 bulky cations is receded to 67.2% of ΔE_{LiF} ; and the average interaction energy of 361 ionic liquids is only about 40% of ΔE_{LiF} ! (**Figure 1.9.**)

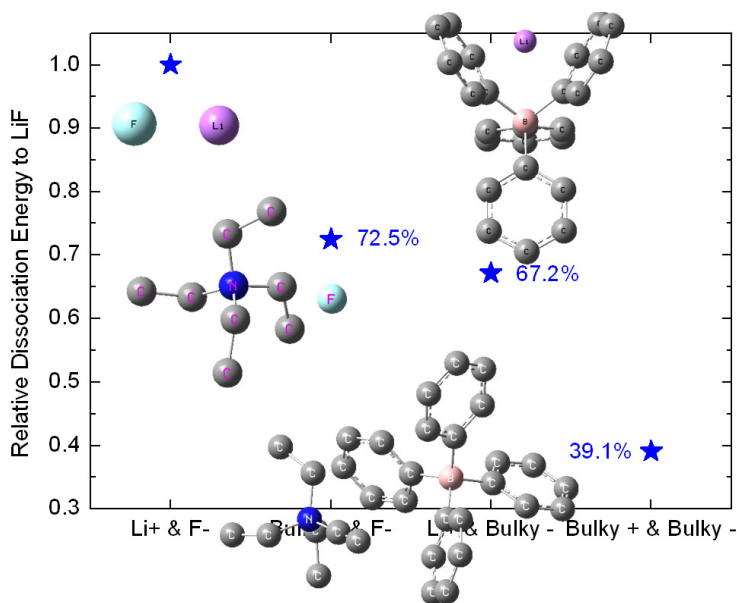


Figure 1.9. Exploring steric hindrance effect by comparison of relative dissociation energy to LiF of bulky cation tetraethyl ammonium with F^- , bulky anion tetraphenyl borate with Li^+ and an ionic liquid formed by these bulky cations and anions.

Because the conducting ion concentration is exponentially leveraged by ion pair interaction energy, the conducting ion concentration in ionic liquids can be 100 times higher than that of LiF. Note that our interest in these ions generally penetrates all chapters. The carboxylate and sulfonate anions pairing with Li^+ will be thoroughly studied in **Chapter 2** by *ab initio* methods. Other cations and anions, and their ion pairs, triple ions and quadrupoles will all be investigated and put into QPT-State Diagram, in **Chapter 3**, to screen for the ion pair that can optimize the ionomer performance, with more conducting ion, higher dielectric constant and lower T_g .

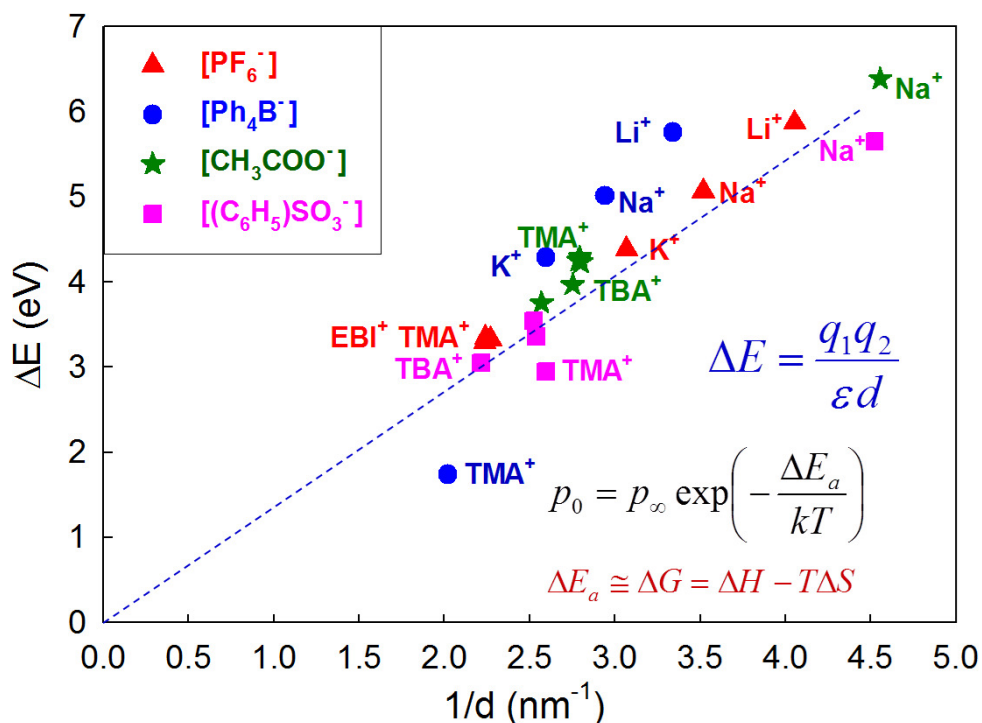


Figure 1.10. Ion pairing energy as a function of reciprocal distance from the cation to the charge center of the anion. Anions are indicated by different symbols in the legend with cations and indicated in the plot: Li = lithium, Na = sodium, K = potassium, TMA = tetramethyl ammonium, TBA = tetrabutyl ammonium, EBI = ethylbutyl imidazolium.

These ion pairing energies are quantitatively correlated with the reciprocal of the distance from charge-centers of the cation and the anion in **Figure 1.10**. For various anions in **Figure 1.10** tetraphenyl borate with tetramethyl ammonium is the best (smallest $1/r$ and ΔE). Clearly, not only the correlation, based on Coulomb energy, is useful but also outliers on the low ΔE side may motivate further ideas for anions to try. In this regard, tetramethyl ammonium with tetraphenyl borate appears to be quite promising, which is hardly surprising considering that the benzene rings spread out the

negative charge and give extra repulsion with the methyl groups on TMA (aromatic always dislikes aliphatic). [54]

III. Other Tricks to Reduce the Pair Energy

Figure 1.11 compares the energy to dissociate an ion pair of various cations with a fluoride anion, using the energy scale as 1 being the pair dissociation energy of LiF. There are three important conclusions from **Figure 1.11**.

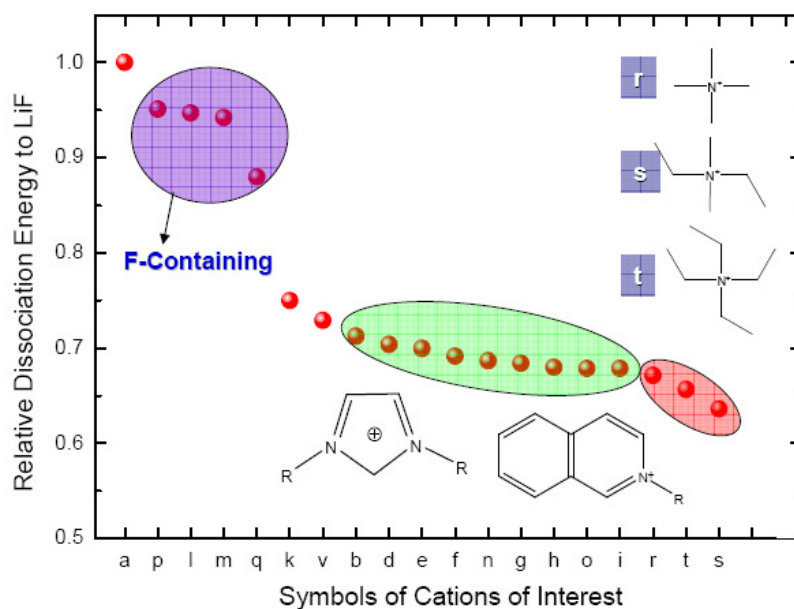


Figure 1.11. Comparison of the dissociation energy of F^- with 19 bulky cations, using the pairing energy of LiF as the reference.

1) Cations containing F (purple circle in **Figure 1.11**) have quite high pair dissociation energy of F^- with various cations. This is simply understood because F withdraws electrons from the cation, effectively hardening the cation (increasing the positive charge

of the cation charge center). This fluorination effect holds true for anions other than F^- as well, meaning that cations should never have F.

2) Interaction energies between F^- and Imidazolium and Isoquinolinium are only very weakly dependent on the structure of those aromatic cations (all are within 25kJ/mol of each other, green oval in **Figure 1.11**).

3) Sterically hindering ammonium cations from F^- effectively lowers the interaction energy (red circle in **Figure 1.11**) because the cation – anion distance is increased.

Figure 1.12 makes a similar comparison for various anions interacting with Li^+ , with the benchmark again the pair energy of LiF . There are again three major conclusions from **Figure 1.12**.

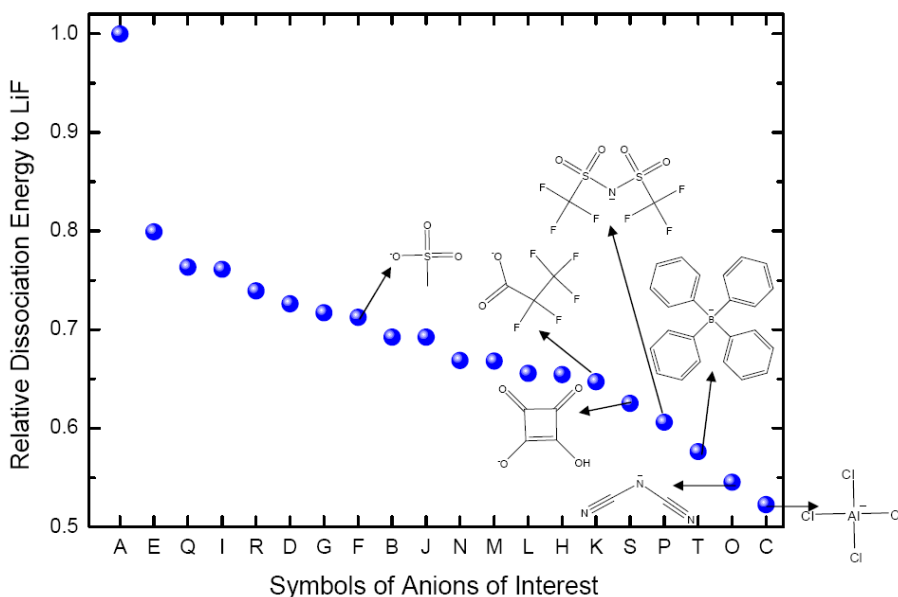


Figure 1.12. Comparison of the dissociation energy of Li^+ with 19 bulky anions.

1) Incorporating F on the anion greatly lowers the interaction energies between Li^+ and anions because the electron withdrawing fluorine softens the anion (weakens the negative charge at the charge center of the anion).

- 2) Sterically hindered anions (bulkier anions) interact more weakly with Li^+ .
- 3) Other ways to spread out the charge on the anion also weaken the cation – anion interaction energy. Diffuse anion charge is the key to truly low pairing energy, as seen for instance in AlCl_4^- , where the four chlorides share the negative charge and in tetraphenyl borate, where the four benzene rings share the negative charge, while lower electronegativity Al and B are positive at the centers of these anions.

Summarizing the principal conclusions from [Figs. 1.12](#) and [1.13](#):

- Adding electron withdrawing groups (F) softens anions and hardens cations
- Bulky anions with diffuse charge have the weakest interactions
- Sterically constrained ions have the weakest interactions
- It is “easy” to choose counterions that lower pairing energy by as much as a factor of 2 relative to LiF but lower pairing energies are not practical for either Li^+ or F^- .

Can the observations from small with bulky ions be generalized to ionic liquid?

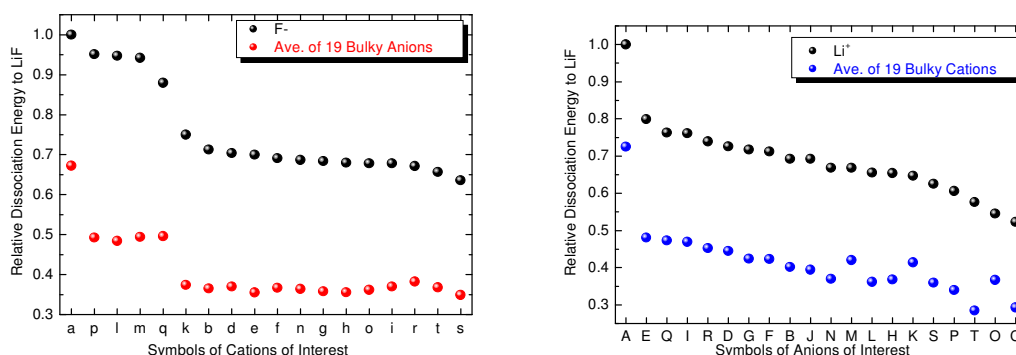


Figure 1.13. Comparison of the dissociation energy of small ion (Li^+ or F^-) with its bulky counterion and ionic liquids.

Take-home message

1. Adding electron withdrawing groups (F) softens anions and hardens cations.
2. Perfluorocarbon alkyl bulky anion + hydrocarbon alkyl bulky cation are weakly binding. A model pair can be perfluorinated tetraphenyl borate + tetrabutyl ammonium.
3. Almost parallel shifts suggest that for simplicity we could use interactions with small ions to predict those with bulky ions.

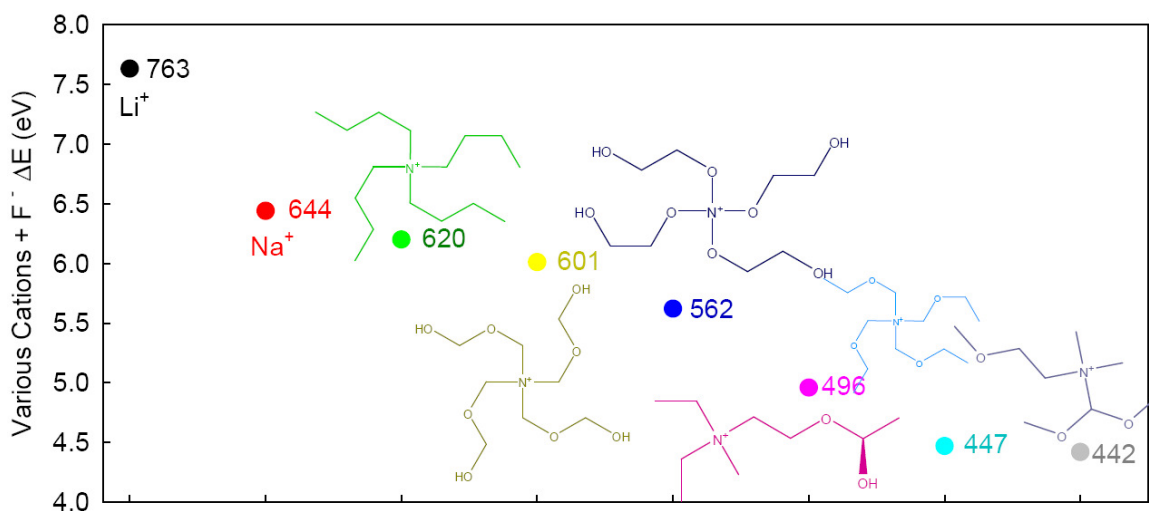


Figure 1.14. Comparison of pairing energy of F^- with hydrocarbon ammonium cation, TBA^+ , and O containing ammonium cations. Replacing CH_2 by O on alkyl cations weakens the ion pair interaction.

A further question then naturally arises: If adding F softens anions and hardens cations, which atom can soften cations and harden anions? Inspired by the specific solvation effect of ether oxygen on Li^+ , we expect that by adding ether oxygen on the arms of ammonium, phosphonium and imidazolium cations, the positive charges can be self-solvated, which will effectively reduce the interaction with the anion. This idea was

immediately proven true! Some of the results are plotted in [Figure 1.14](#). Clearly, comparing with TBA^+ , all the other O-containing ammonium cations interact with F^- less strongly; which is also affected by the number of the O atoms and their locations.

To pursue the answer for the second half of the question, we replaced the C by O on tetra-X-borate anions. As expected, this substitution weakly increased the pair interaction, as the cation can now bind to both the negative charge of the anion and a lone pair of electrons on the O.

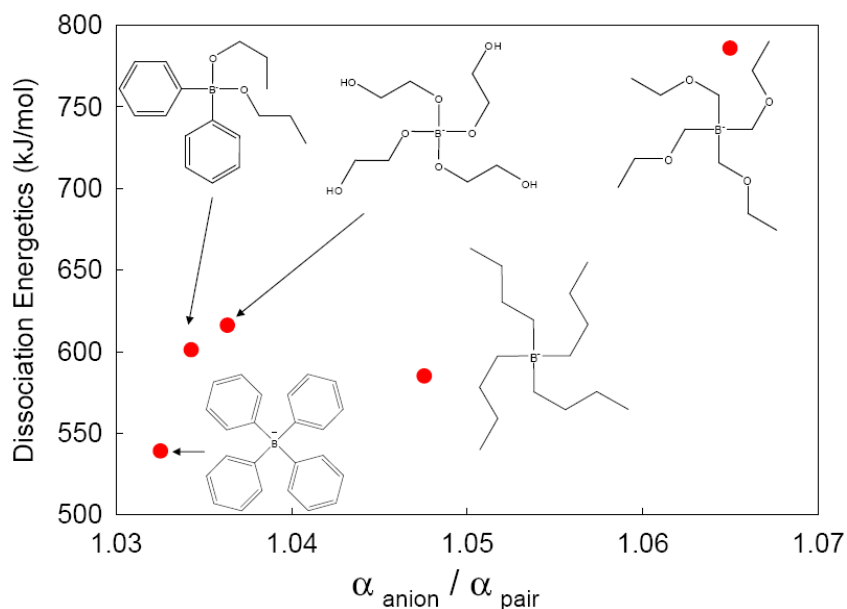


Figure 1.15. Comparison of pairing energy of Li^+ with hydrocarbon borate cation (TPhB^+ , TBuB^+) and O containing borate cations. Apparently, replacing C by O on anions enhances the ion pair interaction, which works oppositely as replacing H by F.

In summary, replacing C with O softens cations and hardens anions, both due to O solvating the positive charge. In the case of cations, the self-solvating effect helps to

keep anions away, but for anions, the O atoms strongly interact with the cation, thus increasing the pairing energy.

IV. Poly(ionic liquid) Actuators

Poly(ionic liquid) actuator is single-ion conductor, made by ionic liquid with polymerizable groups. It is preferable to swelling Nafion with ionic liquid actuators from the viewpoint of bending efficiency, strength generation, processing, treatment, packaging, etc. Polymerized ionic liquids can show good ionic conductivity without liquid components [31-34], and specific functions such as transport of target ions, specific polar environment and mechanical strength, corresponding to their polymer structure. These functions of PILs depend on both IL structure and polymer main chain.

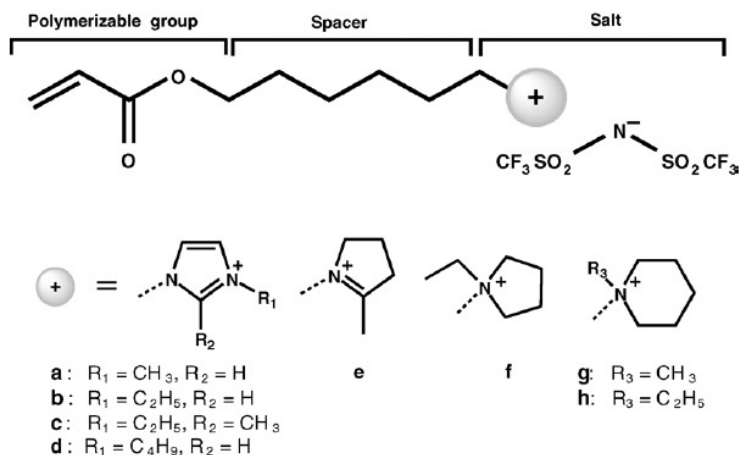


Figure 1.16. Structure of a series of IL monomers used in Dr. Hiroyuki Ohno's group to synthesize PILs to study the effect of cation structure on their electrochemical and thermal properties.[31]

The structure of spacer group between them was also an important factor [32]. In plain terms, if spacers are too short, the total ion content increases, but not necessarily the

conducting ion content. However, T_g will increase due to more temporary crosslinks caused by higher ion density, so that the conducting ion mobility decreases. Conductivity is the product of charge (e) with conducting ion concentration (p_o) and its mobility (μ), so increasing ion content eventually makes the conductivity of the ionomer decrease. On the other hand, if spacers are too long, the total ion content decreases, directly lowering conductivity.

Bulky counterions may boost the free ion content and cause more bending, but they are often less mobile. Another positive suggestion is to use nano-structured membranes (soft phase for ions to move in and a hard phase for mechanical strength). In fact, Shih-Wa Wang in Dr. Colby's group has been studying polyurethane-carboxylate ionomers with ionic liquid counterions [35]. She found polyurethane-carboxylate ionomers with self-solvating ammonium cations would be a great choice to make actuators. We will use one of the self-solvating ammonium ionomers as an example in [Section 1.6](#). Unfortunately, there is not enough contrast for the possible nano structures to be detected by X-ray or TEM.

Another poly(ionic liquid) system, poly(MEBIm) BF_4 / TFSI / PF_6 as potential high performance actuator candidate will be discussed in [Chapter 3](#) at length about their glass transition and electrode polarization relaxations, their conductivities and how those related to the pair, triple ion and quadrupole energies calculated by *ab initio* methods.

V. General Suggestions to Enhance the Performance of Ionic Actuators

Shorten Actuation Response Time and Increase Actuation Amplitude

1) Operation Condition:

- Increase Operation Voltage (U)
- Increase Operation Temperature (T)

2) Device Design:

- Make Thinner Films (d)
- Expand Debye Layer Surface Area (A and S) using structured electrodes

3) Polyelectrolyte Selection:

- Higher Dielectric Constant (ϵ)
- Lower Ion Friction Coefficient (ζ) lower T_g
- Increase Total Ion Concentration (p_∞) up to saturation (controlled by ϵ)

4) Ion Selection:

- Larger Counter Ion Volume Difference (ΔV_{ion})
- Weakly Interacting Mobile Ion (μ_{ion})

Common features in lithium batteries and actuators are that they both require ionomers (single-ion conductors); they both need to raise the dielectric constant to lower the Bjerrum length and decrease the well depth; they both need nano-structured materials containing continuous soft phase for facile ion transport and continuous hard phase for mechanical properties. Above all, we need a better understanding of ion conduction in order to design superior membrane materials.

1.6. Dielectric Spectroscopy and Electrode Polarization Analysis

1.6.1. What is Electrode Polarization?

A physical model is developed that permits determination of mobile ion concentration and ion mobility from measured complex dielectric data on single-ion conductors, with anions or cations (Figure 1.17.) fixed along the polymer chains leaving their counterions mobile. Application of this model to experimental data allows characterization of the parameters influencing conductivity in single-ion conductors, including the determination of dissociated cation concentration and mobility as functions of temperature and cation type.

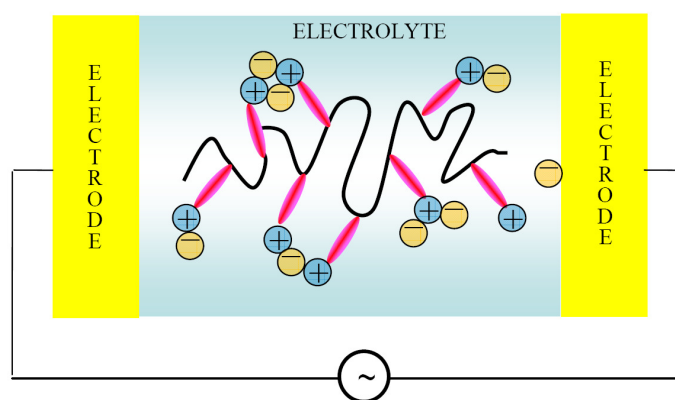


Figure 1.17. Schematic of a single ion conductor with cations fixed along the polymer chains and the anions as mobile counterions between two electrodes in the dielectric spectrometer.

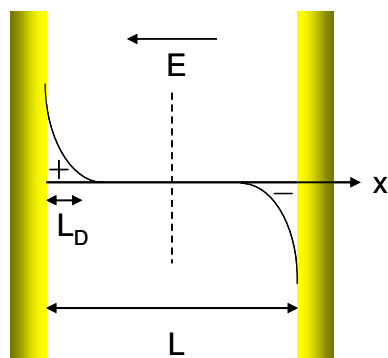


Figure 1.18. Schematic of electrode polarization occurs at low frequencies.

Electrode polarization occurs at low frequencies, where the transporting ions have sufficient time to polarize at the blocking electrodes during the cycle (**Figure 1.18**). That polarization manifests itself in (1) an increase in the effective capacitance of the cell (increasing the dielectric constant) and (2) a decrease in the in-phase part of the conductivity, as the polarizing ions reduce the field experienced by the transporting ions (**Figure 1.19**).

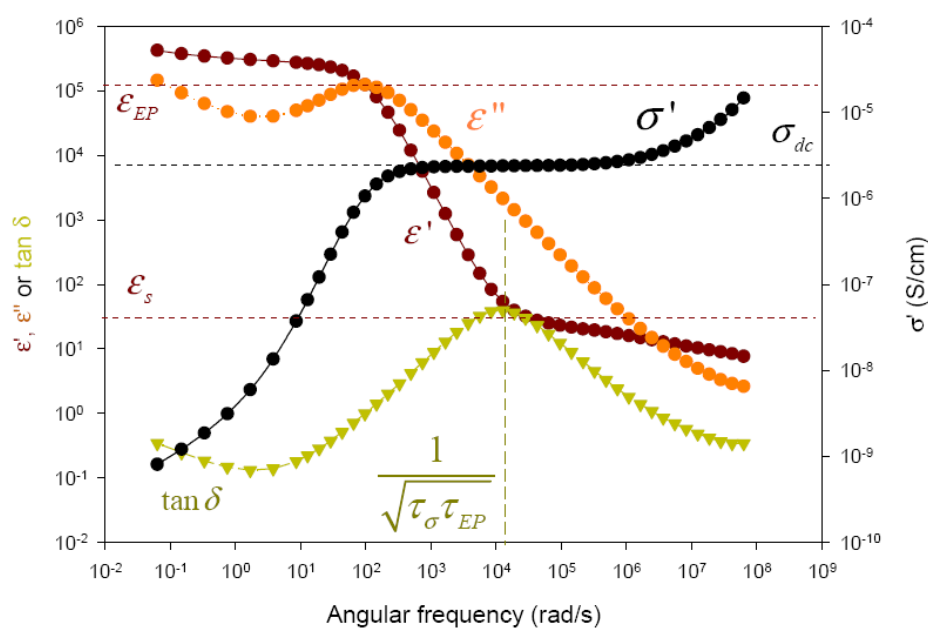
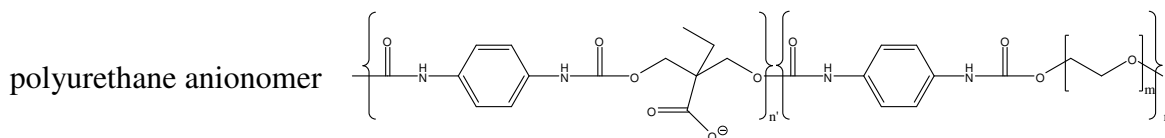
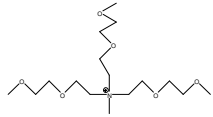


Figure 1.19. The electrode polarization relaxation, the phenomenon by which ions buildup at electrodes under low frequency electric fields, in ϵ' , ϵ'' , and $\tan\delta$ for



with $(\text{EOc})_2\text{Me}(\text{MOE})\text{N}^+$  at 30°C, with peak frequencies, dielectric

relaxation strength, and ϵ_R denoted. Ionomer synthesized and characterized by Shih-Wa Wang, in Dr. Colby group at Penn State University [35].

1.6.2. How to Separate Conducting Ion Concentration and Ion Mobility from Conductivity with EP Analysis?

The natural time scale for conduction is

$$\tau_\sigma \equiv \frac{\epsilon_s \epsilon_0}{\sigma_{DC}} \quad (1.5)$$

where ϵ_s is the static relative permittivity of the sample, ϵ_0 is the permittivity of vacuum and σ_{DC} is the d.c. conductivity, evaluated from a roughly 3-decade frequency range where the in-phase part of the conductivity $\sigma'(\omega) = \epsilon''(\omega) \epsilon_0 \omega$ is independent of frequency. At frequencies far below $1/\tau_\sigma$ the conducting ions start to polarize at the electrodes and fully polarize at the electrode polarization time scale

$$\tau_{EP} \equiv \frac{\epsilon_{EP} \epsilon_0}{\sigma_{DC}} \quad (1.6)$$

where ϵ_{EP} is the (considerably larger) effective permittivity after the electrode polarization is complete. The Macdonald/Coelho model treats electrode polarization as a simple Debye relaxation with loss tangent

$$\tan \delta = \frac{\omega \tau_{EP}}{1 + \omega^2 \tau_\sigma \tau_{EP}} \quad (1.7)$$

In practice, the conduction time scale τ_σ is calculated from the measured conductivity and permittivity of the sample, using [Equation \(1.5\)](#), and then the loss tangent associated with electrode polarization is fit to [Equation \(1.7\)](#) to determine the electrode polarization time τ_{EP} . The Macdonald/Coelho model then determines the number density of conducting ions p and their mobility μ from τ_{EP}

$$p = \frac{1}{\pi l_B L^2} \left(\frac{\tau_{EP}}{\tau_\sigma} \right)^2 \quad (1.8)$$

$$\mu = \frac{e L^2 \tau_\sigma}{4 \tau_{EP}^2 k T} \quad (1.9)$$

where $l_B \equiv e^2 / (4\pi\epsilon_s\epsilon_0 k T)$ is the Bjerrum length, L is the spacing between electrodes, e is the elementary charge, k is the Boltzmann constant and T is absolute temperature. The time scale for electrode polarization τ_{EP} is proportional to the electrode spacing L in the Macdonald/Coelho model, making the number density of conducting ions p and their mobility μ material properties that are independent of L . A material property relevant for actuation is τ_{EP} / L , obtained from [Equation \(1.9\)](#).

$$\frac{\tau_{EP}}{L} = \sqrt{\frac{e\tau_\sigma}{4\mu k T}} = \frac{1}{\mu} \sqrt{\frac{\epsilon_s\epsilon_0}{4p k T}} \quad (1.10)$$

Here we used [Equation \(1.5\)](#) and the relation $\sigma_{DC} = e\mu p$, where e is the elementary ionic charge. For fast actuation, ion-conducting membranes need to be thin (small L) have high mobility μ of conducting ions, and a high conducting ion content p .

1.6.3. A Macroscopic Model for Actuation

Actuation can be modeled as an equivalent resistor-capacitor circuit, with the time scale for polarization (or charging) $\tau_{EP} = RC$, where R is the resistance and C the capacitance of the equivalent circuit. The actuation is created on time scale τ_{EP} by a build-up of conducting ions in the Stern layer (within the Debye length of the electrode). The charge Q built up in the Stern layer is directly proportional to the applied voltage V , as $Q = CV = \tau_{EP}V/R$. With the resistance $R = L/(\sigma_{DC}A)$, where A is the electrode surface area, we have a simple relation for the charge accumulation per unit of electrode surface area (charge density).

$$\frac{Q}{A} = \frac{\tau_{EP}}{L} V \sigma_{DC} \quad (1.11)$$

Hence, the material property τ_{EP}/L multiplied by the conductivity σ_{DC} determines the charge density at the electrode. Combining **Equations. (10) and (11)** writes the charge density in terms of the number density of conducting ions and the dielectric constant.

$$\frac{Q}{A} = V e \sqrt{\frac{\epsilon_s \epsilon_0 p}{4kT}} \quad (1.12)$$

To increase the charge density of polarizing ions (and hence the strain in the actuator) we need membranes with large dielectric constant ϵ_s and large number density of conducting ions p .

1.7. Ion Size and Diffusion Coefficient

The conductivity of ions in an ionomer electrolyte is approximated by the product of the free ion concentration and the ion mobility. The *ab initio* calculations will be presented in [Chapters 2-4](#), together with the four-state model, can predict the impact of composition on free-ion concentration, however, further consideration of mobility can further aid a rational design scheme. *ab initio* calculations can provide useful information, such as ion size, solvation effect, and insight into mobility trends with compositional changes.

1.7.1. How to Estimate Ion Size

Ion size is an important parameter in interpreting the electromechanical properties of the actuators, especially the effective ion size, which is related to ion packing. It is difficult to calculate the effective ion size from *ab initio* method, because it is more a macroscopic property, nevertheless we will use the ion sizes given by *ab initio* method to compare with those given by the method described below.

To estimate the ion size, we used the molecular volumes of four neutral species 4-methyl-2-ethyl- imidazole, 4-butyl-2-methyl-1H-imidazole, fluoroboric acid and triflic acid as the analogies to the isolated ions [EMI⁺], [BMI⁺], [BF₄⁻] and [Tf]. 4-methyl-2-ethyl- imidazole and 4-butyl-2-methyl-1H-imidazole each has one less H atom comparing to [EMI⁺] and [BMI⁺] cations. Fluoroboric acid and triflic acid each has one more H atom

than $[\text{BF}_4^-]$ and $[\text{Tf}^-]$ anions. One can calculate the molecular volume based on molecular weight and density of the molecule, using **Equation (1.13)**

$$V = \frac{M_w(\text{g/mol}) \times 10^{24}}{N_A \rho(\text{g/cm}^3)} = 1.66 M_w / \rho \quad (1.13)$$

We applied this method to the four neutral molecules and the four ionic liquids, and the molecular volumes are listed in **Table 1.2**.

Table 1.2. Molecular weights and densities of four neutral molecules (in analogy to the four ions) and four ionic liquid (formed by the four ions), and their volumes calculated through **Equation (1.13)**.

Neutral molecules		M_w (g/mol)	ρ [36] (g/cm ³)	$V = 1.66 M_w / \rho$ (Å ³)
4-methyl-2-ethylimidazole	$\text{C}_6\text{H}_{10}\text{N}_2$	110.16	0.975	188
4-butyl-2-methyl-1H-imidazole	$\text{C}_8\text{H}_{14}\text{N}_2$	138.21	0.965	238
Tetrafluoroboric acid	BF_4H	87.81	1.36	107
Triflic acid	$\text{CF}_3\text{SO}_3\text{H}$	150.08	1.696	147
$[\text{EMI}^+][\text{BF}_4^-]$	$[\text{C}_6\text{H}_{11}\text{N}_2][\text{BF}_4]$	197.97	1.294	254
$[\text{EMI}^+][\text{Tf}^-]$	$[\text{C}_6\text{H}_{11}\text{N}_2][\text{CF}_3\text{SO}_3]$	260.23	1.387	311
$[\text{BMI}^+][\text{BF}_4^-]$	$[\text{C}_8\text{H}_{15}\text{N}_2][\text{BF}_4]$	226.02	1.21	310
$[\text{BMI}^+][\text{Tf}^-]$	$[\text{C}_8\text{H}_{15}\text{N}_2][\text{CF}_3\text{SO}_3]$	288.29	1.292	370

The combination of one 4-methyl-2-ethylimidazole molecule with one tetrafluoroboric acid molecule, has the same molecular formula as ionic liquid

$[\text{EMI}^+][\text{BF}_4^-]$ (both $\text{C}_6\text{H}_{11}\text{BF}_4\text{N}_2$), but the former has a much larger volume (295\AA^3) than the latter (254\AA^3), as listed in **Table 1.3**, because the ionic interactions in the ionic liquid are stronger than the dipole-dipole interaction in neutral species, therefore ionic liquid has higher density, as a result $[\text{EMI}^+][\text{BF}_4^-]$ has a smaller molecular volume, i.e., when tetrafluoroboric acid molecule delivers the proton to 4-methyl-2-ethylimidazole molecule and forms the ionic liquid, the effective volumes of both molecules shrunk, and the tetrafluoroboric acid even more so because it loses a proton.

Table 1.3. Comparison of the sum of molecular volumes of two neutral molecules and that of the ionic liquid, which has the same molecular formula estimated by **Equation (1.13)**

The sum of molecular volumes of two neutral molecules (\AA^3)		Molecular volume of ionic liquid(\AA^3)		ΔV (\AA^3)
4-methyl-2-ethylimidazole & Fluoroboric acid	295	$[\text{EMI}^+][\text{BF}_4^-]$	254	41
4-methyl-2-ethylimidazole & Triflic acid	335	$[\text{EMI}^+][\text{Tf}^-]$	311	24
4-butyl-2-methyl-1H-imidazole & Fluoroboric acid	345	$[\text{BMI}^+][\text{BF}_4^-]$	310	35
4-butyl-2-methyl-1H-imidazole & Triflic acid	385	$[\text{BMI}^+][\text{Tf}^-]$	370	15

Table 1.4. Molecular volumes estimated by *ab initio* method and by molecular weight and density.

	Molecular dimension (\AA) and volume (\AA^3) (in parenthesis) calculated by <i>ab initio</i>	Van der Waals volumes(\AA^3)[4]	Molecular volume estimated by M_w and density of neutral analogies with corrections (\AA^3)
$[\text{EMI}^+]$	$8.1 \times 5.7 \times 2.8$ (129)	116	178
$[\text{BMI}^+]$	$10.6 \times 6.2 \times 2.8$ (184)	--	235
$[\text{BF}_4^-]$	$3.3 \times 3.3 \times 3.3$ (36)	49	76
$[\text{Tf}^-]$	$4.8 \times 3.7 \times 3.7$ (66)	80	135

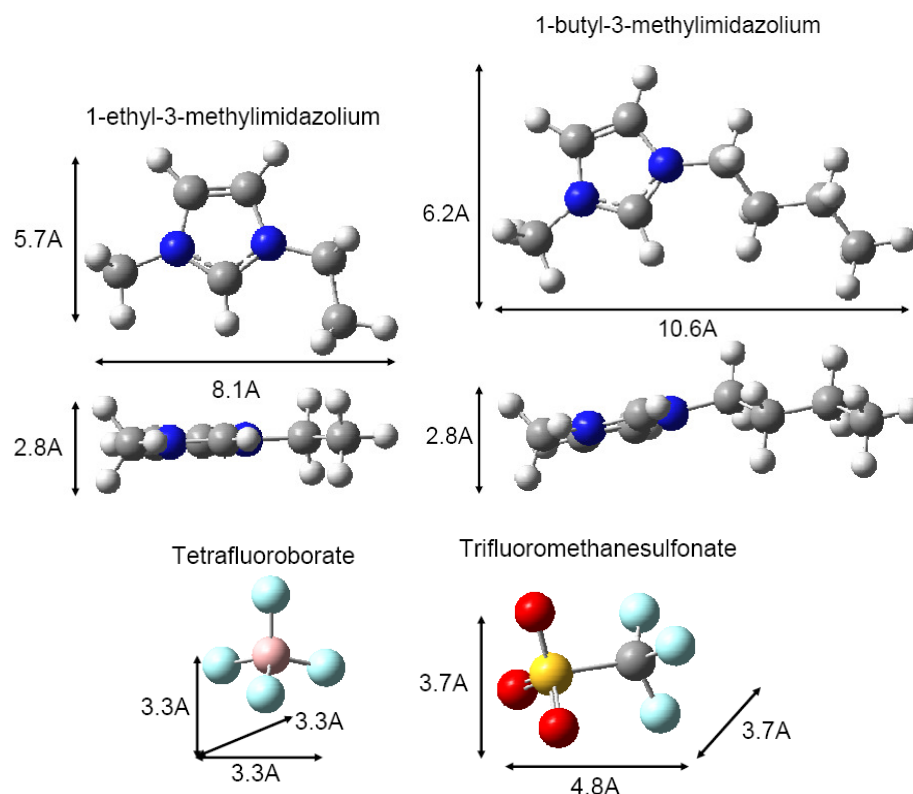


Figure 1.20. Molecular structures and molecular dimensions of 1-ethyl-3-methylimidazolium ([EMI⁺]), 1-butyl-3-methylimidazolium ([BMI⁺]), Tetrafluoroborate ([BF₄⁻]) and Trifluoromethanesulfonate ([Tf⁻]).

Assuming ion occupies the same volume with different counterions, let the volume change of fluoroboric acid to [BF₄⁻] be ΔV_1 , ($\Delta V_1 > 0$), from table 2, we know the volume change of triflic acid to [Tf⁻] is about $\Delta V_1 - 19$; the volume change of 4-butyl-2-methyl-1H-imidazole to [BMI⁺] is about $34 - \Delta V_1$, and the volume change of 4-methyl-2-ethylimidazole to [EMI⁺] is about $41 - \Delta V_1$. Under our definition, all volume changes are positive, so that we have $19 < \Delta V_1 < 34 \text{ \AA}^3$. Moreover, it is reasonable to consider the effective volume of neutral molecule decreases more when it change into anion, not only due to the tighter packing, but also owing to losing a proton, so that $\Delta V_1 - 19 > 41 - \Delta V_1$

finds true. Hence, we have $30 < \Delta V_1 < 34$. Any value coming from the narrow variation range of ΔV_1 is reasonable, and we choose $\Delta V_1 = 31 \text{ \AA}^3$. Consequently, the molecular volume of $[\text{BF}_4^-]$ is $107 - 31 = 76 \text{ \AA}^3$; $[\text{Tf}^-]$ is $147 - 12 = 135 \text{ \AA}^3$; $[\text{BMI}^+]$ is $238 - 3 = 235 \text{ \AA}^3$ and $[\text{EMI}^+]$ is $188 - 10 = 178 \text{ \AA}^3$.

Ab initio calculations can give us a more visualized way to estimate the ion size. We measured the greatest distances (between nuclei) at three dimensions on each ion, and a constant term (1 \AA) is added to account for the van der Waals contribution. For instance, the three greatest dimensions measured on $[\text{EMI}^+]$ is 8.1 \AA , 5.7 \AA and 2.8 \AA , each adds 1 \AA to account for the van der Waals contribution, so that the van der Waals volume is approximately 129 \AA^3 , which is in a good agreement with Makoto Ue's work[37].

1.7.2. How to Estimate Ion Diffusion Coefficient

Method I: Consider the experiment of applying the same voltage (U) upon these four ions. The diffusion coefficient measured with applied electric field is D . Size of the ion is r_{ion} , mass of the ion is m , and the number of charges on the ion is z , here $z = 1$. Assuming $V \propto r_{ion}^3$. As we know, $\text{Velocity}^2 \times \text{Mass} = 2 \times \text{Energy}$

So that $\left(\frac{D}{r_{ion}}\right)^2 m = 2ezU \rightarrow D^2 \cdot r_{ion} \cdot \rho \propto 2ezU$. In our case, $2ezU$ is a constant for

these four ions. Thus we have

$$D \propto (\rho \cdot r_{ion})^{-0.5} \quad (1.14)$$

with Equation (1.13) we have $D \propto \rho^{-1/3} M_w^{-1/6}$.

Method II: Stokes-Einstein Relation: $\mu = \frac{e}{6\pi\eta r_{ion}} \rightarrow D = \frac{kT}{6\pi\eta r} = \frac{kT}{6\pi\rho\eta_{dyn}r_{ion}}$

roughly we have $D \propto (\rho \cdot r_{ion})^{-1}$ (1.15)

with [Equation \(1.13\)](#) we have $D \propto \rho^{-2/3} M_w^{-1/3}$

To determine with method is right, we can compare them with experiment results. However, [Equations. \(1.14\), \(1.15\)](#) only give the qualitative estimations, one is the square of the other, so that the four ions' diffusion coefficients figured by both methods should have the same order. Dr. Jing Li at Dr. Louis Madsen group at Virginia Tech measured the diffusion coefficients of four ions by pulsed-field gradient-nuclear magnetic resonance, which suggested $D_{EMI^+} > D_{BMI^+} > D_{Tf^-}$ and $D_{BF_4^-} > D_{Tf^-}$. Applying the data in [Table 1.2.](#) in [Equations. \(1.14\), \(1.15\)](#), as expected, the order of diffusion coefficients of these four ions estimated by two methods both agree with the NMR measurement.

Dr. Bagchi and Dr. Biswas at Indian Institute of Science have done very interesting work on ionic conductivity in a dilute electrolyte solution and ultrafast solvation dynamics [\[38,39\]](#). The forces acting on the ion in a dilute electrolyte solution can be divided into two type: short range force and the long range ion-dipole forces. The former can be related to viscosity via Stokes relation. The long range force part is the one which is responsible for the anomalous behavior of ionic conductance. Continuum models of Hubbard-Onsagar-Zwanzig neglected the molecularity. The theory of Calef and Wolynes treated the dipolar response as over damped, but emphasized the role of translational motion of the solvent molecules. The mobility of this ion is determined by diffusion which in turn is determined by the friction on the ion, via Einstein relation

$$D = \frac{ekT}{6\pi\eta r_{ion}} \quad (1.16)$$

The classical theory (Hubbard-Onsagar-Zwanzig) finds that the friction on the ion, and hence the mobility, depends inversely on the Debye relaxation time τ_D , which is the slowest time. This leads to the well-known law of Walden's product

$$\Lambda_0 \eta_0 \sim r_{ion}^{-1} \quad (1.18)$$

which states that the product of the limiting ionic conductivity (Λ_0) of an electrolyte and the viscosity (η_0) is inversely proportional to the radius (r_{ion}) of the ion.

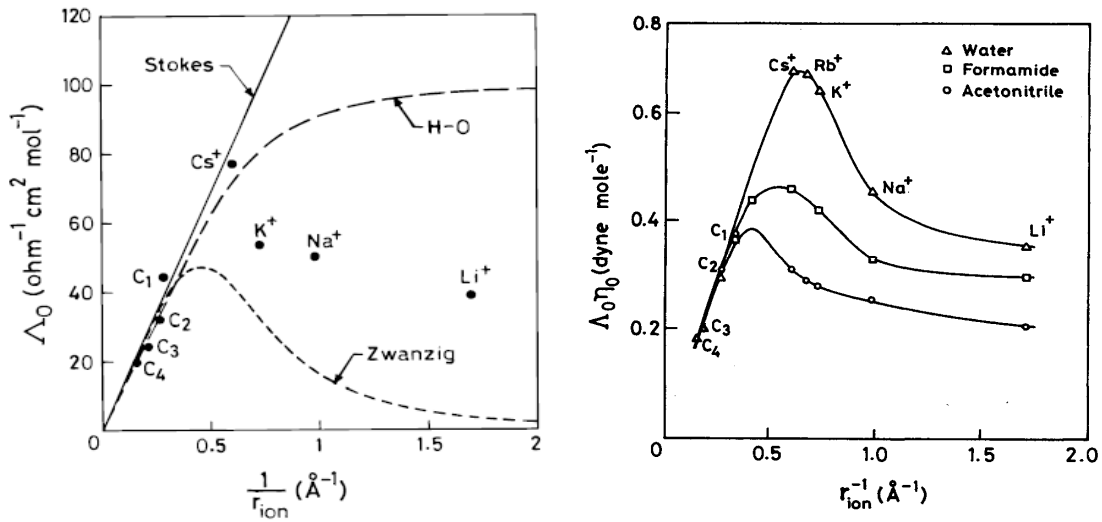


Figure 1.21. Experimental values of limiting ionic conductivity (Λ_0) and the Walden product ($\Lambda_0 \eta_0$) of rigid, monpositive ions in water (*open triangle*), acetonitrile and fomamide (*open squares*) at 298 K are plotted as a function of the inverse of the crystallography ionic radius (r_{ion}^{-1}). [38]

Walden's product $\Lambda_0 \eta_0 \sim r_{ion}^{-1}$ well describes the behavior of bulky ions (RN^+) follow: larger ionic radius lowers conductivity (**Figure 1.21**). Whereas, the r_{ion} accounts

for the four alkali metal cations in **Figure 1.21**, are in the order of $r_{Li^+} > r_{Na^+} > r_{K^+} > r_{Cs^+}$, opposite of the order by the ionic radius. This is because for strongly solvated small ions the **hydrodynamic** (“Stokes”) **radius** rather than ionic radius should be applied in Walden's product. Li^+ has higher charge density than Cs^+ , hence larger hydration sphere. However, H^+ is an exception. Though small, H^+ has high conductivity and mobility. We think this may due to rapid reorientation of water molecules.

1.8. Physical Fundamentals of Dielectrics – Static Dipoles [39]

The total moment of the molecule, also called the internal moment is the sum of its vacuum value and the value induced in it by the reaction field, that is

$$\bar{\mu}_i = \bar{\mu}_v + \alpha \bar{R} = \bar{\mu}_v + \alpha \frac{1}{a^3} \frac{2(\epsilon_s - 1)}{2\epsilon_s + 1} \bar{\mu}_i, \text{ which can be written as } \bar{\mu}_i = \frac{\bar{\mu}_v}{1 - \frac{2\alpha}{a^3} \frac{\epsilon_s - 1}{2\epsilon_s + 1}}$$

(1.19)

If the polarizability α is known, because $\frac{\epsilon_\infty - 1}{\epsilon_\infty + 2} \frac{M}{\rho} = \frac{4\pi N_A \alpha_\infty}{3}$, M is molecular

weight and ρ is density, and $\frac{4\pi a^3}{3} = \frac{V}{N}$, where N is the number of molecules in a volume

V . These two equations lead to $\alpha = a^3 \frac{\epsilon_\infty - 1}{\epsilon_\infty + 2}$ (1.20) Then from **Equations (1.19)** to

$$(1.20) \text{ one obtains } \bar{\mu}_i = \bar{\mu}_v + \alpha \bar{R} = \bar{\mu}_v + \frac{2(\epsilon_s - 1)(\epsilon_\infty - 1)}{3(2\epsilon_s + \epsilon_\infty)} \bar{\mu}_v = \frac{(2\epsilon_s + 1)(\epsilon_\infty + 2)}{3(2\epsilon_s + \epsilon_\infty)} \bar{\mu}_v \quad (1.21)$$

Equation (1.21) the internal dipole moment is calculated in the absence of an external electric field. When this force field is applied, **Equation (1.21)** must be

modified to take into account this effect. In fact the total field in the cavity is now the superposition of the cavity field \mathbf{G} with the reaction field due to the dipole. Accordingly

$$\bar{\mu}_i = \bar{\mu}_v + \alpha \left(\frac{3\epsilon_s}{2\epsilon_s + 1} \bar{E}_0 + \frac{1}{a^3} \frac{2(\epsilon_s - 1)}{2\epsilon_s + 1} \bar{\mu}_i \right) \text{ from which } \bar{\mu}_i = \frac{\bar{\mu}_v + \frac{3\alpha\epsilon_s}{2\epsilon_s + 1} \bar{E}_0}{1 - \frac{\epsilon_s - 1}{\epsilon_s + 2} \frac{2(\epsilon_s - 1)}{2\epsilon_s + 1}}$$

Clausius-Mossotti Equation: $\frac{\epsilon_s - 1}{\epsilon_s + 2} = \frac{4\pi\nu}{3} \alpha$ Relating ϵ_s and the total

polarizability in **dilute system**. It also works for **very high frequencies** when dipolar

contribution to permittivity is negligible. $\frac{\epsilon_\infty - 1}{\epsilon_\infty + 2} = \frac{4\pi\nu}{3} \alpha_d$ Considering the dipolar

contribution to the polarizability. It also provides a way to **measure** dipolar moment.

Debye Equation for the Static Permittivity $\frac{\epsilon_s - 1}{\epsilon_s + 2} = \frac{4\pi\nu}{3} \left(\alpha_d + \frac{\mu_v^2}{12\pi\epsilon_0 kT} \right)$ (in SI

unit system) or $\frac{\epsilon_s - 1}{\epsilon_s + 2} = \frac{4\pi\nu}{3} \left(\alpha_d + \frac{\mu_v^2}{3kT} \right)$ (in cgs unit system) where α_d is the distortional

polarizability, we consider $\alpha_d = \alpha_\infty$ (at very high frequencies)

$$\frac{\epsilon_\infty - 1}{\epsilon_\infty + 2} = \frac{4\pi\nu}{3} \alpha_d \rightarrow \frac{n^2 - 1}{n^2 + 2} = \frac{4\pi\nu}{3} \alpha_d \quad (n \text{ refractive index})$$

Lorentz-Lorenz Equation $\frac{\epsilon_s - 1}{\epsilon_s + 2} - \frac{\epsilon_\infty - 1}{\epsilon_\infty + 2} = \frac{\nu\mu_v^2}{9\epsilon_0 kT}$ (in SI unit system) or

$$\frac{\epsilon_s - 1}{\epsilon_s + 2} - \frac{\epsilon_\infty - 1}{\epsilon_\infty + 2} = \frac{4\pi\nu\mu_v^2}{9kT} \quad (\text{in cgs unit system}), \text{ actually } \frac{\nu\mu_v^2}{9\epsilon_0 kT} = \frac{\Theta}{T} \text{ or } \frac{4\pi\nu\mu_v^2}{9kT} = \frac{\Theta}{T}$$

(Θ **Curie temperature**), this equation suggests that, at temperature Θ , spontaneous polarization should occur and the material should become ferroelectric even in the

absence of an electric field. Ferroelectricity is uncommon in nature, and predictions made by this equation are not experimentally supported. The failure of the theory arises from considering null the contributions to the local field of the dipoles in the cavity. This fact emphasizes the inadequacy of the Lorentz field in a dipolar dielectric and leaves open the question of the **internal field in the cavity**.

Onsager Formula
$$\frac{(\epsilon_s - \epsilon_\infty)(2\epsilon_s + \epsilon_\infty)}{\epsilon_s(\epsilon_\infty + 2)^2} = \frac{\nu \mu_v^2}{9\epsilon_0 kT} \text{ or } \frac{(\epsilon_s - \epsilon_\infty)(2\epsilon_s + \epsilon_\infty)}{\epsilon_s(\epsilon_\infty + 2)^2} = \frac{4\pi\nu \mu_v^2}{9kT} \quad (1.22)$$

Onsager Formula will be used in **Chapter 3** to estimate the ion pair concentration.

$$\therefore (\epsilon_s - 1)\bar{E}_0 = 4\pi\bar{P} = 4\pi\nu\bar{\mu}_i = 4\pi\nu\left(\alpha\bar{E}_i + \frac{\mu_v^2}{12\pi\epsilon_0 kT}\bar{E}_d\right) \text{ or}$$

$$(\epsilon_s - 1)\bar{E}_0 = 4\pi\bar{P} = 4\pi\nu\bar{\mu}_i = 4\pi\nu\left(\alpha\bar{E}_i + \frac{\mu_v^2}{3kT}\bar{E}_d\right) \rightarrow$$

$$\epsilon_s - 1 = 4\pi\nu\left(\alpha_d + \frac{(2\epsilon_s + 1)(\epsilon_\infty + 2)}{3(2\epsilon_s + \epsilon_\infty)} \frac{\mu_v^2}{12\pi\epsilon_0 kT}\right) \frac{\epsilon_s(\epsilon_\infty + 2)}{2\epsilon_s + \epsilon_\infty} \text{ or}$$

$$\epsilon_s - 1 = 4\pi\nu\left(\alpha_d + \frac{(2\epsilon_s + 1)(\epsilon_\infty + 2)}{3(2\epsilon_s + \epsilon_\infty)} \frac{\mu_v^2}{3kT}\right) \frac{\epsilon_s(\epsilon_\infty + 2)}{2\epsilon_s + \epsilon_\infty}$$

Comparing with **Debye Equation**

$$(\epsilon_s - 1)\bar{E}_0 = 4\pi\bar{P} = 4\pi\nu\left(\alpha_d\bar{E}_0 + \frac{\mu_v^2}{12\pi\epsilon_0 kT}\bar{E}_0\right) \frac{\epsilon_s + 2}{3} \text{ or}$$

$$(\epsilon_s - 1)\bar{E}_0 = 4\pi\bar{P} = 4\pi\nu\left(\alpha_d\bar{E}_0 + \frac{\mu_v^2}{3kT}\bar{E}_0\right) \frac{\epsilon_s + 2}{3}, \text{ leading to the conclusion that the}$$

Onsager theory takes for the **internal and directing fields more accurate** values than older theories in which the Lorentz field is used. In view of the coefficients appearing in

Equation (1.22), it is clear that the *Onsager equation does not predict Ferroelectricity* as the Debye equation does. In fact, the cavity field tends to $3E_0/2$ when $\epsilon_s \rightarrow \infty$. Onsager takes into account the *field inside the spherical cavity that is caused by molecular dipoles outside*, which is neglected in the Debye theory. However, following the Boltmann-Langevin methodology, the *Onsager theory neglects dipole-dipole interactions*, or, equivalently, *local directional forces between molecular dipoles are ignored*. The range of applicability of the *Onsager equation is wider than that of the Debye equation*. For example, it is useful to describe the dielectric behavior of noninteracting dipolar fluids, but in general this is not valid for condensed matter.

Onsager treatment of the cavity differs from Lorentz's because the cavity is assumed to be filled with a dielectric material having a macroscopic dielectric permittivity. Also, Onsager studies the dipolar reorientation polarizability on statistical grounds, as Debye does. However, the use of macroscopic arguments to analyze the dielectric problem in the cavity *prevents the consideration of local effects* which are important in condensed matter. This situation led Kirkwood first [40] and Frohlich later on [41] to develop a fully statistical argument to determine the short-range dipole-dipole interactions. For methodological reasons, these two approaches will be considered separately.

Kirkwood deals with distortional polarization by postulating that the polarizability in $P = vE_i \left(\alpha_d + \frac{\mu_v^2}{12\pi\epsilon_0 kT} \right)$ or $P = vE_i \left(\alpha_d + \frac{\mu_v^2}{3kT} \right)$ is also affected by a local field given by $E_i = \frac{3\epsilon_s}{2\epsilon_s + 1} \cdot \frac{3}{\epsilon_s + 2} E_0 = \frac{9\epsilon_s}{(2\epsilon_s + 1)(\epsilon_s + 2)} E_0$ where $\frac{3\epsilon_s}{2\epsilon_s + 1}$ is the Onsager

cavity field for the dipole, and $\frac{3}{\epsilon_s + 2}$ is the local field in the dielectric sphere in vacuum.

We can easily achieve **Kirkwood Equation** from **Debye Equation** by a factor of

$$\frac{9\epsilon_s}{(2\epsilon_s + 1)(\epsilon_s + 2)}$$

under the consideration of correlation parameter $g = \langle \vec{\mu} \cdot \vec{\mu} \rangle / \mu^2$, which

is a measure of the local order in the specimen. $g=1$ means there is no dipolar correlation between neighboring molecules. If the effect of the dipole is to orient the surrounding dipoles in the same direction, then $g>1$, but if a fixed dipole tends to orient the neighbors in an antiparallel direction, then $g<1$.

$$\frac{\epsilon_s - 1}{\epsilon_s + 2} = \frac{4\pi\nu}{3} \left(\alpha_d + \frac{g\mu^2}{12\pi\epsilon_0 kT} \right) \frac{9\epsilon_s}{(2\epsilon_s + 1)(\epsilon_s + 2)} \rightarrow$$

$$\frac{(\epsilon_s - 1)(2\epsilon_s + 1)}{3\epsilon_s} = 4\pi\nu \left(\alpha + \frac{g\mu_i^2}{12\pi\epsilon_0 kT} \right)$$

$$\text{or } \frac{\epsilon_s - 1}{\epsilon_s + 2} = \frac{4\pi\nu}{3} \left(\alpha_d + \frac{g\mu^2}{3kT} \right) \frac{9\epsilon_s}{(2\epsilon_s + 1)(\epsilon_s + 2)} \rightarrow$$

$$\frac{(\epsilon_s - 1)(2\epsilon_s + 1)}{3\epsilon_s} = 4\pi\nu \left(\alpha + \frac{g\mu_i^2}{3kT} \right)$$

where $\nu = N/V$, and μ is the internal moment related to the moment in vacuum by

$$\vec{\mu}_i = \frac{(2\epsilon_s + 1)(\epsilon_s + 2)}{9\epsilon_s} \vec{\mu}_v$$

In Summary

Frohlich-Kirkwood-Onsager Formula

$$\frac{(\epsilon_s - \epsilon_\infty)(2\epsilon_s + \epsilon_\infty)}{\epsilon_s(\epsilon_\infty + 2)^2} = \frac{\nu g \mu_v^2}{9\epsilon_0 kT} \text{ or } \frac{(\epsilon_s - \epsilon_\infty)(2\epsilon_s + \epsilon_\infty)}{\epsilon_s(\epsilon_\infty + 2)^2} = \frac{4\pi\nu g \mu_v^2}{9kT}$$

No External Field: $\bar{\mu}_i = \bar{\mu}_v + \alpha \bar{R}$; $\alpha = \frac{3}{4\pi\nu} \frac{\epsilon_\infty - 1}{\epsilon_\infty + 2}$; $R = \frac{1}{a^3} \frac{2(\epsilon_s - 1)}{2\epsilon_s + 1} \bar{\mu}_i$;

$$\bar{\mu}_i = \bar{\mu}_v + \alpha \bar{R} = \frac{(2\epsilon_s + 1)(\epsilon_\infty + 2)}{3(2\epsilon_s + \epsilon_\infty)} \bar{\mu}_v$$

With External Field: $\bar{\mu}_i = \bar{\mu}_v + \alpha \left(\frac{3\epsilon_s}{2\epsilon_s + 1} \bar{E}_0 + \frac{1}{a^3} \frac{2(\epsilon_s - 1)}{2\epsilon_s + 1} \bar{\mu}_i \right)$;

$$\bar{\mu}_i = \left(\bar{\mu}_v + \frac{3\alpha\epsilon_s}{2\epsilon_s + 1} \bar{E}_0 \right) \left/ \left(1 - \frac{\epsilon_\infty - 1}{\epsilon_\infty + 2} \frac{2(\epsilon_s - 1)}{2\epsilon_s + 1} \right) \right.$$

Clausius-Mossotti Equation: $\frac{\epsilon_s - 1}{\epsilon_s + 2} = \frac{4\pi\nu}{3} \alpha$

Lorentz-Lorenz Equation $\frac{\epsilon_s - 1}{\epsilon_s + 2} - \frac{\epsilon_\infty - 1}{\epsilon_\infty + 2} = \frac{\nu\mu_v^2}{9\epsilon_0 kT}$ or $\frac{\epsilon_s - 1}{\epsilon_s + 2} - \frac{\epsilon_\infty - 1}{\epsilon_\infty + 2} = \frac{4\pi\nu\mu_v^2}{9kT}$

$$\frac{\nu\mu_v^2}{9\epsilon_0 kT} = \frac{\Theta}{T} \text{ or } \frac{4\pi\nu\mu_v^2}{9kT} = \frac{\Theta}{T}$$

Debye Equation for the Static

$$\text{Permittivity } \frac{\epsilon_s - 1}{\epsilon_s + 2} = \frac{4\pi\nu}{3} \left(\alpha_d + \frac{\mu_v^2}{12\pi\epsilon_0 kT} \right) \text{ or } \frac{\epsilon_s - 1}{\epsilon_s + 2} = \frac{4\pi\nu}{3} \left(\alpha_d + \frac{\mu_v^2}{3kT} \right)$$

Kirkwood Equation

$$\frac{(\epsilon_s - 1)(2\epsilon_s + 1)}{3\epsilon_s} = 4\pi\nu \left(\alpha + \frac{g\mu_i^2}{12\pi\epsilon_0 kT} \right) \text{ or } \frac{(\epsilon_s - 1)(2\epsilon_s + 1)}{3\epsilon_s} = 4\pi\nu \left(\alpha + \frac{g\mu_i^2}{3kT} \right)$$

where $\bar{\mu}_i = \frac{(2\epsilon_s + 1)(\epsilon_s + 2)}{9\epsilon_s} \bar{\mu}_v$

Onsager Formula $\frac{(\epsilon_s - \epsilon_\infty)(2\epsilon_s + \epsilon_\infty)}{\epsilon_s(\epsilon_\infty + 2)^2} = \frac{\nu\mu_v^2}{9\epsilon_0 kT}$ or $\frac{(\epsilon_s - \epsilon_\infty)(2\epsilon_s + \epsilon_\infty)}{\epsilon_s(\epsilon_\infty + 2)^2} = \frac{4\pi\nu\mu_v^2}{9kT}$

Frohlich-Kirkwood-Onsager Formula

$$\frac{(\epsilon_s - \epsilon_\infty)(2\epsilon_s + \epsilon_\infty)}{\epsilon_s(\epsilon_\infty + 2)^2} = \frac{\nu g \mu_\nu^2}{9\epsilon_0 kT} \text{ or } \frac{(\epsilon_s - \epsilon_\infty)(2\epsilon_s + \epsilon_\infty)}{\epsilon_s(\epsilon_\infty + 2)^2} = \frac{4\pi\nu g \mu_\nu^2}{9kT}$$

$$\text{where } \nu = \frac{N_A \rho}{M} \quad g = \frac{9\epsilon_0 kT(\epsilon_s - \epsilon_\infty)(2\epsilon_s + \epsilon_\infty)}{\nu \mu_\nu^2 \epsilon_s(\epsilon_\infty + 2)^2} \text{ or } g = \frac{9kT(\epsilon_s - \epsilon_\infty)(2\epsilon_s + \epsilon_\infty)}{4\pi\nu \mu_\nu^2 \epsilon_s(\epsilon_\infty + 2)^2}$$

1.9. Some basics about *ab initio* Calculations

The Latin term "*ab initio*" means from the beginning, "from first principles", because it relies on basic and established laws of nature without additional assumptions or special models. *Ab initio* molecular orbital theory is concerned with predicting the properties of atomic and molecular systems. It is based upon the fundamental laws of quantum mechanics and uses a variety of mathematical transformation and approximation techniques to solve the fundamental equations.

The advantages of *ab initio* calculation are evident. It calculates the interactions controlled by electronic structure. Comparing with experiment, it is the rapidest, easiest and cheapest way to predict properties without synthesis. Furthermore, calculation provides data unreachable by experimental techniques. It can also investigate into individual interactions; generate molecular level data, leads to understand of nanoscale phenomena. For example, sulfonated PEO ionomer with Li^+ . We can use *ab initio* methods to calculates optimal distances and interaction energies and determine the functional groups that bind to these anions and leave the cation to do whatever it likes.

The Schrödinger equation ([Equation \(1.23\)](#)) governs the temporal and spatial evolution of the quantum mechanical wave function:

$$\left(\frac{-\hbar^2}{8\pi^2 m} \nabla^2 + \bar{V} \right) \psi(\bar{r}, t) = \frac{i\hbar}{2\pi} \frac{\partial \psi(\bar{r}, t)}{\partial t} \quad (1.23)$$

In this equation, ψ is the wavefunction, m is the mass of the particle, \hbar is Planck's constant, and \bar{V} is the potential field in which the particle is moving. The product of ψ with its complex conjugate ($\psi \cdot \psi^*$, often written as $|\psi|^2$) is interpreted as the probability distribution of the particle.

We appreciate the fact that the statement Dr. P.A.M. Dirac made in 1926 still holds true 80 years later: " The underlying physical laws necessary for the mathematical theory of a large part of physics and the whole of chemistry are thus completely known, and the difficulty is only that the exact application of these laws leads to equations much too complicated to be soluble." [42]. For poly-electronic atoms and molecules, effects of electron correlation and exchange interactions render an exact solution to Schrödinger equation impossible, but only for the most trivial molecular systems (e.g. simple potential wells, hydrogen atom, dihydrogen ion H_2^+ , simple harmonic oscillator, rigid rotor). A number of simplifying assumptions and procedures must be resorted to make an approximation solution possible for a large range of molecules.

The Born-Oppenheimer approximation [43] is the first applied, which means that the nuclear and electronic motions are decoupled and treated separately. This approximation is reasonable since the nuclei look fixed to the electrons, and electronic motion can be described as occurring in a field of fixed nuclei. Thus, each electronic structure calculation is performed for a fixed nuclear configuration, and therefore the positions of all atoms must be specified in an input file. *Ab initio* methods are available in

many modelling packages, such as *Gaussian*, which is available on a UCS unix machine. *Gaussian* then computes the electronic energy by solving the electronic Schrödinger equation for this fixed nuclear configuration. From this point on, we focus entirely on the electronic problem.

Secondly, the electronic wavefunction is represented in certain finite basis sets, and the Schrödinger equation is transformed into an algebraic equation which can be solved using numerical methods. In Gaussian basis functions are used to approximate the molecular orbital (MO), since the required integrals can be computed very quickly in this basis.

MO theory finds approximate solutions to get energies and orbitals of electrons. **Energies** can be used to determine geometry optimisation, reaction energetics, activation energies for kinetics and UV/vis absorption prediction. **Orbitals** can be used for graphical display (including assessment of where reactants might attack), charges, dipole moments, electrostatic potentials and NMR shieldings.

Once approximations are introduced, it matters how the orbitals are determined. The simplest choice is *Hartree-Fock* (HF) *self-consistent field* (SCF) method, and it is usually the first step in any *ab initio* calculation. To do an *ab initio* calculation, we need to select a method and a basis set. The notation written in papers, and in the command line to Gaussian, is in the form method/basis, e.g. RHF/3-21G*, MP2/6-311G*(d) or B3LYP/6-31G*. The HF method works by calculating orbitals for one electron in an average field of the rest. This method starts with a guess at the electron distribution, coming from a semiempirical calculation. The HF method then uses the guess to calculate the average field of the rest of the electrons, and then calculate coefficients to produce a

set of one-electron MOs and energies, fill the MOs according to the Aufbau principle [44] and get the total electronic energy. Afterwards, this set of MOs is used as the next approximation to the electron distribution. The process is repeated with gradually improving MOs, until the electronic energy converges, i.e. it changes by less than some pre-set limit.

The program can save a lot of time if it knows that all electrons are paired, so it can treat them two at a time. This is so for ordinary, diamagnetic organic compounds, for most main-groups compounds, and for organometallic compounds which obey the 18-electron rule. This is called a restricted Hartree-Fock treatment (RHF). The disadvantage of HF is that it has no knowledge of the positions of these. Thus, even though the Coulomb interaction between the electrons is taken into account in an averaged way, the electrons are unable to avoid each other when they come close, and therefore the electron repulsion is overestimated in Hartree-Fock.

There are three kinds of errors in using the Hartree-Fock method with practicable-sized basis sets. 1) Hartree-Fock Limit: Lower absolute energy and better relative energies would be achieved, if a bigger basis set can be used. However, there is an unreachable theoretical limit that the energy converges to as basis set size goes up. 2) We have taken no account of relativity. Electrons move faster near heavy nuclei, so their masses change. There should be a relativistic correction. 3) Correlation Energy: When we look at single electrons in an average field of the rest, we take no account of time dependence, thus the positions of individual electrons at particular instants are correlated.

$$\text{Altogether, } E_{\text{True}} = E_{\text{HF practical}} - E_{\text{basis set error}} - E_{\text{correlation}} - E_{\text{relativistic}}$$

Considerations to reduce these errors are listed below:

1) A basis set error always has to be tolerated: the question is whether to spend calculation time on a bigger basis set, or whether to spend it on reducing the other errors by using a higher method. [45]

2) Some of the relativistic error can be removed by using the Effective Core Potential (ECP) basis sets for heavy atoms

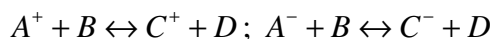
3) What to do about correlation energy is the crunch problem. It is particularly important for loosely bound molecules, like transition states. The traditional next method above Hartree-Fock is the Møller-Plesset Perturbation Theory (MP2). Qualitatively, MP2 adds higher excitations to HF theory as a non-iterative correction, drawing upon techniques from the area of mathematical physics known as many body perturbation theory. MP2 is often used to get more accurate energies, after geometries have been found at the HF level. The first perturbation to the HF energy will always be negative. Lowering the energy is what the exact correction should do, although the MP2 theory correction is capable of overcorrecting it.

1.10. Ion/Molecule Equilibria & Van 't Hoff Equation

We are interested in the calculation of interaction energies of various small cations with common functional groups found on polymers and also carboxylate, sulfonate and phosphonate groups that can be present in anionic ionomers. It goes without saying that we need to verify our calculations by comparing with experiment data. The ion clustering data we used were provided by the NIST [46], such as, a neutral

species with ion clustering data specified, or all matching species which are ligands in at least one ion clustering reaction.

Most of the gas-phase ionization energy data presented in the NIST collection are derived from determinations of the equilibrium constants for ion/molecule reactions:



Since the equilibrium constant

$$K_{eq} = \frac{[C^+][D]}{[A^+][B]}; K_{eq} = \frac{[C^-][D]}{[A^-][B]} \quad (1.24)$$

directly gives a value for the Gibbs free energy change associated with the reaction.

In order to determine the enthalpy changes of these reactions, values for the entropy changes of reaction must be obtained. Conventionally, the relative thermochemical scales are generated by measuring the concentrations of different species at various temperatures, and then we can get the equilibrium constant as a function of temperature using the Van't Hoff equation ([Equation \(1.25\)](#)), which relates the change in temperature (T) to the change in the equilibrium constant (K_{eq}) given the enthalpy change (ΔH°), combined with Gibbs free energy.

$$-RT \ln K_{eq} = \Delta G^\circ = \Delta H^\circ - T\Delta S^\circ \quad (1.25)$$

In [Chapters 3](#) and [4](#), we can apply a reverse usage of [Equation \(1.25\)](#) considering the equilibria between various ion states, to estimate each state population distributions. However, Van't Hoff plots determined in different laboratories usually show poor agreement, indicating possible experimental problems in these determinations. The major uncertainty in data derived from equilibrium constant determinations, aside

from the question of whether thermodynamic equilibrium is actually attained, is in knowing the temperature accurately. It was found that for the large body of data evaluated in the 1984 publication [47] the thermochemical scales had been constricted by as much as 15% because operating temperatures of the instruments used in the experiments had been underestimated. The poorly characterized relative and absolute neutral pressures in such experiments in the past also led to the deviation, which could vary from instrument to instrument, based on design, and from experiment to experiment, based on varying operating conditions. Other possible contributing factors are clustering of neutral molecules to the ions at low temperatures, and pyrolysis of the ions at high temperatures.

Therefore, at the present time, it appears that the most reliable values for entropy changes associated with such ion-molecule equilibria can be obtained by judiciously examining experimentally-determined entropy changes in conjunction with *ab initio* calculations of those quantities. In practice, many studies have been published in which measurements were made at a single temperature [48], with the (usually small) entropy change for the reaction estimated from statistical mechanical considerations.

References

- [1] U.S. Energy Information Administration, *Annual Energy Review 2012*, Tables 1.3, 2.1b-2.1f, 10.3, and 10.4.
- [2] *Renewable Energy Consumption and Electricity 2012 Statistics*. Table 1: U.S. Energy Consumption by Energy Source, 2008-2012 (July 2013)
- [3] M. Stanley Whittingham, *MRS Bulletin*, **33**, 411 (2008).
- [4] <http://www.howstuffworks.com/lithium-ion-battery1.htm>
- [5] J.-M. Tarascon and M. Armand, *Nature* **414**, 359 (2001).
- [6] J. R. Owen, *Chem. Soc. Rev.* **26**, 259 (1997).
- [7] D. Linden and T. B. Reddy, eds., *Handbook of Batteries*, 3rd ed., McGraw Hill, New York, 2002.
- [8] M. Winter, J.O. Besenhard, M.E. Spahr, and P. Novak, *Adv. Mater.* **10**(10), 725–763 (1998).
- [9] M.S. Whittingham, R.F. Savinell, and T. Zawodzinski, eds., *Chemical Reviews* **104**(10), 4243–4886 (2004).
- [10] M. Armand and J.-M. Tarascon, *Nature* **451**, 652 (2008).
- [11] P.G. Bruce, B. Scrosati and J.-M. Tarascon, *Angew. Chem. Int. Ed.* **47**, 2930 (2008).
- [12] F. Gray and M. Armand, in *Energy Storage Systems for Electronics*, T. Osaka and M. Datta, eds., Gordon and Breach (2000), p. 351, Chapter on Polymer Electrolytes.
- [13] G. Cakmak, A. Verhoeven and M. Jansen, *J. Mater. Chem.* **19**, 4310 (2009).
- [14] S-W Ryu, *Polym. J.* **40**, 688 (2008).

- [15] S-W Ryu and A. M. Mayes, *Polymer*, **49**, 2268 (2008).
- [16] A. Eisenberg and J-S Kim. *Introduction to Ionomers*. Wiley 1998.
- [17] B. P. Grady, *Polym. Eng. Sci.* 1029 (2008).
- [18] Y. Bar-Cohen, *Electroactive Polymer Actuators as Artificial Muscles*. SPIE Press, Bellingham, Wash., **2001**.
- [19] K. Oguro, Y. Kawami and H. Takenaka, *J. Micromachine Soc.* **5** (1992).
- [20] Y. Bar-Cohen and Q.M. Zhang, *MRS Bull.* **33**, 173 (2008).
- [21] M. Shahinpoor, *J. Intell. Mater. Syst. Struct.* **6**, 307 (1995).
- [22] M. Shahinpoor, Y. Bar-Cohen, J.Q. Simpson and J. Smith, *Smart Mater. Struct.* **7**, R15 (1998).
- [23] D. Kim and K.J. Kim, *J. Intell. Mater. Syst. Struct.* **17**, 449 (2006).
- [24] D.Y. Lee, I.S. Park, M.H. Lee, K.J. Kim and S. Heo, *Sensors Actuat. A-Phys.* **133**, 117 (2007).
- [25] I.S. Park, K. Jung, D. Kim, S.M. Kim and K.J. Kim, *MRS Bull.* **33**, 190 (2008).
- [26] W. Lu, A.G. Fadeev, B.H. Qi, E. Smela, B.R. Mattes, J. Ding, G.M. Spinks, J. Mazurkiewicz, D.Z. Zhou, G.G. Wallace, D.R. MacFarlane, S.A. Forsyth SA, and M. Forsyth, *Science* **297**, 983 (2002).
- [27] M.D. Bennett and D.J. Leo, *Sensors Actuat. A-Phys.* **115**, 79 (2004).
- [28] J. Wang, C.Y. Xu, M. Taya and Y. Kuga, *Smart Mater. Struct.* **16**, S214 (2007).
- [29] S. Liu, W. Liu, Y. Liu, J.-H. Lin, X. Zhou, M.J. Janik, R.H. Colby and Q.M. Zhang, *Polym. Int.* **59**, 321 (2010).
- [30] M.D. Bennett, D.J. Leo, G.L. Wilkes, F.L. Beyer and T.W. Pechar, *Polymer* **47**, 6782 (2006).

- [31] W. Ogihara, S. Washiro, H. Nakajima and H. Ohno, *Electrochimica Acta* **51**, 2614 (2006).
- [32] M. Yoshizawa, H. Ohno, *Electrochim. Acta* **46**, 1723 (2001).
- [33] M. Yoshizawa, M. Hirao, K. Ito-Akita, H. Ohno, *J. Mater. Chem.* **11**, 1057 (2001).
- [34] M. Yoshizawa, W. Ogihara, H. Ohno, *Polym. Adv. Technol.* **13**, 589 (2002).
- [35] S-W Wang, W. J. Liu and R. H. Colby, *Chem. Mater*, 2010 (In preparation)
- [36] MSDS reports Chemical from their suppliers.
- [37] M. Ue, A. Murakami and S. Nakamura, *J. Electrochem. Soc.* **149** (10) A1385 (2002)
- [38] Biswas and Bagchi *J. Am. Chem. Soc.* **119**, 5946 (1997)
- [39] E. Riande and R. Diaz-Calleja. *Electrical Properties of Polymers*. Marcel Dekker **2004**
- [40] J. G. Kirkwood, *J. Chem. Phys.* **7**, 911 (1939)
- [41] H. Frohlich, *Trans. Far. Soc.* **44**, 238 (1948)
- [42] P.A.M. Dirac. *Quantum mechanics of many-electron systems*, Royal Society of London, Proceedings, 1929, **A123**, 714-733, on 714
- [43] J. M. Goodman. *Chemical Applications of Molecular Modelling*. The Royal Society of Chemistry, Cambridge, 1998, Ch.6, Sec. 6.4.4
- [44] Interview with Mulliken (Archive for History of Quantum Physics).
- [45] W. J. Hehre. *Practical Strategies for Electronic Structure Calculations*. Wavefunction Inc., Irvine, CA, 1995
- [46] NIST Chemistry WebBook: <http://webbook.nist.gov/chemistry/>
- [47] S.G. Lias, J.F. Liebman and R.D. Levin *J. Phys. Chem. Ref. Data*, **13**, 695 (1984).
- [48] E.P. Hunter and S.G. Lias *J. Phys. Chem. Ref. Data*, **27**(3), 413 (1998).

- [49] J.M. Tarascon, and M. Armand, *Nature*, **414**, 359-367 (2001).
- [50] W. Liu, M. J. Janik, R. H. Colby, in *Polymers for Energy Storage and Delivery: Polyelectrolytes for Batteries and Fuel Cells*, ACS Symposium Series Vol. 1096, edited by K. Page, C. Soles, and J. Runt (American Chemical Society, Washington, 2012), Chap. 2, pp. 19–44.
- [51] J.-H. H. Wang and R.H. Colby, *Soft Matter* **9**, 10275 (2013).
- [52] S.W. Liang, U.H. Choi, W.J. Liu, J. Runt, R.H. Colby, *Chem Mater*, **24**, 2316 (2012).
- [53] R. Meziane, J.-P. Bonnet, M. Courty, K. Djellab and M. Armand, *Electrochim. Acta* **57**, 14 (2011).
- [54] T. Ono, T. Sugimoto¹, S. Shinkai and K. Sada, *Nat. Mat.* **6**, 429 (2007)

First Principles Design of Ionomers for Facile Ion Transport*

Ab initio calculations have been performed for the association of lithium and sodium cations with various carboxylate, sulfonate, phosphonate and borate anions, with a particular emphasis on the effects of perfluorinating the anions. Fluorinating the benzene ring on benzene carboxylate, benzene sulfonate or benzene phosphonate makes the pair and positive triple ion binding less favorable by 5-10% due to the electron-withdrawing F placing more of the negative charge on the ring, effectively softening these anions. However, fluorinating the four benzene rings of tetraphenyl borate has a significantly stronger electron-withdrawing effect, destabilizing the pair and positive triple ion energies by 20-30%. We also explore two methods to account for the effects of a surrounding polar medium on ion interactions. The polarizable continuum model was studied with six ion pairs to account for the dielectric constant of the surroundings. We also model specific local solvation of poly(ethylene oxide) on Li^+ and Na^+ with two anions (benzene sulfonate and triflate) and also their ion pairs, by surrounding these with explicit dimethyl ether (DME) molecules. We find a strong local solvation effect on the cations that is particularly strong for Li^+ with four DME in the first solvation shell. There is very little specific solvation of anions by DME and the ion pairs fill their first solvation

* This Chapter has been published as Ch. 2 in *Polymers for Energy Storage and Delivery: Polyelectrolytes for Batteries and Fuel Cells* (ACS, Washington, 2012).

shell with three DME, with all four ion pairs studied showing very similar solvated pair interactions.

2.1. Introduction

Ion-containing polymers are of interest for use as electrolytes in lithium ion batteries, fuel cell membrane electrode assemblies, super-capacitors, sensors and actuators. Ion conduction may be achieved by dispersing a Li or Na salt in poly(ethylene oxide) (PEO) [1] however, salt doped PEO suffers from undesirable concentration polarization, since the anions generally have higher mobility than Li^+ or Na^+ [1-3], and the anions accumulate at the electrode/electrolyte interface over time in either lithium or sodium batteries. This build-up lowers the field the cations see and also can serve to trap/delay cations locally and place enormous stress on the electrolyte/electrode interface, since the anions cannot transfer their charge to the electrode [2]. Covalent bonding of the anions to the polymer to form an ionomer ('single-ion conductors' in the electrochemical literature) can overcome these difficulties [3-7]. Covalent attachment of the anions to the polymer chain means that only the cations are able to migrate over long distances on reasonable time scales, and a cation transference number very close to unity can be achieved. For cation conductors, the choices for composition of the covalently bound anionic group, polymer backbone, and additional side chains or functional groups are extensive, and cannot be efficiently sampled through experiment. We are therefore motivated to develop a rational bottom-up design strategy of superior ionomers for facile ion transport using computational methods.

Ionomer membranes transport different counterions in various applications. The ion is often bulky in actuators, often Li^+ or Na^+ in advanced batteries, and often either H_3O^+ or OH^- in fuel cell membrane-electrode assemblies. In each application, conductivity is enhanced by increasing the concentration of conducting counterions, defined as the (often small) fraction of counterions that simultaneously participate in conduction. Unfortunately, for poly(ethylene oxide)-based sulfonate ionomers with Li^+ or Na^+ counterions, only a fraction, $< 10^{-3}$, of the counterions are simultaneously participating in conduction [4-7]. While the conductivity benchmark for useful Li or Na salts in PEO is 10^{-3} S/cm, since the anions in these systems move 5-10X faster than the cations, the benchmark for single-ion conductors is 10^{-4} S/cm [3]. Current conductivities of the best ionomers are roughly 100X too small for practical applications. Since they also have less than 1/1000th of their countercations simultaneously participating in conduction there is a genuine opportunity to meet the benchmark by higher participation of counterions in conduction. The small fraction of conducting counterions arises because the interaction energy between oppositely charged ions is large. With PEO-based sulfonate ionomers, this forces the vast majority of Li^+ counterions to be less than 4 Å from the S in the sulfonate group, with binding energy of order 25 kJ/mol [4].

Ab initio methods allow for direct quantitative examination of the potential energy surface for pairwise interactions between species. Figure 2.1 schematically illustrates the perturbations of a hypothetical anion-cation potential energy surface with compositional changes in an ionomeric system. Ion conduction would be enhanced by *softening* (lowering the magnitude of) the cation-anion interaction (ΔE_{pair}) to allow a

higher fraction of ions to participate in conduction. This might be accomplished by a combination of the three modifications illustrated schematically in **Figure 2.1**:

- 1) delocalize the anionic charge and sterically hinder cation access to the anion (red dotted curve)
- 2) raise the dielectric constant of the surrounding ionomer medium (blue solid curve)
- 3) locally solvate (stabilize) the conducting ions relative to the ion pair (green solid curve).

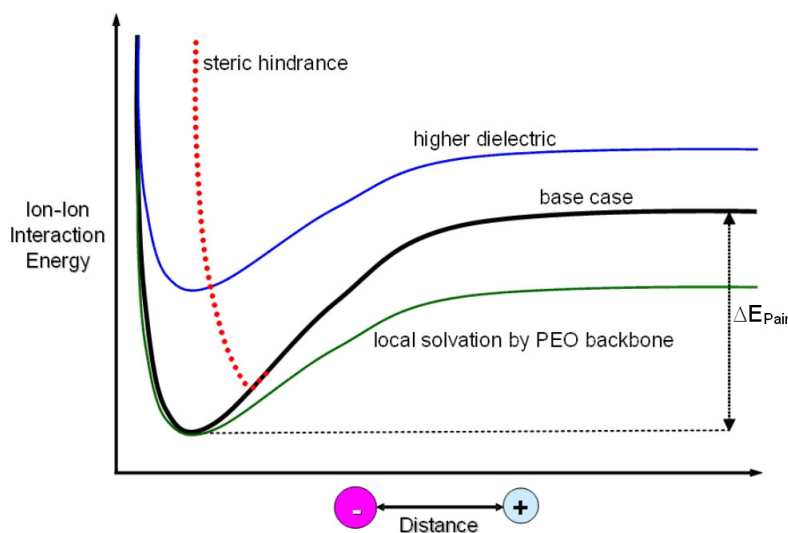


Figure 2.1. Schematic anion-cation interaction potential energy surface (black curve) including perturbations introduced by changes in the ionomer composition that sterically hinder ions (red dashed), raise dielectric constant ϵ (blue) or solvate ions (green).

Ab initio methods have been previously applied to explore interactions between ions in vacuum [8-11]. The majority of these studies have evaluated methodological choices in comparison with experimental data or sought to explain observed experimental behavior through detailed electronic structure studies. Many studies have employed *ab initio* methods to guide the choice of counteranion in lithium ion salts [12-27], but the

application of these methods for large scale evaluation and design of complex ionomer compositions has not been previously attempted.

Though *ab initio* methods are limited in the time and length scales accessible, they will serve to evaluate interaction energies and these values then guide design choices to 1) provide insight into the interactions and molecular level phenomena that impact conductivity; 2) establish relationships between interactions of ions and polar functional groups to guide rational design; and 3) identify promising compositions/combinations of polymer backbone repeat units, functional groups and attached anions.

In this section, we study various common ionomer anions: sulfonates, phosphonates, and carboxylates, as well as highly delocalized borates, and the effect of the dielectric constant of the surrounding medium. We use *ab initio* calculations to evaluate the interaction energies that drive ion pairing and clustering, and consider approaches to including specific local solvation effects of ether oxygen atoms on these interaction energies.

2.2. Computational Methods

All the calculations reported in this section were carried out with the Gaussian03 program [28]. Density-functional theory (DFT) calculations used Becke's three-parameter hybrid method employed with the B3LYP exchange - correlation functional [29-32] and a split valence plus diffuse and polarization functions 6-31+G* basis set. For method validation, B3LYP/6-31+G* was compared with Møller-Plesset 2nd order perturbation theory (MP2) molecular orbital calculations with the triple

split valence plus diffuse and polarization functions 6-311+G* basis set. The magnitude of the interaction energy (ΔE_{int}) between Li^+ or Na^+ cations and neutral or anionic species was evaluated as the difference in the energies of the coordination complexes ($E_{complex}$) to that of the isolated species (E_{cation} and $E_{anion/neutral}$):

$$\Delta E_{int} = E_{cation} + E_{anion / neutral} - E_{complex} \quad (2.1)$$

More positive ΔE_{int} values represent a stronger attractive interaction between species. Structural optimization was continued until convergence criteria of maximum and root mean squared atomic forces and distance variation were met. The default convergence values invoked by the “Opt” keyword were used. Vibrational frequency calculations were performed both to confirm that the obtained structures were true minima on the potential energy surfaces and to add zero-point vibrational energy (ZPVE), thermal enthalpy, and thermal free energy corrections to the total energy. For calculations in which Li^+ or Na^+ cations were paired with neutral or anionic species, multiple local minima were located and the reported results reflect the most stable structure located. Extensive sampling of the potential energy surface was done for each cation with one anion of each type (i.e., with one sulfonate, one phosphonate) and the minimum energy configuration was utilized as the starting point for the same ion state of the same cation with other anions of the same type.

To study global solvation effects, we performed solvation calculations (SCRF) with the polarizable continuum model (PCM), originally developed by Tomasi, and coworkers [33-38] and implemented by Gaussian03, for six salts in 22 solvents. This

method is a straightforward extension of the 1936 Onsager model [39] to ions and ion clusters of non-spherical shapes, creating the solute cavity via a series of overlapping spheres within the solvent reaction field. Solvated interaction energies attempt to include both the electronic energy and electrostatic solute-solvent interactions within the PCM model. The polarizable continuum model has the advantage of incorporating extended solute-solvent interactions with minimal computational requirements and without concerns as to the singularity of the solvation structure adopted. Disadvantages of this approach include the lack of molecular structure inherent in the use of a continuum, difficulties in determining the proper definition of the solute cavity within the polarizable continuum, and the need to approximate a dielectric constant representative of a specific polar group. In using the PCM model, only the electrostatic terms in the solute-solvent interaction were included in determining the forces for geometry optimization and the total energies.

To examine the accuracy of the methods employed, we compared calculated and experimental values of the dipole moments of various species of interest as well as the interaction energies of Li^+ and Na^+ cations with various species. The dipole moment is compared among B3LYP/6-31+G* and MP2/6-311+G* methods and experimentally measured values for neutral polar small molecules. **Table 2.1** lists the dipole moment of 16 neutral polar small molecules calculated by both method/basis sets and the measured values [40]. **Figure 2.2** illustrates the correlation of calculated and experimental values.

Table 2.1. Comparison of calculated dipole moments with vapor phase measurements [40] for small polar molecules.

Polar Small Molecules	Dipole Moment (Debye)			Polar Small Molecules	Dipole Moment (Debye)		
	Meas.	MP2	DFT		Meas.	MP2	DFT
Toluene	0.37	0.38	0.40	Pyridine	2.21	2.45	2.38
Diethyl ether	1.15	1.44	1.23	Oxirane	1.89	2.47	2.15
Phenol	1.22	1.56	1.42	Acetaldehyde	2.75	3.30	2.87
1-Propanol	1.55	1.84	1.70	Acetone	2.88	3.55	3.19
1-Butanol	1.66	1.91	1.76	Benzeneacetonitrile	3.5	4.23	4.03
Fluorobenzene	1.60	1.99	1.75	Acetonitrile	3.92	4.27	4.07
Methyl acetate	1.72	2.04	1.96	Dimethylformamide	3.82	4.59	4.41
Methanol	1.70	2.09	1.94	Benzonitrile	4.18	5.10	4.77

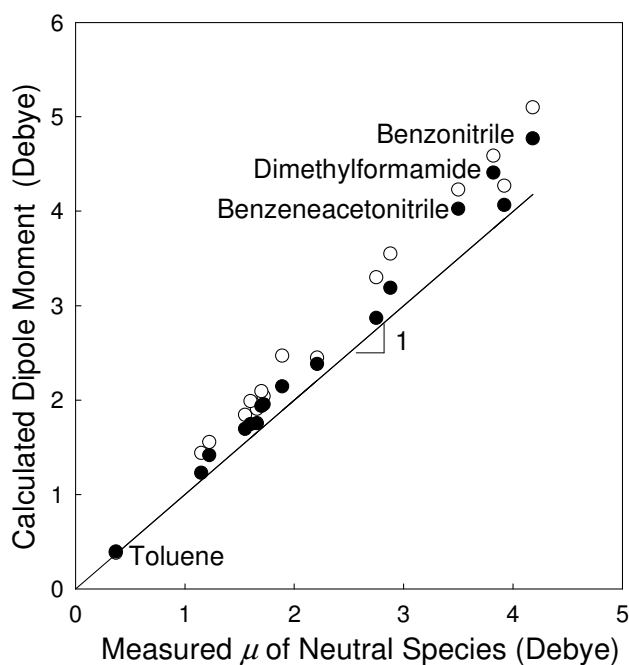


Figure 2.2. Dipole moment of neutral polar small molecules calculated by B3LYP/6-31+G* (filled circles) and MP2/6-311+G* (open circles) plotted versus experimentally measured values in the vapor phase.

Both basis sets systematically overestimate the dipole moments, but within the experimental error in most cases, estimated to be 15% [40]. The results generated by B3LYP/6-31+G* show better agreement with measured values, with the largest deviation being 13.5%. The theoretical overestimation increases as the molecule becomes more polar, such as for dimethylformamide (DMF) (13.4%), benzene acetonitrile (13.5%), and benzonitrile (12.4%). The disagreement with experiment may, in part, be caused by experimental error due to the presence of aggregates of two or more polar molecules lowering the measured value.

We also compared calculated and experimentally measured interaction energies between Li^+ cations and a series of solvents in the gas phase. Experimental gas phase heats of interaction (ΔH_r°) and free energies of interaction (ΔG_r°) were taken from a NIST database [41-45]. In adjusting the 0 K electronic energy differences to temperature dependent free energy differences, all species were assumed to be free of accessible excited electronic states. Enthalpic and entropic terms associated with vibration and molecular rotation were treated with harmonic oscillator and rigid rotor models in the ideal gas limit. The ΔE_{int} values (Equation 2.1) refer to 0 K, non-ZPVE corrected interaction energies. The symbols ΔH_{int} and ΔG_{int} are used to refer to the ZPVE and thermally corrected values at standard state conditions (298.15 K, 1.0 atm) calculated equivalently to Equation 2.1 for the 0 K values. In Table 2.2 and Figure 2.3, the calculated and experimental interaction enthalpies and free energies are compared.

Table 2.2. Interaction energies of a Li^+ cation with a series of polar species. Values calculated with B3LYP/6-31+G* and MP2/ 6-311+G* with zero-point vibrational energy correction and thermal corrections are compared with experimentally measured dissociation enthalpies and free energies [41-45] in kJ/mol.

Solvent	DFT (B3LYP/6-31+G*)			MP2 (MP2/6-311+G*)			Measured	
	ΔE_{int}	ΔH_{int}	ΔG_{int}	ΔE_{int}	ΔH_{int}	ΔG_{int}	ΔH°	ΔG°
Propene [42]	104.8	102.5	74.3	99.8	100.3	72.1	96	
Propyne [42]	110.8	109.2	83.4	104.6	107.1	79.1	119	
Fluorobenzene [44]	121.1	119.7	96.2	121.7	115.1	90.1	147. \pm 21.	
Phenol [44]	153.9	151.3	127.0	160.5	154.1	127.0	178. \pm 17.	
Pyrazine [45]	160.7	157.2	126.8	156.5	154.7	124.7	149. \pm 14.	
Methanol [43]	164.4	159.9	131.1	170.8	167.1	138.1	159	127
Dimethoxyethane [41]	165.0	161.4	131.6	163.4	161.9	134.1	158. \pm 4.	
Dimethylether [43]	165.6	154.5	125.4	168.3	164.0	135.6	165	131
Toluene [44]	167.6	163.4	127.3	172.1	168.6	133.5	183. \pm 17.	
Trimethylamine [43]	174.2	168.9	137.9	171.1	173.6	142.8	176	140
2-Propanol [41]	177.6	173.8	145.4	181.3	176.4	149.7	173. \pm 8.	
Dimethylamine [43]	179.4	173.6	142.8	176.4	177.2	146.5	177	143
1-Propanol [41]	179.6	175.5	146.1	183.5	182.1	150.5	171. \pm 8.	
Methylamine [43]	181.5	175.5	144.8	179.2	178.7	148.1	172	139
1-Butanol [41]	182.6	178.5	149.1	186.1	185.3	152.2	178. \pm 8.	
Acetaldehyde [42]	183.4	177.4	151.7	194.9	167.3	141.8	173	
Acetonitrile [42]	187.4	184.7	154.8	191.3	176.5	147.0	180	
Pyridine [45]	194.7	190.4	159.9	192.6	186.3	156.3	181. \pm 15.	
Methyl acetate [42]	195.0	191.2	163.0	203.1	180.6	149.8	180	
Acetone [42]	197.6	191.7	166.8	207.3	180.7	155.9	186	
Dimethylformamide [42]	243.7	235.3	208.6	250.3	232.3	198.1	210	

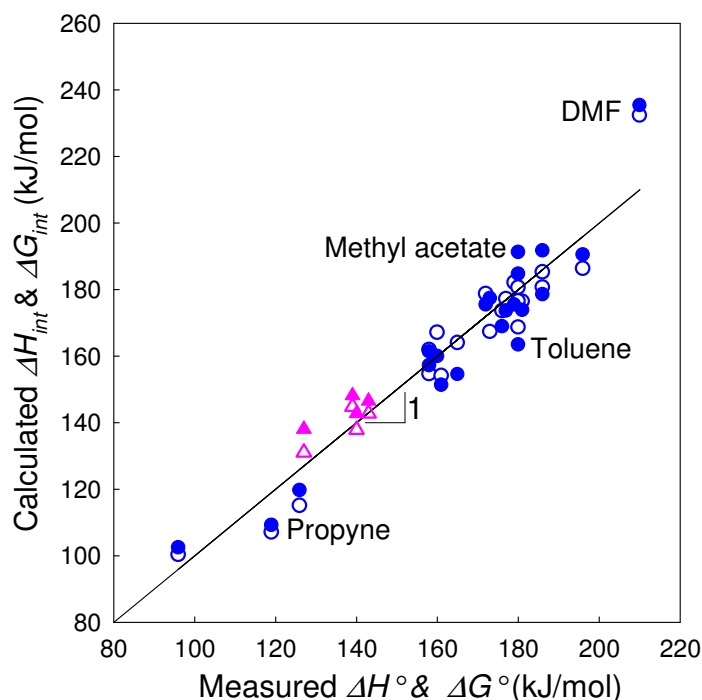


Figure 2.3. Comparison of calculated and experimental interaction enthalpies and free energies [41-45] between neutral polar small molecules with a Li^+ cation. Filled symbols are calculated with B3LYP/6-31+G* and open symbols with MP2/6-311+G*. Blue circles represent interaction enthalpies and pink triangles represent interaction free energies, both with zero-point vibrational energy.

Most of the interaction energies generated by the two sets of calculations are within 7% of experimental values. The sole exception is dimethylformamide, the most polar solvent that we could find Li^+ interaction energy data for. We evaluated the mean squared error of the calculated data sets from the experimental data, as reported in [Table 2.3](#). Though the MP2/6-311+G* basis set does slightly better than B3LYP/6-31+G* on interaction enthalpies, the difference is slight and the DFT method does better on the free

energies. Throughout the remainder of the study, all values are calculated with DFT (B3LYP/6-31+G*).

Table 2.3. The mean squared error of the calculated enthalpies and free energies of interaction versus experimental values for the DFT (B3LYP/6-31+G*) and MP2/6-311+G* basis sets.

	$\Delta H_{int} \leftrightarrow \Delta H^\circ$	$\Delta G_{int} \leftrightarrow \Delta G^\circ$
B3LYP/6-31+G*	9.09	3.70
MP2/6-311+G*	7.85	7.52

2.3. Interactions and Dipoles of Isolated Ion Pairs

We chose a series of 6 sulfonate, 6 phosphonate and 6 carboxylate anions with methyl, ethyl and phenyl functional groups and 3 borate anions, many of which are the perfluorinated versions of these anions to evaluate interactions with Li^+ and Na^+ . All the 21 anions are chemically stable and most of them are commercially available, though synthesis of ionomers containing each anion has not yet been demonstrated. The interaction energies (ΔE_{int}), and dipole moments (μ) of the Li and Na ion pairs with these 21 anions are listed in **Table 2.4**, along with two measures of the anion-cation distance. The distance between the Li atom and the sulfur, phosphorus, carbon or boron atom of the anion is labeled $d_{\text{cation-S/P/C/B}}$. A second distance, derived from the dipole moment, is labeled $d \equiv \mu/e$, representing the charge separation distance implied by the dipole

moment if the anion and cation are assumed to retain their full unit charge in the paired state.

Table 2.4. Ion pair interaction energies (ΔE_{int}) without ZPVE correction, dipole moment (μ), distance calculated from dipole moment ($d \equiv \mu / e$, where e is the elementary charge) and the distance of the Li^+ or Na^+ cation from the sulfur or phosphorus or carbon or boron ($d_{\text{cation-S/P/C/B}}$) of 21 anions.

Anion Name	Chemical Formula	ΔE_{int} (kJ/mol)		μ (Debye)		$d \equiv \mu / e$ (Å)		$d_{\text{cation-S/P/C/B}}$ (Å)	
		Li^+	Na^+	Li^+	Na^+	Li^+	Na^+	Li^+	Na^+
Methyl sulfonate	CH_3SO_3^-	654.2	558.0	5.68	7.66	1.18	1.59	2.37	2.74
Ethyl sulfonate	$\text{C}_2\text{H}_5\text{SO}_3^-$	655.7	558.8	5.52	7.47	1.15	1.56	2.37	2.74
Benzene sulfonate	$\text{C}_6\text{H}_5\text{SO}_3^-$	640.5	544.8	5.74	7.77	1.19	1.62	2.37	2.74
Trifluoromethane sulfonate	CF_3SO_3^-	591.5	506.0	6.56	9.20	1.37	1.92	2.38	2.75
Pentafluoroethane sulfonate	$\text{C}_2\text{F}_5\text{SO}_3^-$	584.1	499.4	6.28	9.30	1.31	1.94	2.38	2.75
Pentafluorobenzene sulfonate	$\text{C}_6\text{F}_5\text{SO}_3^-$	603.9	516.0	5.82	8.31	1.21	1.73	2.37	2.75
Methyl phosphonate	$\text{CH}_3\text{PHO}_3^-$	689.0	587.1	3.27	5.55	0.68	1.16	2.32	2.68
Ethyl phosphonate	$\text{C}_2\text{H}_5\text{PHO}_3^-$	688.7	586.6	3.20	5.48	0.67	1.14	2.32	2.68
Benzene phosphonate	$\text{C}_6\text{H}_5\text{PHO}_3^-$	667.2	570.2	2.61	5.24	0.54	1.09	2.31	2.67
Trifluoromethane phosphonate	$\text{CF}_3\text{PHO}_3^-$	619.6	532.4	4.81	7.38	1.00	1.54	2.32	2.68
Pentafluoroethane phosphonate	$\text{C}_2\text{F}_5\text{PHO}_3^-$	611.6	525.1	4.94	7.59	1.03	1.58	2.32	2.68
Pentafluorobenzene phosphonate	$\text{C}_6\text{F}_5\text{PHO}_3^-$	625.4	535.2	3.76	6.28	0.78	1.31	2.31	2.67
Methyl carboxylate	CH_3CO_2^-	717.8	616.5	3.29	5.59	0.68	1.16	2.12	2.49
Ethyl carboxylate	$\text{C}_2\text{H}_5\text{CO}_2^-$	715.6	613.8	3.35	5.70	0.70	1.19	2.12	2.49
Benzene carboxylate	$\text{C}_6\text{H}_5\text{CO}_2^-$	696.6	596.4	3.20	5.92	0.67	1.23	2.12	2.50
Trifluoromethane carboxylate	CF_3CO_2^-	635.3	547.2	6.40	8.77	1.33	1.83	2.12	2.48
Pentafluoroethane carboxylate	$\text{C}_2\text{F}_5\text{CO}_2^-$	624.6	537.8	6.58	9.03	1.37	1.88	2.12	2.49
Pentafluorobenzene carboxylate	$\text{C}_6\text{F}_5\text{CO}_2^-$	629.7	539.8	6.00	8.89	1.25	1.85	2.12	2.50
Tetrabutylborate	$(\text{C}_4\text{H}_9)_4\text{B}^-$	585.0	463.6	4.68	7.17	0.97	1.49	1.98	2.50
Tetraphenylborate	$(\text{C}_6\text{H}_5)_4\text{B}^-$	538.8	483.5	4.83	10.21	1.00	2.13	2.16	2.66
Tetra(pentafluorophenyl)borate	$(\text{C}_6\text{F}_5)_4\text{B}^-$	448.2	365.7	7.35	10.70	1.53	2.23	2.90	3.57

Figure 2.4 illustrates a subset of the optimized structures. For sulfonates and phosphates, a Li cation prefers to interact with two oxygen atoms, along the edge of the tetrahedron. For the carboxylates, a Li cation interacts with both oxygen atoms. Comparison with structures with a Li cation interacting with one or three oxygen atoms confirmed that the illustrated configurations represent the minimum energy structure. For the tetraphenylborate anion, the optimal Li position is on a C_α -B-Li line, approximately equally spaced between the other three C_α atoms, 2.23 Å from each. The closest atom to Li is the central B atom, at a distance of 2.14 Å. This position is preferred in comparison to a structure where Li interacts more directly with a single phenyl ring.

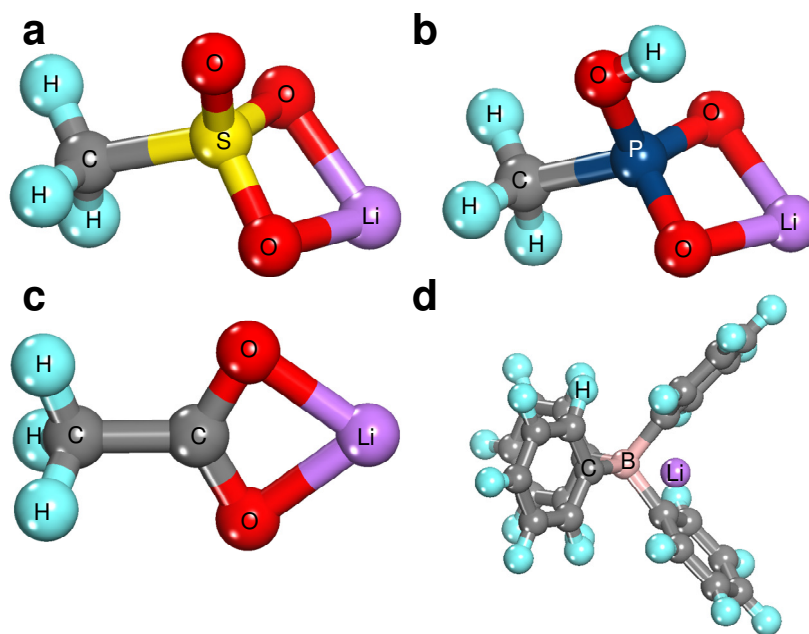


Figure 2.4. Equilibrium pair structures of a) Li-methyl sulfonate, b) Li-methyl phosphonate, c) Li-methyl carboxylate, and d) Li-tetraphenylborate.

Comparing Na^+ and Li^+ , with sulfonates, phosphonates, and carboxylates, the pair energy is consistently about 17% larger for the smaller Li^+ . Comparing sulfonates, phosphonates, and carboxylates, for all anion substituents, the interaction with Na^+ and Li^+ is always weakest for sulfonates, intermediate for phosphonates and strongest for carboxylates. The borates considered show weaker interaction with Na^+ and Li^+ cations than all other anions. Comparing Na^+ and Li^+ , with the borates, the pair energy shows an even larger effect of cation, 26% larger for the smaller Li^+ for tetrabutyl borate, 11% larger for tetraphenylborate and 22% larger for perfluorinated tetraphenylborate. Fluorinating the anion (replacing all C-H with C-F) significantly lowers the interaction energy of anions with Li^+ or Na^+ due to the electron-withdrawing nature of F atoms; fluorinating significantly increases the dipole moment of the ion pair while not significantly changing the cation-P/S/C distance. If weaker pair interactions are presumed to predict the extent to which the conducting cation will be “freed” from the anion in the ionomer, these trends suggest borate or sulfonate anions would produce the greatest amount of Li^+ or Na^+ cations participating in conduction. The cation-P/S/C distances do not correlate with interaction energies and are not sensitive to changing the anion substituents. These distances reflect size differences of the central P/S/C atom rather than the Coulombic interaction distance, as expected since the negative charge of the anions is localized on the oxygen atoms and not the central atom. Larger dipole moments (and dipole moment derived distances) generally indicate weaker interactions. The ratio of distances $ed_{\text{cation}-\text{S,P,C,B}}/\mu$ provides a crude measure of ‘covalency’. Non-fluorinated carboxylates and phosphonates have the most covalent character to their ionic bonds and

perfluorinating the anion always makes the ionic bond less covalent, since the electron-withdrawing F atoms leave less negative charge for these anions to share.

2.4. Polarizable Continuum Model for Solvation and Dielectric Constant

The interaction enthalpies in [Table 2.4](#) (without temperature effects; at 0 K in vacuum) do not consider the extended interactions between the ions and their surroundings that would occur in the ionomer. We refer to these extended interactions as solvating the ion or ion pair state. To examine the effect of solvation on ion pairing interactions, we calculated the interaction energy using the polarizable continuum model (PCM) [\[33-38\]](#). PCM-solvated interaction energies were studied for 6 salts in 22 solvents by computing the energy of the separated and paired ions within the solvent. The six salts were chosen to be able to provide a more transferable definition of separation distance d . The six salts are lithium fluoride (LiF, $d \equiv d_{Li-F}$), lithium trifluoromethanesulfonate (Li[TfO], $d \equiv d_{Li-S}$), lithium tetrafluoroborate (Li[BF₄], $d \equiv d_{Li-B}$), tetramethylammonium fluoride ([TMA]F, $d \equiv d_{N-F}$), tetramethylammonium tetrafluoroborate ([TMA][BF₄], $d \equiv d_{N-B}$) and tetramethylammonium trifluoromethanesulfonate ([TMA][TfO], $d \equiv d_{N-S}$).

Ideally, the distance measurement for each of these would provide a measure of the distance of charge separation, were the bonding between ions purely ionic and the charge on each ion perfectly symmetric (no polarization). These distances should be taken as an approximate measure of this idealized charge separation. Comparison among

anions, even in the consideration of a purely ionic pair binding, should consider the spatial distribution of negative charge in the anion. The structure of the ion pair was re-optimized for each solvent, and therefore the value of d increases somewhat as dielectric constant is increased (by only about 7% for LiF and [TMA][TfO] but by about 12% for [TMA]F and [TMA][BF₄], while d increases significantly more for Li[TfO] and Li[BF₄], as discussed below). **Table 2.5** lists the 22 solvents and their ambient dielectric constants ϵ . There are other parameters used to define solvents within the PCM, such as solvent radius, density and optical dielectric constant which are not listed but these were left at their standard (default) values in the Gaussian03 package.

Table 2.5. The names and dielectric constants of the 22 solvents used for PCM solvation calculations.

Solvent	Argon	Heptane	Cyclohexane	Carbontetrachloride	Benzene
$\epsilon_{\text{solvent}}$	1.43	1.92	2.02	2.23	2.25
Solvent	Toluene	Ether	Chloroform	Chlorobenzene	Aniline
$\epsilon_{\text{solvent}}$	2.38	4.34	4.90	5.62	6.89
Solvent	THF ^a	Dichloromethane	Quinoline	Dichloroethane	Isoquinoline
$\epsilon_{\text{solvent}}$	7.58	8.93	9.03	10.36	10.43
Solvent	Acetone	Ethanol	Methanol	Acetonitrile	Nitromethane
$\epsilon_{\text{solvent}}$	20.70	24.55	32.63	36.64	38.20
Solvent	DMSO ^b	Water			
$\epsilon_{\text{solvent}}$	46.70	78.39			

^a THF = Tetrahydrofuran, ^b DMSO = Dimethylsulfoxide

Examples of the cavities that Gaussian03 uses for the PCM solvation calculations are shown in **Figure 2.5**. In all cases we used the default mode of Gaussian03's implementation of the PCM, which generates a cavity based on overlapping atom-

centered spheres and adjusts this cavity as atomic distances vary during structural optimization.

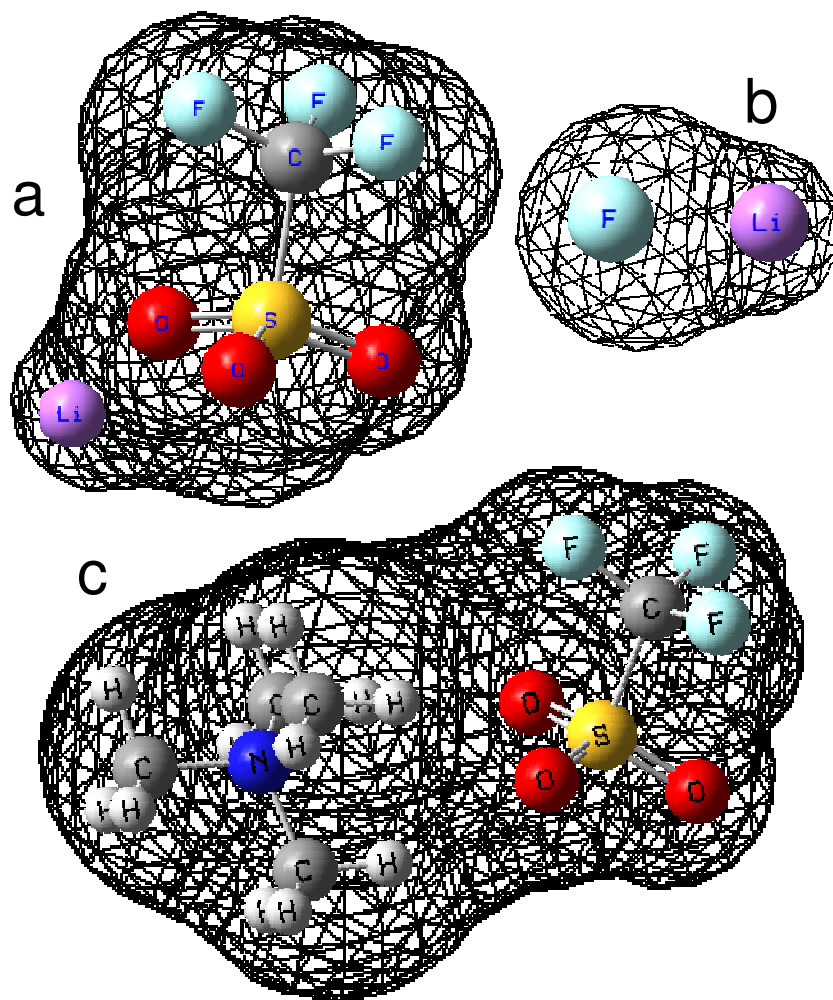


Figure 2.5. The PCM molecular cavities of three ion pairs a) Li[TfO], b) LiF, and c) [TMA][TfO] in the presence of diethylether.

Figure 2.6 illustrates the correlation of pair interaction energy with the reciprocal dielectric constant of the solvent. For a purely Coulombic interaction between ions, a linear correlation with a zero intercept is expected by the Coulomb energy ([Equation 2.2](#)) for each ion pair:

$$\Delta E_{pair} = \frac{e^2}{4\pi\epsilon_0\epsilon d} \quad (2.2)$$

[TMA]F, [TMA][BF₄] and [TMA][TfO] indeed have intercepts very close to zero, as expected by Equation 2.2. However, while the $\epsilon < 3$ points have nearly zero intercept for LiF, the ion pair energies for more polar solvents are systematically *above* this line, resulting in a substantial positive intercept for LiF. Conversely, Li[BF₄] and Li[TfO] points with $\epsilon < 3$ have strongly negative intercept and the points themselves reach a pair energy near zero at $\epsilon \approx 10$, with more polar solvents showing $\Delta E_{pair} \approx 0$ for Li[BF₄] and Li[TfO]. One possible source of the non-zero intercept is variations in d with dielectric constant, as the inter-ion spacing was allowed to reoptimize in each solvent.

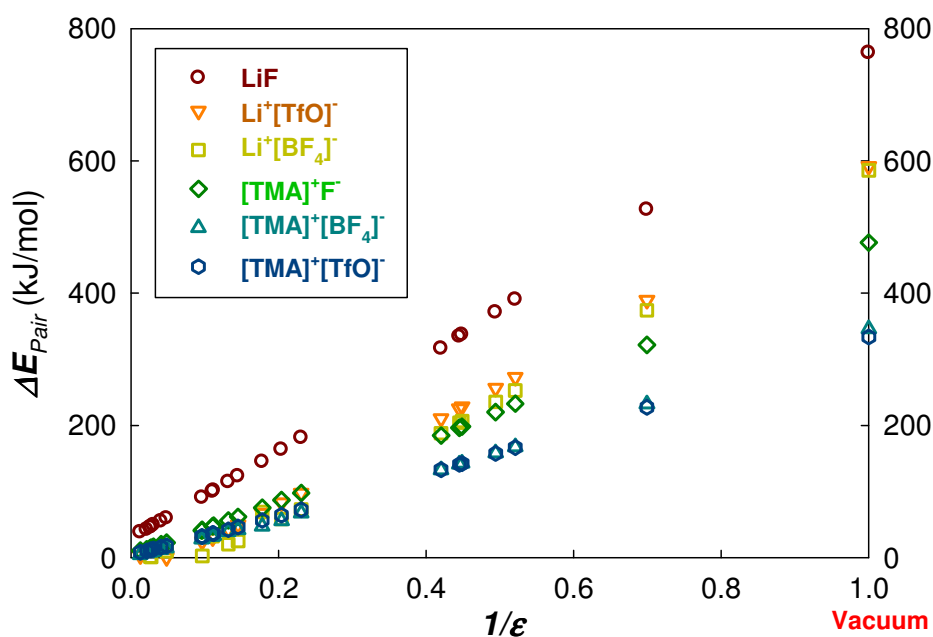


Figure 2.6. Ion pairing energies with no ZPVE correction for six salts as a function of reciprocal dielectric constant of the PCM medium.

Figure 2.7 illustrates the correlation of pair interaction energies with the reciprocal dielectric constant multiplied by the cation-anion distance. Ion pair interaction energies are linearly correlated with $1/(\epsilon \cdot d)$, as expected by the Coulomb energy (**Equation 2.2**), and the data for the various ion pairs come closer to collinear. Non-zero intercepts are still seen for LiF, Li[TfO] and Li[BF₄]. At this time it is not clear whether these non-zero intercepts reflect (1) real ion pair character in different surroundings, (2) problems with B3LYP or (3) problems with Gaussian03's implementation of the PCM. Li[TfO] and Li[BF₄] progressively change their configurations with dielectric constant, from a tightly bound Li that is close to the central atom, allowing interaction with multiple O or F in less polar media, to a highly extended structure that has Li only interacting with a single O or F in polar media. Contributing to this are difficulties in defining d , the partial covalency in the anion-cation interactions, as well as variations in the solute cavity structure among anions or with varying d values. The Coulomb energy of **Equation 2.2** appears to only approximately describe the pair interaction energy. One cause of this is that the definition of d used does not precisely translate to that in **Equation 2.2**, as the negative charge is distributed differently in each anion. Additionally, the bonding interaction is not purely ionic, as pairing will cause a redistribution of charge in each ion which can be described as a combination of polarization and charge transfer. The approximate reduction of all ion pairs to the single line in **Figure 2.7** provides a simplistic picture of solvation effects based solely on the dielectric constant. However, this solvation model lacks variations in the local solvation interactions among solvents, which limits its accuracy. Local solvation considerations are discussed in **Section 2.5**.

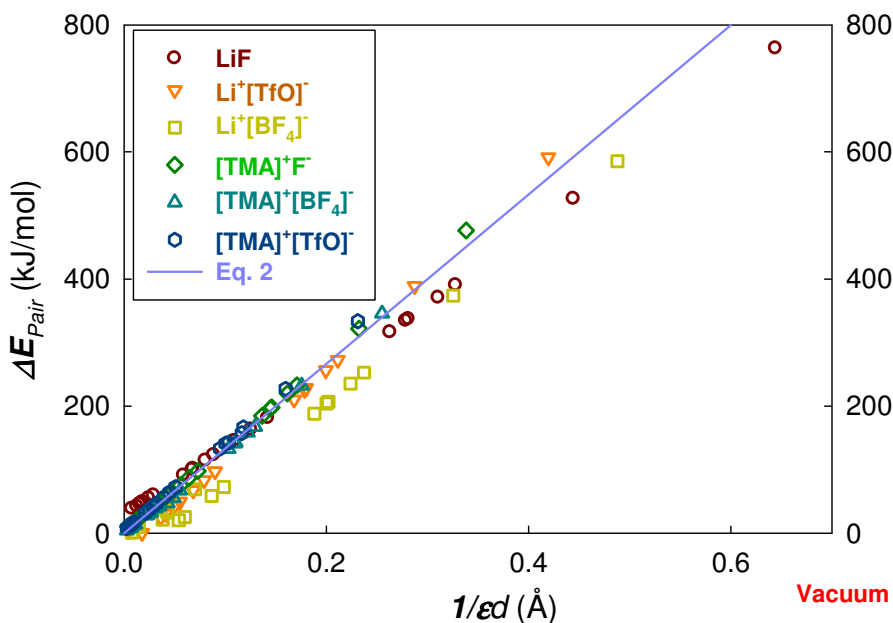


Figure 2.7. PCM calculated ion interaction energies with no ZPVE correction for six salts as a function of reciprocal of the product of dielectric constant ϵ and cation-anion distance d , defined carefully in the first paragraph of [Section 2.4](#). The line is the Coulomb energy ([Equation 2.2](#)).

Analysis of the inclusion of PCM solvation clearly indicates that the strength of the binding interaction between pairs will be altered by interactions within the extended medium of the ionomer. A greater solvation, offered by a larger dielectric constant, will weaken pair interaction and possibly free more cations to participate in conduction. The analysis above illustrates that the quantum/PCM calculations generally provide results that indicate a simple scaling of interactions assuming a purely Coulombic interaction is reasonable, though complexities arise both due to the non-point charge nature of the ions and the partial covalency in ion pairing. Further, the PCM solvation model does not take

into account the local solvation offered, for example, by ether oxygen – Li⁺ interactions, that could differentially impact pairing among a series of Li-anion combinations.

2.5. Specific Solvation with Dimethyl Ether

The PCM solvation model has the disadvantage of neglecting the specific interactions between the solute and the first solvation shell. To explore the impact of specific solvation interactions on ion interaction energies, the stabilization offered by ion interaction with ether oxygens was evaluated. Li⁺ ions are known to coordinate with 4-6 ether oxygen atoms in PEO [46,47]. To mimic the local specific solvation by PEO, 1~6 dimethyl ether molecules were explicitly included in the DFT model and the stabilization energy was determined. The explicit solvent model has the advantage of directly considering the impact of PEO on interactions with isolated cations, anions and their pairs, and by explicitly including the “solvent” molecules within the *ab initio* calculation, a full quantum treatment is provided to the ion-“solvent” interaction. Disadvantages include the concern that global minima on a potential energy surface might not be located, that transitions between solute-solvent and solvent-solvent interactions are difficult to identify, and that computational time requirements will limit the ability to consider large ion-solvent systems. A stabilization energy of a single ion or ion pair ($\Delta E_{\text{stabilization}}$), given for the example of a Li⁺ cation, is defined as:

$$\Delta E_{\text{stabilization}} = E_{\text{Li}^+ - n\text{DME}} - E_{\text{Li}^+} - nE_{\text{DME}} \quad (2.3)$$

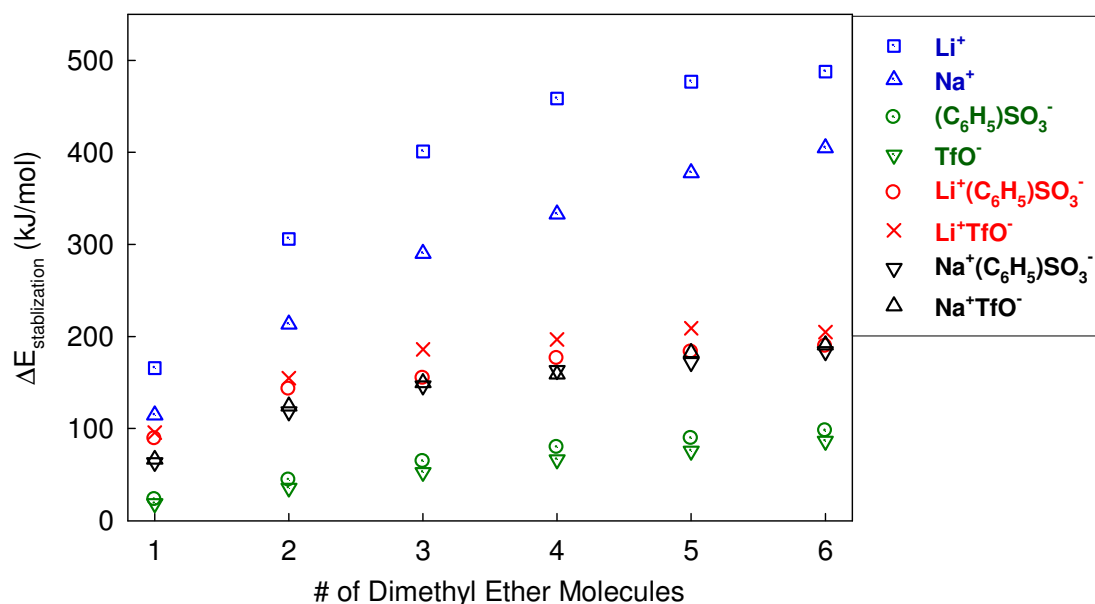


Figure 2.8. The cumulative specific solvation energy from interaction with 1 to 6 dimethyl ether molecules for cations (blue) Li^+ and Na^+ ; anions (green) $\text{C}_6\text{H}_5\text{SO}_3^-$ (benzene sulfonate) and CF_3SO_3^- (triflate) and their four ion pairs (red and black).

Figure 2.8 plots the cumulative specific solvation interactions (stabilization energy of [Equation 2.3](#)) of 1-6 dimethyl ether (DME) molecules with Li^+ cation, Na^+ cation, benzene sulfonate and triflate anions and their ion pairs. The stabilization energies were found to increase steeply up to four DME around the cations, suggesting that their first solvation shell is filled after about four dimethyl ether molecules. The cations have the strongest solvation, particularly for Li^+ as the smallest cation can get closest to the lone electron pairs on the DME oxygen. In contrast, the anions are barely solvated at all by DME. Anions show a gradual increase with little change in slope, reflecting the lack of a significant specific interaction. The ion pairs show solvation intermediate between the cations and anions, filling the first shell around the cations with about three DME

molecules with a specific solvation of 153-186 kJ/mol for all four ion pairs, nearly independent of the choice of ions. Whereas for anions the specific solvation from three DME in the first shell is 52-64 kJ/mol, for Li^+ the specific solvation from the four DME in the first solvation shell is 458 kJ/mol and for Na^+ it is 333 kJ/mol.

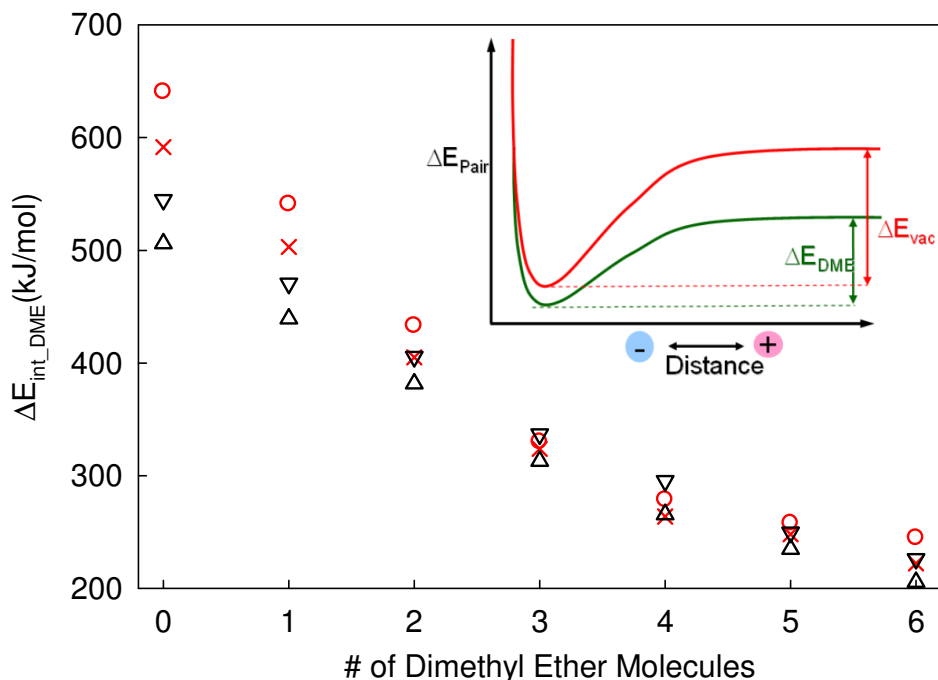


Figure 2.9. The specifically solvated pair interaction energy of $\text{Li}^+ \text{C}_6\text{H}_5\text{SO}_3^-$ (red circles), $\text{Li}^+ \text{CF}_3\text{SO}_3^-$ (red crosses), $\text{Na}^+ \text{C}_6\text{H}_5\text{SO}_3^-$ (black down triangles) and $\text{Na}^+ \text{CF}_3\text{SO}_3^-$ (black up triangles), in the gas phase (no PCM) as functions of the number of dimethyl ether molecules interacting with the ions and the ion pairs.

The pair interaction energy including specific solvation $\Delta E_{\text{pair}+\text{DME}}$, for any value of n , can be calculated by correcting the pair interaction energy ΔE_{pair} in vacuum by the cumulative solvation interaction.

$$\Delta E_{pair+DME} = \Delta E_{pair} + \Delta E_{stabilization,pair} - \Delta E_{stabilization,cation} - \Delta E_{stabilization,anion} \quad (2.4)$$

In **Figure 2.9**, the pair interaction energies that include specific solvation are plotted versus the number of DME solvating (n), where each of the stabilization energies in **Equation 2.4** are calculated with the same value of n . The net solvated pair interaction energy decreases with the number of dimethyl ethers, from ion-specific values (506 - 641 kJ/mol) with zero dimethyl ethers to a less ion-dependent value of approximately 340 kJ/mol with three DME around the ion pairs, for Li^+ or Na^+ ion pairs with benzene sulfonate or triflate. While not identical, the spread in pair interaction energies for these four ion pairs that include specific solvation are within our estimates of uncertainties the same for $3 \leq n \leq 6$, which all have the first solvation shell around the cation filled with anion + 3 DME. Consequently, we conclude that specific solvation is vital for understanding ion interactions (**Equation 2.2** without specific solvation is insufficient) and that specific solvation is in some sense the great equalizer; the ~100 kJ/mol reduction in pair interaction energy per DME added to the first solvation shell is sufficiently strong to soften the ion interactions significantly. Though large differences in pairing energy in vacuum calculations might suggest substantial differences in the relative concentrations of pairs and separated ions, these results suggest that solvation significantly diminishes these differences, such that concentrations are expected to be quite similar among a series of anions in PEO-based ionomer systems.

2.6. A Simple Four-State Model based on 0 K Interactions in Vacuum

The interaction energy of ions at 0 K in vacuum that is directly measured by *ab initio* methods gets diminished by three effects in real ionomer systems.

1) Global Solvation – The dielectric constant of the surroundings directly lowers the Coulomb energy and that effect is enhanced by the fact that the ion separations also increase as dielectric constant increases.

2) Local (specific) Solvation – Favorable interactions of polar functional groups on the polymer (or solvent) act to break up the ion associations because of the steric effect that more specific solvation is able to occur for a given ion when there are fewer other ions nearby.

3) Temperature – The higher T of real systems allows for thermal motions that increase the average ion separation and lower the effective Coulomb interaction. However, the dielectric constant of liquids generally also decreases roughly proportional to 1/T [39], complicating the effect of temperature.

These three effects are actually quite similar for different ionic species and that observation allows us to make use of the 0 K/vacuum *ab initio* energies with no solvation, temperature or dielectric constant effects, to compare different ions for their propensity to aggregate. In this crude way, we can use Gaussian03 as a design tool to select ions worthy of ionomer synthesis.

Table 2.6. Interaction energies of ion pairs, positive triple ions, negative triple ions and quadrupoles for Li^+ and Na^+ cations with various aromatic anions and their perfluorinated counterparts and also tetrabutyl borate for comparison.

	Li^+				Na^+			
Energy (kJ/mol)	ΔE_{Pair}	$\Delta E_{\text{Tr}+}$	$\Delta E_{\text{Tr}-}$	ΔE_{Quad}	ΔE_{Pair}	$\Delta E_{\text{Tr}+}$	$\Delta E_{\text{Tr}-}$	ΔE_{Quad}
$(\text{C}_6\text{H}_5)\text{SO}_3^-$	640.5	891.7	846.1	1474.2	544.8	757.8	736.5	1280.2
$(\text{C}_6\text{F}_5)\text{SO}_3^-$	603.9	818.5	771.5	1380.1	516.0	700.6	695.8	1187.1
$(\text{C}_6\text{H}_5)\text{HPO}_3^-$	667.2	934.2	859.9	1515.2	570.2	785.3	741.3	1335.2
$(\text{C}_6\text{F}_5)\text{HPO}_3^-$	625.4	863.6	820.6	1334.7	535.2	746.7	711.6	1149.9
$(\text{C}_6\text{H}_5)\text{CO}_2^-$	696.6	927.1	893.8	1588.3	596.4	783.2	800.1	1359.5
$(\text{C}_6\text{F}_5)\text{CO}_2^-$	629.7	863.8	838.1	1451.2	539.8	714.9	738.3	1244.8
$(\text{C}_4\text{H}_9)_4\text{B}^-$	585.0	788.2	>592.	1148.1	463.6	615.7	507.1	924.8
$(\text{C}_6\text{H}_5)_4\text{B}^-$	538.8	860. ^a	--	>1126.	483.5	737. ^a	>547.	>952.
$(\text{C}_6\text{F}_5)_4\text{B}^-$	448.2	611. ^a	--	--	365.7	498. ^a	--	--

^a – optimization was performed with “loose” criteria in Gaussian03.

Table 2.6 lists the *ab initio* vacuum interaction energies for four ion states of interest relative to the free (isolated ions). The triple ion states denote the combination of two cations with an anion (“triple+”) or two anions with a cation (“triple-”). The quadrupole state is composed of two pairs interacting, and is representative of larger aggregates that can form in ionomer systems. Each of these states was optimized, with multiple geometries considered, to locate global minimum energy structures. The quadrupole and triple ion interaction energies are defined similarly to **Equation 2.1**, with

the number of isolated anions and cations in the reference state adjusted. All of these ion states are significantly more stable than free isolated ions based on these 0 K energetics. The substantial binding energy associated with these states, in comparison to an anticipated small entropic driving force for dissociation in the ionomeric system, suggests that charged aggregates such as the positive triple ion [48-57] will represent the conducting species.

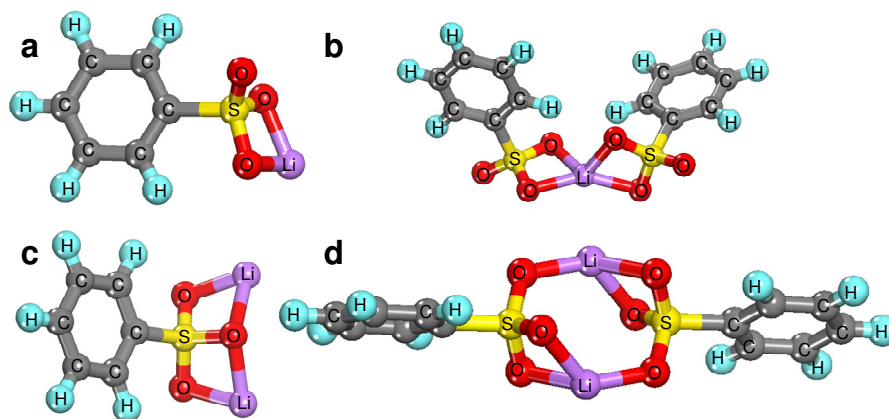


Figure 2.10. Equilibrium structures of $\text{Li}-(\text{C}_6\text{H}_5)\text{SO}_3$ species, a) pair, b) negative triple ion, c) positive triple ion, and d) quadrupole.

As noted in [Section 2.3](#), regardless of whether the cation is Li^+ or Na^+ or whether the anion is perfluorinated or not, the pair energies increase in the order $\text{SO}_3^- < \text{HPO}_3^- < \text{CO}_2^-$. The carboxylates, phosphonates and sulfonates are really quite similar in their interactions with Li^+ and Na^+ , and this persists for the triple ion energies and quadrupole energies. The four ion states are illustrated in [Figure 2.10](#) for $\text{Li}-(\text{C}_6\text{H}_5)\text{SO}_3$ species. As observed for methyl sulfonate, a Li cation prefers to interact with two oxygen atoms in the benzene sulfonate pair and triple ion states. In the quadrupole state, each Li cation

interacts with two oxygen atoms on one anion and a single oxygen atom on the other anion. The last three entries in [Table 2.6](#), tetrabutyl borate, tetraphenyl borate and perfluorinated tetraphenyl borate, have significantly lower interaction energies because of the highly delocalized nature of these borate anions.

In contrast to the direct interaction with oxygen atoms, the negative charge center in the sulfonate, the interaction between lithium and the borate species is more difficult to define. In the pair, the Li cation approaches the B atom center. However, in the aggregated states, the Li ion moves further from the boron atom and interacts with the delocalized negative charge. B has significantly lower electronegativity (2.01) compared with C (2.5), making the B of these anions have an effective positive charge and the net negative charge of these anions is distributed on the hydrocarbon or fluorocarbon exterior. The pair and positive triple ions of the borates converged to global minima but the negative triple ions and quadrupoles (i.e., all ion states with two borate anions) did not necessarily converge to global minima and are indicated as lower bounds on the energies with > sign in [Table 2.6](#). With perfluorinated tetraphenyl borate, optimization of negative triple ions and quadrupoles did not converge to a stable structure after extensive testing starting from multiple initial molecular geometries. Difficulties in finding a converged structure likely indicate the relatively broad, shallow potential energy surface associated with the cation interacting with the diffuse negative charge among multiple borate anions.

The lack of distinguished and deep minima for the aggregated state possibly indicates that this most-delocalized anion may be unlikely to aggregate under any conditions. The effect of fluorination is particularly strong for tetraphenyl borate:

Fluorinating the benzene ring on benzene carboxylate, sulfonate or phosphonate lowers the pair and positive triple ion energies by 5-10% but fluorinating the four benzene rings of tetraphenyl borate lowers the pair and positive triple ion energies by 20-30%. For these reasons, a synthesis goal in our current research is to attach perfluorinated tetraphenyl borate to low- T_g polymer backbones to create a perfluorinated tetraphenyl borate ionomer as a single-ion conductor of Li^+ or Na^+ .

2.7. Conclusion

Calculated values of the dipole moments of common polar small molecules compare favorably with reported measurements [40] using two basis sets. Calculated vapor phase interaction enthalpy and also free energy of Li^+ with various individual common polar small molecules also compare favorably with reported measurements [41-45]. Ion pair interaction energies are estimated in vacuum and via the Polarizable Continuum Model in 22 solvents of different dielectric constant. Those ion pair interaction energies are roughly correlated with $1/(e \cdot d)$ as expected by the Coulomb energy, but with significant data scatter owing to the difficulties in properly defining the cation – anion separation distance d . The specific solvation interactions of 1-6 dimethyl ether molecules with Li^+ , Na^+ and their ion pairs with benzene sulfonate and triflate anions are studied and found to significantly lower the effective pair interaction energy. The net solvated pair interaction energy is found to decrease with the number of dimethyl ethers, from ion-specific values (506 - 641 kJ/mol) with zero dimethyl ethers to an approximately ion-independent value of 340 kJ/mol with three dimethyl ethers around the ion pairs, for Li^+ or Na^+ ion pairs with benzene sulfonate or triflate. Specific solvation is

vital to include, and seems to be the great equalizer once the first solvation shell is filled. For this reason, we are developing a hybrid model that includes specific solvation in the first shell, all inside a PCM cavity.

This work is supported by the Department of Energy, Office of Basic Energy Sciences, under Grant No. DE-FG02-07ER46409.

References

- [1] P.G. Bruce and F.M. Gray, in Solid State Electrochemistry, edited by P.G. Bruce (Cambridge University Press, 1995).
- [2] M. Armand and J.-M. Tarascon, *Nature (London)* **451**, 652 (2008).
- [3] J.B. Kerr, in *Lithium Batteries*, edited by G.-A. Nazri and G. Pistoia, p. 574 (Kluwer, 2004).
- [4] D. Fragiadakis, S. Dou, R. H. Colby and J. Runt, *J. Chem. Phys.* **130**, 064907 (2009).
- [5] D. Fragiadakis, S. Dou, R. H. Colby and J. Runt, *Macromolecules* **41**, 5723 (2008).
- [6] S. Dou, S. Zhang, R. J. Klein, J. Runt and R. H. Colby, *Chem. Mater.* **18**, 4288 (2006).
- [7] R. J. Klein, S. Zhang, S. Dou, B. H. Jones, R. H. Colby and J. Runt, *J. Chem. Phys.* **124**, 144903 (2006).
- [8] P. Kollman and S. Rothenberg, *J. Amer. Chem. Soc.* **99**, 1333 (1977).
- [9] S.F. Smith, J. Chandrasekhar and W.L. Jorgensen, *J. Phys. Chem.* **86**, 3308 (1982).
- [10] R. L. Jarek, T. D. Miles M. L. Trester, S. C. Denson and S. K. Shin, *J. Phys. Chem. A* **104**, 2230 (2000).
- [11] T. Fujii, *Mass Spect. Rev.* **19**, 111 (2000).
- [12] P. Johansson, *J. Phys. Chem. A* **105**, 9258 (2001).
- [13] P. Johansson and P. Jacobsson, *J. Phys. Chem. A* **105**, 8504 (2001).
- [14] P. Johansson and P. Jacobsson, *Electrochimica Acta* **46**, 1545 (2001).
- [15] P. Johansson, J. Tegenfeldt and J. Lindgren, *Polymer* **42**, 6673 (2001).
- [16] J. B. Kerr, G. Liu, L. A. Curtiss and P. C. Redfern, *Electrochimica Acta* **48**, 2305 (2003).

- [17]H. Markusson, H. Tokuda, M. Watanabe, P. Johansson and P. Jacobsson, *Polymer* **45**, 9057 (2004).
- [18]H. Markusson, , P. Johansson and P. Jacobsson, *Electrochem. Solid-State Lett.* **8**, A215 (2005).
- [19]P. Johansson and P. Jacobsson, *Solid State Ionics* **177**, 2691 (2006).
- [20]P. Johansson and P. Jacobsson, *J. Power Sources* **153**, 336 (2006).
- [21]S. J. Paddison, K. D. Kreuer and J. Maier, *Phys. Chem. Chem. Phys.* **8**, 4530 (2006).
- [22]P. Johansson, *Phys. Chem. Chem. Phys.* **9**, 1493 (2007).
- [23]M. Armand and P. Johansson, *J. Power Sources* **178**, 821 (2008).
- [24]J. Scheers, P. Johansson, P. Szczecinski, W. Wieczorek, M. Armand and P. Jacobsson, *J. Power Sources* **195**, 6081 (2010).
- [25]J. Scheers, L. Niedzicki, G. Z. Zukowska, P. Johansson, W. Wieczorek and P. Jacobsson, *Phys. Chem. Chem. Phys.* **13**, 11136 (2011).
- [26]K. Angenendt and P. Johansson, *J. Phys. Chem. B* **115**, 7808 (2011).
- [27]E. I. Izgorodina, *Phys. Chem. Chem. Phys.* **13**, 4189 (2011).
- [28]M.J. Frisch et al., GAUSSIAN 03 Revision B.05, (Gaussian Inc., Pittsburgh, PA, 2003).
- [29]A.D. Becke, *J. Chem. Phys.* **98**, 1372 (1993).
- [30]A. D. Becke, *Phys. Rev. A* **38**, 3098 (1988).
- [31]C. Lee, W. Yang and R. G. Parr, *Phys. Rev. B* **37**, 785 (1988).
- [32]P. J. Stephens, F. J. Devlin, C. F. Chabalowski and M. J. Frisch, *J. Phys. Chem.* **98**, 11623 (1994).
- [33]S. Miertus, E. Scrocco and J. Tomasi, *Chem. Phys.* **55**, 117 (1981).

- [34]M. T. Cancès, B. Mennucci and J. Tomasi, J. Chem. Phys. **107**, 3032 (1997).
- [35]M. Cossi, V. Barone, B. Mennucci, and J. Tomasi, Chem. Phys. Lett. **286**, 253 (1998).
- [36]B. Mennucci and J. Tomasi, J. Chem. Phys. **106**, 5151 (1997).
- [37]M. Cossi, G. Scalmani, N. Rega, and V. Barone, J. Chem. Phys. **117**, 43 (2002).
- [38]J. Tomasi, Theor. Chem. Acc. **112**, 184 (2004).
- [39]L. Onsager, J. Amer. Chem. Soc. **58**, 1486 (1936).
- [40]CRC Handbook of Chemistry and Physics, 87th ed., Editor-in-Chief: David R. Lide (2006).
- [41]M. T. Rodgers and P. B. Armentrout, Mass Spectrom. Rev. **19**, 215 (2000).
- [42]R. H. Staley and J. L. Beauchamp, J. Amer. Chem. Soc. **97**, 5920 (1975).
- [43]R. L. Woodin and J. L. Beauchamp, J. Amer. Chem. Soc. **100**, 501 (1978).
- [44]R. Amunugama and M. T. Rodgers, J. Phys. Chem. A **106**, 9718 (2002).
- [45]R. Amunugama and M. T. Rodgers, Int. J. Mass Spectrom. **195/196**, 439 (2000).
- [46]G. Mao, M.-L. Saboungi, D. L. Price, M. B. Armand and W. S. Howells, Phys. Rev. Lett. **84**, 5536 (2000).
- [47]O. Borodin and G. D. Smith, Macromolecules **39**, 1620 (2006).
- [48]R. M. Fuoss and C. A. Kraus, J. Amer. Chem. Soc. **55**, 2387 (1933).
- [49]R. M. Fuoss and K.-L. Hsia, Proc. Nat. Acad. Sci. **57**, 1550 (1967).
- [50]S. Onishi, H. Farber and S. Petrucci, J. Phys. Chem. **84**, 2292 (1980).
- [51]M. Hojo and Y. Imai, Bull. Chem. Soc. Japan **56**, 1963 (1983).
- [52]J. Barthel, R. Gerber and H.-J. Gores, Ber. Bunsenges. Phys. Chem. **88**, 616 (1984).

- [53]M. Hojo, T. Takiguchi, M. Hagiwara, H. Nagai and Y. Imai, J. Phys. Chem. **93**, 955 (1989).
- [54]J. M.G. Barthel, H. Krienke and W. Kunz, Physical Chemistry of Electrolyte Solutions (Springer 1998).
- [55]S. Petrucci, M. C. Masiker and E. M. Eyring, J. Sol. Chem. **37**, 1031 (2008).
- [56]M. Hojo, T. Ueda, H. Hamada, Z. Chen and S. Umetani, J. Mol. Liq. **145**, 24 (2009).
- [57]M.N. Roy, R. Chanda and A. Bhattacharjee, Fluid Phase Equil. **280**, 76 (2009).

A Four-State Model to Screen for Weak Association of Ion Pairs

In the previous chapter we addressed the theoretical background and *ab initio* methodology used to determine interaction energies. In this chapter we will detail the development of the four-state model, import *ab initio* results into the four-state model diagram, correlate this diagram with physical properties of ionomers, such as glass transition temperature, dielectric constant, and conducting ion concentration, and compare with DSC and DRS experimental results to develop general concepts in screening for weak association of ion pairs, with the explicit intention to design ionomers for facile ion transport.

3.1. Introduction

Ionomers are of considerable interest since they have been proposed for use as single-ion conductors in fuel cell membrane electrode assemblies [1,2], the cation conduction medium between the electrodes of advanced batteries [3], ionic actuators [4,5] and supercapacitors. While the attractiveness of these materials comes from the fact that they selectively transport only one ionic species, this is mitigated by the fact that the presence of isolated aggregates can make ion conduction a very slow transport process.

In fact, in the melt state (without solvent but above the glass transition temperature T_g), nearly all counterions on ionomers are strongly condensed onto the chain to form ion pair dipoles that attract each other, illustrated in **Figure 3.1**. The dipolar electrostatic interactions that dominate their conformation and dynamics often lead to the formation of ionic aggregates [6,7]. The energy required to break up a quadrupole into two pairs can be many times kT near room temperature making the T_g of the ionic domains higher than the T_g of the backbone, and act to trap any free ions, resulting in a typically low conduction in conventional ionomers.

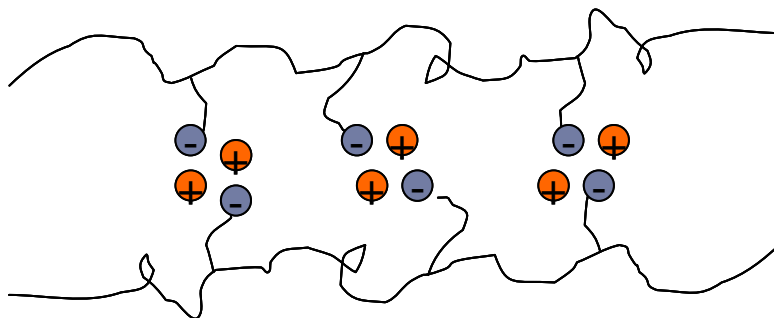
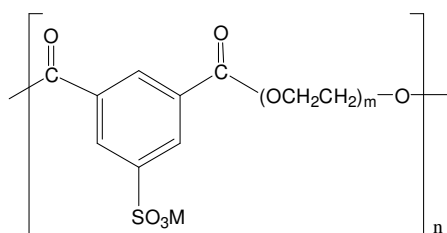


Figure 3.1. In ionomers, nearly all counterions are strongly condensed onto the ion that is covalently bonded to the chain, and additionally these neutral ion pairs may form neutral aggregates, such as the quadrupoles shown here. These physical crosslinks increase the T_g of the ionomer and lower ionic conductivity.

Aggregation can be directly detected through SAXS, and the effect of aggregation on T_g can be collaterally proved by DSC. In **Chapter 1**, we have also introduced the dielectric spectroscopy methods to determine conducting ion content and mobility and ion pair content in ionomers, directly assessing the extent of ion pair and quadrupole formation. These methods were recently developed by Prof. Runt and Prof. Colby's groups at Penn State University [8-10], based on the 1953 Macdonald electrode

polarization Model [11] and the 1936 Onsager Equation [12]. Moreover, the self-assembly of ion pairs into aggregates is associated with a signature that is akin to a glass transition, with dynamics and rheology strongly depending on whether the counterions are free, paired or clustered. A comprehensive understanding of the populations of various ion states shall be developed to complement these studies with the use of *ab initio* calculations.

The morphology of ionic domains depends on the detailed chemical makeup of the ionomer; large-scale ion aggregation (microphase separation of ions from the polymer) can be suppressed by clever chemistry. Prof. Colby's group has prepared and studied sulfonated ionomer melts based on poly(ethylene oxide) (PEO) (Scheme 3.1.) with T_g far below room temperature, as model single-ion conductors for studying cation transport in polymer electrolytes relevant to advanced batteries. Using arbitrary intensity units, no SAXS peaks (Figure 3.2.) were found for the sodium salts of this class of ionomer [13], suggesting that the ether oxygens of the PEO segments stabilized the ion pairs, preventing the usual clustering of ion pairs seen in hydrocarbon ionomers [14].



Scheme 3.1. PEG-based sulfonated polyester ionomers with well-defined PEG spacer (PEG M_n = 400, 600, 900 g/mol, and m = 9, 13, 20). M represents the cationic counterion (M = Li, Na, or Cs) associated with the sulfonate group.

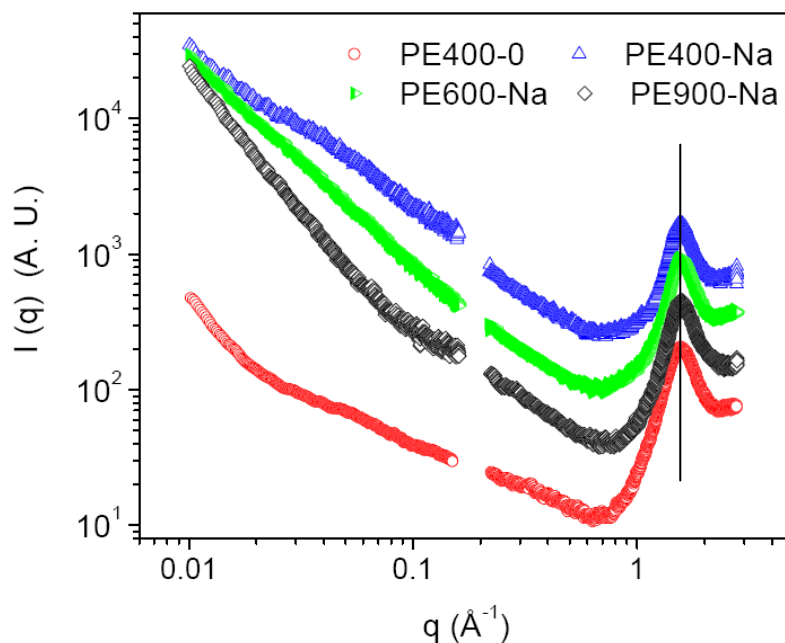


Figure 3.2. Combined SAXS and WAXD intensities (arbitrary units and offset for clarity) as a function of scattering wavevector for the sodium salt of sulfonated polyester ionomers made from $M = 400, 600$ and 900 g/mol PEG, and a neutral polymer (PE400-0) made from $M = 400$ g/mol PEG and a neutral isophthalate [13]. The peak at $q = 1.8 \text{ \AA}^{-1}$ is the amorphous halo of PEO. There is no large-scale aggregation / microphase separation in these single-ion conductors.

In collaboration with Prof. Winey's group at University of Pennsylvania, to obtain quantitative comparison between the scattering data from ionomers neutralized with Li^+ , Na^+ and Cs^+ , Wenqin Wang normalized the wide-angle X-ray scattering intensities of PEG600-100%M ($M = \text{Li}^+, \text{Na}^+$ and Cs^+) by sample thickness, data collection time and percent transmission **Figure 3.3a** [15]. PEG600-100%M ionomers showed stronger amorphous peak intensity at $14\text{-}16 \text{ nm}^{-1}$ compared to PEG600-0%, which is caused by the additional scattering from S, O, and metal cations. Next she subtracted the scattering

from PEG600-0% in **Figure 3.3b** [15] showing apparent peaks at $q = 2$ - 12 nm^{-1} from PEG600-100%M. These peaks result from the interparticle scattering from closely assembled and strongly interacting ions in various associated states, such as isolated ion pairs, quadrupoles, or larger aggregates.

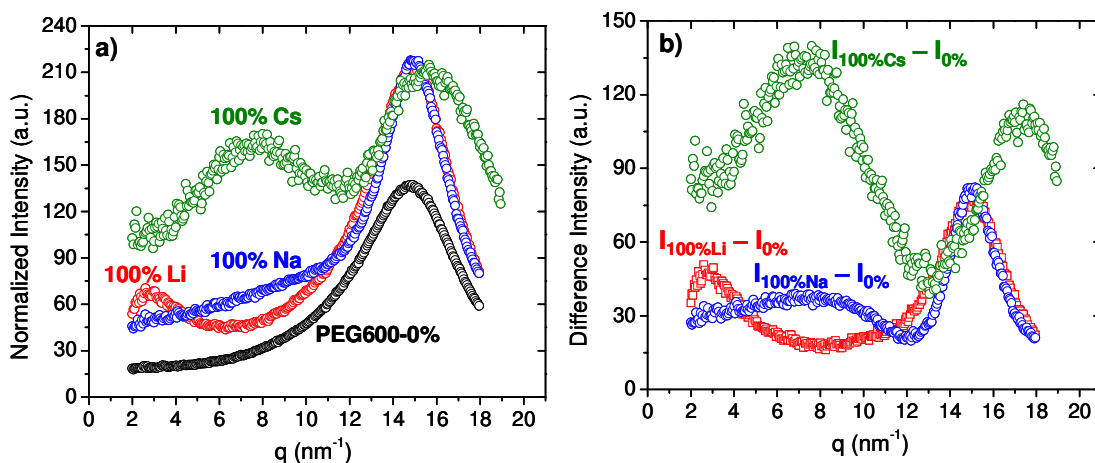
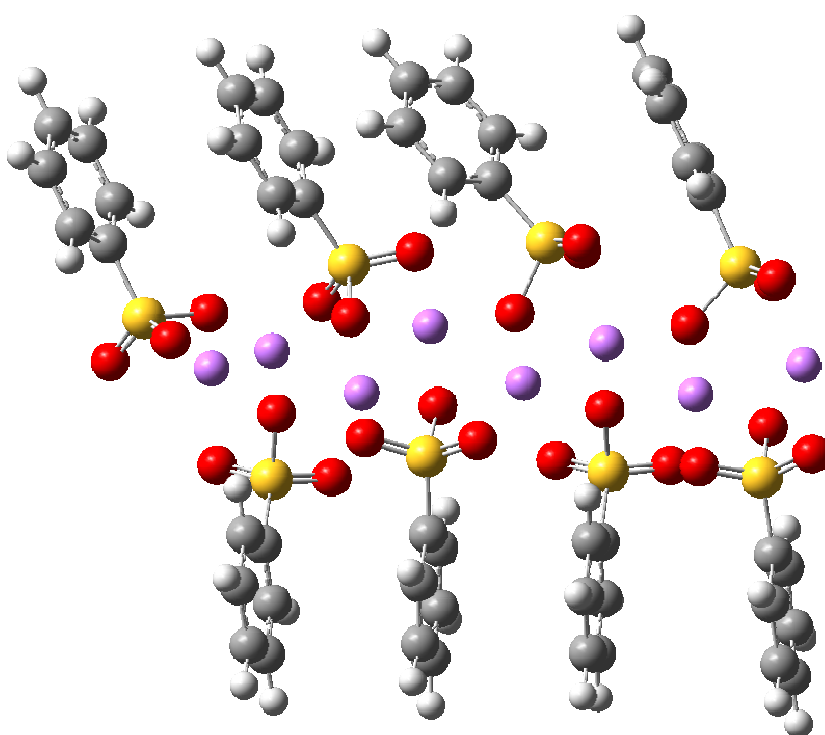
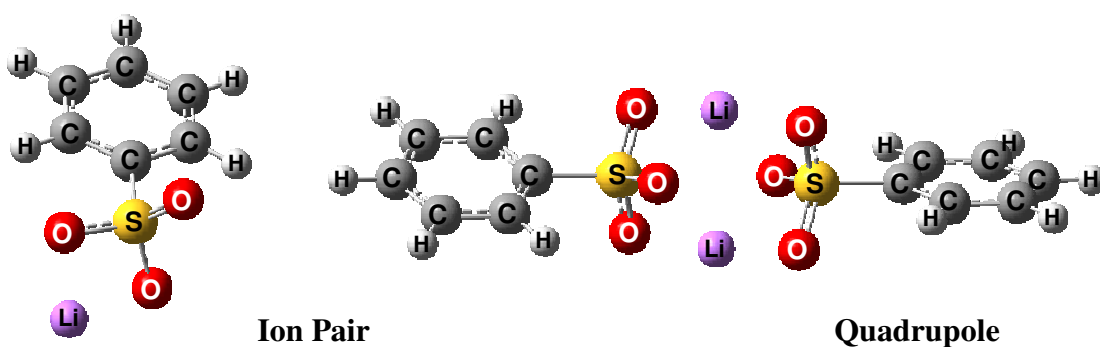


Figure 3.3. a) Wide-angle X-ray scattering intensity from PEG600-100%M (M = Li, Na, Cs) and PEG600-0% normalized by sample thickness, collection time, and percent of transmission. **b)** Difference intensity of PEG600-100%M after subtracting scattering intensity of PEG600-0% from PEG600-100%M [15].

Figure 3.4. shows equilibrated structures of a Li – benzene sulfonate ion pair, a quadrupole and an ion chain formed by 8 pairs, generated by *ab initio* calculations. All the calculations reported in this chapter were carried out with the Gaussian03 program [16] with the anion on the polymer modeled by benzene sulfonate. Calculations for Li^+ and Na^+ used the 6-31+G* basis set, which considers all electrons in its optimization of configurations. Cs^+ has many electrons, so the LANL2DZ basis set, with a frozen core for Cs, was used for all calculations involving Cs^+ .



Ion chain formed by 8 ion pairs

Figure 3.4. Equilibrated configurations for a Li – benzene sulfonate ion pair, quadrupole, and 8-ion-pair ion chain, each equilibrated at 0 K in vacuum using *ab initio* calculations.

Both methods use density functional theory with Becke's three-parameter hybrid method and the LYP correlation functional (B3LYP) as the exchange - correlation

functional [17-20]. Configurations were optimized and calculations were made for individual ions, ion pairs, positive and negative triple ions, quadrupoles and ion chains.

To facilitate interpretation, *ab initio* calculations at 0K in vacuum were made on ion pairs, positive triple ions, negative triple ions, quadrupoles and ion chains (with 5~8 ion pairs) of benzene sulfonate with various alkali cations (M), with some of the results shown in **Table 3.1**. In ion pairs, only the sulfur-cation (S-M) distances are shown for comparison with x-ray scattering experiments, since sulfur has significantly higher electron density than oxygen and x-ray contrast depends on the square of electron density. In quadrupoles and ion chains, three interatomic spacings are considered: sulfur-cation (S-M), sulfur-sulfur (S-S), and cation-cation (M-M). Interatomic distances at room temperature in the significantly more polar environment of our ionomers are expected to be ~10% larger than those listed in **Table 3.1** due to thermal expansion and softening of the potential due to higher dielectric constant of the surrounding medium.

Table 3.1. *Ab initio* calculations of interatomic spacings at 0 K in vacuum for benzene sulfonate with alkali cations (M = Li⁺, Na⁺, K⁺ or Cs⁺).

Cation	Ion Pair S-M (Å)	Quadrupole			Ion Chain (formed by 8 pairs)		
		S-M (Å)	S-S (Å)	M-M (Å)	S-M (Å)	S-S (Å)	M-M (Å)
Li ⁺	2.4	2.9 (2), 2.5 (2)*	4.1	3.5	2.8	4.7	3.3
Na ⁺	2.7	2.9 (4)	4.6	3.3	3.2	4.9	3.3
K ⁺	3.1	3.3 (4)	5.1	4.1	--	--	--
Cs ⁺	3.3	3.8 (4)	5.9	4.7	3.9	5.9	4.9

* Li – benzene sulfonate forms a surprisingly non-symmetric quadrupole

The higher q peaks (**Figure 3.3.**) at $12\text{--}18\text{ nm}^{-1}$ arise from interatomic scattering, some of which is due to ionic groups in various states. The broad peak centered at $\sim 7\text{ nm}^{-1}$ from subtracted PEG600-100%Cs corresponds to a correlation distance of 9.0 \AA . If all the ionic groups form isolated ion pairs, the distance between ion pairs estimated from the total concentration of cations ($\sim 0.75\text{ nm}^{-3}$) [16] is about 11 \AA , assuming simple cubic packing. Since the ion pairs are randomly distributed in the matrix, we expect the average distance between ion pairs to be slightly smaller than 11 \AA , which is comparable to the distance obtained from X-ray scattering, indicating the majority of the ions in PEG600-100%Cs exist in isolated ion pairs. Hence, we expect the higher q peak in PEG600-100%Cs corresponds to the spacing between ion pairs, which is consistent with *ab initio* results; this peak at 17.4 nm^{-1} (with $d = 3.6\text{ \AA}$) is $\sim 10\%$ larger than the S-Cs spacing (3.3 \AA) in ion pairs at 0 K in vacuum.

Quite different from PEG600-100%Cs, the ions in PEG600-100%Li form aggregated structures, which would include quadrupoles. S has higher electron density than Li^+ , therefore we expect most scattering in quadrupoles come from S-S contributions. The *ab initio* calculated S-S distance of 4.1 \AA for Li – benzene sulfonate quadrupoles fits closely with the S-S distance of $d = 4.2\text{ \AA}$ (at $q = 15.0\text{ nm}^{-1}$) inferred from Wang's X-ray scattering data for the PEG600-100%Li ionomer at room temperature.

For PEG600-100%Na, there is a sharp peak in the subtracted SAXS data of **Figure 3.3b**, with peak wavevector $q = 15.0\text{ nm}^{-1}$ (similar to PEG600-100%Li) giving an experimental d value (4.2 \AA) that lies between the calculated S-S spacing of the quadrupoles (4.6 \AA) and M-M spacing of the quadrupoles (3.3 \AA). Since S ($Z=16$) and Na ($Z=11$) are close in electron density, S-S and Na-Na have comparable contributions to

the X-ray scattering, which averages out the scattering peak position. The weakness of this peak relative to PEG600-100%Cs corresponds to the smaller contrast in electron density between SO_3Na and PEG. However, more accurate prediction of the peak shape and intensity would require form factor and structure factor simulation, as well as the exploration of additional types of ionic assemblies.

For PEG600-100%Na there is also a particularly broad ion peak in the subtracted SAXS data of [Figure 3.3b](#), with peak wavevector centered at 7nm^{-1} corresponding to a distance of 9.0 \AA , which suggests a wide range of spacings between ion aggregates. These results also tell us that the morphology of ionic domains not only depends on the choice of backbone and polar group, but also depends on the ions involved. The association energies of cations with anions and of both ions with the polar functional groups on the polymer, result in different coordination structures and local morphologies.

In the following section we will propose several possible larger ion aggregates, estimate their association energies assuming all ions are hard spheres of uniform size, compare these ion states with ion pairs, triple ions and quadrupoles, and identify a reasonable ground state for *ab initio* calculation to screen for weaker association of ion pairs for ionomer design.

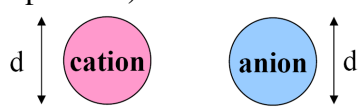
3.2. Association energies of various ion states using a simple hard sphere model

Ionomers with ionic aggregates have been studied extensively [\[27\]](#). Reciprocal-space SAXS and real-space STEM have been used to determine the size of ionic aggregates and the typical distance between ionic domains to assess the state of

aggregation in ionomers [28]. Khokhlov and his coworkers [29,30] have modeled the aggregation of charge pairs into clusters, however, they didn't account for the local solvation effect as we discussed in Chapter 2. Monojoy Goswami, Sanat K. Kumar and their co-workers performed MD simulations on a simple model of an ionomer / polyelectrolyte [31], taking into account the other interactions in the system, namely Lennard-Jones interactions between the polymer and solvent, as well as the dispersive component of the interaction between the charges and the solvent. They found that the stable low-T structure is sheets with anti-parallel stacking of dipoles, analogous to block copolymers in the strong segregation limit [32]. The most intensively studied ionomer is Nafion, and the first model for Nafion's morphology, called the Cluster-Channel or Cluster-Network Model, consisted of an equal distribution of sulfonate ion clusters (also described as 'inverted micelles'[33]) with a 40 Å (4 nm) diameter held within a continuous fluorocarbon lattice.

We simplified the previous studies and propose three possible larger ion aggregates only in 1D and 2D: single ion chain (formed by a line of alternating cations and anions), double ion chain (two single ion chains attracting each other by their co-ions forming zipper like double chain) and ion sheet (2D anti-parallel stacking of ion-pair dipoles on a square lattice).

This simple hard sphere model is based on two assumptions 1) monovalent cations (pink) and anions (blue) have the same diameter d ; and



2) ions are closely packed (hard spheres in contact) in all possible combinations: ion pair, triple ions, quadrupole, single ion chain, double ion chain and ion sheet. Let the

magnitude of attraction / repulsion force between two ions in contact be $F = \frac{e^2}{d^2}$, and

then the energy to bring these two ions together from infinity is $E = \frac{e^2}{d}$.

The energy to bring three ions from infinity to form a stable linear positive or negative triple ion (**Figure 3.5.**) is $E_{tr-} = E_{tr+} = 2E - \frac{E}{2} = \frac{3}{2}E$ because there are two attractions at distance d and one repulsion at distance $2d$.

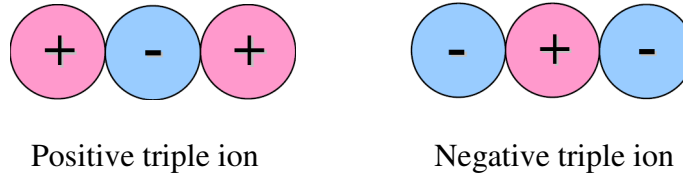


Figure 3.5. Structures of two types of triple ions.

Two cations and two anions might form two types of quadrupoles (**Figure 3.6.**). The force exerted on cation A from the other three ions in type I is pulling A to the center of the quadrupole $F_A = \sqrt{2}F - \frac{F}{2} = 0.914F$, so are the forces on the other three ions, therefore type I quadrupole is stable. On the other hand, the force exerted on cation A from the other three ions in type II, $F_A = \sqrt{\sqrt{2}^2 + (1/2)^2} F = 1.5F$, is pulling A to anion C but away from the center of the quadrupole. Taking all forces into consideration, the type II quadrupole will break into two ion pairs. The energies to form these two types of quadrupoles also suggest type I is the stable structure because it is a lower energy state than two pairs: $E_Q = 4E - \frac{2}{\sqrt{2}}E = 2.586E > 2E_p = 2E$, moreover, $\frac{E_Q}{2E_p} = 1.298$, while

type II is unstable and will break into two pairs: $E_Q = \frac{2}{\sqrt{2}}E = 1.414E < 2E_p = 2E$.

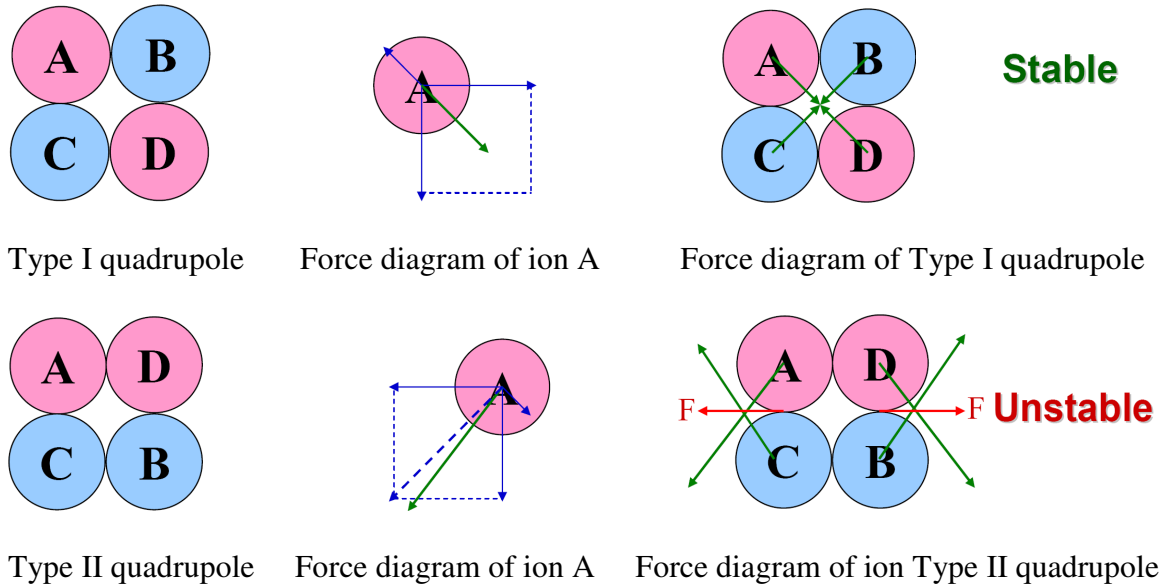


Figure 3.6. Structures and force analysis of two types of quadrupoles, A, D and C, B are of opposite charge.

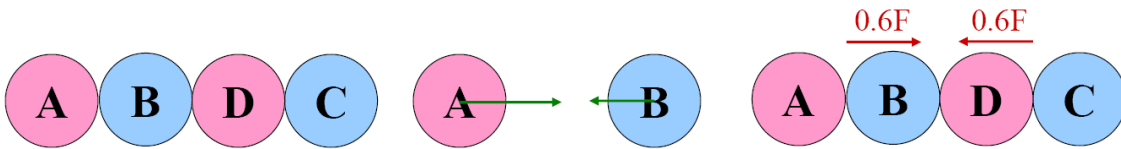


Figure 3.7. Structure and force analysis of a four-ion single chain.

Two cations and two anions can also form a 1D ion chain (**Figure 3.7.**). The force exerted on ions A and B are $F_A = F - \frac{F}{4} + \frac{F}{9} = 0.861F$ and $F_B = F - F - \frac{F}{4} = -0.250F$.

The resultant force of this pair ($0.6F$) brings them to the center of the ion chain, so does that of the other pair formed by ion C and D. Consequently, this four-ion chain is stable, which can be confirmed by comparison of its energy with that of two ion pairs:

$E_{4\text{-ion single chain}} = 3E + \frac{E}{3} - 2 \cdot \frac{E}{2} = 2.333E > 2E_p = 2E$. Note that it is less stable than the

quadrupole, which can also be viewed as a four-ion double chain.

$E_Q = 2.586E > E_{4\text{-ion single chain}} = 2.333E > 2E_p = 2E$. Stability analysis on this four-ion

single chain to quadrupole / four-ion double chain will be done in [Section 3.3.3](#)

The energy to form a five-ion single chain is $E_5 = 4E - \frac{3E}{2} + \frac{2E}{3} - \frac{E}{4} = 2.917E$

([Figure 3.8](#)). Extending to an n -ion single chain that starts with a cation, the n^{th} ion is a cation when n is odd number, and an anion when n is even number. Its energy ratio with an ion pair can be calculated by [Equation \(3.1\)](#)

$$\begin{aligned} \frac{E_{n\text{-ion single chain}}}{E} &= (n-1) - \frac{n-2}{2} + \frac{n-3}{3} - \frac{n-4}{4} + \frac{n-5}{5} - \frac{n-6}{6} \dots \\ &= (1 - \frac{1}{2} + \frac{1}{3} - \frac{1}{4} + \frac{1}{5} - \frac{1}{6} + \dots) n - 1 + 1 - 1 + 1 - 1 + 1 - \dots \end{aligned} \quad (3.1)$$

Dividing n into three cases: denumerable even number, denumerable odd number and n approaching infinity as a limit, we have [Equation \(3.2\)](#), plotted in [Figure 3.9](#)

$$\frac{E_{n\text{-ion single chain}}}{E} = \begin{cases} \left(1 - \frac{1}{2} + \frac{1}{3} \dots + \frac{1}{n-1}\right) n - 1 & (n : \text{even number}) \\ \left(1 - \frac{1}{2} + \frac{1}{3} - \frac{1}{4} \dots - \frac{1}{n-1}\right) n & (n : \text{odd number}) \\ n \cdot \ln 2 & (n \rightarrow \infty) \end{cases} \quad (3.2)$$

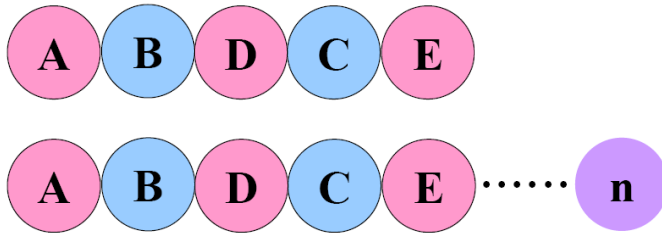


[Figure 3.8](#). Structures of a five-ion chain and n -ion single chain.

Red circles in **Figure 3.9.** are the ratios of the energy of n -ion single chains and the energy of an isolated ion pair calculated by **Equation (3.2)**, of which the best linear fitting has a slope of 0.69, approximately equal to $\ln 2$. **Figure 3.9.** shows minor fluctuations in the first four points, starting from the 10th ion the slope maintains 0.69.

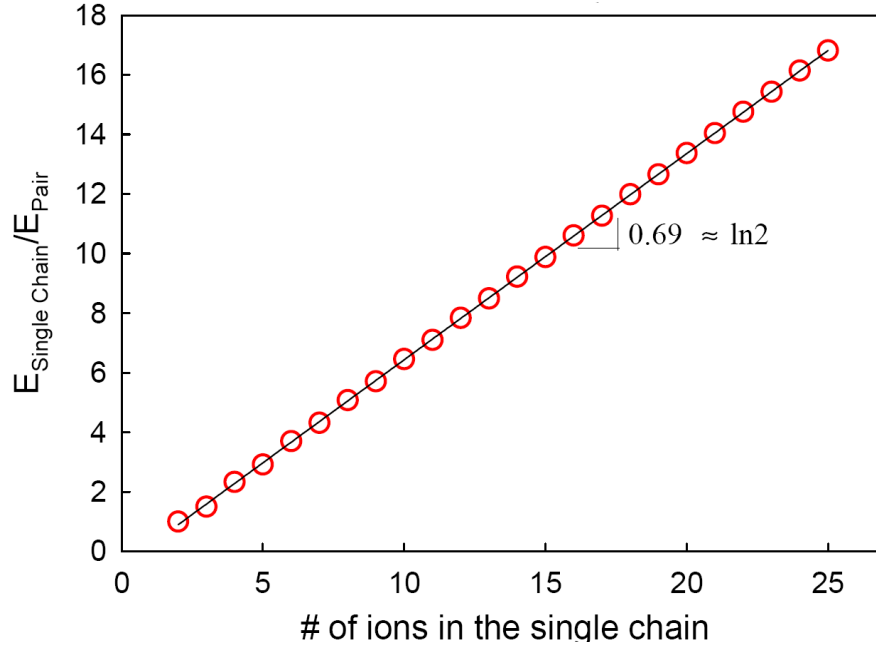
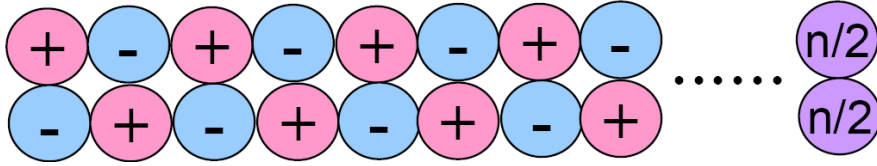


Figure 3.9. The ratio of energies of n -ion single chains and an isolated ion pair as the function of numbers of ions in the chain.

$$\begin{aligned}
 & \frac{E_{n\text{-ion double chain}}}{E} \\
 &= 2 \cdot \left(\frac{n}{2} - 1 \right) + \frac{n}{2} - \frac{2 \cdot (n/2 - 1)}{\sqrt{2}} - \frac{2(n/2 - 2)}{2} + \frac{2(n/2 - 2)}{\sqrt{5}} + \frac{2(n/2 - 4)}{3} - \frac{2(n/2 - 4)}{\sqrt{10}} - \dots \\
 &= \frac{3 - \sqrt{2}}{2} n - 2 + \sqrt{2} - \left(\frac{1}{2} - \frac{1}{\sqrt{5}} \right) (n - 4) + \left(\frac{1}{3} - \frac{1}{\sqrt{10}} \right) (n - 6) - \dots \\
 &= \frac{3 - \sqrt{2}}{2} n - 2 + \sqrt{2} - \sum_{i=2}^{n/2-2} (-1)^i \left(\frac{1}{i} - \frac{1}{\sqrt{1+i^2}} \right) (n - 2i)
 \end{aligned} \tag{3.3}$$

The energy to form an n -ion double chain (as shown below) is expressed as **Equation (3.3)**, plotted in **Figure 3.10**. A double chain is more stable than a single chain

with the same total number of ions (n) and $n/4$ quadrupoles.



Ion sheets were observed in the MD simulations of Goswami, et al. [25]. For simplicity, we start with 2D square ion sheets: 4, 9, 16 and 25- ion sheets, shown in **Figure 3.10**.

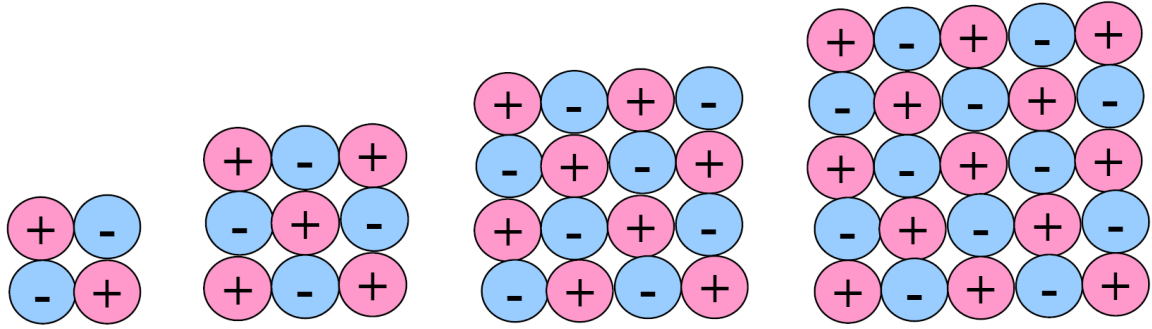


Figure 3.10. Structures of 2D 4, 9, 16 and 25- ion square sheets.

4-ion square sheet is also known as a quadrupole or 4-ion double chain, whose energy is $2.568E$. The energies of 9, 16 and 25 ion square sheets calculated by the equations listed below are $6.214E$, $11.796E$ and $18.737E$, respectively. Those are all more stable than the single ion chains containing same number of ions: $E_{Single\ chain_9} = 5.711E$, $E_{Single\ chain_16} = 10.606E$, $E_{Single\ chain_25} = 16.819E$. Note that the 16-ion single chain is more stable than 4 quadrupoles $4E_Q = 10.344E$. The comparison of square ion sheets with quadrupoles, single ion chains and double ion chains are plotted in **Figure 3.11**.

$$\begin{aligned}
E_{Sheet_9} &= 12E - \frac{8}{\sqrt{2}}E - \frac{6}{2E} + \frac{8}{\sqrt{5}}E - \frac{2}{2\sqrt{2}}E = 6.214E \\
E_{Sheet_16} &= 24E - \frac{18}{\sqrt{2}}E - \frac{16}{2}E + \frac{24}{\sqrt{5}}E + \frac{8}{3}E - \frac{8}{2\sqrt{2}}E - \frac{12}{\sqrt{10}}E + \frac{8}{\sqrt{13}}E - \frac{2}{3\sqrt{2}}E = 11.796E \\
E_{Sheet_25} &= 40E - \frac{32}{\sqrt{2}}E - \frac{30}{2}E + \frac{48}{\sqrt{5}}E - \frac{18}{2\sqrt{2}}E + \frac{20}{3}E - \frac{32}{\sqrt{10}}E + \frac{24}{\sqrt{13}}E \\
&\quad - \frac{8}{3\sqrt{2}}E - \frac{10}{4}E + \frac{16}{\sqrt{17}}E - \frac{12}{2\sqrt{5}}E + \frac{8}{5}E - \frac{2}{4\sqrt{2}}E = 18.737E
\end{aligned} \tag{3.4}$$

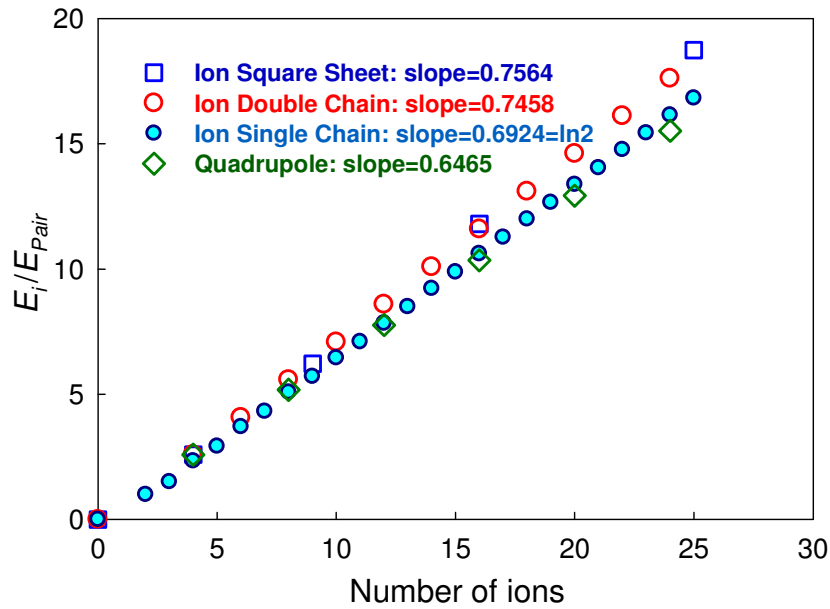


Figure 3.11. Comparison of energy levels of $n/4$ quadrupoles, n -ion single chain, n -ion double ion chain and n -ion square sheet as functions of the number of ions in the ion structures.

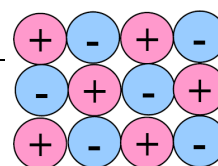
Figure 3.11. indicates that quadrupoles and single ion chains are less stable than either double ion chains or square ion sheets, but the differences are not significant, basically because the attractions between neutral charged quadrupoles when they form

larger aggregates are weak relative to the ion pairing energy. Moreover, in ionomers, half of the ions (either all of the positive ions or all of the negative ions) are attached to the polymer, the penalty of configurational entropy is large for ions to aggregate, which favors formation of the smaller ion structure, the quadrupole. Taking all of these factors into account, it is reasonable to create a simplified four-state model with the quadrupole as the ground state, to analyze the population distribution of various ion states. This simplifies the ion states enormously, by effectively excluding from consideration many possible ion aggregate structures, leaving the quadrupole as their representative. We will detail this four-state model in [Section 3.3](#).

At this point, we would like to take a moment and look at all possible aggregates that can be formed by 12 ions and compare their energies. $12 = 1 \times 12 = 2 \times 6 = 3 \times 4$.

Table 3.2. Comparison of energy levels for all nine possible single-state aggregation states of 12 ions.

	Possible conformations	E_i / E_{Pair}
1 x 12	One 12-ion single chain	7.839
2 x 6	Six pairs	6.000
	Two 6-ion single chains	7.400
	Two 6-ion double chains	8.132
	One 12-ion double chain	8.587
3 x 4	Three 4-ion single chains	7.000
	Three quadrupoles	7.758
4 x 3	Four triple ions	6.000
	One 12-ion sheet*	8.651 *



Next we list all conformations by the order of stability from high to low:

12-ion sheet > 12-ion double chain > Two 6-ion double chains > One 12-ion single chain > Three quadrupoles > Two 6-ion single chains > Four triple ions = Six pairs

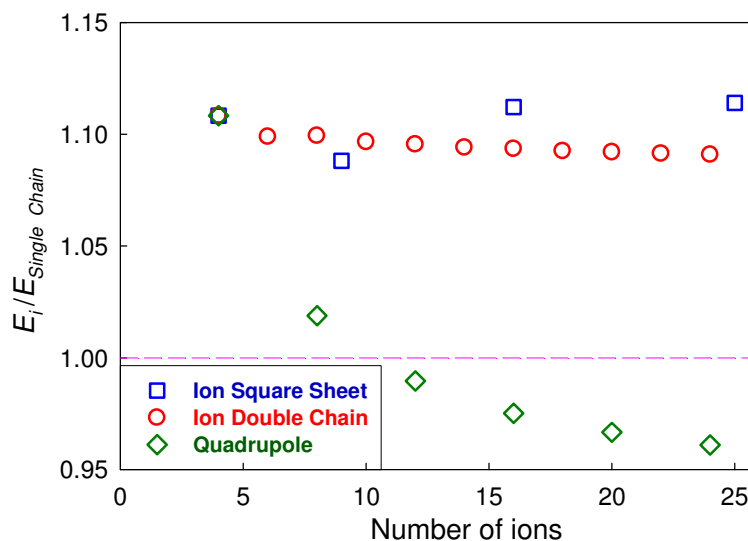
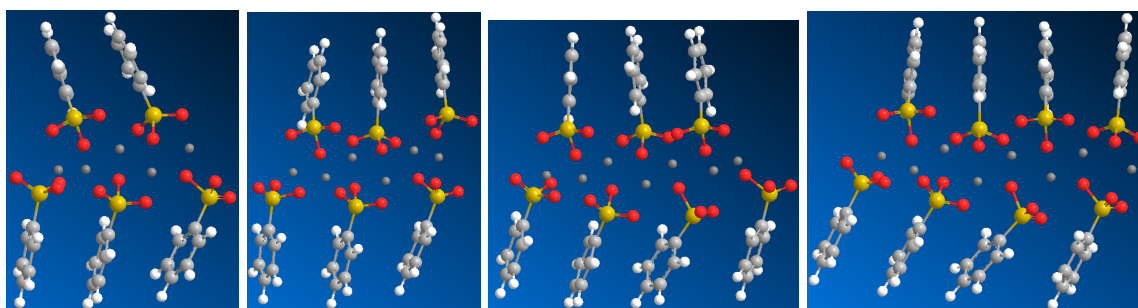


Figure 3.12. The ratios of quadrupole, double ion chain and square ion sheet energies to single ion chain energy as functions of the number of ions.

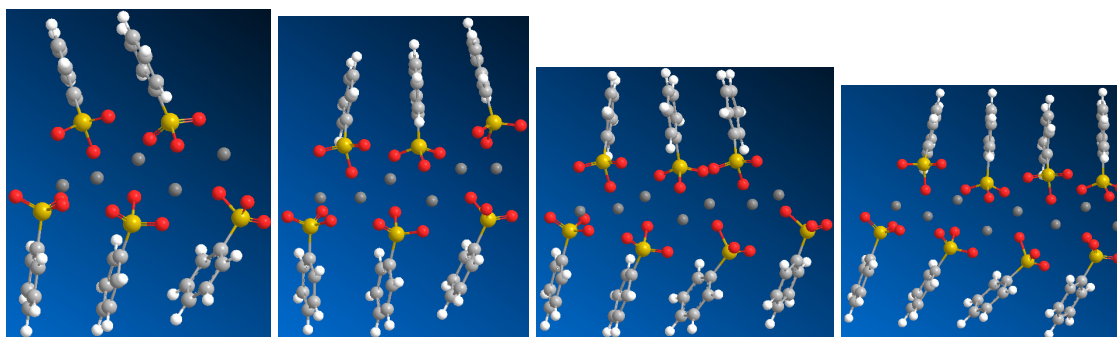
Apparently, ions like to aggregate, which is restricted by entropy loss on aggregation and steric effects from the polymer to a certain extent. Neglecting the steric hindrance effect, the difference between three quadrupoles with the most stable configuration, the ion sheet is $8.651E - 7.758E = 0.893E$. Using sulfonated PEG600-100%M (M = Li, Na, Cs) as an example, the three cation's pairing energies with benzene sulfonate anion at 0K, vacuum, calculated by *ab initio* methods are $E_{LiPair} = 6.64$ eV, $E_{NaPair} = 5.64$ eV and $E_{CsPair} = 4.38$ eV. ($1\text{eV} \approx 38.37$ kT at room temperature). The room temperature dielectric constants of the three ionomers are $\epsilon_{Li} = 35$, $\epsilon_{Na} = 110$ and $\epsilon_{Cs} = 120$ [8], reducing the three pairing energies to $E_{LiPair}/\epsilon_{Li} \approx 7.3$ kT, $E_{NaPair}/\epsilon_{Na} \approx 2.0$ kT

and $E_{CsPair}/\epsilon_{Cs} \approx 1.4 kT$. Therefore the energy differences between three quadrupoles and a 4 x 3 12-ion sheet for the three ionomers are only $\Delta E_{Li} \approx 6.5 kT$, $\Delta E_{Na} \approx 1.8 kT$ and $\Delta E_{Cs} \approx 1.3 kT$. This exercise once again helps us rationalize our use of the four-state model with the quadrupole as the ground state.

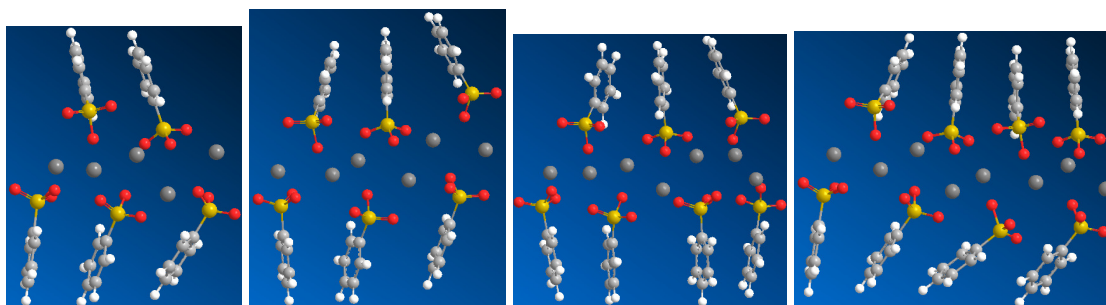
To magnify the energy differences between four ion aggregation states, we divided the energies of quadrupole, double ion chain and square ion sheet by the energy of single ion chains with the same number of ions. The results are plotted in [Figure 3.12](#). The horizontal pink line stands for $E_i = E_{Single Chain}$. Most points are above this line, except for quadrupoles when there are more than 8 ions, which suggests that short single ion chains will snap into quadrupoles or form double ion chains or ion sheets when there are less than 8 ions in the chain. Double ion chains and ion sheets are at quite similar energy levels, roughly 10% more stable than single ion chains. Since the ionomers of interest are linear polymers, the double ion chain seems more likely to be formed. That's why we started *ab initio* calculations in the double ion chain configurations for sulfonated PEG600-100%M (M = Li, Na, Cs) (refer to [Figure 3.4](#) and [Table 3.1](#)). [Figure 3.13](#) shows the configurations for Li / Na / Cs– benzene sulfonate 10 / 12 / 14 / 18 - ion chains built in Chem3D and MM optimized. [Table 3.3](#) lists energies of ion pair, quadrupoles and double ion chains with the same number of ions calculated by *ab initio* methods for Li / Na / Cs– benzene sulfonate, which we will use to validate the predictions from this simple hard sphere model.



Li-benzenesulfonate ion chains



Na-benzenesulfonate ion chains



Cs-benzenesulfonate ion chains

Figure 3.13. The configurations for a Li / Na / Cs– benzene sulfonate 5 / 6 / 7 / 8 ion pair – double ion chains built in Chem3D and MM optimized.

Table 3.3 Energies of ion pairs, quadrupoles and ion chains with the same number of ions calculated by *ab initio* methods for Li / Na / Cs– benzene sulfonate.

Cation	# of ions: n	$E_{Ion\ Chain}$ (eV)	$E_{Quadrupole} \times n/4$ (eV)	$E_{Pair} \times n/2$ (eV)
Li^+	10	39.95	38.18	33.18
	12	46.87	45.82	39.81
	14	53.57	53.45	46.45
	16	62.13	61.09	53.09
Na^+	10	34.55	33.16	28.22
	12	40.79	39.79	33.86
	14	46.47	46.42	39.51
	16	53.81	53.05	45.15
Cs^+	10	28.95	26.51	21.92
	12	34.63	31.82	26.30
	14	39.65	37.12	30.69
	16	45.82	42.42	35.07

1) $E_Q/2E_P$ ratio estimated by the hard sphere model is 1.298, while *ab initio* calculations give 1.151, 1.175 and 1.210 for benzene sulfonate with Li^+ , Na^+ and Cs^+ , respectively, which are close to, but consistently smaller than, the hard sphere estimation. This is because the hard sphere model assumes the ions are non-polarizable hard spheres in contact in all states, so that the distance between two nearest neighbors' charge centers are always the same as the ion diameter d . In reality, the S-M spacing of the isolated ion pairs are consistently shorter than those of the quadrupole, as listed in [Table 3.1.](#), since the latter has cation-cation and sulfonate-sulfonate repulsions in addition to cation-sulfonate attractions. Moreover, the tighter the ionic bond is in the pair state, the more the bond length extends when the quadrupole is formed, making $E_Q/2E_P$ smaller. Hence, the

hard sphere model consistently overestimates E_Q , and the error is magnified when the ion pairing energy is stronger. More importantly, ion pairs have charge transfer and therefore lower dipole moments than expected based on integer point charges, and therefore a lower tendency to form quadrupoles.

2) Estimated by the hard sphere model, $E_{10\text{-ion double chain}}/5E_P = 1.416$; $E_{12\text{-ion double chain}}/6E_P = 1.431$; $E_{14\text{-ion double chain}}/7E_P = 1.441$ and $E_{16\text{-ion double chain}}/8E_P = 1.450$.

ab initio calculation is precise but extremely expensive, limiting its utility for study of larger ion aggregates. The hard sphere model is a simple but powerful tool. We employed this model to compare the energy of quadrupoles with single ion chains, double ion chains and ion sheets with the same number of ions, with the robust conclusion that the quadrupole can be taken to be the ground state, representative of all larger ion aggregates. Based on this concept, we will then detail the four-state model using *ab initio* calculation results to probe trends among the various ion pairs and the results here can provide valuable information in understanding the experimental results.

The form of ion aggregates in anionic polymer systems is impacted by a number of factors. Ions aggregate in PEO ionomer systems because the dielectric constant is small enough that cation-anion attractions are larger than the thermal energy (kT). If there were no solvation of ions, three-dimensional aggregates would form. However, the ether oxygen strongly solvates small cations, favoring more “open” aggregate structures such as sheet-like or chain-like configurations. The specific ether oxygen solvation energy of 39 kJmol^{-1} , approximately one half of the Li - benzene sulfonate pairing energy, promotes the cation – anion dissociation [34]. Two-dimensional aggregates might be

energetically less favorable than one-dimensional aggregates because the latter is further exposed for solvation by PEO groups. However, more coordinated PEO chains decrease the entropy associated with polymer conformational freedom [34-37].

Free energies leverage ion species' population distributions, but both dielectric constant and entropy are ignored in our hard sphere model so far. We have simulated ion aggregates in a poly(ethylene oxide) (PEO) solvating environment using a cluster-continuum *ab initio* solvation model. The interplay of specific solvation energy, entropy and ion associations is investigated regarding the transition from “sparse” aggregates to “dense” aggregates. This work will be published under the title of “Quantum Mechanical Analysis of Ion Aggregation in Poly(ethylene oxide)-based Sulfonate Ionomers” soon.

3.3. Four-State Model and Quadrupole-Pair-Triple Ion (QPT) State Diagram

3.3.1. Background on Four-State Model Analysis in ionomer systems

The four-state model proposed here includes (a) the quadrupole state in which two ion pairs interact, as ground state, (b) the paired state, (c) the triple ion state involving two cations / anions and one anion / cation, and (d) the free-ion state with no direct anion-cation interaction. It will provide a data set useful for analysis of correlations and concepts, beyond the identification of candidates for synthesis.

We use Sulfonated PEG600-100% Li ionomer to demonstrate. Fragiadakis' EP analysis on DRS data at 20 °C found only a very small fraction (<0.1%) of Li⁺ ions are actually conducting [9]. Wang's X-ray measurements suggest of order 90% of ions are in

the quadrupole state [15], The other ~10% of the Li^+ cations are in the ion pair state. By comparing the energy levels of triple ion state and free ion state, we speculate [8-10] only $10^{-4}\%$ of the conducting ions are in the free ion state and the rest of the conducting ions are likely positive triple ions. These four equilibrium ion states in sulfonated PEG600-100%Li (inset) are depicted in Figure 3.14..

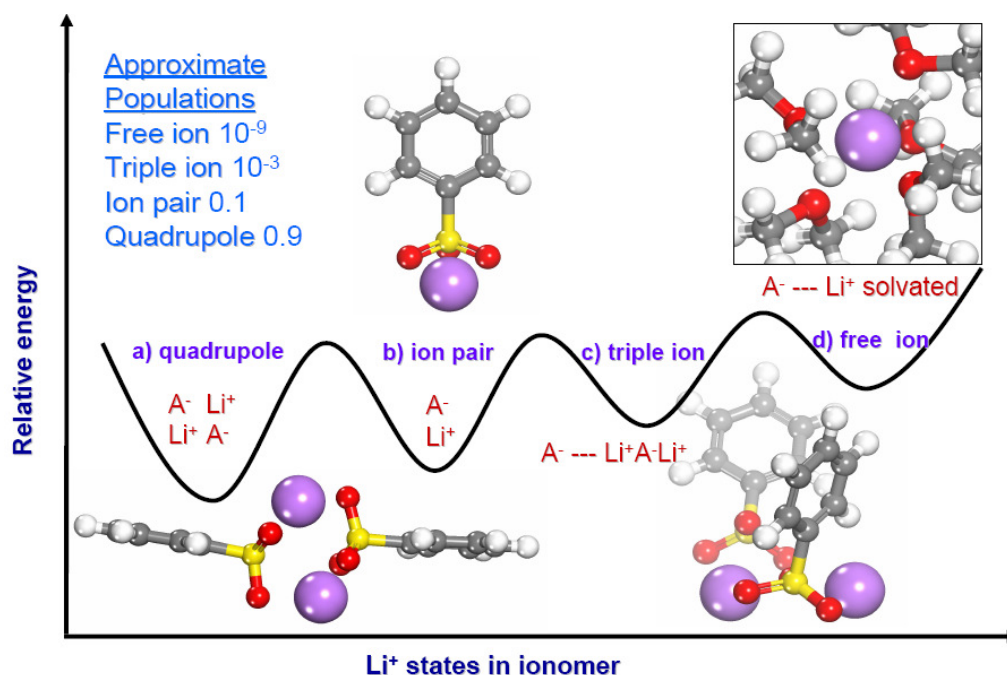


Figure 3.14. The relative energies of possible coordination states of Li^+ ions in an ionomer with benzene sulfonate anionic groups. (a) a quadrupole state with two Li^+ cations shared between two anionic groups, (b) an ion pair state, (c) a triple ion state, and (d) the free ion state. All of these ion states expose cations for solvation from the surrounding media; such solvation is only shown here for the free ions.

a) The **quadrupole state** ($\text{A}^- \text{C}^+ \text{---} \text{A}^- \text{C}^+$) is usually a symmetric arrangement of two cations (C^+) and two anions (A^-) that can be thought of as two ion pairs aligned anti-parallel. Ions in this state do not participate in conduction and the symmetry of the

quadrupole means those ions also do not contribute to the dipolar polarization and hence they are electrostatically less active compared with other ion states. Quadrupoles also act as temporary cross-links that retard segmental motion of the polymer, raising the glass transition temperature, lowering mobility and reducing conductivity.

b) The ion pair state (A^-C^+) consists of two ions directly interacting but more than 1 nm from other ions. Isolated ion pairs act like very polar functional groups on polymers and significantly raise the dielectric constant of ionomers. Ion pairs do not directly contribute to the conducting ion content but may well participate in conduction by accepting the extra ion from a triple ion.

c) Triple ions ($A^-C^+A^-$ and $C^+A^-C^+$) were postulated by Fuoss and Kraus in 1933 [28] to explain the extrema in molar conductance as functions of salt concentration in media of low dielectric constant ($\epsilon < 20$) and these triple-ions are now firmly established [29-33] for systems with $\epsilon < 30$ and possibly even some systems with higher ϵ and insufficient solvation to have significant populations of free ions. Paddison et al. consider conversion of the quadrupole state to triple ion state in evaluating the relative protogenic abilities of anionic groups for polymer electrolyte membranes [38]. In our model herein, ions in this state are considered to be participating in conduction, with the conduction mechanism involving the extra ion being transferred to a nearby ion pair.

d) Free ions are considered as separated ions coordinated with neutral, polar ionomer side-chain or backbone groups and not associated with (more than 1 nm from) their counter-ions. Dielectric spectroscopy with a specific electrode polarization model [9,10], and vibrational spectroscopy (Raman [39] and infrared [40]) account differently for free-ions, or better stated, ions that participate in conduction. Dielectric spectroscopy

analysis includes triple-ions as participating in conduction while noting that solvent separated pairs do not contribute to conduction. Vibrational spectroscopy estimates higher populations of “free-ion” states because solvent separated pair states are effectively counted as “free”. In contrast, vibrational spectroscopy that focuses on the sulfur – oxygen stretching absorption counts the positive triple ions as “clustered” due to the close proximity of two cations to the sulfonate anion.

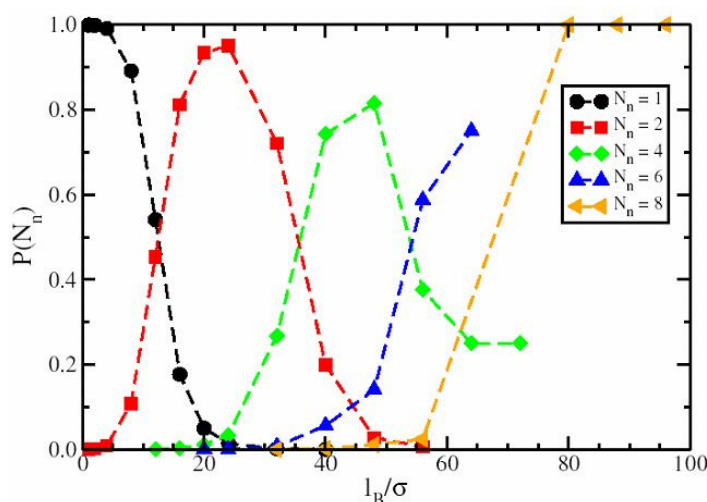


Figure 3.15. Populations of ion states as a function of binding energy of a contact pair: circles are free ions, squares are ion pairs, diamonds are quadrupoles, triangles are higher order aggregates. [41]

The dependence of the population of ion states on the contact pair binding energy, ion size, and ionomer dielectric constant can be estimated classically. Wang and Rubinstein investigated the conformational properties of symmetric flexible diblock polyampholytes by scaling theory and molecular dynamics simulations. [41] They found the strong association or ion binding regime starts with ion pair formation, followed by a cascade of multipole formation (quadrupole, hexapole, octupole, etc.), leading to

multiplets analogous to those found in ionomers. The populations of the dominant ion states as functions of the Bjerrum length l_B divided by ion size σ (a dimensionless indicator of contact pair binding energy) are depicted in **Figure 3.15**.

For very high dielectric constant [small $l_B = e^2/(\epsilon kT)$] the dominant state is free ions and we hope to get there by designing very polar ionomers. However, our best ionomers thus far (sulfonated phthalate polyesters based on PEO **[8,10,13]**) have $20 < l_B/\sigma < 30$ with essentially zero free ions. In these ionomers ions mostly exist as isolated pairs and quadrupoles, as discussed above. The conducting ions in this range of ϵ are triple-ions (not depicted in **Figure 3.15** and discussed below). Conventional non-polar ionomers, such as the lithium salt of sulfonated polystyrene, have $l_B/\sigma > 100$ and microphase separate large ion clusters called multiplets.

Figure 3.15 clearly demonstrates why raising ϵ is so vital. Higher dielectric constant stabilizes charge separation, breaking the quadrupoles into ion pairs. A higher fraction of ion pairs relative to quadrupoles further raises ϵ (moving to the left in **Figure 3.15**.) and eventually could break the ion pairs into a significant fraction of free ions. Near room T:

1.) In low polarity media (with $\epsilon < 5$, such as sulfonated polystyrene) the main equilibria is between quadrupoles and larger ion aggregates, with vanishingly small conduction.

2.) In more polar media, (with $7 < \epsilon < 15$, such as our PEO-based Li sulfonate ionomers) there are no free ions, with the main equilibria between quadrupoles and ion pairs, and the conducting species is a triple ion that involves two counterions bound to one polymer-ion.

3.) For a broad range of dielectric constant ($7 < \epsilon < 60$) the quadrupole is the expected ground state of ionomers and this is a primary reason why the ionomers that have been synthesized thus far have inadequate conductivities.

4.) In high dielectric constant media ($\epsilon > 60$) with strong ion solvation (such as water) the ion pair is the ground state, whereby many of the counterions pair by ‘condensation’ onto the polyion to lower charge repulsion [42-44], effectively spacing unpaired charges by the Bjerrum length along the chain.

Because free energies leverage these population distributions, precise estimations of solvation energy and entropy are crucial. In [Chapter 3](#), considering the target applications of our research in single ion conductors and ionic liquids are advanced Li battery and actuator, both of which have moderate dielectric constant $7 < \epsilon < 60$ and operating at moderate temperature, we discuss the four-state model and QPT-state diagram as simplified ways to consider ion interactions without consideration of entropy. Both dielectric constant and entropy are ignored. These presumably affect all ion equilibria in similar ways for different pairs of ions, so relative rankings of different ion combinations may be preserved.

Note that, under the condition of moderate ϵ and T , the quadrupole is expected to be the ground state, free ion concentration is expected to be vanishingly low and the dominant conducting species are expected to be triple ions. The main equilibrium is between quadrupole and ion pairs, and the secondary equilibrium is between ion pairs and triple ions. Focusing on these two equilibria, we developed the Quadrupole-Pair-Triple Ion (QPT) State Diagram.

3.3.2. The Quadrupole-Pair-Triple Ion (QPT) State Diagram

Multiple equilibria can create triple ions, ion pairs and quadrupoles, but for simplicity, we focus on one quadrupole dissociating into two pairs; and two asymmetric triple ions in equilibrium with three pairs. The Quadrupole-Pair-Triple Ion (QPT) State Diagram is built on these two equilibria, shown schematically in **Figure 3.16**.

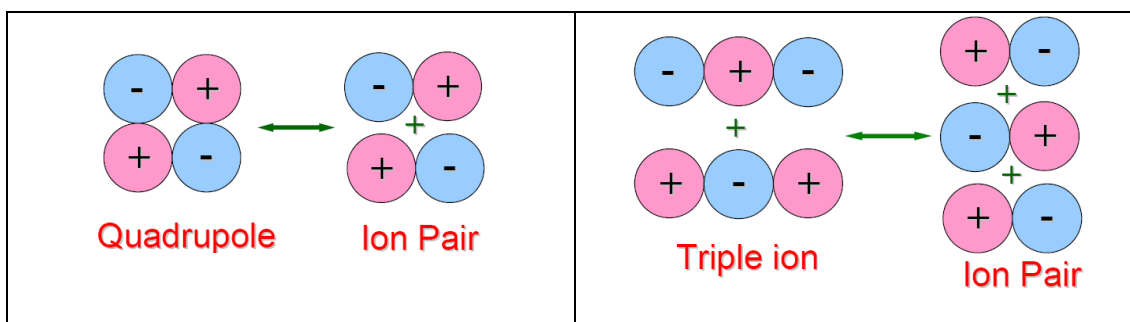


Figure 3.16. Two equilibria in ionomers depicted by the simple hard sphere model: On the left one quadrupole is in equilibrium with two pairs; and on the right two asymmetric triple ions are in equilibrium with three pairs.

A third equilibrium involving two sets of asymmetric triple ions formed from three quadrupoles will be considered later. The equilibrium constant of that balance is not independent (it can be constructed from the equilibrium constants of the two equilibria shown in **Figure 3.16**).

We define the quadrupole factor $\frac{E_{quad}}{2E_{pair}}$ and triple ion factor $\frac{E_{tr-} + E_{tr+}}{3E_{pair}}$ to be the

coordinates of X-axis and Y-axis of the Quadrupole-Pair-Triple Ion (QPT) State Diagram. The quadrupole factor indicates whether quadrupoles are energetically favored

over ion pairs and by how much. For $\frac{E_{quad}}{2E_{pair}} < 1$, there is no energetic driving force to

the entropically unfavorable quadrupole formation, but for the vast majority of ions that

we have studied thus far, the quadrupole is the ground state and $\frac{E_{quad}}{2E_{pair}} > 1$. As

$\frac{E_{quad}}{2E_{pair}}$ increases, the ion pair content should diminish (quadrupoles become more favored

relative to ion pairs). As discussed above, quadrupoles do not contribute to dielectric

constant and they raise ionomer T_g , while isolated ion pairs raise the dielectric constant

and they don't raise T_g (or at least not nearly as much as quadrupoles). To improve the

performance of the ionomer as an ion-conductor, we want to identify ion combinations

with lower quadrupole factor. For constant distances and symmetric quadrupoles, the

hard sphere model expects $\frac{E_{quad}}{2E_{pair}} = 1.293$. However, as we will see below, quantum

effects change the quadrupole factor of different ion combinations, with

$0.9 < \frac{E_{quad}}{2E_{pair}} < 1.3$ observed for the ion combinations studied thus far.

The triple ion factor indicates whether triple ions are favored over ion pairs and

by how much. Triple ions are believed to be the conducting ion species [\[9,10,31-33\]](#) and

the hard sphere model expects $\frac{E_{tr-} + E_{tr+}}{3E_{pair}} = 1$. Larger $\frac{E_{tr-} + E_{tr+}}{3E_{pair}}$ means that those ion

combinations should have higher conducting ion concentration, and presumably higher

conductivity. For the vast majority of ion combinations studied to-date, $\frac{E_{tr-} + E_{tr+}}{3E_{pair}} < 1$,

meaning that there should be more ion pairs than triple ions, consistent with the low

conducting ion contents observed for ionomers in dielectric spectroscopy.

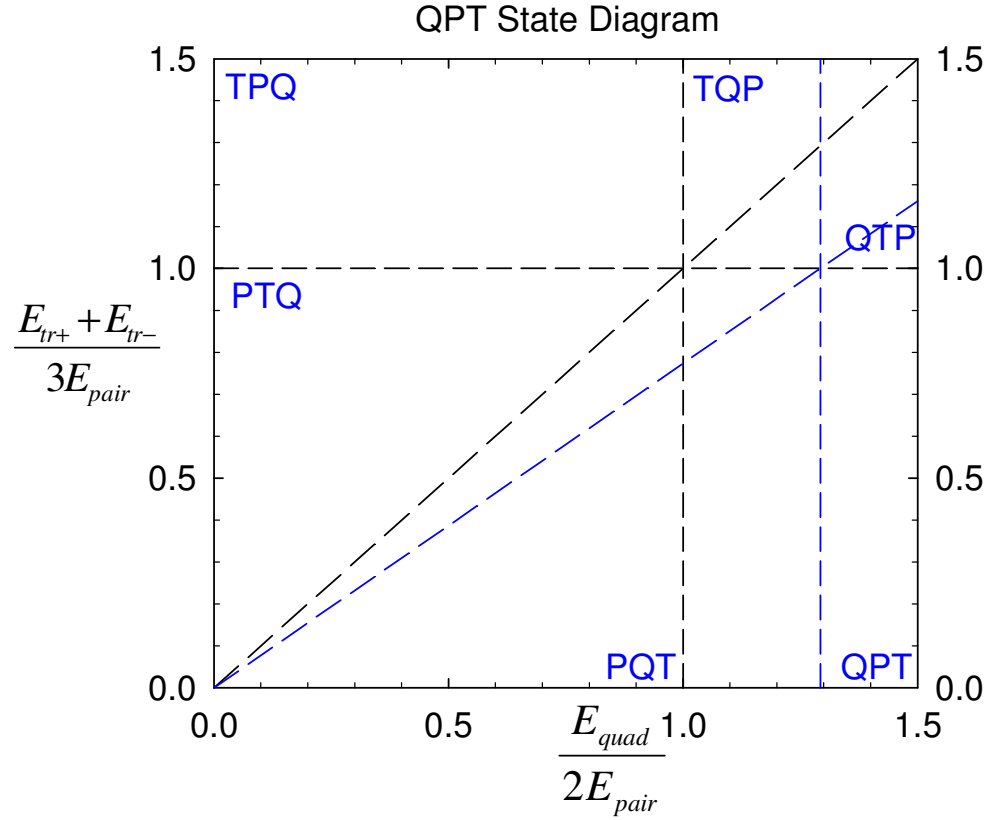


Figure 3.17. The Quadrupole-Pair-Triple Ion (QPT) State Diagram, plotting the triple ion factor against the quadrupole factor.

The QPT State Diagram (without any *ab initio* data) is shown in **Figure 3.17**.

The black dashed lines, corresponding to $\frac{E_{tr-} + E_{tr+}}{3E_{pair}} = 1$, $\frac{E_{quad}}{2E_{pair}} = 1$ and $\frac{E_{tr-} + E_{tr+}}{1.5E_{quad}} = 1$, separate the diagram into six regions.

TPQ) For $\frac{E_{tr-} + E_{tr+}}{3E_{pair}} > 1$ and $\frac{E_{quad}}{2E_{pair}} < 1$ triple ions should be the dominant

species, with some ion pairs and very few quadrupoles (hence denoted TPQ).

PTQ) For $\frac{E_{tr-} + E_{tr+}}{3E_{pair}} < 1$, $\frac{E_{quad}}{2E_{pair}} < 1$ and $\frac{E_{tr-} + E_{tr+}}{1.5E_{quad}} > 1$ ion pairs should be the

dominant species, with some triple ions and very few quadrupoles (hence denoted PTQ).

PQT) For $\frac{E_{tr-} + E_{tr+}}{3E_{pair}} < 1$, $\frac{E_{quad}}{2E_{pair}} < 1$ and $\frac{E_{tr-} + E_{tr+}}{1.5E_{quad}} < 1$ ion pairs should be the

dominant species, with some quadrupoles and very few triple ions (hence denoted PQT).

QPT) For $\frac{E_{tr-} + E_{tr+}}{3E_{pair}} < 1$ and $\frac{E_{quad}}{2E_{pair}} > 1$ quadrupoles should be the dominant

species, with some ion pairs and very few triple ions (hence denoted QPT)

QTP) For $\frac{E_{tr-} + E_{tr+}}{3E_{pair}} > 1$, $\frac{E_{quad}}{2E_{pair}} > 1$ and $\frac{E_{tr-} + E_{tr+}}{1.5E_{quad}} < 1$ quadrupoles should be

the dominant species, with some triple ions and very few ion pairs (hence denoted QTP)

TQP) For $\frac{E_{tr-} + E_{tr+}}{3E_{pair}} > 1$, $\frac{E_{quad}}{2E_{pair}} > 1$ and $\frac{E_{tr-} + E_{tr+}}{1.5E_{quad}} > 1$ triple ions should be the

dominant species, with some quadrupoles and very few ion pairs (hence denoted PQT).

As mentioned above, the hard sphere model expects $\frac{E_{tr-} + E_{tr+}}{3E_{pair}} = 1$ and

$\frac{E_{quad}}{2E_{pair}} = 1.293$. The blue dashed line in [Figure 3.17](#) goes through the hard sphere

prediction and the origin, representing an expectation of correlations between triple ion factor and quadrupole factor. As seen in [Figure 3.18](#), the observations for the simplest anion fluoride with a wide variety of cations lie just above this expectation line.

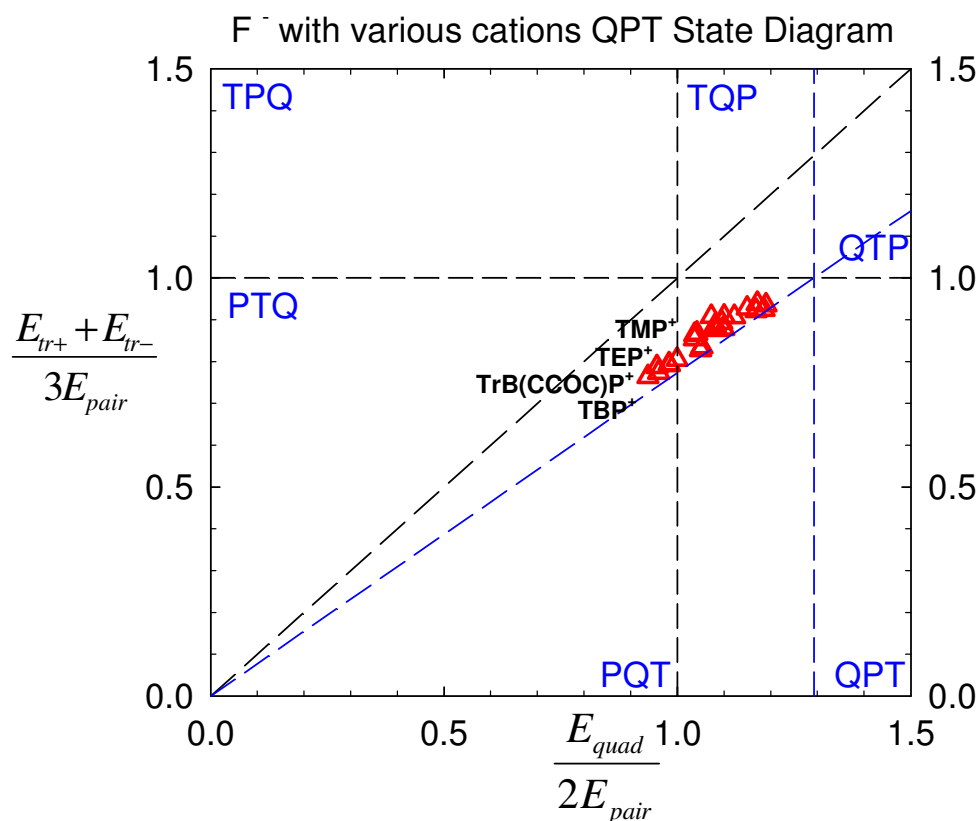


Figure 3.18 QPT diagram for fluoride anions with a variety of cations. Extrema are noted: TMP^+ is tetramethyl phosphate, TEP^+ is tetraethyl phosphate, TBP^+ is tetrabutyl phosphate and $\text{TrB}(\text{CCOC})\text{P}^+$ is the only other phosphate cation studied. The three cations closest to the hard sphere expectation point (1.293, 1.0) are Li^+ , Na^+ and K^+ .

Slightly above the expectation line makes sense because the extra repulsion in real quadrupoles consistently makes the anion – cation spacings in quadrupoles slightly larger than those in ion pairs, effectively lowering the quadrupole factor (placing observations to the left of the expectation line). Moreover, ion pairs have charge transfer and therefore lower dipole moments than expected based on integer point charges, and therefore a lower tendency to form quadrupoles. A QPT diagram with nine anions and a wide range

of cations is shown in [Figure 3.19](#). More than 90% of all ion combinations studied are located above the expectation line in the QPT region of the diagram, meaning that quadrupoles are the dominant state (with the deepest potential energy well).

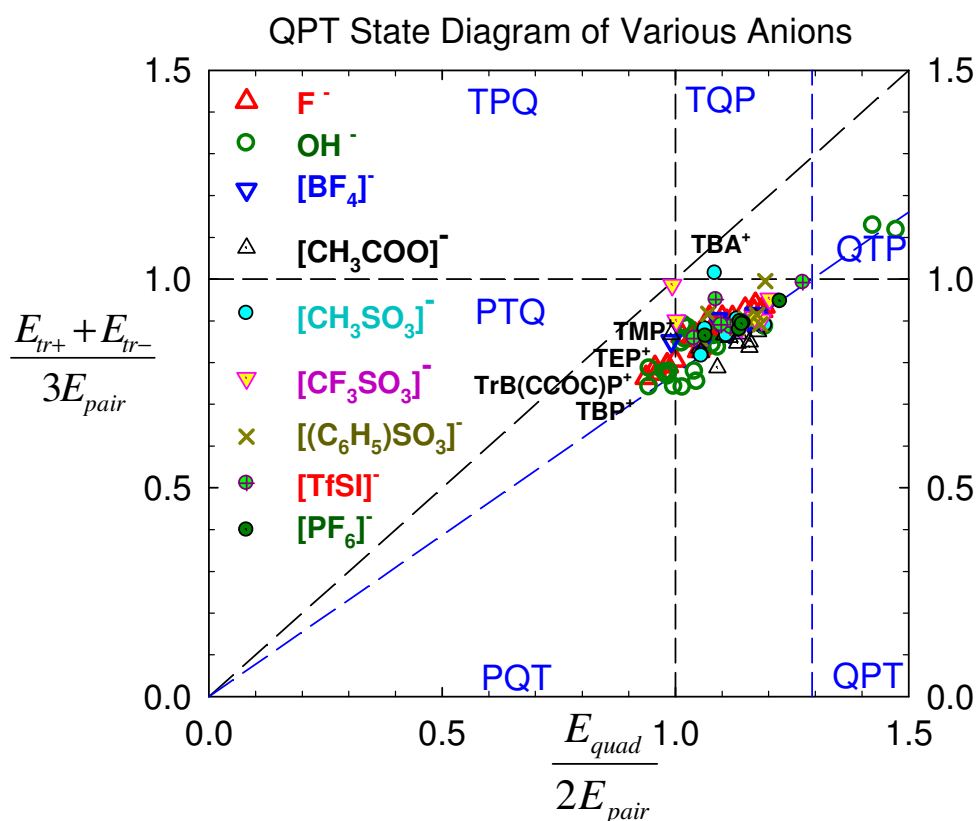


Figure 3.19 QPT diagram for eight anions with a variety of cations.

3.3.3. Explanations for trends in the QPT diagram

The hard sphere model predicts that all ion combinations should collapse onto a single point (1.293, 1.000). However, as shown in [Figure 3.18](#), fluoride anions with various cations cover a range of quadrupole factors and triple ion factors that correlate to lie slightly above the expectation line. The hard sphere model is of course oversimplified

for several reasons. Firstly, the anion – cation separations are not identical in various states, as mentioned above. Secondly, there are specific and interesting quantum effects that arise from the detailed chemical make-up of the ions involved, which are particularly important for ionic liquid ions with multiple atoms, including ion polarizability, electron sharing (partial covalent character of dominantly ionic bonds) and placements of charges on the atoms. Thirdly, there are size mismatch effects that can be understood by consideration of hard sphere ions of different size. These three reasons are discussed in more detail in the remainder of this section.

1) Anion – cation separations vary systematically between states. For nearly all anions and cations studied, the anion – cation bond length extends systematically when progressing from the ion pair state to the triple ion state and on to the quadrupole state. Both the triple ion factor and the quadrupole factor calculated by *ab initio* methods are consistently smaller than the expectation from the hard sphere model, with the quadrupole factor reduced more than the triple ion factor. The result is that they slide down and to the left, just above the blue dashed expectation line. An interesting observation is that the hard sphere prediction point (1.293, 1.0) actually has a low population of observations nearby. **Figure 3.19** shows two ion combinations with quadrupole factor larger than 1.3: $\text{TMA}^+ \text{OH}^-$ and $\text{TMP}^+ \text{OH}^-$. These cations are simple enough that we do not expect systems to get stuck in secondary minima and various starting states have been probed, so these results appear to be robust, but since these two observations are such outliers, they continue to be checked and rechecked. Both $\text{TMA}^+ \text{OH}^-$ and $\text{TMP}^+ \text{OH}^-$ ion pairs have *longer* anion – cation spacings than their peers. On the contrary, for ion combinations with the usual observation of quadrupole factor lower

than the hard sphere expectation, its triple ions and quadrupole have ion spacings increase relative to the ion pair, as the quadrupole factor decreases.

Table 3.4. Pair energies, quadrupole factors, triple ion factors and cation – F⁻ spacings for selected alkali fluorides, ammonium fluorides and phosphonium fluorides.

Cation	E_{pair} (eV)	$\frac{E_{quad}}{2E_{pair}}$	$\frac{E_{tr-} + E_{tr+}}{3E_{pair}}$	$d_{P/N-F}$ (Å) Ion Pair	$d_{P/N-F}$ (Å) +Triple Ion	$d_{P/N-F}$ (Å) -Triple Ion	$d_{P/N-F}$ (Å) Quadrupole
Na ⁺	6.668	1.190	0.935	1.937	2.021	2.046	2.078
Li ⁺	7.905	1.169	0.921	1.586	1.678	1.695	1.735
[TEA] ⁺	4.567	1.099	0.878	3.214	3.217 3.753	3.202 3.398	3.836
							3.299
							3.497
							3.603
[TMA] ⁺	4.936	1.082	0.888	2.955	3.156	3.154 3.156	3.380
							4.084
							3.398
							3.111
[TBA] ⁺	4.563	1.037	0.854	3.224	4.340 3.482	3.170 3.716	3.810
							4.043
							3.921
							3.884
[TMP] ⁺	5.442	0.982	0.794	1.826	3.093 3.081	3.088 3.082	3.431
							3.457
							4.026
							3.883
[TEP] ⁺	5.236	0.960	0.774	1.875	3.094 3.721	3.110 3.337	3.838
							3.563
							3.644
							3.165
[TBP] ⁺	5.052	0.937	0.764	1.882	3.450 3.541	3.066 3.668	3.355
							3.890
							4.024
							3.561

$\frac{E_{quad}}{2E_{pair}}$ for phosphonium fluorides are 32-38% smaller than 1.293, whereas for

ammonium fluorides only have $\frac{E_{quad}}{2E_{pair}}$ 18-25% smaller than 1.293, while Li⁺ F⁻ and Na⁺

F⁻ have $\frac{E_{quad}}{2E_{pair}}$ 9-11% smaller than 1.293.

To clarify this point, **Table 3.4** lists the pair energies, quadrupole factors, triple ion factors and distances between two ion charge centers for extremely low and high observations in **Figure 3.18**. Li⁺ F⁻ and Na⁺ F⁻ have the largest quadrupole factors and triple ion factors in **Figure 3.18**, and the anion – cation spacing increases by less than 10% when two ion pairs form a quadrupole. Ammonium fluorides have the anion – cation spacing increase by 12-21% when two ion pairs form a quadrupole. In sharp contrast, the structurally similar phosphonium fluorides have the lowest quadrupole factors and triple ion factors in **Figure 3.18**, and have their anion – cation spacing increase by 83-97% when two ion pairs form a quadrupole. Moreover, in comparing the ion spacings in ammonium fluorides and phosphonium fluorides in **Table 3.4**, it is clear that the ion pair spacings in phosphonium fluorides are the anomaly responsible for this enormous change in ion spacing. The quadrupoles have similar ion spacings in ammonium fluorides and phosphonium fluorides, while the ion pair spacings in phosphonium fluorides are surprisingly short.

2) Quantum chemistry (electron placement) effects on QPT positions. The underlying origin of the differences between phosphonium and ammonium cations noted in **Figure 3.18** and **Table 3.4** come from the electronegativities of the elements making up these cations.

As pointed out first by Pauling, electronegativity tends to decrease in moving left or downwards in the periodic table. Of interest here is the fact that nitrogen is more electronegative than carbon and carbon is more electronegative than phosphorous. This

means that the N atom at the center of the ammonium cation is partially *negatively* charged ($-0.7e$), with the four CH_2 groups bonded to N bearing most of the effective positive charge of ammonium cations. In contrast, the P atoms at the center of phosphonium cations has a strong positive charge ($+1.5e$), with the four CH_2 groups bonded to P having partial negative charges [45]. The Mulliken charge distributions on these two free ions are depicted in **Figure 3.20**.

→ Atomic radius decreases → Ionization energy increases → Electronegativity increases →

Group (vertical)	1	2	3	4	5	6	7	8	9	10	11	12	13	14	15	16	17	18
Period (horizontal)																		
1	H 2.20																	He
2	Li 0.98	Be 1.57												C 2.04	N 2.55	O 3.04	F 3.44	Ne
3	Na 0.93	Mg 1.31												Al 1.61	Si 1.90	P 2.19	S 2.58	Ar
4	K 0.82	Ca 1.00	Sc 1.36	Ti 1.54	V 1.63	Cr 1.66	Mn 1.55	Fe 1.83	Co 1.88	Ni 1.91	Cu 1.90	Zn 1.65	Ga 1.81	Ge 2.01	As 2.18	Se 2.55	Br 2.96	Kr
5	Rb 0.82	Sr 0.95	Y 1.22	Zr 1.33	Nb 1.6	Mo 2.16	Tc 1.9	Ru 2.2	Rh 2.28	Pd 2.20	Ag 1.93	Cd 1.69	In 1.78	Sn 1.96	Sb 2.05	Te 2.1	I 2.66	Xe
6	Cs 0.79	Ba 0.89	*	Hf 1.3	Ta 1.5	W 2.36	Re 1.9	Os 2.2	Ir 2.20	Pt 2.28	Au 2.54	Hg 2.00	Tl 1.62	Pb 2.33	Bi 2.02	Po 2.0	At 2.2	Rn
7	Fr 0.7	Ra 0.9	**	Rf 1.3	Db 1.5	Sg 2.36	Bh 1.9	Hs 2.2	Mt 2.20	Ds 2.28	Rg 2.54	Uub 2.00	Uut 1.62	Uuq 2.33	Uup 2.02	Uuh 2.0	Uus 2.2	Uuo
Lanthanoids	*	La 1.1	Ce 1.12	Pr 1.13	Nd 1.14	Pm 1.13	Sm 1.17	Eu 1.2	Gd 1.2	Tb 1.1	Dy 1.22	Ho 1.23	Er 1.24	Tm 1.25	Yb 1.1	Lu 1.27		
Actinoids	**	Ac 1.1	Th 1.3	Pa 1.5	U 1.38	Np 1.36	Pu 1.28	Am 1.13	Cm 1.28	Bk 1.3	Cf 1.3	Es 1.3	Fm 1.3	Md 1.3	No 1.3	Lr 1.3		

Periodic table of electronegativity using the Pauling scale

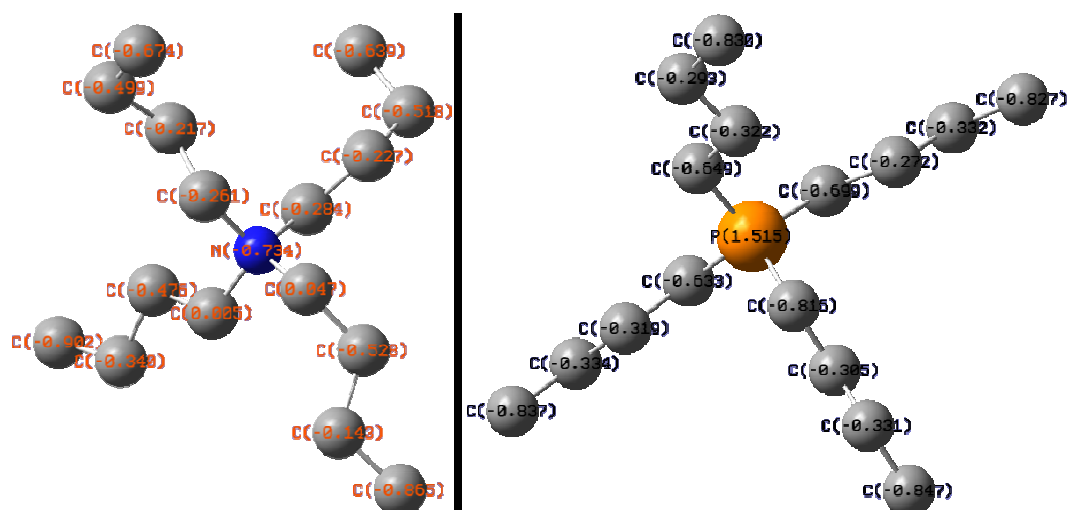


Figure 3.20. Comparison of tetrabutyl ammonium (left) and tetrabutyl phosphonium (right) Mulliken charge distributions.

The strong positive charges on the CH₂ bonded to N make ammonium cations form strong quadrupoles, as it is easy for two anions to interact strongly with these positive CH₂ groups. In contrast, the phosphonium cations have effective shielding of the strongly positive P by the negative CH₂ groups bonded to P, severely restricting the interaction of phosphoniums with anions and destabilizing phosphonium quadrupoles.

3) Cation – anion size mismatch effects destabilize quadrupoles. There is a simple ion size effect on the quadrupole – pair equilibrium that we illustrate with a natural extension of the hard sphere model to hard sphere anions and cations that differ in size. We take the radius of the hard sphere anion to be a and the radius of the hard sphere cation to be c and focus on the case of $a > c$. The general structure of the symmetric quadrupole, defining clearly a , c and angle θ is shown in **Figure 3.21**. The energy of this symmetric quadrupole is

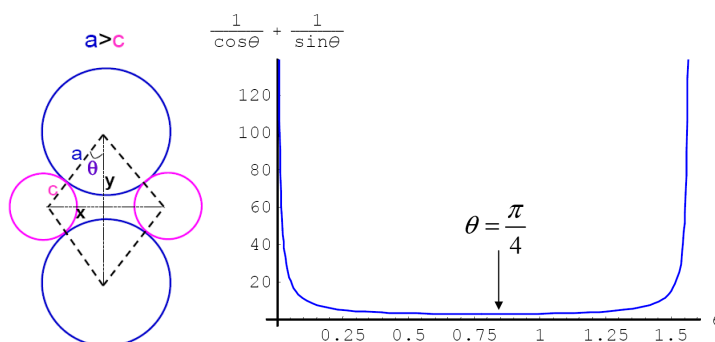


Figure 3.21. General structure of the size mismatched hard-sphere quadrupole and the angular dependence of the quadrupole potential energy well (see **Equation 3.5**).

$$E_Q = \frac{4e^2}{a+c} - \frac{e^2}{2(a+c)\sin\theta} - \frac{e^2}{2(a+c)\cos\theta} = \frac{e^2}{2(a+c)} \cdot \left(8 - \frac{1}{\sin\theta} - \frac{1}{\cos\theta} \right) \quad (3.5)$$

We can locate the extrema at $\frac{\partial E_Q}{\partial \theta} = 0$, i.e., $\frac{\partial(\sin \theta)^{-1}}{\partial \theta} + \frac{\partial(\cos \theta)^{-1}}{\partial \theta} = 0$, for which

$\sin^3 \theta = \cos^3 \theta$, thus $\theta = \frac{\pi}{4}$. At $\theta = \frac{\pi}{4}$, the quadrupole energy E_Q reaches a maximum.

There are two potential ‘contact’ ground states of the quadrupole (Cases I and II) to consider, both of which are planar, depicted in [Figure 3.22](#), with energies given by [Equation 3.6](#).

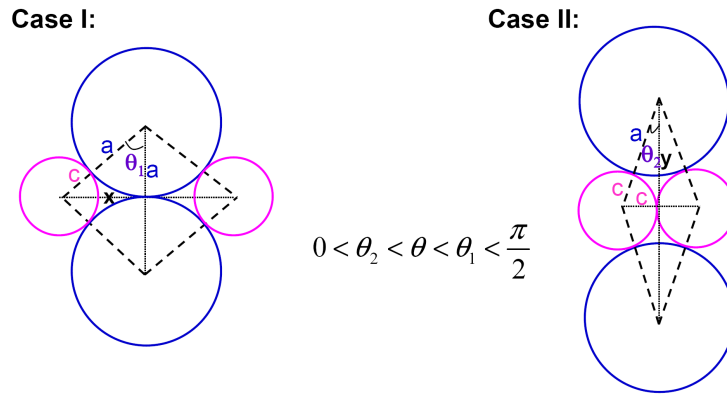


Figure 3.22. Two possible contact ground states of size mismatched quadrupoles.

$$E_{Q1} = \frac{4e^2}{a+c} - \frac{e^2}{2\sqrt{(a+c)^2 - a^2}} - \frac{e^2}{2a} \quad E_{Q2} = \frac{4e^2}{a+c} - \frac{e^2}{2\sqrt{(a+c)^2 - c^2}} - \frac{e^2}{2c} \quad (3.6)$$

When $a > c$, $E_{Q1} > E_{Q2}$, meaning that we can rule out Case II, and the contact quadrupole always has large ions in contact and small ions not in contact. For large asymmetry, with $a+c < \sqrt{2}a$, $\theta_1 < \pi/4$, then the contact quadrupole is the ground state (deepest potential energy well) as depicted in [Figure 3.23](#), with energy E_{Q1} in [Equation 3.6](#), with quadrupole factor given by [Equation 3.7](#), where $s = c/a$ is the ratio of cation and anion radii.

When $a + c < \sqrt{2}a$, $\theta_1 < \pi/4$,
then four ions tend to form

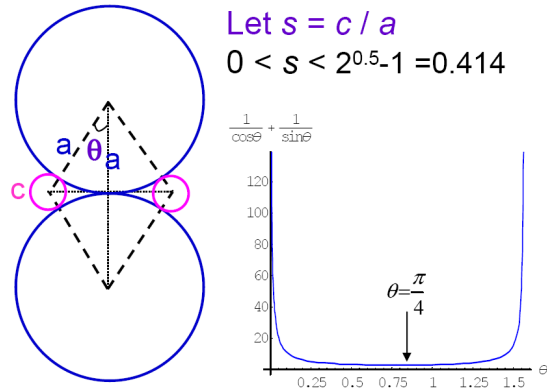


Figure 3.23. The contact quadrupole is the ground state of highly asymmetric ions.

$$\frac{E_Q}{2E_P} = 2 - \frac{a+c}{4a} - \frac{a+c}{4\sqrt{(a+c)^2 - a^2}} = 2 - \frac{1+s}{4} - \frac{1+s}{4\sqrt{2s+s^2}} \quad \text{for } s < 0.414 \quad (3.7)$$

For weaker asymmetry ($0.414 < s < 1$) the stable quadrupole no longer has the anions in contact and the optimum θ reverts to $\pi/4$, depicted in **Figure 3.24**, with

$$E_Q = \frac{4e^2}{a+c} - \frac{2e^2}{\sqrt{2}(a+c)} \quad \text{and} \quad E_P = \frac{e^2}{a+c}, \quad \text{we have} \quad \frac{E_Q}{2E_P} = \frac{4-\sqrt{2}}{2} = 1.293, \quad \text{which is}$$

identical to the quadrupole factor of symmetric the hard sphere model with $a = c$.

When $a + c > \sqrt{2}a$, $\theta_1 > \pi/4$,
then four ions tend to form

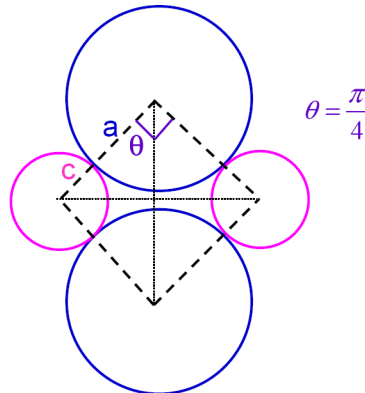


Figure 3.24. The stable quadrupole with weakly asymmetric hard sphere ions (with 0.414

$s < 1$) always has $\theta = \pi/4$, with quadrupole factor identical to the symmetric case.

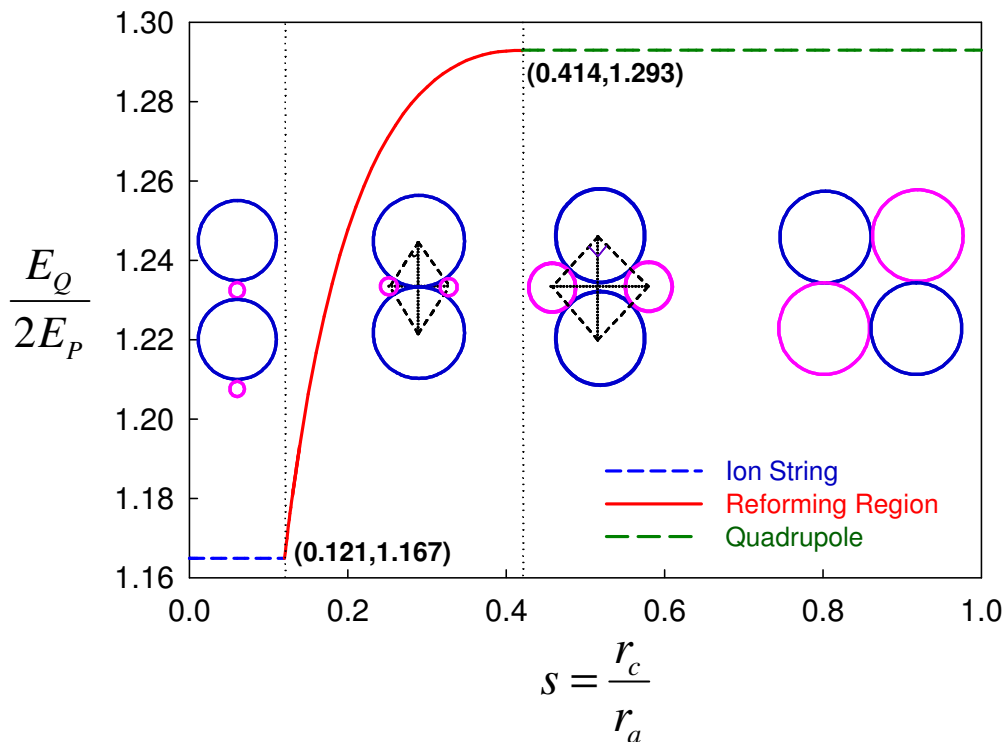


Figure 3.25. Quadrupole factors of asymmetric ions with anion larger than cation at 0 K in vacuum.

For $0.414 < s < 1$, $E_Q / 2E_P$ is identical to the symmetric hard sphere model, for $0.121 < s < 0.414$, contact quadrupoles are the ground state and $E_Q / 2E_P$ is given by [Equation 3.7](#), and for extremely asymmetric quadrupoles with $s < 0.121$, the linear ion chain is the ground state. [Figure 3.25](#) is only half of the story, as with ionic liquids the more common case has $c > a$, and the full story for quadrupole factor of asymmetric hard spheres is shown in [Figure 3.26](#).

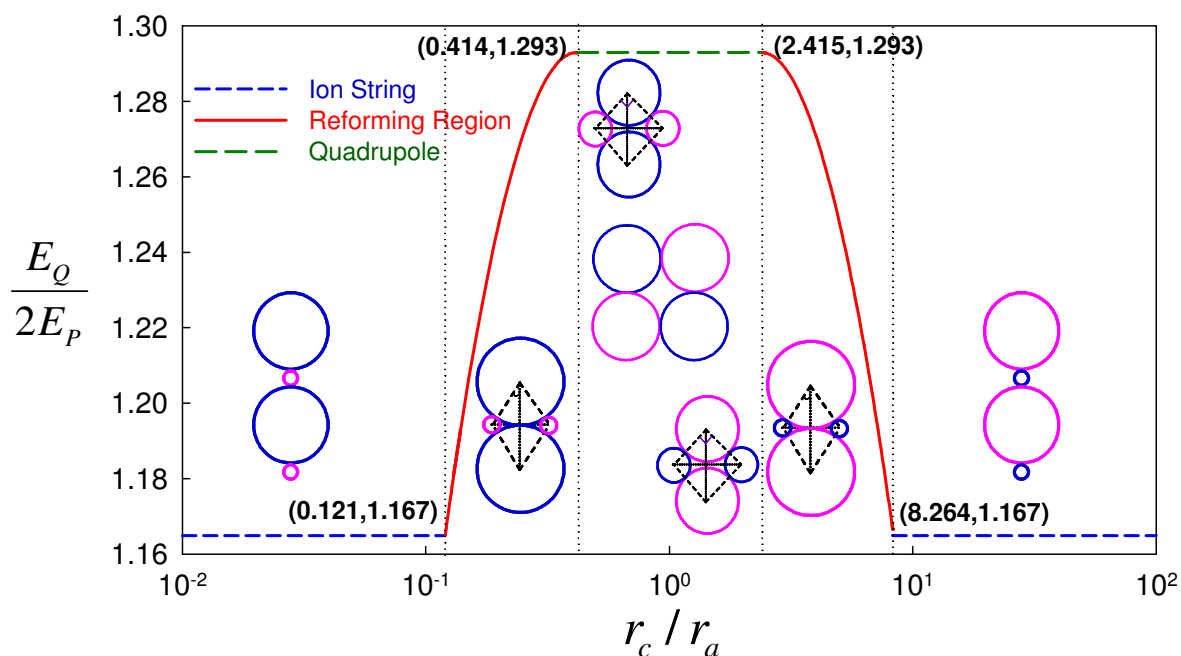


Figure 3.26. Quadrupole factors of asymmetric ions at 0 K in vacuum. For $0.414 < s < 2.415$, $E_Q / 2E_P$ is identical to the symmetric hard sphere model, for $0.121 < s < 0.414$ or for $2.415 < s < 8.264$, contact quadrupoles are the ground state, and for extremely asymmetric quadrupoles with $s < 0.121$ or $s > 8.264$, linear ion chains are the ground state of four ions.

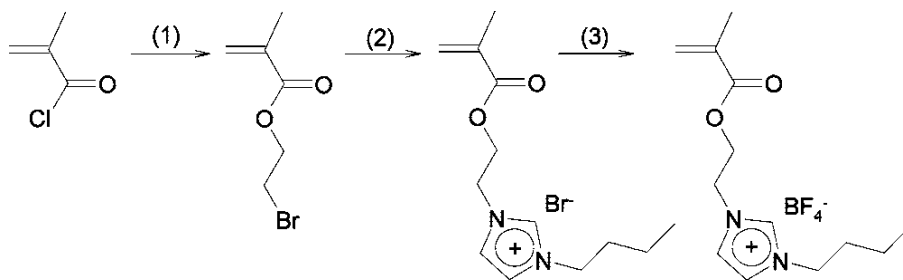
Relative ion size affects the quadrupole/pair equilibrium, gradually favoring more pairs if the size ratio falls below 0.4, where quadrupoles start to destabilize. As the size mismatch is further increased, quadrupoles give way to more and more pairs until a size ratio of 0.06 is reached and the quadrupoles disappear entirely, even at 0 K in vacuum. Consequently, size mismatch in ionic liquids can reduce the fraction of ions forming quadrupoles, thereby lowering T_g and increasing the dielectric constant by forming more isolated ion pairs.

For hard sphere ions, the triple ion factor $\frac{E_{tr-} + E_{tr+}}{3E_{pair}} = 1$, regardless of ion sizes,

because the hard sphere triple ions are all perfectly linear. It is important to point out that real triple ions are often not linear structures and consequently can have sizeable dipole moments, owing to chemical details influencing how ions pack near each other.

3.3.4. Validation of QPT-State Diagram Predictions

In this section, we will put the QPT-State Diagram to the test, demonstrating how the QPT diagram might be useful in practice, based on cationic ionomers made by Dr. Hong Chen, in Prof. Yossef Elabd's group at Drexel [46], with a variety of anionic counterions. The choice of counterion has large impact on the dielectric constant and glass transition temperature of ionomers, which both in turn alter conductivity of these single-ion conductors.



(1) 2-bromoethanol, triethylamine, dichloromethane, room temperature, 16 h

(2) 1-butylimidazole, 40 °C, 24 h

(3) NaBF₄, acetonitrile, room temperature, 48 h

Scheme 3.2. Synthesis of Polymerizable Ionic Liquid MEBIm-BF₄

Hong Chen firstly made 1-[2-methacryloyloxy)ethyl]-3-butylimidazolium bromide (MEBIm-Br) by quaternizing 1-butylimidazole with 2-bromoethyl methacrylate (**Scheme 3.2.**), and then exchanged Br⁻ into BF₄⁻ (tetrafluoroborate) to produce the desired

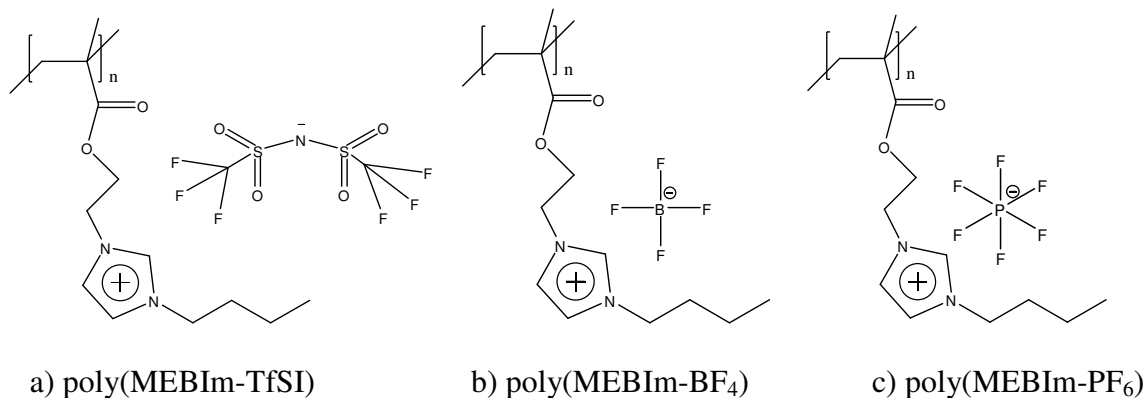
imidazolium tetrafluoroborate monomer. Halide residue in the final product was dialyzed away by extensive diafiltration with de-ionized water. After the MEBIm-BF₄ monomers were made, she polymerized them by a conventional free-radical polymerization, taken to roughly 15% conversion to keep the molar mass distribution fairly narrow. The product was purified by precipitation (pouring a DMF solution of the ionomer into an excess of cold methanol). The PEO-equivalent weight-average molecular weight determined by GPC in the presence of 0.05 M LiBr in water was $M_w = 382\,000$ with a polydispersity index of $M_w/M_n = 1.27$.

Table 3.5. Ion pair, positive triple ion, negative triple ion, and quadrupole energies and quadrupole factors and triple ion factors of three ionic liquids, representing three ionomers. Dipole moment of the isolated ion pairs are also listed, to be used later.

	E_P (eV)	E_{T+} (eV)	E_{T-} (eV)	E_Q (eV)	$\frac{E_{quad}}{2E_{pair}}$	$\frac{E_{tr-} + E_{tr+}}{3E_{pair}}$	m_{pair} (Debye)
[MEBIm] ⁺ [TFSI] ⁻	3.210	4.275	4.298	7.051	1.098	0.890	14.06
[MEBIm] ⁺ [BF ₄] ⁻	3.566	4.900	4.748	8.097	1.135	0.902	13.02
[MEBIm] ⁺ [PF ₆] ⁻	3.321	4.324	4.564	7.589	1.143	0.892	15.13

Based on poly(MEBIm-BF₄), two more ionomers were made by anion-exchange: poly[1-[2-methacryloyloxy]ethyl]-3-butyl-imidazolium trifluoromethanesulfonyl] (poly(MEBIm-TFSI), and poly[1-[2-methacryloyloxy]ethyl]-3-butyl-imidazolium hexafluorophosphate] (poly(MEBIm-PF₆)). Their structures are depicted in **Scheme 3.3**. Therefore, this series of ionomers are identical in structure, molecular weight, side chain and cation, but with markedly different anionic counterions. Surprisingly, their physical properties,

such as T_g , dielectric constant, conducting ion concentration, etc., are quite different. Using the $[\text{MEBIm}]^+$ monomer to represent the cation of the ionomer, energies for of ion pairs, positive and negative triple ions, and quadrupoles calculated by *ab initio* methods are listed in **Table 3.5**.



Scheme 3.3. Structures of Polymerized Ionic Liquid Poly(MEBIm)

The data in **Table 3.5** are imported into a QPT-State Diagram in **Figure 3.27**. As discussed above, higher quadrupole factor suggests that the ionomer should have higher T_g and lower dielectric constant, because it should have more quadrupoles (and possibly other ion aggregates) and lower ion pair concentration. Also, the 1% higher triple ion factor drops a hint that there might be a slightly higher conducting ion concentration for poly(MEBIm-BF₄). From the relative positions of the three points, we predict the orders of some macroscopic physical properties of the three ionomers, only using their anion for abbreviation:

- 1) Glass transition temperature: T_g $\text{PF}_6^- \cong \text{BF}_4^- > \text{TfSI}^-$
- 2) Dielectric constant: ϵ_s $\text{TfSI}^- > \text{BF}_4^- \cong \text{PF}_6^-$
- 3) Fraction of ion pairs: f_{pair} $\text{TfSI}^- > \text{BF}_4^- \cong \text{PF}_6^-$

4) Fraction of conducting ions: $f_{cond} \text{ BF}_4^- > \text{TfSI}^- \approx \text{PF}_6^-$

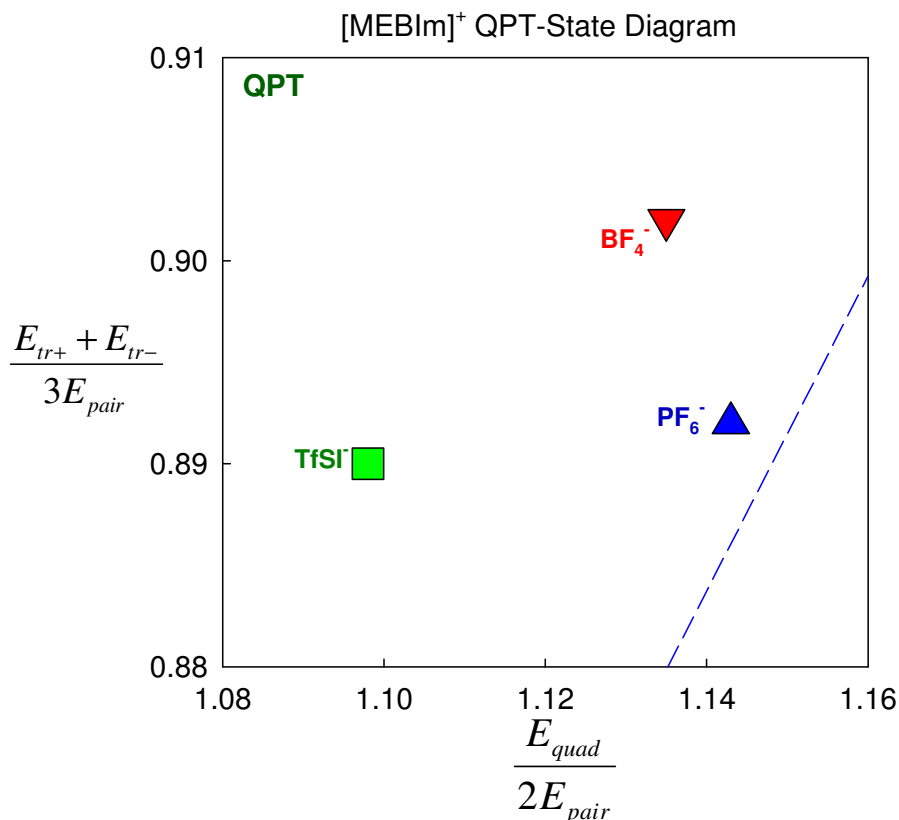


Figure 3.27. QPT-State Diagram of $[\text{MEBIm}]^+ [\text{TfSI}]^-$, $[\text{MEBIm}]^+ [\text{BF}_4]^-$, $[\text{MEBIm}]^+ [\text{PF}_6]^-$, representing poly(MEBIm-TfSI), poly(MEBIm-BF₄) and poly(MEBIm-PF₆).

The calorimetric glass transition temperature T_g was measured by SSC/5200 from Seiko Instruments. Poly(MEBIm-TfSI) has the lowest $T_g = -12^\circ\text{C}$, while the T_g of (poly(MEBIm-BF₄)) is 83°C higher, $= 71^\circ\text{C}$, and T_g of (poly(MEBIm- PF₆)) is even higher, $= 94^\circ\text{C}$. Apparently, the 1st prediction is true.

In **Chapter 1**, we introduced the dielectric spectroscopy methods to determine conducting ion content and mobility and ion pair content in ionomers, directly assessing the extent of ion pair and quadrupole formation. These methods were recently developed

by Prof. Runt and Prof. Colby's groups at Penn State University [8-10], based on the 1953 Macdonald electrode polarization model [11] and the 1936 Onsager Equation [12]. Dielectric (impedance) spectra are measured by U Hyeok Choi in Prof. Colby's group at Penn State University, using a Novocontrol GmbH Concept 40 broadband dielectric spectrometer in the frequency range of 10^{-2} ~ 10^7 Hz with 0.1 mV amplitude. Samples are allowed to reach equilibrium with temperature for at least 30 minutes before each measurement.

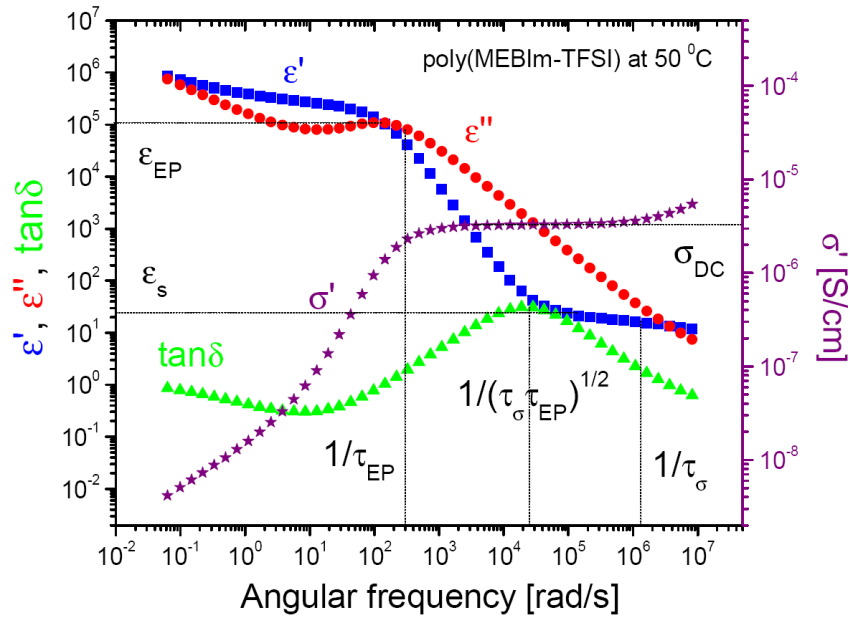


Figure 3.28. Measured dielectric response showing the electrode polarization relaxation via the in-phase dielectric constant ϵ' (blue), the out-of-phase dielectric loss ϵ'' (red), $\tan\delta = \epsilon''/\epsilon'$ (green), and the in-phase part of the conductivity σ' (purple) for poly(MEBIm-TfSI) at 50°C ($T_g + 62$ K), with peak frequencies, dielectric constant after polarization ϵ_{EP} , and static dielectric constant (a material property without electrode polarization) ϵ_s , and d.c. conductivity σ_{DC} denoted. Data of U Hyeok Choi.

Figure 3.28. plotted the electrode polarization relaxation, the phenomenon by which ions buildup at electrodes under low frequency electric fields, in ε' , ε'' , and $\tan\delta$ for poly(MEBIm-TfSI) at 50°C, with peak frequencies, dielectric relaxation strength, and ε_R denoted.

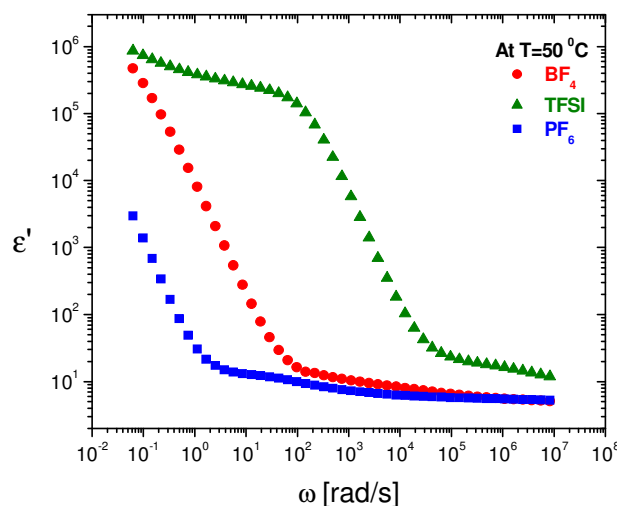


Figure 3.29. The frequency dependence of dielectric constant for poly(MEBIm) at 50 °C with three different anionic counterions (TfSI green > BF₄⁻ red ≥ PF₆⁻ blue). Data of U Hyeok Choi.

The in-phase (real) part of the dielectric constant (ε') increases markedly, from $\varepsilon_s = 25$ to $\varepsilon_{EP} = 10^5$, due to the enormous increase of effective capacitance when a small fraction of the counterions polarize at the electrodes (EP) [12]. Simultaneously, the in-phase part of the conductivity σ' decreases due to the polarized ions lowering the field that the other ions in the sample see. The frequency dependences of the in-phase (real)

part of the dielectric constant of the ionomer with three different counterions (at 50 °C) are plotted in **Figure 3.29**.

Another observation from **Figure 3.29** is that the TfSI-ionomer relaxes the fastest out of the three ionomers at 50 °C, while PF₆-ionomer is the slowest. This is another proof that the T_g of TfSI-ionomer is the lower than BF₄-ionomer than PF₆-ionomer. Note that, the dielectric (impedance) spectra of the neutral counterpart homopolymer poly[1-[2-methacryloyloxy)ethyl]-3-butyl-imidazole] was also measured, whose data were much easier to process, because of the absence of EP. ϵ_s and ϵ_∞ obtained from the measurement will later on be used in **Equation (3.4)** to estimate the pair concentration.

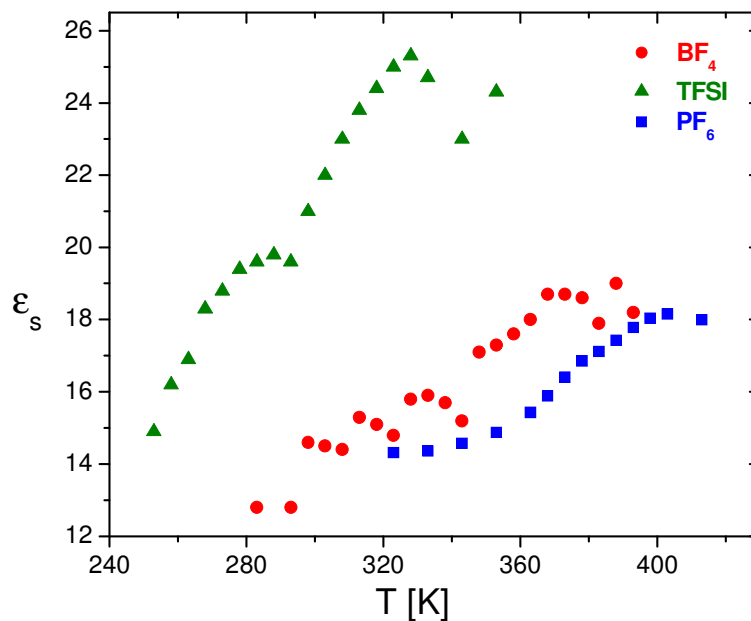


Figure 3.30. Temperature dependence of static dielectric constant ϵ_s of poly(MEBIm) ionomers with three different counterions TfSI⁻ (green) > BF₄⁻ (red) \geq PF₆⁻ (blue). Data of U Hyeok Choi.

The single property that our group is most interested in as a barometer for single ion-conduction is the static dielectric constant ϵ_s , which was obtained from the low-frequency plateau of the dielectric storage spectra after subtracting the (huge) contribution of EP. The temperature dependence of static dielectric constant ϵ_s of three ionomers is plotted in **Figure 3.30**, which clearly shows that dielectric constant ϵ_s increases $\text{TfSI} > \text{BF}_4^- \geq \text{PF}_6^-$, exactly as expected: *the 2nd prediction is proven true*.

Table 3.6. The total ion concentration of the three ionomers calculated from the molecular weight of one repeat unit and the density of the ionomers.

	Formula	M_0 (g·mole ⁻¹)	ρ (g·cm ⁻³)	V_{tot} (cm ⁻³)
$[\text{MEBIm}]^+ [\text{TfSI}]^-$	$\text{C}_{12}\text{H}_{19} \text{N}_2\text{O}_2 \cdot \text{C}_2\text{F}_6\text{NO}_4\text{S}_2$	503	1.38	1.65×10^{21}
$[\text{MEBIm}]^+ [\text{BF}_4]^-$	$\text{C}_{12}\text{H}_{19} \text{N}_2\text{O}_2 \cdot \text{BF}_4$	310	1.12	2.18×10^{21}
$[\text{MEBIm}]^+ [\text{PF}_6]^-$	$\text{C}_{12}\text{H}_{19} \text{N}_2\text{O}_2 \cdot \text{PF}_6$	368	1.21	1.91×10^{21}

Fractions of ion pair and conducting ion are plotted in **Figure 3.31**, which clearly shows fraction of ion pair: $f_{\text{pair}} \text{TfSI} > \text{BF}_4^- \geq \text{PF}_6^-$ but fraction of conducting ion $\text{BF}_4^- \approx \text{TfSI} > \text{PF}_6^-$. The 3rd prediction is proven true and 4th prediction (Conducting ion concentration: $f_{\text{cond}} \text{BF}_4^- > \text{TfSI} \approx \text{PF}_6^-$) inaccurate. We suspect the discrepancy is caused by different total ion number densities and the nanoscale heterogeneity of these three ionomers.

The contributions of the ion pairs and polymer chains to the dielectric constant of the ionomer can be separated utilizing **Equation (3.8)**, based on the Onsager equation [12], assuming quadrupoles are dielectrically inert [10].

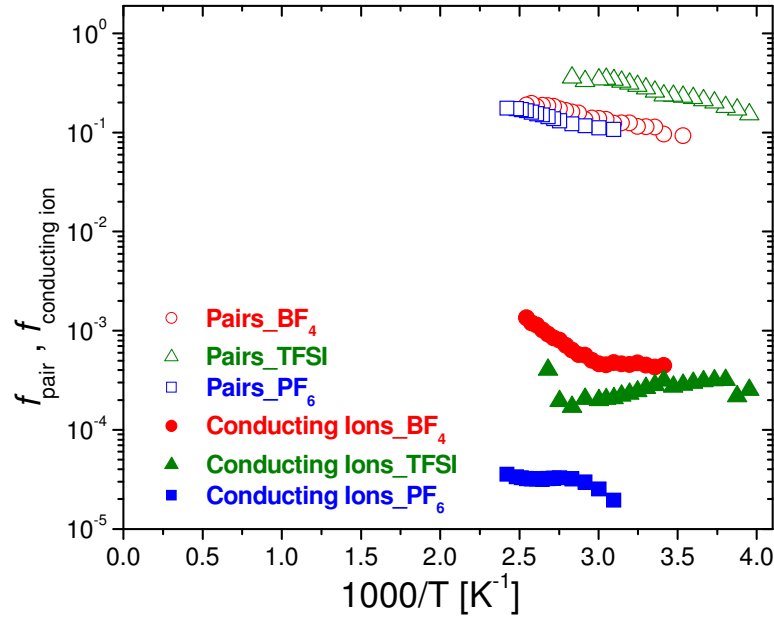


Figure 3.31. Fractions of conducting ions (lower, filled symbols) and ion pairs (upper, open symbols) as a function of inverse temperature for poly(MEBIm) ionomers with three different counterions TFSI[−] (green) > BF₄[−] (red) ≥ PF₆[−] (blue). Data of U Hyeok Choi.

$$\nu_{pair} m_{pair}^2 = 9\epsilon_0 kT \left\{ \frac{(\epsilon_s - \epsilon_\infty)(2\epsilon_s + \epsilon_\infty)}{\epsilon_s (\epsilon_\infty + 2)^2} - \left[\frac{(\epsilon_s - \epsilon_\infty)(2\epsilon_s + \epsilon_\infty)}{\epsilon_s (\epsilon_\infty + 2)^2} \right]_{\text{Neutral Form}} \right\} \quad (3.8)$$

where m_{pair} is dipole moment of corresponding ion pairs calculated from *ab initio* simulation (last column of [Table 3.5](#)) and ν_{pair} is the number density of isolated ion pairs. For the high-frequency limit of the dielectric constant for poly(MEBIm-TFSI), poly(MEBIm-BF₄) and poly(MEBIm-PF₆), we use an approximate value of $\epsilon_\infty = n^2$, where n is the refractive index of the ionomer accordingly, estimated by group

contribution theory [47]. The number density of ion pairs v_{pair} can then be computed from the static dielectric constant ϵ_s , utilizing Equation (3.8). Furthermore, the number density of conducting ions can be separated from mobility in conductivity by the Macdonald EP model [11].

To obtain the fractions of ion pairs and conducting ions, we need to know the total number density of counterions. The total ion concentration was calculated by $\frac{N_A \rho}{M_0}$, where M_0 is the molecular weight of one repeat unit, containing one ion pair, in unit of $\text{g}\cdot\text{mole}^{-1}$. ρ is the density of the ionomer.

In conclusion, even though both dielectric constant and entropy are ignored in our QPT Diagram, predictions of ion state populations agree nicely with estimations from dielectric spectroscopy based on the *1953 Macdonald EP model* and the *1936 Onsager equation*. We can utilize the QPT-State diagram to effectively screen 10^6 possible ion pairs with regular salts and ionic liquids, for those that prefer forming pairs over quadrupoles, as these have low T_g and high dielectric constant. The QPT-State diagram then becomes a powerful tool in the design of ionomers for facile ion transport, and well may have far-reaching consequences in the applications of advanced lithium batteries, actuators and supercapacitors.

3.4. Inspirations from the QPT State Diagram

3.4.1. F⁻ Anion Battery

In recent times, the trend towards “green” cars and power production has

increased the demand for electrical energy storage in devices. Better batteries are necessary to help achieve successful futures for these more environmentally friendly products. While much research recently has involved lithium ion battery technology, an area that is fertile and relatively untouched is that of fluoride ion batteries. Dr. Rachid Yazami at Cal Tech and CF_x Battery [48], who discovered the currently used graphite as the negative electrode material in lithium-ion batteries in 1980, is recently turning his attention to fluoride-ion batteries. Inspired by the specific solvation study in [Chapter 2](#) and QPT-diagram for fluoride ions in [Figure 3.18](#), we think fluoride ion batteries have potential to be a strong candidate for superior battery technology. This argument is based on the reasons listed below:

- 1) Fluoride ion batteries can avoid some of the safety issues that plague lithium ion batteries. During charging, dendrites of lithium can form which can after a few cycles cross the separator and short circuit the battery, resulting in a potential fire hazard and side reactions can occur from metallic lithium which is explosive when in contact with water. Meanwhile fluorides are non-metallic and very stable, and are therefore a safer alternative to lithium batteries.
- 2) It has been shown [49] that a fluoride ion battery is capable of voltages slightly higher than lithium ion batteries (3.5-5.5V vs. 3-5V) and has a maximum theoretical energy density 6.2 times higher (2615Wh/kg vs 420Wh/kg) using CF_x ($x = 0.8$) as cathode and magnesium as anode. These electrodes can be produced relatively cheaply, as rare elements are not necessary like in some lithium ion electrodes.
- 3) We focus on developing the ionomer membrane in lithium batteries to achieve better performance, such as, higher conductivity with high modulus. Derived in [Chapter 1](#),

the power of the battery can be improved by making the membrane more conductive and thinner. **Chapter 2** taught us that the specific solvation by functional groups on the polymer only temporarily helps Li^+ to dissociate, but this solvation energy needs to be overcome when Li^+ eventually leaves the electrolyte separator and enters either electrode. Moreover, this interaction also slows down Li^+ because the motion of the ion is coupled strongly to the segmental motion of the polymer [8-10].

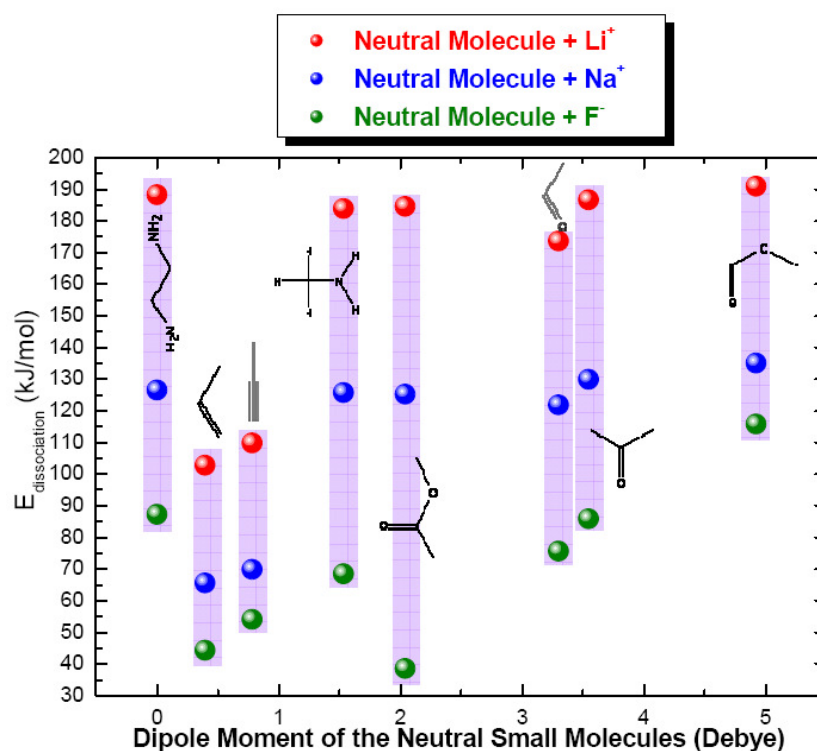


Figure 3.32. The comparison of interaction energies of F^- (green), Li^+ (red) and Na^+ (blue) with various neutral molecules representing polar groups of interest.

The energy barrier at the interface holds up battery charging and reduces the efficiency of the Li battery. Also learned from **Chapter 2**, the specific solvation effect is much weaker on anions (**Figure 2.10**), which means F^- should be able to easily migrate from cathode to anode in a battery system. **Figure 3.32** confirms that the F^- anion is

barely solvated by common polar groups of interest, compared with Li^+ and Na^+ . That observation is common to most polar groups that could be attached to polymers because the negative part of the dipole invariably points outward away from the chain.

- 4) F^- and Li^+ cover the similar territory in QPT-State diagram, but F^- has more counterion choices falling in the PQT region (see [Figure 3.18](#) for F^- and [Figure 3.33](#) for a comparison of F^- with Li^+), remembering that ionomers with lower quadrupole factor should have more ion pairs and have lower T_g and higher ϵ .

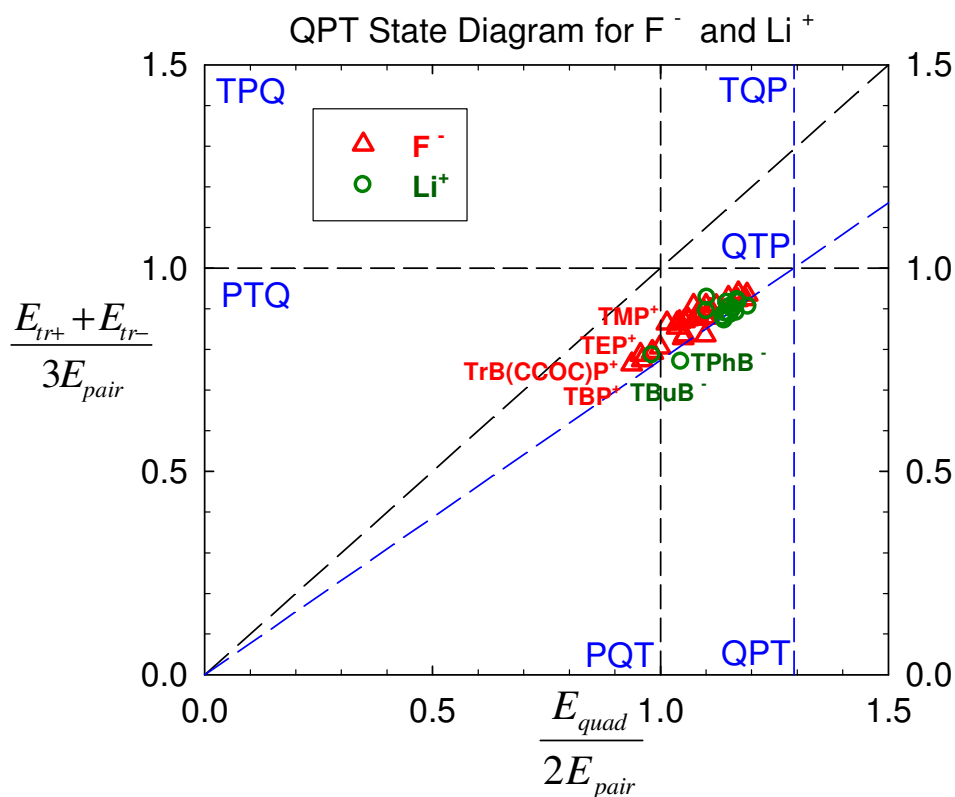


Figure 3.33. Comparison of QPT Diagrams for F^- with Li^+ , each paired with varieties of counterions. Li^+ only has very low quadrupole factor for tetra-substituted borates (tetrabutyl borate and tetraphenyl borate) while F^- has many choices of cation to pair with that have even lower quadrupole factors (mostly phosphonium cations).

We conclude that a variety of phosphoniums may be good choices for the cations attached to the polymer membrane, to transport F^- . It is also very interesting that conduction of OH^- anions may require quite similar phosphonium ionomers, as [Figure 3.34](#) shows that most phosphonium hydroxides also have low quadrupole factors.

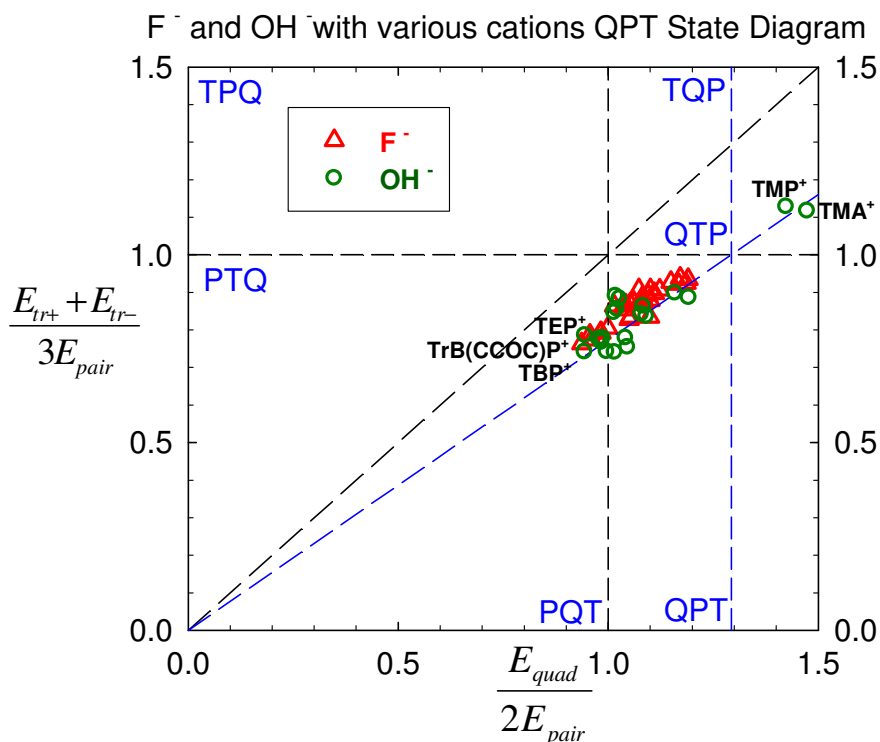


Figure 3.34. Comparison of QPT Diagrams for F^- with OH^- for a wide range of cations.

3.4.2. Li^+ Cation Battery

[Figure 3.35](#) shows that tetrasubstituted borate anions have very low quadrupole factors (near 1.0) with Li^+ and hence might be useful anions to attach to polymers for Li^+ single ion conducting membranes for Li battery separators. Boron is an unusual element, with an empty orbital in neutral molecules. Trisubstituted boranes, such as triphenyl

borane, are neutral molecules but tetrasubstituted borates are anions. **Figure 3.35** compares the QPT Diagrams for Li^+ and Na^+ paired with a variety of anions. Most of these are clustered in the $1.1 < \frac{E_{quad}}{2E_{pair}} < 1.2$ range of quadrupole factor, as discussed above in **Figure 3.33**. TFSI is an exception with Na^+ , and is actually quite close to the hard sphere prediction (although TFSI is nowhere near a hard sphere!). More interesting exceptions are found for $\frac{E_{quad}}{2E_{pair}} < 1.1$, which are all tetrasubstituted borate anions for both Li^+ and Na^+ .

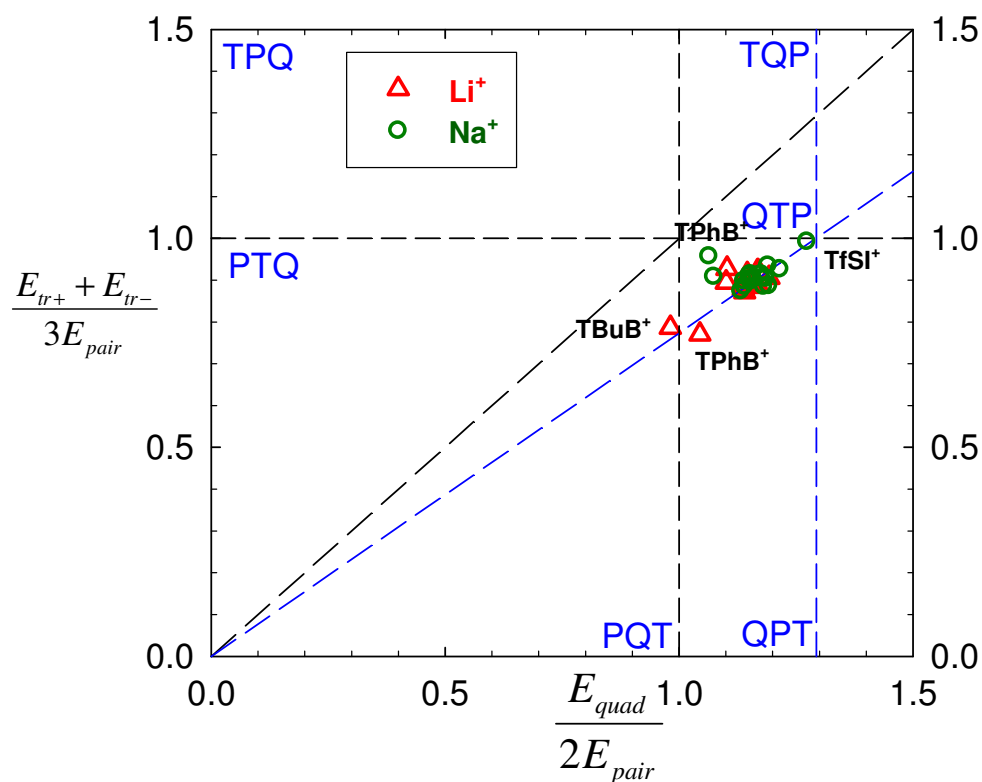


Figure 3.35 R_4B^- ($\text{R} = \text{Et}, \text{Bu}, \text{Ph}, \text{PrFPh}$, etc.). TFSI has high conducting ion concentration.

With Li^+ , the APT charge (determined from the derivative of the dipole moment with respect to distance) on boron is roughly $+0.6e$ in neutral triphenyl borane and anionic tetraphenyl borate (whether free, paired, triple or quadrupole). That means the four phenyl rings of the tetraphenyl borate anion share $-1.6e$ (roughly $-0.4e$ each).

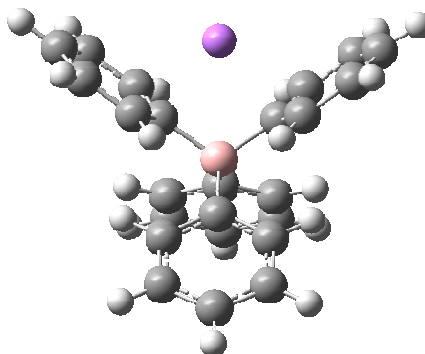


Figure 3.36. The equilibrated ion pair for lithium tetraphenyl borate shows that the Li^+ cation goes between two of the negatively charged benzene rings making it challenging for such ion pairs to form quadrupoles.

We expect that the bulky anion groups (such as tetraphenyl borate) should greatly discourage association of ion pairs, based on the ion pair structure in **Figure 3.36**. Those bulky anions also have considerably lower pairing energy with Li^+ (see **Table 3.7**.) and consequently are expected to have higher fractions of conducting counterions. The small cations actually reside within the pervaded volume of the tetraphenyl borate anion (**Figure 3.36**) but the negative charge is widely distributed, precluding a strong interaction. Moreover, the energy to form a quadrupole from two pairs ($E_{\text{quad}} - 2E_{\text{pair}}$) is nearly zero for tetraphenyl borate with Li^+ and actually negative for perfluorinated tetraphenyl borate with Li^+ , suggesting that these lithium salts should not be expected to associate pairs much at all.

Table 3.7. Comparison of estimated ion pairing energies and the energy gain in forming a quadrupole from two ion pairs, for lithium salts with benzene carboxylate, benzene sulfonate, tetraphenyl borate and perfluorinated tetraphenyl borate anions, in PEO-based ionomers at 300K.

Anion	Pairing Energy with Li ⁺	Quadrupole Energy from Pairs
Benzene carboxylate	13.4 kJ/mol	3.7 kJ/mol
Benzene sulfonate	12.3 kJ/mol	7.5 kJ/mol
Tetraphenyl borate	10.7 kJ/mol	0.3 kJ/mol
F-tetraphenyl borate	8.6 kJ/mol	< 0

3.5. Summary

1. Although free energies leverage ion species' population distributions, both dielectric constant and entropy are ignored in our calculation in this chapter, which presumably affect all ion equilibria in similar ways for different pairs of ions, so rankings of different ion combinations are preserved.
2. With Ionic Liquids, there are 10^6 possible ion pairs and we are using *ab initio* to screen for those that prefer forming pairs over quadrupoles, as these are expected to have lower T_g and higher dielectric constant.
3. Size mismatch in ionic liquids can reduce the fraction of ions forming quadrupoles, thereby lowering T_g and increasing the dielectric constant by forming more isolated ion pairs. Because as the size mismatch is further increased, quadrupoles give way to more and more pairs until a size ratio of 0.06 is reached and the quadrupoles disappear entirely, even at 0 K in vacuum. Consequently, size mismatch in ionic liquids can reduce the fraction of ions forming quadrupoles,

thereby lowering T_g and increasing the dielectric constant by forming more isolated ion pairs.

4. Borates are good for Li^+ , with several having quad factor < 1 .
5. Phosphoniums are good for F^- , with several having quad factor < 1 .
6. Larger ions with more delocalized electrons are better for allowing more pairs which lowers T_g and increases dielectric constant.
7. Hard sphere model predicts quad factor and triple ion factor that are larger than real ions, and small ions paired with large ions with delocalized electrons have the lowest quad factors and triple ion factors, with quadrupole factors even smaller than unity (favoring ion pairs) for several phosphoniums paired with F^- and several borates paired with Li^+ .

References

- [1] K.E. Thomas, S.E. Sloop, J.B. Kerr and J. Newman, *J. Power Sources* **89**, 132 (2000).
- [2] P.V. Wright, *MRS Bull.* **27**, 597 (2002).
- [3] J.B. Kerr, In *Lithium Batteries Science and Technology*; G.-A.Nazri, G. Pistoia, Eds.; Kluwer Academic: Boston, MA, 2004; Chapter 19.
- [4] M.D. Bennett and D.J. Leo, *Sensors Actuat. A-Phys.* **115**, 79 (2004).
- [5] M.D. Bennett, D.J. Leo, G.L. Wilkes, F.L. Beyer and T.W. Pechar, *Polymer* **47**, 6782 (2006).
- [6] K.I. Winey, J.H. Laurer and B.P. Kirkmeyer, *Macromolecules* **33**, 507 (2000).
- [7] B.P. Kirkmeyer, A. Taubert, J.-S. Kim, and K.I. Winey, *Macromolecules* **35**, 2648 (2002).
- [8] R.J. Klein, S. Zhang, S. Dou, B.H. Jones, R.H. Colby, and J. Runt, *J. Chem. Phys.* **124**, 144903 (2006).
- [9] D. Fragiadakis, S. Dou, R.H. Colby, and J. Runt, *Macromolecules* **41**, 5723 (2008).
- [10] D. Fragiadakis, S. Dou, R.H. Colby, and J. Runt, *J. Chem. Phys.* **130**, 064907 (2009).
- [11] J.R. Macdonald, *Phys. Rev.* **92**, 4 (1953).
- [12] L. Onsager, *J. Am. Chem. Soc.* **58**, 1486 (1936):.
- [13] S. Dou, S. Zhang, R.J. Klein, J. Runt and R.H. Colby, *Chem. Mater.* **18**, 4288 (2006).
- [14] A. Eisenberg and J.-S. Kim, *Introduction to Ionomers*; Wiley: New York, 1998.
- [15] W. Wang, G.T. Tudryn, R.H. Colby and K.I. Winey, *J. Am. Chem. Soc.* **133**, 10826 (2011).

- [16] M. J. Frisch, et al. GAUSSIAN 03, Revision B.05; Gaussian Inc.: Pittsburgh, PA, 2003.
- [17] A.D. Becke, J. Chem. Phys. **98**, (2), 1372 (1993).
- [18] A.D. Becke, Phys. Rev. A **38**, (6), 3098 (1988).
- [19] C.T. Lee, W.T. Yang and R.G. Parr, Phys. Rev. B **37**, (2), 785(1988).
- [20] P.J. Stephens, F.J. Devlin, C.F. Chabalowski and M.J. Frisch, J. Phys. Chem. **98**, (45), 11623 (1994).
- [21] A. Eisenberg and J.-S. Kim, Introduction to Ionomers, Wiley (1998).
- [22] D.J. Yarusso and S.L. Cooper, Polymer **26**, 372 (1985).
- [23] A.R. Khokhlov, K.B. Zeldovich and E.Y. Kramarenko, Counterions in polyelectrolytes, in Electrostatic Effects in Soft Matter and Biophysics (C. Holm, Editor) Kluwer (2001).
- [24] E.Y. Kramarenko, I.Y. Erukhimovich and A.R. Khokhlov, Macromol. Theory Simul. **11**, 462 (2002).
- [25] M. Goswami, S.K. Kumar, A. Bhattacharya and J.F. Douglass, Macromolecules, **40** (12), 4113–4118 (2007).
- [26] W.F. Edmonds, Z. Li, M.A. Hillmyer and T.P. Lodge, Macromolecules **39**, 4526 (2006).
- [27] T.D. Gierke, G.E. Munn and F.C. Wilson, J. Polym. Sci., Polym. Phys. **19**, 1687 (1981).
- [28] R.M. Fuoss and C. A. Kraus, J. Am. Chem. Soc. **55**, 2387 (1933).
- [29] H. Weingartner, V.C. Weiss and W. Schroer, J. Chem. Phys. **113**, 762 (2000).

- [30] J. Barthel, H. Krienke, R. Neueder and M.F. Holovko, *Fluid Phase Equilib.* **107**, 194 (2002).
- [31] M. Hojo, *Pure and Appl. Chem.* **80**, 1539 (2008).
- [32] S. Petrucci, M.C. Masiker and E.M. Eyring, *J. Solut. Chem.* **37**, 1031 (2008).
- [33] J.M.G. Barthel, H. Krienk and W. Kunze. Physical chemistry of electrolyte solutions : modern aspects. New York, Springer, (1998).
- [34] H.S. Shiau, W. Liu, R. H. Colby, and M.J. Janik, *J. Chem. Phys.* **139**, 204905 (2013).
- [35] J.M.G. Cowie, A.C.S. Martin, A.M. Firth, *Brit. Polym. J.*, **20** 247 (1988).
- [36] Y. Marcus, *J. Solut. Chem.*, **16** 735 (1987).
- [37] Y. Marcus, *J Phys Chem B*, **111**, 572 (2007).
- [38] S.J. Paddison, K D. Kreuer and J. Maier, *Phys. Chem. Chem. Phys.* **8**, 4530 (2006).
- [39] S. Schantz, *J. Chem. Phys.* **94**, 6296 (1991).
- [40] C. Guha, J.M. Chakraborty, S. Karanjai and B. Das, *J. Phys. Chem. B* **107**, 12814 (2003).
- [41] Z. Wang and M. Rubinstein, *Macromolecules* **39**, 5897 (2006).
- [42] F. Oosawa, *J. Polym. Sci.* **23**, 421 (1957).
- [43] G. S. Manning, *J. Chem. Phys.* **51**, 924 (1969).
- [44] F. Oosawa Polyelectrolytes. New York, M. Dekker (1971).
- [45] M.G. Benavides-Garcia, M. Monroe, *Chem. Phys. Lett.* **479**, 238 (2009).
- [46] H. Chen and Y. A. Elabd, *Macromolecules*, **42**, 3368 (2009).
- [47] D.W. Vankrevelen, P.J. Hoftyer, *Properties of Polymers*, Oxford (1976).
- [48] Y. Rachid and H. André, US Patent No. 7,563,542 B2.

[49] I. Darolles, C.M. Weiss, M.M. Alam, A. Tiruvannamalai and S.C. Jones, US Patent No. 20120164541 A1.

The Applications of Four State Model in Rational Ionomer Design and Understanding the Dynamics and Ion Conduction Mechanism in Ionomers

In [Chapter 3](#) dielectric constant and entropy are ignored in the four-state model and QPT-state diagram. These presumably affect all ion equilibria for different pairs of ions. In [Chapter 4](#), we will introduce a model to estimate the population distribution of lithium cations among the four states by applying Boltzmann statistics to the relative energies. In our 2012 paper [\[1\]](#), the cluster-continuum solvation model (CCM) that includes specific solvation in the first shell surrounding the cation, all surrounded by a polarizable continuum was used to determine the relative energies of these four states at real temperature and dielectric constant to predict their relative concentrations in an equilibrium ion-ionomer system. In [Chapter 4](#), three practical applications of *ab initio* calculations in rational ionomer design and understanding the dynamics and ion conduction mechanism in ionomers will be discussed.

4.1. Background of Four State Model

Were one to capture a snap-shot of the position of atoms in an ionomer system, a wide array of local environments would be observed about the Li^+ ions. For our purposes, we seek to discretize these into model states that can be used to evaluate the propensity

for Li^+ ions to exist detached from other ions, in anion-cation pairs, or in larger aggregated states. We are interested in ion interactions in a polar-solvating environment, which leads to few large ion aggregates. Four model states of the Li-anion systems were considered to represent the various states that the ions may reside within the ionomer system. Using Li^+ ions in an ionomer with benzene sulfonate anionic groups as an example, the equilibrium ion states to be considered within the four-state model are depicted in [Figure 4.1](#).

In the melt state (above the glass transition temperature), nearly all counterions of ionomers are condensed onto the chains to form ion pairs due to strong electrostatic forces. (a) A "quadrupole" state containing two interacting $\text{Li}^+\text{-A}^-$ pairs was used to examine the tendency of the ion pairs to associate. A "quadrupole" state is the simplest form of ion aggregate. Larger ion aggregates are neglected here to simplify calculations due to the assumption of large dielectric polarization offered by the polar medium. Consequently we consider the quadrupole as the ground state of our model; (b) A paired $\text{Li}^+\text{-A}^-$ state includes a direct bonding interaction between the two ions; (c) A triple ion coordination ($\text{Li}^+\text{A}^-\text{Li}^+$ and $\text{A}^-\text{Li}^+\text{A}^-$) are likely to exist in polymer electrolytes [\[2-6\]](#). The electrostatic attractions between ion pairs ($\text{Li}^+\text{-A}^-$) and free Li^+ ions are strong enough to form positive triple ions ($\text{Li}^+\text{A}^-\text{Li}^+$), which we consider as a second conducting species, since states involving a single anion can move by segmental motion of the polymer. Positive triple ions may exchange their extra Li^+ ion when they meet an isolated ion pair, transporting Li^+ ions [\[7\]](#); and (d) the separated ions are coordinated with neutral, polar

ionomer side-chain or backbone groups. These four states are all solvated by the ionomer with dielectric constant ϵ .

The relative energies of these four ion states are considered to evaluate the propensity of cations to pair with anions, cluster in ion aggregates, or remain in a locally charged single cation or cation-anion-cation state. Negative triple ions cannot conduct because the two anions are attached to the polymer and effectively crosslinked by Li^+ and hence unable to move by polymer segmental motion. In contrast, isolated anions can move by segmental motion to receive a Li^+ , thereby playing a role in conduction.

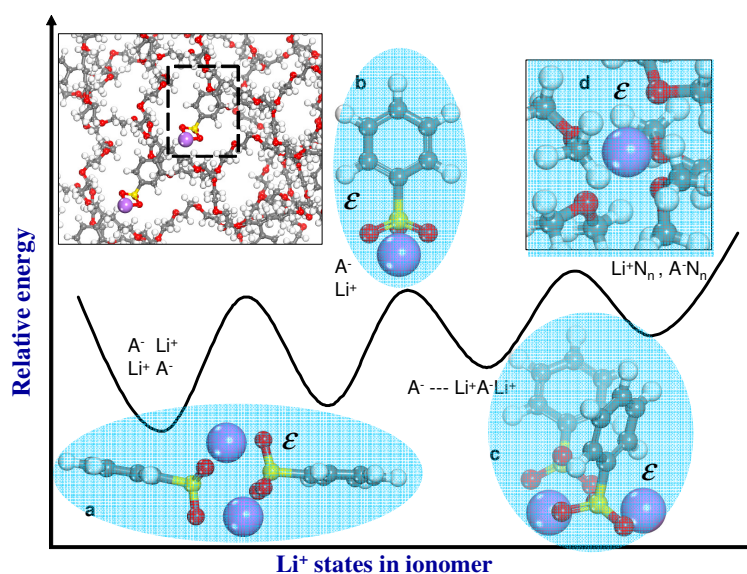


Figure 4.1. Schematics of the relative energies of possible coordination states of Li^+ ions in an ionomer with benzene sulfonate anionic groups (inset). (a) a quadrupole coordination with two Li^+ cations shared between two anionic groups, (b) an ion pair coordination, (c) a triple ion coordination, and (d) the separated ions are coordinated with neutral, polar ionomer side-chain or backbone groups. These four states are all solvated by the ionomer with the dielectric constant ϵ .

In **Chapter 2**, we studied the solvent effect by *ab initio* calculations with the polarizable continuum model (PCM), for 6 ion pairs in 22 solvents. Ion pairing energy correlates nicely with the reciprocal of dielectric constant of the medium following Coulomb's law, $\Delta E_{pair} = \frac{q^2}{\epsilon d}$ in **Figure 2.6**.

The specific solvation effect was studied in **Chapter 2**. **Figure 2.8** shows the cumulative specific solvation energy of Li^+ , Na^+ , benzene sulfonate, triflate and their four ion pairs as a function of the number of dimethylether (DME, a PEO model) molecules interacting. The pairs are weakly solvated by DME molecules, because of their electroneutrality. We expect the same for the charge neutralized quadrupoles. Specific solvation energies on triple ions should be stronger, just like on the four single ions in **Figure 2.8**. The previous studies [8-11] suggested the conducting ion concentration in sulfonated phthalate polyesters based on PEO is vanishingly low. Essentially we won't consider this state, and focus on the dominant conducting ion species, the triple ion.

A four-state model, including a free Li cation, Li^+ -anion pair, triple ions and quadrupole was used to represent the states of Li^+ within the ionomer. Equation 4.1 details the relationship between the quadrupole binding energy (ΔE_{quad}) and the reference state of two isolated anions (E_{anion}) and two isolated Li^+ ions in the gas phase:

$$\Delta E_{quad}^g = 2 E_{anion}^g + 2 E_{Li}^g - E_{quad}^g. \quad (4.1)$$

Equation 4.2 – 4.4 are used to calculate formation energies of the other states:

$$\Delta E_{pair}^g = E_{anion}^g + E_{Li}^g - E_{pair}^g, \quad (4.2)$$

$$\Delta E_{triple+}^g = E_{anion}^g + 2E_{Li}^g - E_{triple+}^g, \quad (4.3)$$

$$\Delta E_{triple-}^g = 2E_{anion}^g + E_{Li}^g - E_{triple-}^g. \quad (4.4)$$

Each ΔE_{state}^g is positive, denoting that coordination lowers the energy relative to the isolated ions. These binding energies can be used to represent the extent of ion associations. For example, subtraction of ΔE_{quad}^g from $2\Delta E_{pair}^g$ represents the “reaction energy” for the quadrupole formation reaction from two pairs (AC+AC→ACAC, where A is an anion and C is a cation).

Entropy difference estimates are needed for populations to better match the true ionomer system. The total entropy change is considered to consist of four contributions: translational, rotational, electrostatic and solvent immobilization entropies. Marcus has proposed an expression for the total entropy change on ion association in solutions [12,13]. Similar method has been applied in our publication in Journal of Chemical Physics [1], where we estimate the entropy for our Li-benzene sulfonate system, dominated by four contributions: translational, rotational, electrostatic and solvent immobilization entropies.

The binding energies of the four ion states are considered to evaluate the propensity of Li^+ to pair with anions, cluster in ion aggregates, or remain in a locally charged single Li^+ or Li^+ -anion- Li^+ state. For comparison among anions, we estimate the population distribution of Li ions among different states by applying Boltzmann statistics to binding energies. The binding energies, together with proper stoichiometric relationships, are used to calculate the relative energies between the various ion states.

Equation 4.5 defines the nomenclature. Boltzmann factors determine equilibrium constants (**Equations 4.6-4.9**) and together with a charge balance (**Equation 4.10**) and a mass balance (**Equation 4.11**) the equilibrium distribution of ions among the four states can be determined. This initial analysis directly uses the binding energies in place of standard state free energy differences.

$$[ACAC]=q \quad [AC]=p \quad [ACA]=t_2 \quad [CAC]=t_1 \quad [A]=f_1 \quad [C]=f_2 \quad (4.5)$$

$$AC \rightarrow A + C \quad \frac{f_1 f_2}{p} = \exp\left(\frac{-\Delta E_{pair}^{CCM}}{RT}\right) \quad (4.6)$$

$$ACAC \rightarrow AC + AC \quad \frac{p^2}{q} = \exp\left(\frac{2\Delta E_{pair}^{CCM} - \Delta E_{quad}^{CCM}}{RT}\right) \quad (4.7)$$

$$ACAC \rightarrow CAC + A \quad \frac{t_1 f_1}{q} = \exp\left(\frac{\Delta E_{tr+}^{CCM} - \Delta E_{quad}^{CCM}}{RT}\right) \quad (4.8)$$

$$ACAC \rightarrow ACA + C \quad \frac{t_2 f_2}{q} = \exp\left(\frac{\Delta E_{tr-}^{CCM} - \Delta E_{quad}^{CCM}}{RT}\right) \quad (4.9)$$

$$\text{Charge balance: } t_1 + f_2 = t_2 + f_1 \quad (4.10)$$

$$\text{Cation mass conservation: } 2q + 2t_1 + t_2 + f_2 + p = 1 \quad (4.11)$$

Entropy differences among states are needed for the population to better match the true ionomer system. In our other paper [1], we first present a model for populations that ignores entropy differences (section A) followed by a model that includes some entropy approximations (section B). Predicted concentrations of Li⁺-conducting states (free Li⁺

and positive triple ions) are compared among a series of anions to indicate favorable features for selection of an optimal Li^+ -conducting ionomer (section C).

The Boltzmann distribution of Li ions in various states is a function of the ratio of a purely Coulombic pair energy and thermal energy, which is independent of temperature. Approximating the pair energy as purely Coulombic, we can define an effective ion separation distance in the pair, σ , such that

$$\Delta E_{pair}^{Coulombic} = \frac{e^2 N_{Av}}{4\pi\epsilon_0 \epsilon \sigma}, \quad (4.12)$$

where e is the elementary charge and Avogadro's number appears in the numerator if the pair energy is given on a molar basis. We further note that by the definition of the Bjerrum length

$$\frac{\Delta E_{pair}^{Coulombic}}{RT} = \frac{l_B}{\sigma}, \quad (4.13)$$

the dimensionless energy of pair interaction (normalized by RT) is simply l_B / σ . Equation (4.12) suggests that we can scale interaction energies with the reciprocal dielectric constant. In polar solvents, the dielectric constant scales approximately as $1/T$ [14]. Equation (4.12) would then suggest that a purely Coulombic pair energy scales linearly with T , making the RT -normalized pair energy (Equation (4.13)) independent of T . The dimensionless pair interaction energy may only be changed by choosing a different anion (altering σ) or a different polar medium with different ϵ . Therefore, ion populations determined as a function of $\Delta E_{pair}^{Coulombic} / RT$ (or equivalently, l_B / σ) are better thought of as giving population variations dependent on the strength of ion pairing.

In our paper [1], the population of ion states is reported as a function of Bjerrum length divided by ion-pair separation with/without entropy considered to investigate the transition between states. Predicted concentrations of Li^+ -conducting states (free Li^+ and positive triple ions) are compared among a series of anions to indicate favorable features for design of an optimal Li^+ -conducting ionomer; the perfluorotetraphenylborate anion maximizes the conducting positive triple ion population among the series of anions considered.

In the next three sections, we will present examples of how the expectations from *ab initio* calculations are consistent with our experimental results, to convince the readers that quantum chemistry calculations can be utilized to design single-ion conductors to transport ions.

4.2. Lithium Ion Conduction of Polysiloxane Single-Ion Conductors Containing Novel Weak-Binding Borates [15]

Polymer electrolytes are of great interest as energy materials in energy storage and conversion devices, such as lithium ion batteries, fuel cells, solar cells, supercapacitors, and actuators. Salt-in-polymer systems have been extensively studied using various polymeric matrixes and salts.[16-18] Single-ion conductors that have anions covalently bonded to polymers are generally accepted to have advantages over polymer/salt mixtures for application in lithium-ion batteries: unity transference number and the absence of detrimental anion polarization. [19,20] Unfortunately, low conductivity of current single-ion conductors hinders their practical application. Herein

we take a fresh approach to solve this problem: Use quantum chemistry calculations of ion interaction energies to guide rational single-ion conductor design.

Polysiloxane-based ionomers are promising polymer electrolyte candidates, owing to their highly flexible backbone imparting low glass transition temperature (T_g). Nagaoka et al. [21] introduced dimethyl siloxane groups into a predominantly poly(ethylene oxide) (PEO) backbone via polycondensation. The highest conductivity observed was 1.5×10^{-4} S/cm for a polymer/salt system at 25 °C with T_g near -80 °C. Different complex systems of alkali metal salts and polysiloxane-based ionomers were explored afterward. Inspired by Walden's rule that electrolyte conductivity is inversely proportional to viscosity, [22] West and coworkers [23] developed a series of low viscosity polymers based on polysiloxane oligomers and PEO oligomers (typically 2 to 7 repeat units). After mixing with salt, the highest conductivities of the mixtures, of order 3×10^{-3} S/cm, are high enough for practical application. [17,20] To prepare polysiloxane-based single-ion conductors, novel anions such as di-*t*-butyl phenolate, naphtholate, hexafluoropropanolate, [24] $\text{CF}_3\text{SO}_2\text{N}^-\text{CH}_2\text{CH}_2$, [25] and $\text{CH}_2\text{CH}_2\text{CF}_2\text{CF}_2\text{OCF}_2\text{CF}_2\text{SO}_3^-$ [26] anions have been fastened to polysiloxane backbones. The conductivities of those single-ion conductors are still of order 10^{-5} S/cm at 25 °C, 10 times lower than the minimum practical requirement for single-ion conductors. [27] Fujinami et al. [28] synthesized single-ion conductors based on siloxyaluminate, having conductivity as high as 10^{-4} S/cm at 25 °C, with $T_g = -53$ °C. This is the highest ionic conductivity reported for a single-ion solvent-free conductor that is a free-standing film and is considered the benchmark. Like aluminum, boron has much lower electronegativity than sulfur or

nitrogen. As a result, borate anions are more inclined to delocalize charge. Different borate salts have been studied as key components of polymer electrolytes, for example, lithium bis(oxalato)borate, [29] tetraphenyl borate, [30-32] tetrabutyl borate, [31] and other borates with novel structures. [33] Of particular interest is tetraphenyl borate (LiBPh_4). LiBPh_4 had been extensively studied as an electrolyte in 1965 by Bhattacharyya and co-workers. [34] Later, Klemann et al. [35] proposed its application in batteries with alkali metal anodes. According to the hard-soft acid-base principles suggested by Pearson, [36] Li^+ is one of the hardest cations and BPh_4^- is one of the softest anions. [37] The ion dissociation energy of LiBPh_4 is similar to that of $\text{LiN}(\text{SO}_2\text{CF}_3)_2$ as shown by our *ab initio* calculations, [38] and much lower than that of LiClO_4 , [39] which can be attributed to the four benzene rings around boron greatly delocalizing the negative charge. Besner et al. [30] compared BPh_4^- and $\text{N}(\text{SO}_2\text{CF}_3)_2^-$, and their results demonstrated that BPh_4^- has greater polarizability, resulting in low ion-dipole stabilization energy. The lattice energies of tetraphenyl borate salts are relatively low, and they have little tendency to form contact pairs. In addition, the extreme size difference between anion and lithium cation discussed in Chapter 3 makes the simplest ion aggregate (the quadrupole; two ion pairs antiparallel to each other) difficult to form. Replacing the H atoms of BPh_4^- with F atoms is predicted to soften the interactions with Li^+ , lower the ion pair energy by 20% and positive triple ion energy by 40%, as summarized in Table 4.1. Kida et al. [40] explored $\text{LiB}(\text{C}_6\text{F}_5)_4$ as the electrolyte in a secondary lithium battery and found the battery they prepared exhibits superior charge-discharge cycle performance, especially at elevated temperature, compared to

batteries containing conventional lithium salts such as LiPF_6 and LiBF_4 . This was attributed to the absence of weak B–F or P–F bonds in $\text{LiB}(\text{C}_6\text{F}_5)_4$. Moreover, the primary decomposition products of $\text{LiB}(\text{C}_6\text{H}_5)_4$ are benzene and phenol. [41] So $\text{LiB}(\text{C}_6\text{F}_5)_4$ might generate $\text{C}_6\text{F}_5\text{H}$ and $\text{C}_6\text{F}_5\text{OH}$ which are far less corrosive than the HF produced on decomposition of either PF_6 or BF_4 .

Many single-ion conductors of Li^+ in the literature are based on a polymer that is primarily PEO [7,9-11,24–26,42] and since the dielectric constant of PEO $\epsilon_{\text{PEO}} = 7$ at 300 K, two columns of Table 4.1 estimate the ion pair energy and positive triple ion energy in such PEO-ionomers by dividing the 0 K/vacuum energies by $\epsilon_{\text{PEO}} = 7$ (since ϵ is in the denominator of the Coulomb energy). While reasonably polar for a polymer, this dielectric constant is too small for construction of a good single-ion conductor. Cyclic carbonates have higher dielectric constant; [43] ethylene carbonate $\epsilon_{\text{EC}} = 90$ at 40 °C and propylene carbonate $\epsilon_{\text{PC}} = 65$ at 25 °C. Both are fine examples of the classical $1/T$ Onsager temperature dependence of dielectric constant of polar liquids, with magnitudes well-anticipated by the dipoles calculated at 0 K in *ab initio* (Figure 4.2). Siloxane polymers with highly polar cyclic [(allyloxy) methyl] ethylene ester carbonic acid (CECA) side chains have been reported to have 300 K dielectric constant [44,45] as high as $\epsilon_{\text{CECA}} = 52$ and selecting this base-polymer dielectric constant allows us to divide the 0 K/vacuum energies by $\epsilon_{\text{CECA}} = 52$ for the last two columns in Table 4.1. This results in significantly reduced ion interactions, suggesting such ionomers might be superb single-ion conductors of Li^+ . BPh_4^- and its perfluorinated counterpart have interesting charge distributions revealed by Gaussian 03, shown and discussed in Figure 4.3.

Table 4.1. Lithium Ion Pair and Positive Triple Ion Energies at 0 K in vacuum [37] (left two columns) and in polar polymers at 300 K (PEO middle two columns; CECA right two columns).

Anion	E_{pair} (kJ/mol)[21]	$E_{triple+}$ (kJ/mol)[21]	$E_{pair} / \epsilon_{PEO}$ (kJ/mol) a	$E_{triple+} / \epsilon_{PEO}$ (kJ/mol) a	$E_{pair} / \epsilon_{CECA}$ (kJ/mol) b	$E_{triple+} / \epsilon_{CECA}$ (kJ/mol) b
$C_2H_5SO_3^-$	656	893	94	128	12.6	17.2
$C_2F_5SO_3^-$	584	778	83	111	11.2	15
$(C_6H_5)SO_3^-$	641	892	92	127	12.3	17.2
$(C_6F_5)SO_3^-$	604	819	86	117	11.6	15.8
$(C_6H_5)_4B^-$	539	860	77	123	10.4	16.5
$(C_6F_5)_4B^-$	448	611	64	87	8.6	11.8

a. Calculated for PEO-ionomers [43-46] using the 300 K dielectric constant of PEO $\epsilon_{PEO} = 7$.

b. Calculated for CECA-ionomers relevant to this paper using the 300 K dielectric constant of the siloxane-CECA homopolymer [7,9-11,40-42] $\epsilon_{CECA} = 52$.

The temperature dependence of static (low frequency) dielectric constant ϵ_s for ethylene carbonate, propylene carbonate, cyclic carbonate (CECA) monomer and its siloxane [9] homopolymer are shown in **Figure 4.2 a**, along with lines that show the values predicted by the Onsager equation assuming the Kirkwood $g = 1$.

As elaborately deduced in **Section 1-8**, in the Frohlich-Kirkwood-Onsager Formula

$$\frac{(\epsilon_s - \epsilon_\infty)(2\epsilon_s + \epsilon_\infty)}{\epsilon_s(\epsilon_\infty + 2)^2} = \frac{\nu g \mu_v^2}{9\epsilon_0 kT}$$

ε_∞ is the high frequency dielectric constant, ν is the number density of dipoles of strength μ_ν , ε_0 is the permittivity of vacuum, k is Boltzmann's constant and T is absolute temperature. While ethylene carbonate and propylene carbonate have nearly the predicted temperature dependence, the CECA monomer and its siloxane polymer have much stronger than expected temperature dependence of ε_s . It is not yet clear what role this plays in the siloxane ionomers based on CECA.

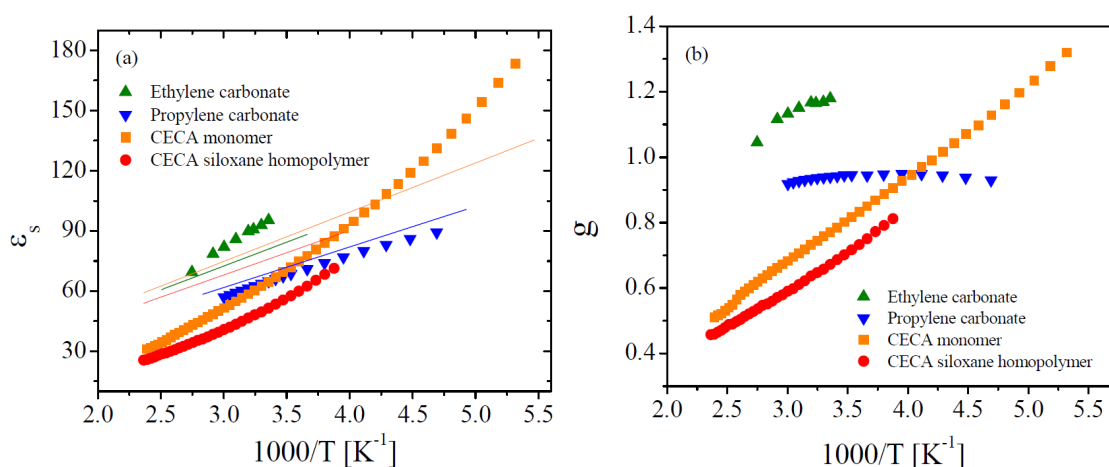


Figure 4.2. Temperature dependence of (a) static dielectric constant ε_s with lines shown as predictions of the Onsager equation and (b) Kirkwood g factor for ethylene carbonate, [48,49] propylene carbonate, [48,49] CECA monomer and CECA siloxane homopolymer. [51]

In **Figure 4.2 b** we see that the Kirkwood g factors of ethylene carbonate and propylene carbonate are nearly temperature-independent and nearly unity, both as expected by Onsager ($g_{EC} = 1.18$ and $g_{PC} = 0.93$) [48,49] while the cyclic carbonate (CECA) and its siloxane homopolymer have stronger-than-Onsager temperature dependence of ε_s , yielding an unusual temperature dependence of their Kirkwood g factor.

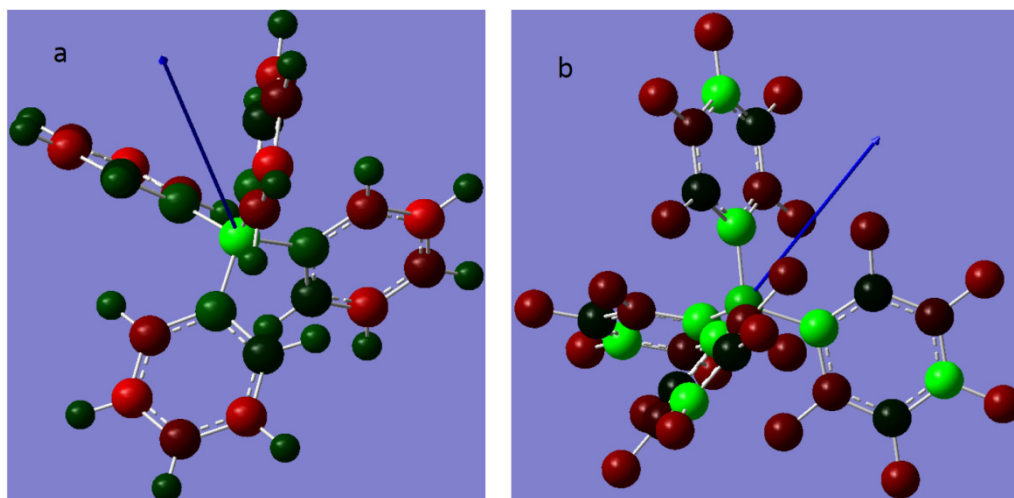


Figure 4.3. Electronic charge distribution in (a) tetraphenyl borate anion and (b) perfluorinated tetraphenyl borate anion, calculated by Gaussian 03 using the B3LYP/6-31+G* basis set. Light green denotes a positive charge; red denotes a negative charge, with brighter red indicating stronger negative charge. The boron in the center of these borate anions is positively charged. The tetraphenyl borate anion has the negative charge distributed on the 24 carbons in the phenyl rings, particularly the ortho carbons (each with roughly $-0.5e$). The perfluorinated tetraphenyl borate anion has the negative charge distributed on the 20 fluorines (roughly $-0.3e$ each), with strong positive charge on boron (roughly $+0.5e$), the alpha carbons (roughly $+0.7e$) and the para carbons (roughly $+0.8e$). The charge distributions impart strong dipoles to these anions (shown by arrows) of 16 D for tetraphenyl borate and 13 D for perfluorinated tetraphenyl borate.

Motivated by the low ion interaction energies for CECA borate copolymers denoted in bold in **Table 4.1**, in this chapter Siwei Liang's the synthesis of polysiloxane-based single-ion conductors with cyclic carbonates and three different lithium tetraphenyl borates as side chains are reported. The ionomers with ethylene oxide (EO) spacers

display higher conductivities and dielectric constants compared to PEO-based sulfonate ionomers previously reported by our group. [7,9-11] Comparison of ionomers with different ionic groups but similar ion molar content indicates that ionomers containing perfluorotetraphenyl borate salts have 3 times higher conducting ion concentration, consistent with the 40% lower triple ion energy in **Table 4.1**, since the 20 F atoms strongly delocalize the charge (**Figure 2b**).

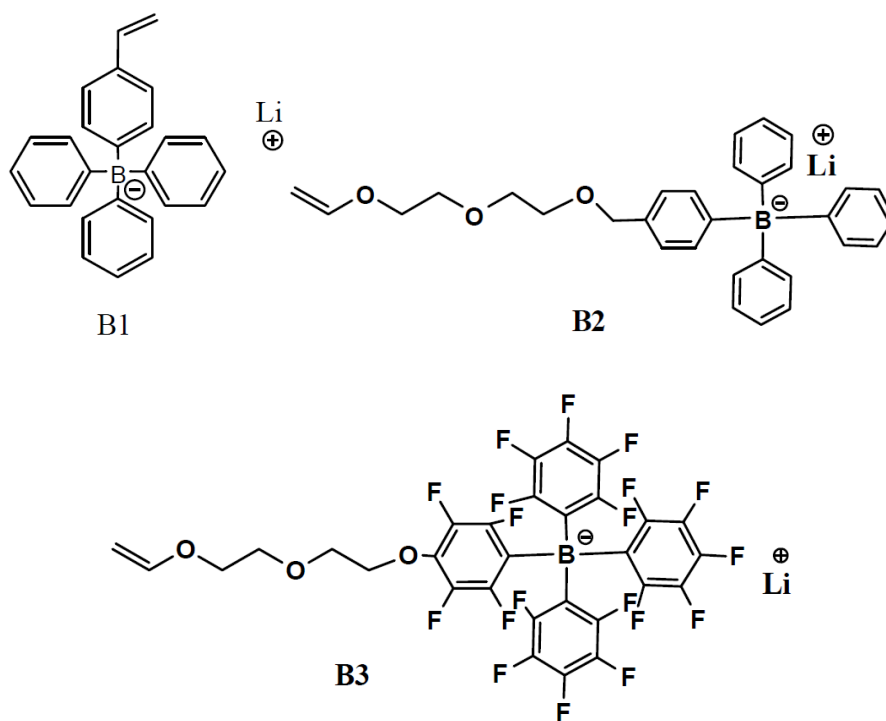


Figure 4.4. Chemical structures of a) lithium triphenylstyrylborate (B1); b) lithium triphenyl(4-((2-(2-vinyloxy)ethoxy)ethoxy)methyl) phenyl) borate (B2) and c) lithium tris (perfluorophenyl) (2,3,5,6-tetrafluoro-4-(2-(2-(vinyloxy) ethoxy)ethoxy)phenyl) borate (B3).

Three borate monomers: lithium triphenylstyryl borate (B1, **Figure 4.4 a**), a variant with three ethylene oxides between the vinyl and the borate (B2, **Figure 4.4 b**)

and a third with perfluorinated phenyl rings (B3, **Figure 4.4 c**) were synthesized and used to prepare polysiloxane ionomers based on cyclic carbonates via hydrosilylation.

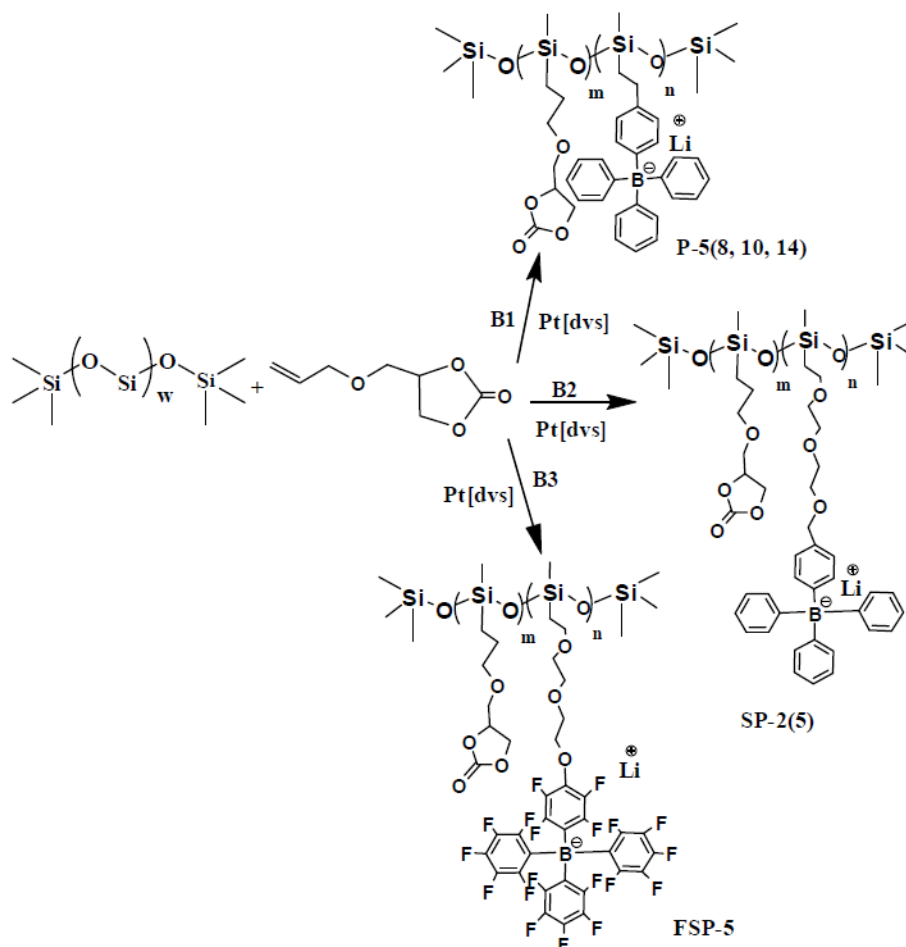


Figure 4.5. Synthesis of comb polysiloxanes with CECA and B1, (B2, or B3 anions) as side chains.

These weak binding monomer salts B1, B2, and B3 were then successfully attached to the polysiloxane backbone via hydrosilylation reaction [15], which provided a straightforward and efficient way to produce polysiloxane-based ionomers. The synthesis of comb polysiloxanes with CECA and B1, (B2, or B3 anions) as side chains are shown in **Figure 4.5**. P-5 (8, 10, 14) stands for polysiloxane ionomers with CECA and

tetraphenyl borate (B1) as side chains, where $n/(n+m) = 0.05$ (0.08, 0.1, 0.14), respectively. SP-2 (5) stands for polysiloxane ionomers with CECA and B2 as side chains, where $n/(n+m) = 0.02$ (0.05), respectively. FSP-5 stands for polysiloxane ionomers with CECA and B3 as side chains, where $n/(n+m) = 0.05$.

Ionomer T_g generally increases with ion content. [49] As shown in Table 4.2, T_g increases roughly 4 K/mol % lithium borate, roughly half the slope of Li- PEO-sulfonate ionomers, [10] owing to the weaker binding borate anions. Comparing T_g of P-5, SP-5, and FSP-5, having similar ion content, demonstrates that EO spacers between the borate and the polysiloxane backbone in SP-5 and FSP-5 lower T_g by 4–5 K. Ether oxygens solvate Li^+ and discourage ion aggregates, reducing physical cross-linking and hence lowering T_g .

The purpose of attaching the polar carbonate group (CECA) to the polysiloxane backbone is to increase the dielectric constant, which weakens ionic interactions and may allow more counterions to participate in conduction. At the same time, carbonate functional groups are expected to solvate Li^+ ions, as PEO does. In Table 4.2, the CECA homopolymer exhibits much higher dielectric constant compared to that of pure polysiloxane. [45] Ionomers with some of the carbonate groups replaced by lithium borates (P-5, 8, 10 and 14) exhibit slightly lower dielectric constant. This is an unexpected result, as ion pairs have large dipoles that dramatically increase the dielectric constant of properly solvated ionomers. [7,9,11,50] This might be explained by microphase separation, induced by incompatibility of the aromatic borate and CECA. If correct, that suggests a need to design some favorable interaction between the polar

neutral monomer and the anionic monomer. When short EO spacers are placed between the polymer backbone and functional groups, the conductivity is boosted. Moreover, the dielectric constant increases to become comparable to, or slightly higher than, the CECA homopolymer. Indeed, comparing siloxane homopolymers with vinyl carbonate versus CECA side chains, [45] the 25 °C dielectric constant is found to be more than twice as large with CECA presumably, because of the flexible EO spacer imparting less hindrance to motion of the large dipole.

Table 4.2. Physical Properties of Polysiloxane Single-ion Conductors

	Anion	T_g (°C)	Total ion concentration p_0 (nm ⁻³)	ϵ_s Static Dielectric Constant (at 25 °C)	Conductivity σ_0 at 25 °C (S/cm)
P-5	B1	-11	0.076	43	$10^{-7.7}$
P-8	B1	-6	0.12	39	$10^{-7.1}$
P-10	B1	10	0.15	40	$10^{-8.2}$
P-14	B1	30	0.21	38	$10^{-11.0}$
SP-2	B2	-17	0.024	61	$10^{-7.0}$
SP-5	B2	-15	0.06	49	$10^{-7.2}$
FSP-5	B3	-16	0.042	53	$10^{-6.9}$
CECA Homopolymer	none	-30	0	52	N/A

Figure 4.6 displays the direct current (dc) ionic conductivity as a function of T/T_g , and the inset shows conductivity vs $1000/T$. The conductivity of 10^{-11} S/cm at T_g is typical of Li single-ion conductors. The highest 25 °C conductivity obtained is $10^{-6.9}$ S/cm in **Table 4.2** for the ionomer with perfluorophenyl borate anions. This

disappointing result is comparable to the results reported previously by our group [7,9-11] for PEO-based sulfonate ionomers. For ionomers without ethylene oxide (EO) spacers, the conductivities show a maximum value when ion content is around 8%, easily explained by the conduction mechanism proposed in the literature. [7,9,11,16,42,50,51] The conducting species are most likely triple ions of $\text{Li}^+\text{BPh}_4^-\text{Li}^+$. Ion “hopping” is required for ion transport, whereby a triple ion moves by segmental motion and exchanges its extra Li^+ with a nearby ion pair. The ion mobility not only depends on polymer chain segmental motion, but also on the potential barriers, E_{hop} , that cations must overcome to move. [18] At low ion concentration, as ion content increases, E_{hop} decreases because of overlapping segmental exploration volumes of neighboring ion pairs, and conductivity increases. Increasing ion content further leads to more ion aggregation, higher T_g , and lower conductivity.

EO spacers between the borate anion and the polymer backbone provide more freedom for ionic side chains to respond to the external electric field, resulting in higher dielectric constant and conductivity (see Table 4.2). The ionomer SP-2, with the lowest total ion content, has the highest static dielectric constant (61) at 25 °C. Additionally, EO spacers can assist in dissociating ion aggregates, lowering T_g , and boosting the mobility of the conducting ions. When H atoms on the phenyl groups of the B2 borate are replaced by F atoms to give B3, the borate’s charge is even more delocalized and ionic interactions are further softened, boosting carrier concentration.

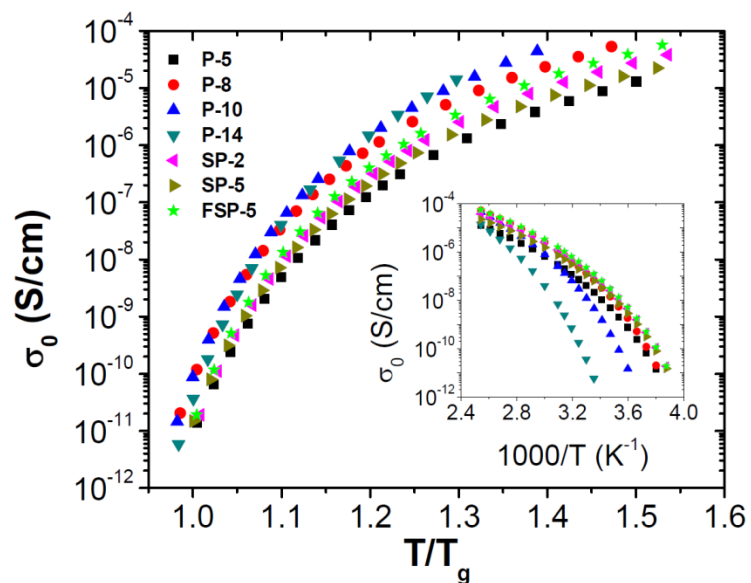


Figure 4.6. Temperature dependence of ionic conductivity for siloxane borate ionomers vs. T/T_g (and vs. $1000/T$ in the inset). The short EO spacer between the borate ion and the siloxane backbone raises the conductivity by lowering T_g .

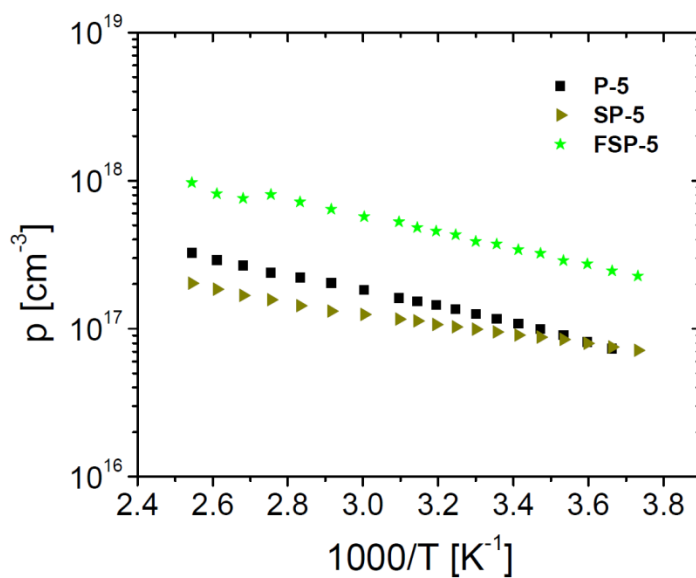


Figure 4.7. Temperature dependence of simultaneously conducting ion concentrations for three siloxane borate ionomers with borate fraction 5%.

Figure 4.7 compares electrode polarization analysis results [9,11] of three of our single-ion conductors, containing the three different borates at similar ion content (~5%). The ionomer with the perfluoroborate anion exhibits >3 times higher simultaneously conducting ion concentration compared to the other two ionomers. For each ionomer, the conducting ion content shows Arrhenius temperature dependence: $p = p_{\infty} \exp(-E/RT)$

The value of p_{∞}/p_o (p_o is the calculated total ion concentration of the ionomer in **Table 4.2**) of ionomer FSP-5 is 0.12, compared to 0.012 and 0.05 for P-5 and SP-5, respectively. This indicates that the ionomer with the perfluoroborate has the largest portion of ions participating in conduction, as anticipated by the *ab initio* calculations presented in **Table 4.1**. The Arrhenius temperature dependence of the conducting ion concentration in Figure 4 shows activation energy in the range of 7 to 10 kJ/mol, much lower than Li single-ion conductors containing either sulfonate groups (18–22 kJ/mol) [9,11] or bis(trifluoromethanesulfonyl) imide groups (17–20 kJ/mol) [51] that have recently been used to construct lithium single-ion conductors. [53–55] This substantially lower activation energy suggests that our borate anions have enormous potential for ion conduction, if T_g can be kept low. When normalized by T_g , the conductivity far above T_g actually increases strongly with ion content (**Figure 4.6**), suggesting that high ion contents would be beneficial for single-ion conductors, if T_g can be kept low. At high ion content, 10^{-4} S/cm requires $T = 1.5 T_g$, meaning that $T_g = -70$ °C is needed to achieve 10^{-4} S/cm at room temperature. Such has been realized in polymer/salt mixtures [18,21] but remains a challenge for single-ion conductors, without addition of polar solvent to solvate ions and lower T_g .

Conclusion:

In this section, quantum chemistry calculations of ion interaction energies were used to guide rational single-ion conductor design. Weak association novel borates lithium salts suggested by *ab initio* calculations were attached to polysiloxane-based ionomers. B1 ion content variations show maximum 25 °C conductivity at 8mol%, reflecting a tradeoff between carrier density and T_g increase. Ethylene oxide spacers (B2) lower T_g , and increase dielectric constant, both raising conductivity. Perfluorinating the four phenyl rings (B3) lowers the ion association energy, as anticipated by *ab initio* estimations. This increases conductivity, a direct result of 3X higher measured carrier density. The ~ 9 kJ/mol activation energy of simultaneously conducting ions is less than half that of ionomers with either sulfonate or bis(trifluoromethanesulfonyl) imide anions, suggesting that ionomers with weakbinding borate anions may provide a pathway to useful single-ion Li^+ conductors, if their T_g can be lowered.

All of our experimental results are consistent with expectations from our *ab initio* calculations, strongly suggesting that such can be utilized to design single-ion conductors to transport ions. The conductivities of the borate-containing ionomers are still relatively low, which is likely due to their relatively high T_g . Further improvement in the conductivity is observed when either incorporating PEO side chains on the polymer backbone or short poly(ethylene glycol) (PEG) oligomer as plasticizer.

4.3. Ionic Conduction and Dielectric Response of Poly(imidazolium acrylate) Ionomers [56]

In this section, we perform *ab initio* calculations to determine the pair dipole moment, the interaction energies of ion pair, positive triple ion, negative triple ion and quadrupoles for 1-butyl-3-methylimidazolium cation with Tf_2N^- and PF_6^- counterions. We also use DSC to study the thermal property and dielectric spectroscopy to study ionic conduction and dielectric response of imidazolium-based single-ion conductors with two different counterions [hexafluorophosphate (PF_6^-) or bis(trifluoromethanesulfonyl) imide ($\text{F}_3\text{CSO}_2\text{N}^-\text{SO}_2\text{CF}_3 = \text{Tf}_2\text{N}^-$)] with different imidazolium pendant structures, particularly tail length (n-butyl vs n-dodecyl). All of our experimental results are consistent with expectations from our *ab initio* calculations.

Ionic conduction in ion-containing polymers is of considerable interest from both fundamental and applied points of view. Recently, ionic liquids, which are composed entirely of large cations and anions with weak interactions (310 kJ/mol for 1-butyl-3-methylimidazolium cation with Tf_2N^- counterion at 0 K in vacuum), [57] have attracted significant interest due to their unique physical properties such as high thermal and chemical stability, negligible vapor pressure, broad electrochemical window (many are stable up to 5 V), and high ionic conductivity. [58–65] In particular, a number of groups have described imidazolium salts in which the geometric packing constraints of the planar imidazolium ring, its dangling alkyl groups, and the delocalization of the charge over the N–C–N moiety in the ring together reduce ion–ion interactions. [62,56–67]

These remarkable characteristics make it possible for ionic liquids to be used as novel and safe electrolytes for advanced devices such as electrochemical membranes for capacitors, lithium batteries, fuel cells, and electromechanical transduction devices for actuators and sensors. [68–77] There is a wide chemical composition range of ionic liquids, achieved by pairing various organic cations with numerous anions that allows for fine control of their physicochemical properties. Moreover, imidazoliums and other organic ionic liquid, which carry an ionic liquid species in each of the repeating units. [78–90] The major advantages of using the polymeric forms of ionic liquids are the enhanced stability and improved mechanical durability resulting from polymerization and the simplification that only the counterions are able to move large distances rapidly, making polymerized ionic liquids single-ion conductors. Polymerized ionic liquids are single-ion conductors, and this allows not only a transference number close to unity as required for advanced electrochemical devices but also the absence of concentration polarization of cations that is a common problem encountered in the conventional solid polymeric electrolytes in which both cation and anion are mobile. [97]

We selected two ionic liquid counterions: $\text{F}_3\text{CSO}_2\text{NSO}_2\text{CF}_3^-$ (referred to as Tf_2N^-) and PF_6^- to study. All calculations were performed using density functional theory methods with the Gaussian 03 software package. Exchange and correlation were included using the hybrid-GGA B3LYP functional. [103–105] Both only bind weakly to imidazolium cations: Table 4.3 compares 0 K energies of formation for ion pairs, positive triple ions, negative triple ions, and quadrupoles of butylmethylimidazolium with Tf_2N^- and PF_6^- . Tf_2N^- binds more weakly than PF_6^- , particularly for the quadrupole

energy. Since there is an equilibrium between quadrupoles and two ion pairs, **Table 4.3** also lists the ratio of quadrupole energy to twice the pair energy a useful gauge of the propensity to aggregate, which is larger for PF_6^- than Tf_2N^- . This is important because it indicates immediately that imidazolium– Tf_2N^- should aggregate less than imidazolium– PF_6^- , and this directly affects the glass transition temperature of these ionomers, with resultant effects on ion conduction.

Table 4.3. *Ab Initio* Interaction Energies and Pair Dipole Moment at 0 K in a Vacuum for 1-Butyl-3-methylimidazolium Cation with Tf_2N^- and PF_6^- Counterions.

Counter anion	Ion pair	Triple(+)	Triple(–)	Quadrupole	Aggregation factor	Charged factor	Pair dipole
	E_{pair} (kJ/mol)	$E_{\text{tr+}}$ (kJ/mol)	$E_{\text{tr–}}$ (kJ/mol)	E_{quad} (kJ/mol)	$E_{\text{quad}}/2E_{\text{pair}}$	$(E_{\text{tr+}} + E_{\text{tr–}})/1.5 E_{\text{quad}}$	m_{pair} (D)
PF_6^-	320	417	440	732	1.14	0.78	15.1
Tf_2N^-	310	413	415	680	1.10	0.81	14.1

In **Section 3-3.2.**, we defined quadrupole factor $E_{\text{quad}}/2E_{\text{pair}}$, indicating whether quadrupoles are energetically favored over ion pairs and by how much; triple ion factor $(E_{\text{tr+}} + E_{\text{tr–}})/3 E_{\text{pair}}$, indicating whether triple ions are favored over ion pairs and by how much, and the dotted diagonal line in **Figure 3.16.** is $(E_{\text{tr+}} + E_{\text{tr–}})/1.5 E_{\text{quad}} = 1$. Ion aggregation is effectively the correlation of neighboring dipoles of ion pairs. Here, we name quadrupole factor as aggregation factor, representing the degree of ion aggregation. Since quadrupole is the ground state of our four state model, the reciprocal

of aggregation factor indicates the degree of ion aggregation separating into uncharged species, i.e., ion pairs. We also name $(E_{tr+} + E_{tr-}) / 1.5 E_{quad}$ as charged factor, representing the degree of ion aggregation separating into charged species, i.e., positive triple ion and negative triple ion.

The relative charged factor $(E_{tr+} + E_{tr-}) / 1.5 E_{quad}$ indicates the relative conducting ion concentration in two identical polycations, with only different anions. The charged ion factor of 1-butyl-3-methylimidazolium cation with Tf_2N^- is higher than that of 1-butyl-3-methylimidazolium cation with PF_6^- , so that we predict that (**Prediction III**) the ion concentration of simultaneously conducting counterions for ionomers with Tf_2N^- anion shall be higher than those with the same structure but containing PF_6^- counterions at the same temperature. This prediction will be verified by dielectric measurement and electrode polarization analysis.

Based on the above predictions that Tf_2N^- ionomers have higher ion mobility and higher conducting ion concentration, naturally, (**Prediction IV**) they will show higher ionic conductivity at the same temperature. This prediction will be verified by dielectric measurement.

To verify these predictions, and investigate ion and polymer dynamics, the glass transition temperatures (T_g), ionic conductivities, and dielectric constants of these polymers were measured.

The dielectric measurement is a particularly powerful tool to investigate the motion of molecules or substituent groups over a broad time range, 10^{-7} – 10^2 s. [98,99] Segmental motion of polymers and ionomers are observed in a wide frequency range

New acrylate polymers with ionic imidazolium units were synthesized [109]; to compare the dielectric properties, nonionic polymer *e* was prepared similarly to the imidazolium ionomers as shown in Figure 4.8. The new imidazolium pendant homopolymers each have a single glass transition, as reported in Table 4.4. The polymers do not display crystallization or melting in the temperature range of -80 to 200 $^{\circ}\text{C}$ by DSC. Replacing PF_6^- with Tf_2N^- consistently lowered T_g by ~ 22 K. The Tf_2N^- counterion has previously been shown to act as a plasticizer for imidazolium ionic liquids [65,74] and their polymers. [83,89,90] Since association of ion pairs allows them to act as temporary cross-links that raise T_g , the more strongly associating PF_6^- imparts higher T_g than Tf_2N^- for the poly(imidazolium acrylate)s, as anticipated from the *ab initio* results of Table 4.3. Prediction I is proven true.

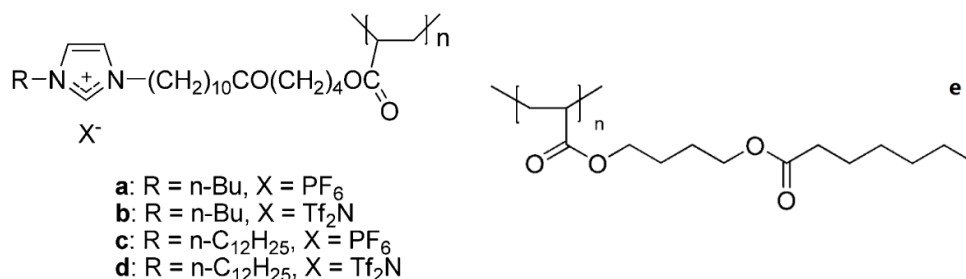


Figure 4.8. Chemical structures of poly(N-alkylimidazolium acrylate)s *a–d* and nonionic polymer *e*.

Table 4.4. DSC thermal analysis of ionomers.

Sample	C ₄ -PF ₆ (a)	C ₄ -Tf ₂ N (b)	C ₁₂ -PF ₆ (c)	C ₁₂ -Tf ₂ N (d)
DSC T_g (K)	256	230	244	226

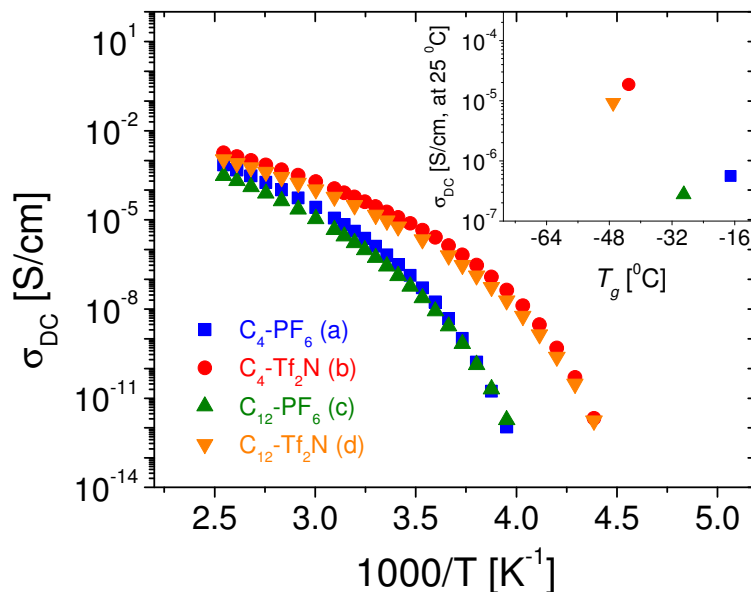


Figure 4.9. Temperature dependence of ionic conductivity for PF₆[−] and Tf₂N[−] ionomers. Tf₂N[−] (C₄-Tf₂N (b) and C₁₂-Tf₂N (d)) ionomers have consistently higher conductivities than PF₆[−] (C₄-PF₆ (a) and C₁₂-PF₆ (c)) ionomers. The inset shows ionic conductivity at room temperature as a function of glass transition temperature for these four ionomers (a(■), b(●), c(▲), and d(▼)).

To understand the influence of anions on ionic conductivity, the temperature dependence of DC conductivity shown in **Figure 4.9** is evaluated from a roughly 3 decade frequency range where the in-phase part of the conductivity $\sigma'(\omega) = \epsilon''(\omega)\epsilon_0\omega$ is independent of frequency, as shown in **Figure 1.19**. The inset in **Figure 4.9** shows the

strong correlation between ionic conductivity at 25 °C and T_g for these monomers and their polymers. As predicted, two Tf_2N^- ionomers: $\text{C}_4\text{-Tf}_2\text{N}$ (b) and $\text{C}_{12}\text{-Tf}_2\text{N}$ (d) both show higher ionic conductivities than PF_6^- ionomers at the same temperature. **Prediction IV** is proven true.

A physical model of electrode polarization (EP) makes it possible to separate ionic conductivity into the number density of simultaneously conducting ions and their mobility, [98,100,110,111] as has been done for other single-ion conductors above T_g . [88,11-103,112,113] Electrode polarization occurs at low frequencies, where the transporting ions have sufficient time to polarize at the blocking electrodes during the cycle. That polarization manifests itself in (1) an increase in the effective capacitance of the cell (increasing the apparent dielectric constant) and (2) a decrease in the in-phase part of the conductivity, as the polarizing ions reduce the field experienced by the transporting ions. The natural time scale for conduction is the time where counterion motion becomes diffusive. Refer to **Section 1.6** for elaborated discussion. The temperature dependence of the number density of simultaneously conducting ions p calculated from **Equation 1.8** is plotted in **Figure 4.10** and the fraction of ions participating in conduction (p/p_0 wherein p_0 , listed in **Table 4.5**, is the total anion number density) is shown in the **Figure 4.10** inset. The insert clearly shows that Tf_2N^- ionomers have higher conducting ion concentrations than PF_6^- ionomers at the same temperature. **Prediction III** is proven true.

The temperature dependence of simultaneously conducting ion concentration for these imidazolium-based ionomers is well described by an Arrhenius equation

$$p = p_{\infty} \exp\left(-\frac{E_a}{RT}\right) \quad (4.14)$$

wherein p_{∞} and E_a , listed in [Table 4.5](#), are the conducting ion concentration as $T \rightarrow \infty$ and the activation energy for conducting ions, respectively.

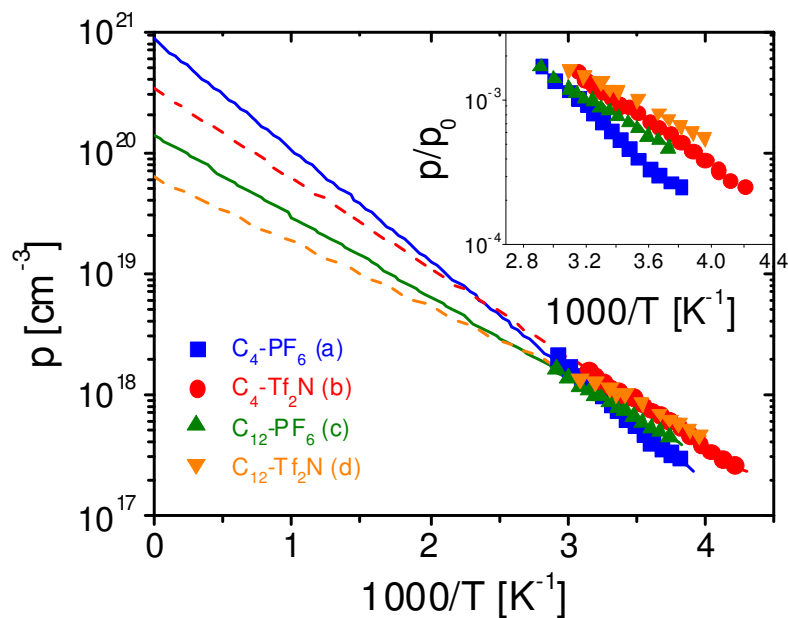


Figure 4.10. Temperature dependence of simultaneously conducting ion concentration p . Solid (PF_6^- ionomers) and dashed (Tf_2N^- ionomers) lines are Arrhenius fits to [Equation 4.14](#) with two fitting parameters (E_a and p_{∞} , listed in [Table 4.5](#)). The inset displays the fraction of anions simultaneously participating in conduction (p divided by the total anion concentration p_0).

Table 4.5. Fitting Parameters (**Equation 4.14**) for the Temperature Dependence of the Number Density of Simultaneously Conducting Ions.

Sample	$\log(p_0)$ (cm ⁻³)	Conducting ion concentration		
		$\log(p_\infty)$ (cm ⁻³)	E_a (kJ/mol)	$1-p_\infty/p_0$
C₄-PF₆ (a)	21.1	20.9	17.5	0.29
C₄-Tf₂N (b)	21.0	20.5	14.1	0.68
C₁₂-PF₆ (c)	21.0	20.1	12.8	0.86
C₁₂-Tf₂N (d)	20.9	19.8	10.2	0.93

The fact that for some ionomers p_∞ is smaller than p_0 indicates some of the counterions are too strongly aggregated to participate in ionic conduction, and $1 - p_\infty / p_0$ (listed in **Table 4.5**), tells us the fraction of counterions that are trapped and are unable to participate in conduction. [113] The activation energies for the PF₆⁻ ionomers (**C₄-PF₆ (a)** and **C₁₂-PF₆ (c)**) are higher than those for Tf₂N⁻ ionomers (**C₄-Tf₂N (b)** and **C₁₂-Tf₂N (d)**), indicating a lower binding energy for the imidazolium ions with the larger Tf₂N⁻ ions than for the PF₆⁻ ions, [83] as anticipated by the *ab initio* calculations presented in **Table 4.3**.

The inset in **Figure 4.10** indicates that the fraction of counterions simultaneously participating in conduction (p/p_0) in these single-ion conductors is quite low, < 0.1% of the total number of counterions, except at the highest temperatures studied. The conducting ion content evaluated from the EP model is the number density of ions in a conducting state in any snapshot, which sets the boundary condition for the solution of the Poisson-Boltzmann equation. Only a small fraction of total ions is in a conducting

state at any given instant in time, similar to observations on other single-ion conducting ionomers with alkali metal counterions [11-103] or ionic liquid counterions.[88,112,113]

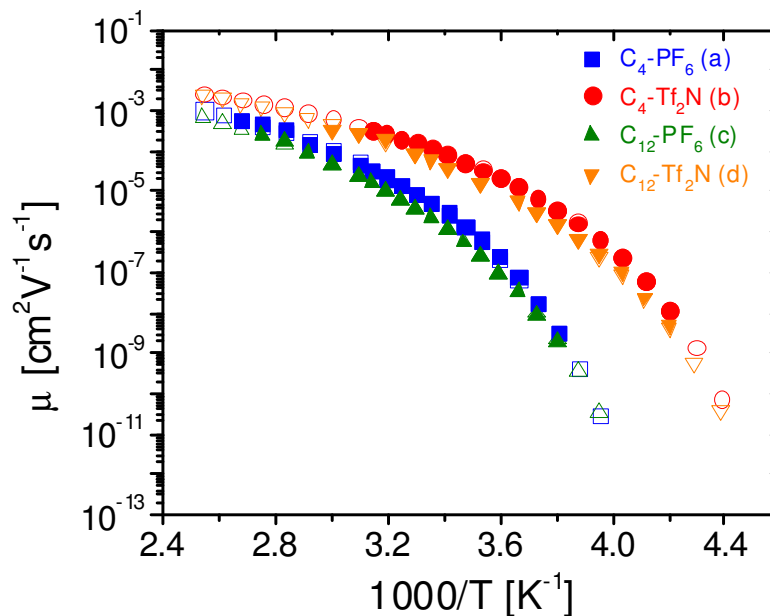


Figure 4.11. Temperature dependence of simultaneously conducting ion mobilities for PF_6^- and Tf_2N^- ionomers, determined from (1) the EP model (filled symbols) and (2) dividing the DC conductivity data by the product of the elementary charge e and the Arrhenius fit to **Equation 4.14** of simultaneously conducting ion number density p (open symbols, referred to as extended mobility). Tf_2N^- ionomers (**C₄-Tf₂N (b)** and **C₁₂-Tf₂N (d)**) have consistently higher mobilities than PF_6^- ionomers (**C₄-PF₆ (a)** and **C₁₂-PF₆ (c)**).

The temperature dependence of the mobility of the simultaneously conducting ions determined from the EP model is displayed in **Figure 4.11** as the filled symbols. Since conductivity can be measured over a far wider temperature range, we divide the

DC conductivity data in [Figure 4.9](#) by the elementary charge e and by the Arrhenius fit to [Equation 4.14](#) of simultaneously conducting ion number density p to determine an extended mobility, plotted in [Figure 4.11](#) as the open symbols. Tf_2N^- ionomers (**C₄-Tf₂N (b)** and **C₁₂-Tf₂N (d)**) have consistently higher mobilities than PF_6^- ionomers (**C₄-PF₆ (a)** and **C₁₂-PF₆ (c)**) at the same temperature. **Prediction II** is proven true.

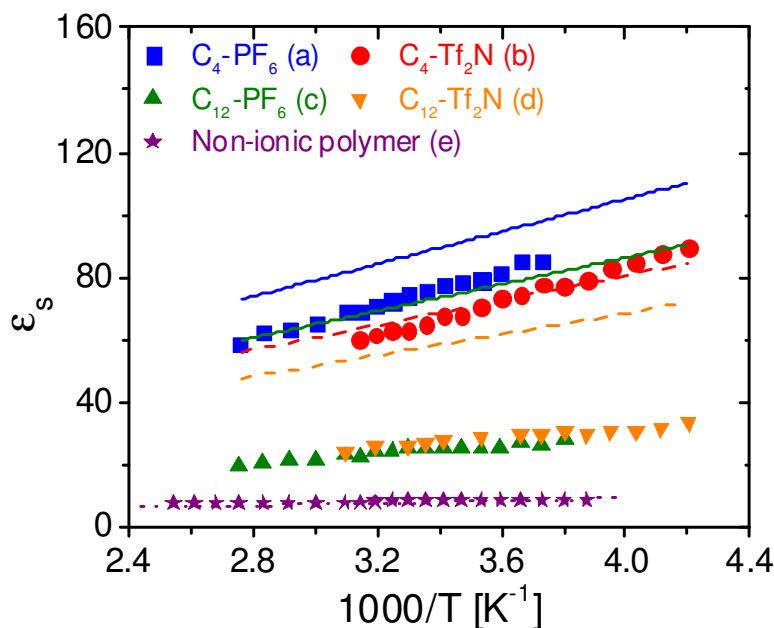


Figure 4.12. Temperature dependence of static dielectric constant ϵ_s for imidazolium-based ionomers and a non-ionic polymer. The lines are predictions of the Onsager equation with fixed concentration and strength of dipoles: the purple dotted line is [Equation 4.15](#) for non-ionic polymer e with $\sum_i v_i m_i^2 / (9\epsilon_0 k) = 249 \text{ K}$ as the sole fitting parameter and the colored solid and dashed lines are [Equation 4.16](#) for the four imidazolium-based ionomers, assuming all ions exist as isolated contact pairs

($v_{pair} = p_0$) with dipoles given by the *ab initio* estimates in [Table 4.3](#) and assuming the Kirkwood correlation factor $g = 1$.

The static dielectric constant ϵ_s is defined as the low-frequency plateau of $\epsilon'(\omega)$ before electrode polarization (EP) begins, shown in [Figure 1.19](#) and calculated using [Equation 1.5](#) from the measured σ_{DC} and τ_σ obtained from fitting EP to [Equation 1.7](#). [\[103,117,118\]](#) [Figure 4.12](#) displays the static dielectric constant for these imidazolium-based ionomers and the nonionic polymer e vs inverse temperature. The nonionic polymer e having no imidazolium cation nor anion exhibits $\epsilon_s = 8$ at room temperature. ϵ_s for the ionomers with imidazolium cation and either PF_6^- or Tf_2N^- anion is much larger, especially for those with n-butyl tails ($\text{C}_4\text{-PF}_6$ (a) and $\text{C}_4\text{-Tf}_2\text{N}$ (b)) with $\epsilon_s \approx 80$ at the lowest temperatures studied.

To further understand the contributions from non-ionic polymer and the ionic groups to the static dielectric constant of the ionomers, we will use the pair dipole moment from *ab initio* calculations (listed in [Table 4.3](#)) in the Onsager equation.

The temperature dependence of ϵ_s for the nonionic polymer can be understood through the Onsager equation [\[120–122\]](#)

$$\left[\frac{(\epsilon_s - \epsilon_\infty)(2\epsilon_s + \epsilon_\infty)}{\epsilon_s(\epsilon_\infty + 2)^2} \right]_{\text{nonionic}} = \frac{1}{9\epsilon_0 kT} \sum_i v_i m_i^2 \quad (4.15)$$

wherein v_i is the number density of dipoles, m_i is their dipole moment, and ϵ_∞ is the high-frequency limit of the dielectric constant (here taken to be an approximate value of

$\epsilon_\infty = n^2$, where n is the refractive index from the group contribution method [108], listed in **Table 4.6**).

Table 4.6. Refractive Index n and Total Ion Concentration p_0 of ionomers.

Sample	C ₄ -PF ₆ (a)	C ₄ -Tf ₂ N (b)	C ₁₂ -PF ₆ (c)	C ₁₂ -Tf ₂ N (d)
n^a	1.461	1.462	1.468	1.469
p_0^a ($\times 10^{20}$ cm ⁻³)	12.1	10.3	9.62	8.46

^a Refractive index and total ion concentration determined from group contribution method based on structure. [108]

The purple dotted line in **Figure 4.12** is fit to **Equation 4.15** with the $\sum_i v_i m_i^2$ term as the sole fitting parameter, showing that ϵ_s of the nonionic polymer e is well described by the Onsager equation. The polymerized ionic liquids have an imidazolium cation attached to each side chain with the associated anion (PF₆⁻ or Tf₂N⁻) and for such ionomers the contribution of the ions to the static dielectric constant can be analyzed [102,112] by simply adding the effect of ion pairs in **Equation 4.16**:

$$\left[\frac{(\epsilon_s - \epsilon_\infty)(2\epsilon_s + \epsilon_\infty)}{\epsilon_s (\epsilon_\infty + 2)^2} \right]_{\text{ionomer}} = \frac{v_{\text{pair}} m_{\text{pair}}^2}{9\epsilon_0 kT} + \left[\frac{(\epsilon_s - \epsilon_\infty)(2\epsilon_s + \epsilon_\infty)}{\epsilon_s (\epsilon_\infty + 2)^2} \right]_{\text{nonionic}} \quad (4.16)$$

wherein v_{pair} is the number density of ion pairs and m_{pair} is their dipole moment. The solid and dashed lines in **Figure 4.12** are the Onsager predictions of **Equation 4.16** for each ionomer, assuming all ions are in the isolated ion pair state ($v_{\text{pair}} = p_0$, listed in **Table 4.6**) with the contact pair dipole from *ab initio* listed in **Table 4.3**.

Another way to view ion aggregation is that this effectively correlates neighboring dipoles of ion pairs. Correlation of neighboring dipoles was considered by Kirkwood [119,120] and Fröhlich [118] by introducing a prefactor g into Equation 4.16 and this idea is extensively utilized. [96,117,118] For example, the dielectric constants for highly associating liquids such as acids, alcohols, and water are underestimated by the Onsager theory. [120] On the other hand, molecules with internal hindered rotation or restricted rotational degrees of freedom that prohibit alignment with the field cannot fully respond to the field as expected from their individual dipole moments, and therefore, the Onsager model overestimates the resulting dielectric constant. [121]

$$g = \frac{9\epsilon_0 kT}{\nu_{pair} m_{pair}^2} \left\{ \frac{(\epsilon_s - \epsilon_\infty)(2\epsilon_s + \epsilon_\infty)}{\epsilon_s (\epsilon_\infty + 2)^2} - \left[\frac{(\epsilon_s - \epsilon_\infty)(2\epsilon_s + \epsilon_\infty)}{\epsilon_s (\epsilon_\infty + 2)^2} \right]_{nonionic} \right\} \quad (4.17)$$

If there are no specific correlations, $g = 1$ and the Kirkwood-Fröhlich equation reduces to the Onsager equation. For polar liquids in which dipoles tend to orient with parallel dipole alignments, $g > 1$. For example, hydrogen bonding in water makes $g = 2.9$ at 0 °C, decreasing steadily as temperature is increased, to $g = 2.3$ at 100 °C. When dipoles either prefer antiparallel alignment or a significant fraction of dipoles are unable to move in response to the field, $g < 1$.

Conclusions:

In this section, we performed *ab initio* calculations to determine the pair dipole moment, the interaction energies of ion pair, positive triple ion, negative triple ion and quadrupoles for 1-butyl-3-methylimidazolium cation with Tf_2N^- and PF_6^- counterions. We also defined aggregation factor and charged factor as the gauges for ion aggregation and conducting ion concentration, respectively. We made four predictions based on these calculations:

Prediction I: The PF_6^- ionomers have higher T_g than Tf_2N^-

Prediction II: The Tf_2N^- ionomers have higher mobility than PF_6^- ionomers at the same temperature.

Prediction III: The Tf_2N^- ionomers have higher conducting ion concentration than PF_6^- ionomers at the same temperature.

Prediction IV: The Tf_2N^- ionomers have higher ionic conductivity than PF_6^- ionomers at the same temperature.

To verify these predictions and investigate ion and polymer dynamics, new imidazolium-based single-ion conductors with two different counterions [hexafluorophosphate (PF_6^-) or bis(trifluoromethanesulfonyl) imide ($\text{F}_3\text{CSO}_2\text{N}^-\text{SO}_2\text{CF}_3 = \text{Tf}_2\text{N}^-$)] were synthesized, the glass transition temperatures (T_g), ionic conductivities, and dielectric constants of these polymers were measured. A physical model of electrode polarization is used to separate ionic conductivity of the ionomers into number density of conducting ions and their mobility. We also used the pair dipole moment from *ab initio*

calculations in the Onsager theory to analyse the static dielectric constant of the ionomers. All of our experimental results are consistent with expectations from our *ab initio* calculations.

All four predictions are shown to be correct. By far the most important prediction is **Prediction I** that Tf_2N^- gives lower T_g than PF_6^- , as this strongly impacts **Predictions II and IV**. These predictions were made in 2009 and influenced the research in Prof. Colby's group since that time. **Prediction I** is now understood more generally as a correlation of T_g with molecular volume of the repeat unit (including the counteranion) in imidazolium polymers [151,152]. Lowering T_g obviously boosts ion mobility and conductivity. **Prediction III** is more delicate as it seems to involve also issues about specific solvation that are not yet fully understood.

4.4 Influence of various cationic counterions on T_g of PEO-based polyurethane carboxylate ionomers [113]

In this section, polyurethane carboxylate ionomers based on poly(ethylene glycol) ($M_n = 600$) with sodium and various ammonium, phosphonium and imidazolium cations are synthesized for systematic comparison of different cationic counterions. We use *ab initio* calculations to determine interaction energies of quadrupoles, and the charge distribution of cations. We also used DSC to study the thermal property of the ionomers. The correlations of T_g with quadrupole energy and charge distribution are explored.

Many applications of polymer ion conductors simultaneously require high ionic conductivity and high modulus. Lithium ion battery separator membranes and ion-

transport actuators are two high-profile examples. Polyethylene glycol (PEG or PEO) and PEO-based polymer electrolytes have been the mainstream research focus since 1973 because of their excellent ability to solvate cations. [17,123,124] Although PEO-based homopolymer electrolytes have reasonable ionic conductivities; many of them suffer from poor mechanical strength due to the low glass-transition temperature (T_g) of PEO. [125] Ionic conductivity benefits from the fast segmental motion of low T_g materials but the modulus is at best the plateau modulus of the polymer melt ($\sim 1 \times 10^6$ Pa). With single-phase systems, ionic conductivity increases and modulus decreases as T_g is lowered, resulting in a correlation (trade-off) between modulus and conductivity. [125] To obtain materials with simultaneous high modulus and high conductivity, polymers that spontaneously microphase separate into hard domains (high modulus) and soft domains that transport ions, are needed. Block copolymers have been used [126,127] but here we focus on segmented copolymers. Polyurethane (PU) ionomers can be quite interesting candidates, as their microphase separation can allow a hard phase that provides high modulus to coexist with a continuous soft phase that transports ions. Various strategies have been used to attach ionic groups to polyurethanes. [128-131] Different metal cations can change T_g and morphology. The modulus can reach 1×10^7 to 1×10^9 Pa even far above the T_g of the soft phase when attaching ionic groups in the hard segment.[132-134] In terms of ionic conductivity, 1×10^{-7} to 1×10^{-8} S/cm at room temperature has been achieved for Li^+ or Na^+ counterions, with modulus of 1×10^8 Pa when replacing the urethane proton with a sulfonated group in the hard segment. [135] However, unlike the many studies of mechanical properties of PU ionomers[128,129] conductivity and

dielectric studies are less common and more focusing on varying metal counterions. [136] Dielectric relaxation spectroscopy (DRS) has proved to be a very useful tool for PU ionomer studies. [97,137] Combined with thermal and mechanical tests, DRS allows understanding of both microphase separation and dipole/polymer chain relaxation in the soft phase, as well as ionic conductivity.[8,137,138]

In this section, PEG with $M_n = 600$ and $M_w/M_n < 1.2$ was chosen as the soft segment because of its famous ability to solvate cations¹⁻³ and being short enough to inhibit crystallization. About 2 orders of magnitude higher ionic conductivity has been reported for PEO- than poly(tetramethylene oxide)-based PU ionomers. [138,139] Para-Phenylene diisocyanate (pPDI) was used as the hard segment because its symmetry facilitates microphase separation.[140,141] Carboxylic acid containing diol was used as the chain extender, effectively placing the ionic group between two pPDI segments. By varying from the small alkali metal Na^+ to large multiatom cations like ammonium, imidazolium and phosphonium, we hope to understand how both the counterion size and species affect the glass transition temperature in PU ionomers. A principal finding is that these materials do not microphase separate in the conventional sense but counterions are trapped by the pPDI-carboxylate-pPDI segments, unable to participate in ionic conduction.

Carboxylic acid containing polyurethane (PU) is synthesized by Shih-Wa Wang [113]. The chemical structure of the product polyurethane is shown in Figure 4.13. It is a random segmented copolymer with pPDI segments between PEG 600 and carboxylic acid sections.

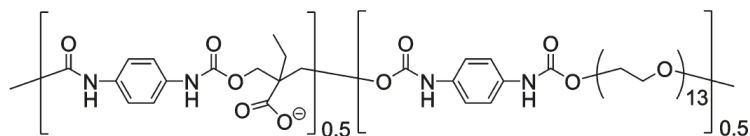


Figure 4.13. Chemical structures of polyurethane anionomer. (The cations' structures are shown in **Figure 4.14.**)

The resources of cations, the ammonium and phosphonium salts, such as, sodium hydroxide, tetrabutylammonium hydroxide-30 hydrate ($\text{Bu}_4\text{N}^+\text{-OH}$), tetrabutylphosphonium hydroxide (40 wt % aqueous solution) ($\text{Bu}_4\text{P}^+\text{-OH}$) and N-methylimidazole and butyl-methyl-imidazolium chloride ($\text{BuMeIm}^+\text{-Cl}$) were purchased from Aldich. Tetramethylammonium hydroxide-5 hydrate ($\text{Me}_4\text{N}^+\text{-OH}$) was purchased from Fluka. Tris[2-(methoxyethoxy)ethyl]methyl ammonium iodide ($(\text{MOEOE})_3\text{MeN}^+\text{-I}$), N-(2-methoxyethyl)-N-methylmorpholinium bromide ($(\text{EO})_2\text{Me-(MOE)N}^+\text{-Br}$), (2-methoxyethyl)-tributylphosphonium bromide ($\text{Bu}_3(\text{MOE})\text{P}^+\text{-Br}$) and methoxyethyl methyl imidazolium bromide ($(\text{MOE})\text{MeIm-Br}$) were synthesized by Shih-Wa Wang. [113].

The ammonium and phosphonium salts above were ion exchanged with Amberlite IRA-400 ion-exchange resin to prepare hydroxide aqueous solutions and stored in a refrigerator for later use. The concentration was determined by titration with 0.1N HCl standard solution. One gram of the carboxylic acid containing polyurethane was dissolved in the counterion- hydroxide aqueous solution (with 10% excess hydroxide to ensure 100% neutralization) and then dialyzed in a dialysis cassette (M_w cutoff = 2000) in deionized water for 1 week to remove any extra ions. The product was then dried at 70 °C under vacuum. The dried PU ionomers are fully water-soluble. The chemical

structures of cations studied: Na^+ , Me_4N^+ , Bu_4N^+ , $(\text{EO}_c)_2\text{Me}(\text{MOE})\text{N}^+$, $(\text{MOEOE})_3\text{MeN}^+$, BuMeIm^+ , $(\text{MOE})\text{MeIm}^+$, Bu_4P^+ , $\text{Bu}_3(\text{MOE})\text{P}^+$ are shown in **Figure 4.14**.

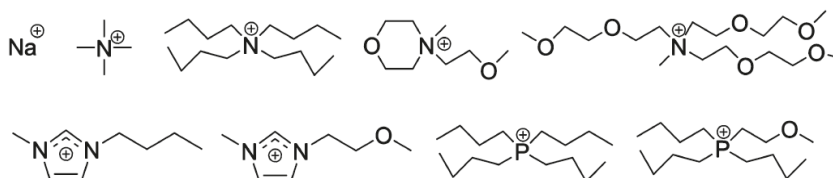


Figure 4.14. Chemical structures of cations studied: Na^+ , Me_4N^+ , Bu_4N^+ , $(\text{EO}_c)_2\text{Me}(\text{MOE})\text{N}^+$, $(\text{MOEOE})_3\text{MeN}^+$, BuMeIm^+ , $(\text{MOE})\text{MeIm}^+$, Bu_4P^+ , $\text{Bu}_3(\text{MOE})\text{P}^+$ (from left to right, top to bottom)

The size of cationacetate salt and the glass transition temperature of the ionomers are summarized in **Table 4.7**. The ionomer has $M_w = 12000$, $M_n = 8400$, $M_w/M_n = 1.4$ (polystyrene equivalent molar masses) determined by size exclusion chromatography with 0.01 M LiBr DMF solution as the mobile phase. This number agrees with the estimation ($M_n = 9000$) by ^1H NMR. The cation to ether oxygen ratio is 1/13. The calorimetric glass transition temperature T_g was measured using a Seiko Instruments SSC/5200. All samples were dried at 75 °C under vacuum for 2 days before measurement. T_g was obtained from the change in heat capacity during the second heating at a heating rate of 10 K/min under dry nitrogen purge after cooling from 80 °C at 10 K/min.

Ab initio calculations were employed to determine interaction energies of quadrupoles (**Table 4.7**), and the charge distribution of cations (**Table 4.8**). All calculations were performed using density functional theory methods with the Gaussian

03 software package. Exchange and correlation were included using the hybrid-GGA B3LYP functional. [142-145]

Table 4.7. The size of cationacetate salt,^a glass transition temperature of the ionomers and quadrupole formation energy $\Delta E_{quadrupole}$ ^b of the ion pair in the gas phase calculated by *ab initio* at 0K in vacuum.

	$[M/(\rho N_{av})]^{1/3}$ (Å)	T_g (K)	$\Delta E_{quadrupole}$ (kJ/mol)
Na ⁺	5.1	323	1400
Me ₄ N ⁺	6	308	930
BuMeIm ⁺	6.9	304	880
(MOE)MeIm ⁺	6.9	298	890
(EO _c) ₂ Me(MOE)N ⁺	7	291	860
Bu ₄ N ⁺	7.9	289	820
Bu ₄ P ⁺	8.1	273	790
Bu ₃ (MOE)P ⁺	8.1	284	790
(MOEOE) ₃ MeN ⁺	8.7	267	900

^a The size of cationacetate salt is calculated from the molar mass of the cationacetate salt, assuming density $\rho = 1 \text{ g/cm}^3$.

^b $\Delta E_{quadrupole}$ is defined as the energy difference between the quadrupole state and 2 free cations plus 2 free anions at 0 K in vacuum.

Table 4.8. Charge distribution of Bu₄P⁺, Bu₄N⁺ and BuMeIm⁺ from *ab initio* calculations.

	Center (P or N)	α -CH ₂	β -CH ₂	CH ₃	CH=CH	CH
Bu ₄ P ⁺	1.1	-0.2	0	/	/	/
Bu ₄ N ⁺	-0.5	0.3	0	/	/	/
BuMeIm ⁺	-0.3, -0.3	0.4	0	0.4	0.2	0.4

As described in the literature, different metal cations can have very different impact on T_g , depending on the chemical composition of the PU ionomers.[132,146] In our system, only one T_g has been seen and T_g decreases dramatically with increasing cation size.

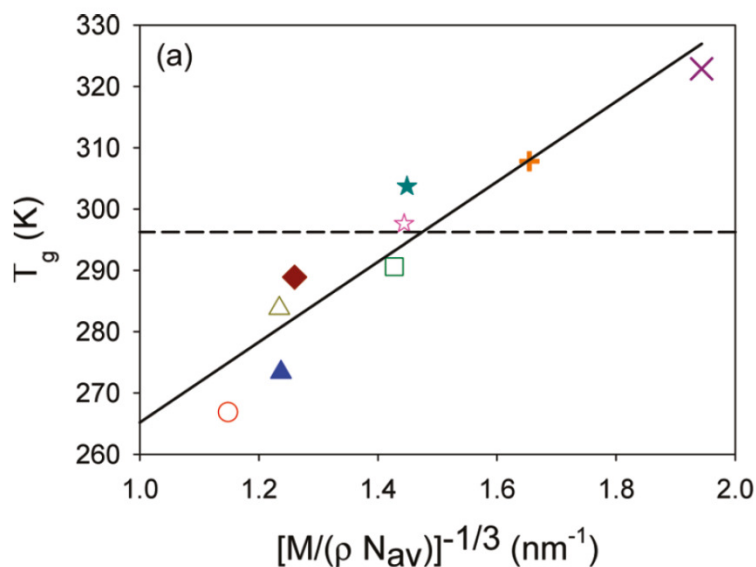


Figure 4.15. T_g from DSC as a function of reciprocal size of corresponding acetate salts (assuming the same density ρ of 1.0 g/cm³). Open symbols are cations containing ether oxygen. Solid symbols are cations without ether oxygen. Purple X is Na⁺; orange plus is Me₄N⁺; cyan solid star is BuMeIm⁺; pink open star is (MOE)MeIm⁺; green open square is (EO_c)₂Me(MOE)N⁺; dark red solid diamond is Bu₄N⁺; blue solid triangle is Bu₄P⁺; olive green open triangle is Bu₃(MOE)P⁺; red open circle is (MOEOE)₃MeN⁺; solid line is fitting result of equation $T_g = 200 + 65.4 [M/(\rho N_{av})]^{1/3}$.

Figure 4.15 shows T_g as a function of inverse size of corresponding cation-acetate salts (assuming all the salts have the same density of 1 g/cm³). The precursor acid form

PU has $T_g = 23$ °C. Introduction of small sodium ions increases the T_g to 47 °C. The increase of T_g with alkali metal counterions is common,[147] possibly originating from some combination of (1) mixing soft and hard segment and (2) the Coulombic force between cations and anions acting as physical cross-links.

The PEO soft segment is well-known for its ability to solvate cations so it is not surprising that the presence of sodium cations in the hard segment helps mix the soft and hard segment, increasing the T_g . Simultaneously, with Na^+ counterions, many ion pairs associate, which also increases T_g . Other evidence of phase mixing in the Na-ionomer is that it has much higher T_g than a PEG600 based polyester ionomer PEG600- Na^+ ($T_g = -5$ °C) with similar ion concentration. [11] Although nonionic PU with pPDI hard segment tends to microphase separate, [140] there is no evidence from our DSC study for microphase separation in both the acid form precursor and the ionomers. It is clear in **Figure 4.15** that T_g scales inversely with cation acetate salt size.

Similar phenomena with various metal ions have also been observed in different ionomer systems. [146,148,149] Ion pairs associate to form physical cross-links and T_g reflects the energy required to separate associated ion pairs. [49,148] Larger cations have a longer distance between the positive and negative charge and require much less energy to separate them, originating from Coulomb's law: $E \sim e^2/d$, where e and $-e$ are charges carried by cation and anion and d is the distance between two charges. The lower interaction energy results in reduced T_g with an apparent inverse correlation with the ion size. Meanwhile, lower T_g also indicates fewer ionic cross-links [132,133] also due to weaker Coulombic interaction.

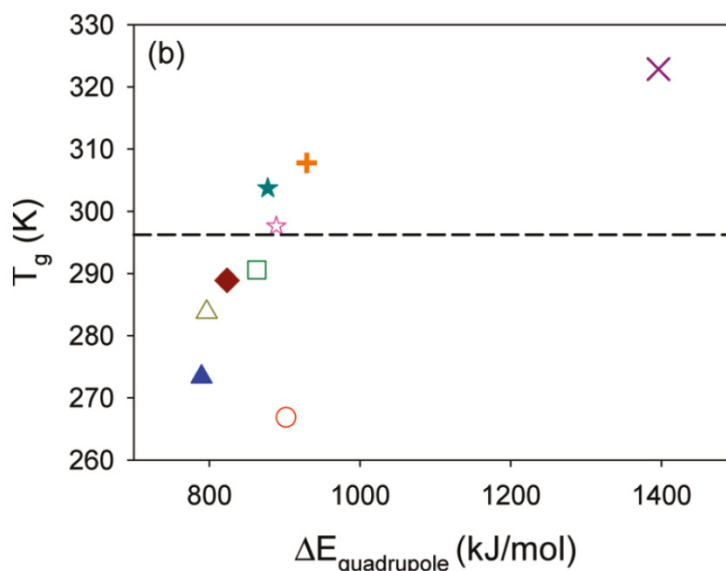


Figure 4.16. T_g from DSC as a function of quadrupole energy at 0K in vacuum. Open symbols are cations containing ether oxygen. Solid symbols are cations without ether oxygen. Purple X is Na^+ ; orange plus is Me_4N^+ ; cyan solid star is BuMeIm^+ ; pink open star is $(\text{MOE})\text{MeIm}^+$; green open square is $(\text{EO}_c)_2\text{Me}(\text{MOE})\text{N}^+$; dark red solid diamond is Bu_4N^+ ; blue solid triangle is Bu_4P^+ ; olive green open triangle is $\text{Bu}_3(\text{MOE})\text{P}^+$; red open circle is $(\text{MOEOE})_3\text{MeN}^+$; dash line is acid form for the reference.

T_g as a function of quadrupole energy (energy required to break quadrupoles) from *ab initio* calculation is also plotted in **Figure 4.16**. It shows similar results as **Figure 4.15** since quadrupole energy is strongly affected by counterion size due to Coulombic force. It is interesting that $(\text{MOEOE})_3\text{MeN}^+$ has the lowest T_g . The quadrupole energy of $(\text{MOEOE})_3\text{MeN}^+$ is not the lowest (an outlier in **4.16**), possibly because this energy is calculated at 0K under vacuum without consideration of any entropy contribution, which might be more important for $(\text{MOEOE})_3\text{MeN}^+$ due to its three much longer side chains.

Note also that tetrabutylphosphonium (Bu_4P^+) has T_g 20K lower than tetrabutylammonium (Bu_4N^+) despite similar size and chemical structure. This is due to the different electronegativity [150] of the nitrogen and phosphorus atoms in these two cations. This effect was carefully studied and discussed in [Section 3-3.3](#).

Table 4.8 shows the charge distribution of three classes of cations we study in this section: Bu_4P^+ , Bu_4N^+ , and BuMeIm^+ . The phosphorus atom at the center of Bu_4P^+ carries positive charge (+1.1e) because it is less electronegative than carbon and leaves the outer atoms to share -0.1e, whereas the nitrogen atom in Bu_4N^+ is more electronegative than carbon and carries negative charge (-0.5e) and leaves the surrounding atoms sharing +1.5e. The negatively charged outer layer of Bu_4P^+ provides better shielding of the positive charge at the center from anions, resulting in weaker Coulombic force and lower T_g (the two phosphonium cations have the smallest quadrupole energy in [Table 4.7](#) for the same reason). For Bu_4N^+ , the more positively charged molecule surface has stronger attraction with anions and thus has higher T_g . For imidazolium, although the nitrogen atom still is weakly negative like ammonium, the steric structure is very different. The nearly flat structure of the imidazole ring makes most of the atoms exposed to anions have a shorter effective distance compared to the tetrahedral ammonium and phosphonium, raising T_g of the ionomers with imidazolium counterions relative to the similar sized $(\text{EO}_c)_2\text{Me}(\text{MOE})\text{N}^+$ ammonium.

It is also interesting that attachment of ether-oxygen containing alkyl chains to the counterions have different effects on T_g : T_g is suppressed in ammonium and imidazolium but raised in phosphonium, again because of the electronegativity of C, O, N, and P and

different charge distributions. Ether-oxygen makes the adjacent carbon more positively charged which changes the surface charge distribution of phosphonium and increases T_g . In ammonium and imidazolium, where carbon atoms already carry positive charges, ether oxygens provide some shielding from anions and decrease T_g .

Conclusion:

Size and species of cations play important roles on glass transition temperature of ionomers. In this section, polyurethane carboxylate ionomers were synthesized by Shih-Wa Wang, based on poly(ethylene glycol) ($M_n = 600$) with various cations, from the small alkali metal Na^+ to large multiatom cations like ammonium, imidazolium and phosphonium. *ab initio* calculations were performed to determine the interaction energies of quadrupoles and charge distribution. These results were used to correlate with the glass transition temperature measured by DSC. Generally, larger cations result in lower T_g because of weaker Coulombic attraction with anions. Tetrabutylphosphonium (Bu_4P^+) has T_g 20K lower than tetrabutylammonium (Bu_4N^+) despite similar size and chemical structure, due to the different electronegativity of the nitrogen and phosphorus atoms in these two cations. Moreover, the attachment of ether-oxygen containing alkyl chains to the counterions have different effects on T_g : T_g is suppressed in ammonium and imidazolium but raised in phosphonium, because of the electronegativity of C, O, N, and P and different charge distributions. Ether-oxygen makes the adjacent carbon more positively charged which changes the surface charge distribution of phosphonium and increases T_g . In ammonium and imidazolium, where carbon atoms already carry positive charges, ether oxygens provide some shielding from anions and decrease T_g . To further

reduce the T_g of the ionomer, large phosphonium cations with a suitable amount of ether oxygen atoms attached in a low T_g polymer matrix is the right direction.

4.5. Summary

We presented three practical applications of *ab initio* calculations in rational ionomer design and understanding the dynamics and ion conduction mechanism in ionomers. *Ab initio* calculations can provide physically meaningful data such as, ion pair dipole moment, charge distribution, the interaction energies of ion pair, positive triple ion, negative triple ion and quadrupoles. We also defined aggregation factor and charged factor as the gauges for ion aggregation and conducting ion concentration.

The ion pair dipole moment from *ab initio* calculations was used in the Onsager theory to analyse the static dielectric constant of the ionomers ([Section 4.3](#)).

The electronic charge distributions on the ions of interest can reveal the underlying physics of ion interactions and the strengths of ion pair dipoles, such as, fluorination weakens the ion interaction, and imparts strong dipoles to these anions ([Section 4.2](#)). Another example of the usage of charge distribution, the negatively charged outer layer of phosphonium cations provides better shielding of the positive charge at the center from anions than ammonium cations, resulting in weaker Coulombic force and lower T_g (the two phosphonium cations have the smallest quadrupole energy in [Table 4.7](#) for the same reason) ([Section 4.4](#)). The third example, the electronegativity of C, O, N, and P and different charge distributions explained why the attachment of ether-

oxygen containing alkyl chains to the counterions have different effects on T_g : T_g is suppressed in ammonium and imidazolium but raised in phosphonium ([Section 4.4](#)).

A "quadrupole" state containing two interacting pairs was used to examine the tendency of the ion pairs to associate. A "quadrupole" state is the simplest form of ion aggregate. For the ionomers with similar structure but only different counterions, the higher the quadrupole energy is, the stronger and more aggregation the ionomer has, therefore the higher T_g ([Section 4.4](#)).

Based on the interaction energies of ion pair, positive triple ion, negative triple ion and quadrupoles coming from *ab initio* calculations, we defined the aggregation factor and charged factor as the gauges for ion aggregation and conducting ion concentration. For the ionomers with similar structures but only different counterions, the lower the aggregation factor, the lower the T_g is, and the higher the charged factor, the higher the conducting ion concentration gets. Lowering T_g obviously boosts ion mobility and conductivity. Conducting ion concentration is more complicated as it seems to involve also issues about specific solvation that are not yet fully understood ([Section 4.3](#)), which we tempt to include in the *ab initio* calculations by using the cluster-continuum solvation model (CCM) that includes specific solvation in the first shell surrounding the cation, all surrounded by a polarizable continuum to determine the relative energies of these four states at real temperature and dielectric constant to predict their relative concentrations in an equilibrium ion-ionomer system [1].

Hopefully, by these three examples of practical applications of *ab initio* calculations, we convinced you that first principle calculates are powerful tools and our

four state model provides insightful parameters to assist rational ionomer design and understanding the dynamics and ion conduction mechanism in ionomers.

References

- [1] H.S. Shiau, W. Liu, R. H. Colby, and M.J. Janik, J. Chem. Phys. **139**, 204905 (2013).
- [2] R.M. Fuoss and C.A. Kraus, J Am Chem Soc, **55**, 2387 (1933).
- [3] J. Barthel, R. Gerber, H.J. Gores and Ber. Bunsen-Ges. Phys. Chem. Chem. Phys. **88**, 616 (1984).
- [4] M. Hojo, T. Takiguchi, M. Hagiwara, H. Nagai and Y. Imai, J Phys Chem-Us **93**, 955 (1989).
- [5] S. Petrucci, M.C. Masiker, E.M. Eyring and J. Solut. Chem. **37**, 1031 (2008).
- [6] M. Hojo, T. Ueda, H. Hamada, Z.D. Chen and S. Umetani, J. Mol. Liq. **145**, 24 (2009).
- [7] M. Duclot, F. Alloin, O. Brylev, J.Y. Sanchez, and J.L. Souquet, Solid State Ionics **136-137**, 1153 (2000).
- [8] D. Fragiadakis, S. Dou, R.H. Colby, and J. Runt, Macromolecules **41**, 5723 (2008).
- [9] D. Fragiadakis, S. Dou, R.H. Colby, and J. Runt, J. Chem. Phys. **130**, 064907 (2009).
- [10] S. Dou, S. Zhang, R.J. Klein, J. Runt, and R.H. Colby, Chem. Mater. **18**, 4288 (2006).
- [11] R.J. Klein, S. Zhang, S. Dou, B.H. Jones, R.H. Colby, and J. Runt, J. Chem. Phys. **124**, 144903 (2006).
- [12] Y. Marcus, J. Solut. Chem. **16**, 735 (1987).
- [13] Y. Marcus, J Phys Chem B **111**, 572 (2007).
- [14] L. Onsager, J Am Chem Soc **58**, 1486 (1936).

- [15] S.W. Liang, U.H. Choi, W.J. Liu, J. Runt and R.H. Colby, *Chem Mater* **24**, 2316 (2012).
- [16] M.A. Ratner and D.F. Shriver, *Chem. Rev.* **88**, 109 (1988).
- [17] W.H. Meyer, *Adv. Mater.* **10**, 439 (1998).
- [18] (a) U. Chandrasekhar, *Adv. Polym. Sci.* **15**, 140 (1998). (b) J.-M. Tarascon and M. Armand, *Nature* **414**, 359 (2001). (c) D.R. Sadoway, *J. Power Sources* **129**, 1 (2004). (d) M. Armand and J.-M. Tarascon, *Nature*, **451** 652 (2008). (e) M.B. Armand, P.G. Bruce, M. Forscyth, B. Scrosati and W. Wieczorek, In *Energy Materials*; D.W. Bruce, D. O'Hare, R.I. Walton, Eds.; Wiley: New York, 2011; Chapter 1.
- [19] K.E. Thomas, S.E. Sloop, J.B. Kerr and J. Newman, *J. Power Sources* **89**, 132 (2000).
- [20] P.V. Wright, *MRS Bull.* **27**, 597 (2002).
- [21] K. Nagaoka, H. Naruse, I. Shinohara and M. Watanabe, *J. Polym. Sci.:Polym. Lett. Ed.* **22**, 659 (1984).
- [22] P.Z. Walden, *Phys. Chem.* **55**, 207 (1906).
- [23] (a) L. Zhang, Z. Zhang, S. Haring, M. Straughan, R. Butorac, Z. Chen, L. Lyons, K. Amine and R. West, *J. Mater. Chem.* **18**, 3713 (2008). (b) R.C. West, K. Amine, Z. Zhang, Q. Wang, and D.R. Vissers, U.S. Patent 0035154 A1, 2006. (c) N.A.A. Rossi, Z. Zhang, Y. Schneider, K. Morcom, L.J. Lyons, Q. Wang, K. Amine, and R. West, *Chem. Mater.* **18**, 1289 (2006). (d) Z. Zhang, L.J. Lyons, J.J. Jin, K. Amine and R. West, *Chem. Mater.* **17**, 5646 (2005). (e) Z. Zhang, L.J. Lyons, R. West and K. Amine, *Silicon Chem.*

- 3**, 259 (2005). (f) B. Oh, R.C. West and K. Amine, U.S. Patent 7588859 B1, 2009. (g) N.A.A. Rossi and R. West, Polym. Int. **58**, 267 (2009).
- [24] Y. Okamoto, T.F. Yeh, H.S. Lee, and T.A. Skotheim, J. Polym. Sci., Part A: Polym. Chem. **31**, 2573 (1993).
- [25] D.P. Siska and D.F. Shriver, Chem. Mater. **13**, 4698 (2001).
- [26] J.F. Snyder, J. C. Hutchison, M.A. Ratner and D.F. Shriver, Chem. Mater. **15**, 4223 (2003).
- [27] J.B. Kerr, In Lithium Batteries Science and Technology; G.-A.Nazri, G. Pistoia, Eds.; Kluwer Academic: Boston, MA, 2004; Chapter 19.
- [28] (a) T. Fujinami, A. Tokimune, M.A. Mehta, D.F. Shriver and G.C. Rawsby, Chem. Mater. **9**, 2236 (1997). (b) T. Fujinami and Y. Buzoujima, J. Power Sources **119**, 438 (2003).
- [29] (a) W. Xu, M.D. Williams and A. Angell, Chem. Mater. **14**, 401 (2002). (b) W. Xu, and A. Angell, Electrochim. Acta **48**, 2029 (2003). (c) X. Sun and J.B. Kerr, Macromolecules **39**, 362 (2006). (d) V. Aravindan and P. Vickraman, Solid State Sci. **9**, 1069 (2007). (e) N. Matsumi and H. Ohno, Main Group Chem. **5**, 297 (2006). (f) N. Matsumi, K. Sugai, K. Saramoto, T. Mizumo and H. Ohno, Macromolecules **38**, 4951 (2005). (g) T. Aoki, A. Konno and T. Fujinami, Electrochim. Acta **151**, A887 (2004).
- [30] S. Besner, A. Vallee, G. Bouchard and J. Prud'homme, Macromolecules **25**, 6480 (1992).
- [31] L.W. Shacklette, European Patent 0122381 A1, 1984.
- [32] T. Nagai, K. Matsumoto and K. Kajita, Japanese Patent 61214364 A, 1986.

- [33] J. Barthel, A. Schmid and H.J. Gores, *J. Electrochem. Soc.* **147**, 21 (2000).
- [34] D.N. Bhattacharyya, C.L. Lee, J. Smid and M. Szwarc, *J. Phys. Chem.* **69**, 608 (1965).
- [35] (a) L.P. Klemann and G.H. Newman, U.S. Patent 4, 060, 674, 1977; (b) L.P. Klemann and G.H. Newman, U.S. Patent 4, 104, 451, 1978; L.P. Klemann, G.H. Newman and E.L. Stogryn, E. L. U.S. Patent 4, 139, 681, 1979.
- [36] R.G. Pearson, *J. Am. Chem. Soc.* **85**, 3533 (1963).
- [37] F.M. Gray, *Solid Polymer Electrolytes: Fundamentals and Technological Applications*: VCH Publishers, Inc.: New York, 1991.
- [38] W. Liu, M.J. Janik and R.H. Colby, *ACS Symp. Ser.* 2011, 1096, 19, Ch. 2 of *Polymers for Energy Storage and Delivery: Polyelectrolytes for Batteries and Fuel Cells*; Soles, C., Runt, J., Eds.; Page K.
- [39] M. Salomon, *Electrochim. Acta* **30**, 1021 (1985).
- [40] Y. Kida, K. Yanagida, A. Yonai, A. Funahashi, T. Nohma and I. Yonezu, U.S. Patent 6, 537, 697 B2, 2003
- [41] C.L. Crawford, M.J. Barnes, R.A. Peterson, W.R. Wilmarth and M.L. Hyder, *J. Organomet. Chem.* **581**, 194 (1999).
- [42] M. Duclot, F. Alloin, O. Brylev, J.Y. Sanchez and J.L. Souquet, *Solid State Ionics* **136**, 1153 (2000).
- [43] (a) Y. Chernyak, *J. Chem. Eng. Data* **51**, 416 (2006). (b) R. Payne, I.E. Theodorou, *J. Phys. Chem.* **76**, 2892 (1972).

- [44] Z. Zhu, A.G. Einset, C.-Y. Yang, W.-W. Chen and G.E. Wnek, G. E. Macromolecules **27**, 4076 (1994).
- [45] Y.-J. Wang, S. Liang, W. Liu, U H. Choi and R.H. Colby, Polym. Prepr. **50** (2), 866 (2009).
- [46] R. Sablong, J.I.V.D. Vlugt, R. Thomann, S. Mecking, and D. Vogt, Adv. Synth. Catal. **347**, 633 (2005).
- [47] H. Noth and B. Wrackmeyer, Nuclear Magnetic Resonance Spectroscopy of Boron Compounds; Springer-Verlag: New York, 1978.
- [48] P. Romanato, S. Duttwyler, A. Linden, K.K. Baldridge and J.S. Siegle, J. Am. Chem. Soc. **132**, 7828–7829 (2010).
- [49] A. Eisenberg and J.-S. Kim, Introduction to Ionomers; Wiley: New York, 1998.
- [50] W. Wang, G.T. Tudryn, R.H. Colby and K.I. Winey, J. Am. Chem. Soc. **133**, 10826 (2011).
- [51] P.G. Bruce, F.M. Gray, Solid State Electrochemistry; Cambridge University Press: Cambridge, U.K., 1995.
- [52] R.J. Klein, D.T. Welna, A.L. Weikel, H.R. Allcock, and J. Runt, J. Macromolecules **40**, 3990 (2007).
- [53] R. Meziane, J.-P. Bonnet, M. Courty, K. Djellab and M. Armand, Electrochim. Acta **57**, 14 (2011).
- [54] A.S. Shaplov, P. S. Vlasov, M. Armand, E.I. Eozinskaya, D.O. Ponkratov, I.A. Malyshkina, F. Vidal, O.V. Okatova, G.M. Pavlov, C. Wandrey, I.A. Godovikov and Y.S. Vygodskii, Polym. Chem. **2**, 2609 (2011).

- [55] A.S. Shaplov, E.I. Lozinskaya, D.O. Ponkratov, I.A. Malyshkina, F. Vidal, P.-H. Aubert, O.V. Okatova, G.M. Pavlov, L.I. Komarova, C. Wandrey and Y.S. Vygodskii, *Electrochim. Acta* **57**, 74 (2011).
- [56] U H. Choi, M. Lee, S. Wang, W. Liu, K. I. Winey, H. W. Gibson and R. H. Colby, Ionic Conduction and Dielectric Response of Poly(imidazolium acrylate) Ionomers, *Macromolecules* **45**, 3974 (2012).
- [57] H. Weingärtner, *Angew. Chem. Int. Ed.* **47**, (4), 654 (2008).
- [58] M.D. Green and T.E. Long, *Polym. Rev.* **49**, (4), 291 (2009).
- [59] T. Welton, *Chem. Rev.* **99**, (8), 2071 (1999).
- [60] R.J. Soukup-Hein, M.M. Warnke and D.W. Armstrong, *Annu. Rev. Anal. Chem.* **2**, 145 (2009).
- [61] P. Hapiot and C. Lagrost, *Chem. Rev.* **108**, (7), 2238 (2008).
- [62] M. Armand, F. Endres, D.R. MacFarlane, H. Ohno and B. Scrosati, *Nat. Mater.* **8**, (8), 621 (2009).
- [63] M.C. Buzzeeo, R.G. Evans and R.G. Compton, *ChemPhysChem* **5**, (8), 1106 (2004).
- [64] H. Ohno, *Electrochemical Aspects of Ionic Liquids*. Wiley-Interscience/J. Wiley: Hoboken, 2005.
- [65] J. Leys, M. Wübbenhorst, C.P. Menon, R. Rajesh, J. Thoen, C. Glorieux, P. Nockemann, B. Thijs, K. Binnemans and S. Longuemart, *J. Chem. Phys.* **128**, (6), 064509 (2008).
- [66] J.G. Huddleston, A.E. Visser, W.H. Reichert, H.D. Willauer, G.A. Broker and R.D. Rogers, *Green Chem.* **3**, (4), 156 (2001).

- [67] Q. Zhu, Y. Song, X.F. Zhu and X.L. Wang, *J. Electroanal. Chem.* **601**, (1-2), 229 (2007).
- [68] T.L. Greaves and C. Drummond, *J. Chem. Rev.* **108**, (1), 206 (2008).
- [69] A. Fernicola, B. Scrosati and H. Ohno, *Ionics* **12**, (2), 95 (2006).
- [70] W. Xu and C.A. Angell, *Science* **302**, (5644), 422 (2003).
- [71] M. Galinski, A. Lewandowski and I. Stepniak, *Electrochim. Acta* **51**, (26), 5567 (2006).
- [72] H. Sakaebe and H. Matsumoto, *Electrochem. Commun.* **5**, (7), 594 (2003).
- [73] C. Nanjundiah, S.F. McDevitt and V.R. Koch, *J. Electrochem. Soc.* **144**, (10), 3392 (1997).
- [74] M. Ue, M. Takeda, A. Toriumi, A. Kominato, R. Hagiwara, and Y.J. Ito *Electrochem. Soc.* **150**, (4), A499 (2003).
- [75] M. Doyle, S.K. Choi and G. Proulx, *J. Electrochem. Soc.* **147**, (1), 34 (2000).
- [76] W. Lu, A.G. Fadeev, B.H. Qi, E. Smela, B.R. Mattes, J. Ding, G.M. Spinks, J. Mazurkiewicz, D.Z. Zhou, G.G. Wallace, D.R. MacFarlane, S.A. Forsyth and M. Forsyth, *Science* **297**, (5583), 983 (2002).
- [77] W. Ogihara, N. Suzuki, N. Nakamura and H. Ohno, *Polym. J.* **38**, (2), 117 (2006).
- [78] W. Ogihara, S. Washiro, H. Nakajima, and H. Ohno, *Electrochim. Acta* **51**, (13), 2614 (2006) .
- [79] H. Ohno, *Macromol. Symp.* **249**, 551 (2007).
- [80] H. Ohno, M. Yoshizawa and W. Ogihara, *Electrochim. Acta* **50**, (2-3), 255 (2004).
- [81] H. Nakajima and H. Ohno, *Polymer* **46**, (25), 11499 (2005).

- [82] S. Washiro, M. Yoshizawa, H. Nakajima and H. Ohno, *Polymer* **45**, (5), 1577 (2004).
- [83] O. Green, S. Grubjesic, S.W. Lee, and M. A. Firestone, *Polym. Rev.* **49**, (4), 339 (2009).
- [84] A. Noda, M. Watanabe, *Electrochim. Acta* **45**, (8-9), 1265 (2000).
- [85] P. Snedden, A.I. Cooper, K. Scott and N. Winterton, *Macromolecules* **36**, (12), 4549 (2003).
- [86] M.R. Xie, H.J. Han, L. Ding and J.X. Shi, *Polym. Rev.* **49**, (4), 315 (2009).
- [87] H. Chen, J.H. Choi, D. Salas-de La Cruz, K.I. Winey and Y.A. Elabd, *Macromolecules* **42**, (13), 4809 (2009).
- [88] M. Lee, U H. Choi, R.H Colby, and H.W. Gibson, *Chem. Mater.* **22**, (21), 5814 (2010).
- [89] Y.T Wang and G.A. Voth, *J. Am. Chem. Soc.* **127**, (35), 12192 (2005).
- [90] Y.T.Wang and G.A. Voth, *G. A. J. Phys. Chem. B* **110**, (37), 18601 (2006).
- [91] W. Jiang, Y.T. Wang, T.Y. Yan, and G.A. Voth, *J. Phys. Chem. C* **112**, (4), 1132 (2008).
- [92] J.N.A.C. Lopes and A.A.H. Padua, *J. Phys. Chem. B* **110**, (7), 3330 (2006).
- [93] C.J. Margulis, *Mol. Phys.* **102**, (9-10), 829 (2004).
- [94] M. Delsignore, H.E. Maaser and S. Petrucci, *J. Phys. Chem.* **88**, (11), 2405 (1984).
- [95] X.G. Sun, J.B. Kerr, C.L. Reeder, G. Liu, and Y.B. Han, *Macromolecules* **37**, (14), 5133 (2004).
- [96] C.J.F. Böttcher, *Theory of Electric Polarization*. Elsevier: Amsterdam, 1973; Vol. 1.

- [97] F. Kremer and A. Schönhal, Broadband Dielectric Spectroscopy. Springer-Verlag: New York, 2002.
- [98] J.R. Macdonald, Phys. Rev. **92**, (1), 4 (1953).
- [99] R. Coelho, Rev. Phys. Appl. **18**, (3), 137 (1983).
- [100] E. Barsoukov and J.R. Macdonald, J. R., Impedance Spectroscopy Theory, Experiment and Applications. Wiley: New York, 2005.
- [101] M. Tosoni, S. Laschat and A. Baro, Helv. Chim. Acta **87**, (11), 2742 (2004).
- [102] P.A. Heiney, Commission on Powder Diffraction Newsletter **32**, 9 (2005).
- [103] The Beilstein test was done as follows. A copper wire was heated in a burner flame until there was no further coloration of the flame. The wire was allowed to cool slightly, then dipped into the monomer and again heated in the flame. A green flash is indicative of halide ions, whereas pure Tf_2N^- and PF_6^- salts give orange or red colors.
- [104] H.V.R. Annapureddy, H.K. Kashyap, P.M. De Biase and C.J. Margulis, J. Phys. Chem. B **114**, (50), 16838 (2010).
- [105] D. Salas de la Cruz, M.D. Green, Y. Ye, Y.A. Elabd, T.E Long and K.I. Winey, J. Polym. Sci., Part B: Polym. Phys. **49**(12), 873 (2011).
- [106] W.Q. Wang, W.J. Liu, G.J. Tudryn, R.H. Colby and K.I. Winey, Macromolecules **43**, (9), 4223 (2010).
- [107] W. Wang, G.J. Tudryn, R.H. Colby and K.I. Winey, J. Am. Chem. Soc. **133**, (28), 10826 (2011).

- [108] Q. Russina, A. Triolo, L. Gontrani, R. Caminiti, D. Xiao, L.G. Hines, R.A. Bartsch, E.L. Quitevis, N. Pleckhova and K.R. Seddon, *J. Phys.: Condens. Matter* **21**, (42), 424121 (2009).
- [109] B.L. Bhargava, R. Devane, M.L. Klein and S. Balasubramanian, *Soft Matter* **3**, (11), 1395 (2007).
- [110] R. Coelho, *J. Non-Cryst. Solids* **131**, 1136 (1991).
- [111] R. Coelho, *Physics of Dielectrics for the Engineer*. Elsevier: New York, 1979.
- [112] G.J. Tudryn, W.J. Liu, S.W. Wang and R.H. Colby, *Macromolecules* **44**, (9), 3572 (2011).
- [113] S.W. Wang, W.J. Liu and R.H. Colby, *Chem. Mater.* **23**, (7), 1862 (2011).
- [114] H. Tokuda, K. Hayamizu, K. Ishii, M.A.B.H. Susan and M. Watanabe, *J. Phys. Chem. B* **109**, (13), 6103 (2005).
- [115] A. Kumar and T. Singh, *J. Phys. Chem. B* **112**, (41), 12968 (2008).
- [116] L. Onsager, *J. Am. Chem. Soc.* **58**, (8), 1486 (1936).
- [117] N.E. Hill, W.E. Vaughan, A.H. Price and M. Davies, *Dielectric Properties and Molecular Behaviour*. Van Nostrand Reinhold Company: London, 1969.
- [118] H. Fröhlich, *Theory of Dielectrics : Dielectric Constant and Dielectric Loss*. Oxford : Clarendon Press: London, 1949.
- [119] J.G. Kirkwood, *J. Chem. Phys.* **7**, (10), 911 (1939).
- [120] G. Oster and J.G. Kirkwood, *J. Chem. Phys.* **11**, (4), 0175 (1943).
- [121] E.I. Izgorodina, M. Forsyth and D.R. MacFarlane, *Phys. Chem. Chem. Phys.* **11**, (14), 2452 (2009).

- [122] M. Wübbenhorst and J. van Turnhout, *J. Non-Cryst. Solids* **305**, (1-3), 40 (2002).
- [123] D.E. Fenton, J.M. Parker and P.V. Wright, *Polymer* **14**, 589 (1973).
- [124] Z. Gadjourova, Y.G. Andreev, D.P. Tunstall and P.G. Bruce, *P. G. Nature* **412**, 520 (2001).
- [125] J.F. Snyder, R.H. Carter and E.D. Wetzel, *Chem. Mater.* **19**, 3793 (2007).
- [126] M. Singh, O. Odusanya, G.M. Wilmes, H.B. Eitouni, E.D. Gomez, A.J. Patel, V.L. Chen, M.J. Park, P. Fragouli, H. Iatrou, N. Hadjichristidis, D. Cookson, and N.P. Balsara, *Macromolecules* **40**, 4578 (2007).
- [127] E.D. Gomez, A. Panday, E.H. Feng, V. Chen, G.M. Stone, A.M. Minor, C. Kisielowski, K.H. Downing, O. Borodin, G.D. Smith and N.P. Balsara, *Nano Lett.* **9**, 1212 (2009).
- [128] S. Ramesh and G. Radhakrishnan, *J. Polym. Mater.* **16**, 135 (1999).
- [129] Y.S. Ding, R.A. Register, C.-Z. Yang and S.L. Cooper, *Polymer* **30**, 1204 (1989).
- [130] S.A. Visser and S.L. Cooper, *Macromolecules* **24**, 2576 (1991).
- [131] S.R. Williams, W. Wang, K.I. Winey and T.E. Long, *Macromolecules* **41**, 9072 (2008).
- [132] C.-Z. Yang, T.G. Grasel, J.L. Bell, R.A. Register and S.L. Cooper, *J. Polym. Sci., Part B: Polym. Phys.* **29**, 581 (1991).
- [133] S.-A. Chen and J.-S. Hsu, *Polymer* **34**, 2769 (1993).
- [134] D.-C. Lee, R.A. Register, C.-Z. Yang and S.L. Cooper, *Macromolecules* **21**, 1005 (1988).
- [135] H.-S. Xu and C.-Z. Yang, *J. Polym. Sci., Part B: Polym. Phys.* **33**, 745 (1995).

- [136] R. Jayakumar, S. Nanjundan and M. Prabakaran, *J. Macromol. Sci., Part C: Polym. Rev.* **45**, 231 (2005).
- [137] P. Pissis, G. Polizos, In *Handbook of Condensation Thermoplastic Elastomers*; S. Fakirov, Ed.; Wiley-VCH: Weinheim, Germany, 2005, pp 381-434.
- [138] G. Polizos, G. Georgoussis, A. Kyritsis, V.V. Shilov, V.V. Shevchenko, Y.P. Gomza, S.D. Nesin, N.S. Klimenko, S. Wartewig and P. Pissis, *Polym. Int.* **49**, 987 (2000).
- [139] X. Wei and X. Yu, *J. Polym. Sci., Part B: Polym. Phys.* **35**, 225 (1997).
- [140] J.P. Sheth, D.B. Klinedinst, G.L. Wilkes, I. Yilgor and E. Yilgor, *E. Polymer* **46**, 7317 (2005).
- [141] M. Ishida, K. Yoshinaga and F. Horii, *Macromolecules* **29**, 8824 (1996).
- [142] A.D. Becke, *J. Chem. Phys.* **98**, 5648 (1993).
- [143] C.T. Lee, W.T. Yang, and R.G. Parr, *Phys. Rev. B* **37**, 785 (1988).
- [144] S.H. Vosko, L. Wilk and M. Can. Nusair, *J. Phys.* **58**, 1200 (1980).
- [145] P.J. Stephens, F.J. Devlin, C.F. Chabalowski, M.J. Frisch, *J. Phys. Chem.* **98**, 11623 (1994).
- [146] H.A. Al-Salah, K.C. Frisch, H.X. Xiao and J.A.Jr. McLean, *J. Polym. Sci., Part A: Polym. Chem.* **25**, 2127 (1987).
- [147] H. Chen, D. Chen, Q. Fan and X. Yu, *J. Appl. Polym. Sci.* **76**, 2049 (2000).
- [148] A. Eisenberg, *Macromolecules* **4**, 125 (1971).
- [149] R.A. Weiss, P.K. Agarwal, and R.D. Lundberg, *J. Appl. Polym. Sci.* **29**, 2719 (1984).

- [150] L. Pauling, *The Nature of the Chemical Bond and the Structure of Molecules and Crystals: An Introduction to Modern Structural Chemistry*, 3rd ed.; Cornell University Press: Ithaca, NY, 1960.
- [151] U H. Choi, A. Mittal, T.L. Price, Jr., H.W. Gibson, J. Runt and R.H. Colby, *Macromolecules* **46**, 1175 (2013).
- [152] U H. Choi, Y. Ye, D. Salas de la Cruz, W. Liu, K.I. Winey, Y.A. Elabd, J. Runt and R.H. Colby, *Macromolecules* **47**, 777 (2014).

VITA

Wenjuan Liu

Wenjuan Liu was born in Henan, China, on Sept. 13, 1980. In September 1999, she enrolled in Mechanics and Engineering Science Department at Fudan University in Shanghai, China. In the summer of her sophomore year, Wenjuan was invited to do research in Chemical Engineering at National Tsing Hua University in Taiwan on liquid crystal displays and electronic memory devices. In July 2003, Wenjuan received her Bachelor of Science degree with distinctive honor. Her Bachelor thesis was entitled: Fabrication and Simulation of Holographic Polymer-dispersed Liquid Crystal Films for the applications of Liquid Crystal Displays and Electronic Memory Devices. Wenjuan was admitted to the Graduate School at The Pennsylvania State University in August, 2004. She was awarded her Master of Science degree in Materials Science and Engineering Department in August 2007. Her Master thesis was entitled: Effect of Thermally Driven Fluctuations on Segmental Dynamics of Polymer Melts. She then continued to pursue her Ph.D. degree in the same research group, focusing on designing ion-containing polymers for facile ion transport in the application of lithium ion batteries and actuators. In the winter of 2009, Wenjuan Liu was invited to do research at Kyoto University and Waseda University on rheo-dielectric behavior of ionomers/ionic liquids and organic radical batteries. Wenjuan successfully defended her doctoral dissertation in public in Mar. 2010.